Growth of epitaxial graphene on SiC (0001) by sublimation at low argon pressure

Tianlin Wang

THÈSE POUR OBTENIR LE GRADE DE DOCTEUR
DE L'UNIVERSITÉ DE MONTPELLIER

En : Physique

École doctorale : Information, Structures, Systèmes (I2S)

Unité de recherche : Laboratoire Charles Coulomb, L2C-UMR 5221

Growth of epitaxial graphene on SiC (0001) by sublimation at low argon pressure

Présentée par Tianlin WANG

Le 12 octobre, 2018

Sous la direction de Sylvie CONTRERAS

Devant le jury composé de

Nedjma BENDIAB, Maître de conférences	Institut Néel-CNRS, Université Grenoble Alpes	Rapporteur
Lucyna FIRLEJ, Professeur	L2C-CNRS, Université de Montpellier	Présidente
Rositsa YAKIMOVA, Professeur	IFM, Université de Linköping	Examinatrice
Abdelkarim OUERGHI, Chargé de recherche	C2N-CNRS, Université Paris Sud	Rapporteur
Philippe GODIGNON, Professeur	CNM-CSIC, Barcelone	Examinateur
Gabriel FERRO, Directeur de recherche	LMI-CNRS, Université Claude Bernard Lyon I	Examinateur
Adrien MICHON, Chargé de recherche	CRHEA, Valbonne	Invité
Jean-Manuel DECAMS, PhD	Annealsys, Montpellier	Invité
Sylvie CONTRERAS, Chargée de recherche	L2C-CNRS, Université de Montpellier	Directrice de thèse
Périne LANDOIS, Maître de conférences	L2C-CNRS, Université de Montpellier	Co-Encadrante de thèse

UNIVERSITÉ DE MONTPELLIER

Remerciements

Le travail présenté dans ce mémoire a été réalisé au sein de Laboratoire Charles Coulomb (L2C) à Montpellier. En premier lieu je remercie très sincèrement Sylvie Contreras, Chargée de Recherche au CNRS et Périne Landois, Maître de conférences à l'Université de Montpellier, pour avoir dirigé et encadré mes travaux durant ces trois années. J'exprime ici toute ma gratitude à ces deux chefs pour leurs compétences scientifiques et leur dynamisme qui ont permis de mener à bien cette étude. Elles m'ont toujours soutenu tout en m'offrant beaucoup de liberté.

Je suis honorée et heureuse d'avoir défendu ma thèse devant le jury constitué de Nedjma Bendiab, Lucyna Firlej, Rositsa Yakimova, Abdelkarim Ouerghi, Philippe Godignon et Gabriel Ferro, Sylvie Contreras et Périne Landois. Merci en particulier à Madame Nedjma Bendiab, Maître de conférences à l'Institut Néel et à Monsieur Abdelkarim Ouerghi, Chargé de recherche au Centre de Nanosciences et de Nanotechnologies, d'avoir accepté d'être rapporteurs de ce mémoire. Je tiens également à remercier Madame Rositsa Yakimova, Professeur Émérite à l'Université de Linköping (Suède), pour sa participation à mon jury de thèse.

Je remercie Matthieu Paillet, Chargé de Recherche au CNRS, et Jean-Roch Huntzinger, Maître de conférences à l'Université de Montpellier pour m'avoir fait profiter de leurs connaissances scientifiques en spectrométrie Raman ainsi que pour leurs contributions à ce travail et les discussions enrichissantes que nous avons eu. Merci aussi pour leurs relectures et les conseils avisés qu'ils m'ont souvent donnés.

Mes remerciements vont aussi à l'ensemble des membres de notre équipe avec qui j'ai eu l'occasion de travailler : Benoit Jouault, Wilfried Desrat, Leszek Konczewicz, Sébastien Nanot, Christophe Roblin, Sandrine Juillaguet, Hervé Peyre. Merci aussi à Matthieu Moret, Antoine Tiberj et Olivier Briot qui ont supporté mes nombreuses visites dans leurs salles pour utiliser l'AFM et l'appareil de mesure de transport. Je n'oublie pas non plus Ahmed-Azmi Zahab et Maxime Bayle pour m'avoir aidé à analyser au mieux les spectres Raman grâce au logiciel RAC.

J'adresse mes remerciements à Franck Laporte, Président de la société ANNEALSYS (Montpellier, France) et Jean-Manuel Decams, Directeur de la recherche et du développement de la société ANNEALSYS pour leurs réponses toujours efficaces et positives concernant le four Zenith-100 et les process associés.

Je suis reconnaissante envers Clemens Winkelmann, Maître de conférence à l'Institut Néel, Alessandro De Cecco et Hervé Courtois pour leurs mesures indispensables en microscopie à effet tunnel. Merci Clemens pour le travail de relecture sur les parties STM. Merci Alessandro pour ces belles images STM.

Merci à toutes les personnes que j'ai côtoyé au laboratoire pendant ces trois années et qui m'ont rendu la vie agréable. Je pense notamment à Phuong Vuong, Huong Ngo et Abir Natchawaty pour tout ce que nous avons partagé. Je suis très heureuse d'avoir passé tout ce temps à vos côtés.

Finalement, je remercie mes parents pour m'avoir offert la possibilité de faire ces études ainsi que pour leur encouragement durant toute cette période.

Table of contents

List of abbreviations

1LG	monolayer graphene
$A_{G\text{-}graphene}$	integrated intensity of G-peak of graphene
$A_{G\text{-}HOPG}$	integrated intensity of G-peak of HOPG
AES	Auger electron spectroscopy
AFM	atomic force microscopy
ARPES	angle-resolved photoemission spectroscopy
BL	buffer layer
BL_0	bare buffer layer from direct growth
BL_{1LG}	interfacial buffer layer between graphene and SiC
$BL_{1LGminusG}$	covered interfacial buffer layer after subtract G-peak of graphene
BZ	Brillouin zone
CCS	confinement-controlled sublimation
CMOS	complementary metal-oxide semiconductor
CMP	chemical-mechanical planarization
CVD	chemical vapor deposition
DIC	differential interference contrast
DOS	density of states
EG	epitaxial graphene
FLG	few layer graphene
FT	Fourier transform
FWHM	full width at half maximum
GFET	graphene field effect transistor
HOPG	high oriented pyrolytic graphite

ITO	indium tin oxide
LDOS	local density of states
LEED	low-energy electron diffraction
LEEM	low-energy electron microscopy
LL	Landau level
MOSFET	metal-oxide-semiconductor field effect transistor
QHE	quantum Hall effect
RMS	root mean square
RT	room temperature
RTP	rapid thermal processing
SEM	scanning electronic microscopy
SiC	silicon carbide
STM	scanning tunneling microscopy
STS	scanning tunneling spectroscopy
UHV	ultra-high vacuum
XPS	x-ray spectroscopy

List of figures

List of tables

Résumé en français de la thèse

Le graphène, la dernière forme allotropique du carbone découverte, est une seule couche d'atomes de carbone sp^2 organisés sous forme d'un réseau hexagonal en nid d'abeille. Ce matériau bidimensionnel (2D) avec une structure électronique en « cône de Dirac » suscite depuis quelques années un engouement dans la communauté scientifique et la spectroscopie Raman s'avère être une technique centrale pour sa caractérisation et l'étude de ses propriétés physiques.

En 2004, deux chercheurs ont réussi à isoler le graphène par exfoliation mécanique, et en caractériser quelques plans. Andre Geim et Konstantin Novoselov ont reçu pour cette découverte le Nobel de physique 2010. Depuis, le graphène est souvent présenté comme un candidat potentiel pour de futures applications en « nanoélectroniques ». Ses propriétés exceptionnelles telles que les hautes mobilités mesurées, permettent d'envisager une nouvelle génération de dispositifs en micro et nano électronique. De plus, d'autres propriétés du graphène, telle que sa transparence, sa conductivité thermique et son élasticité, permettent des applications dans l'électronique flexible en remplacement par exemple de l'ITO (indium tin oxide). Ces dernières années, un étalon quantique de résistance, très précis pour la métrologie, a été développé à base de graphène sur carbure de silicium (SiC). Ces étalons de résistance fonctionnent à des températures de l'ordre de 10 K, des champs magnétiques de seulement 3 teslas et des courants de mesure allant jusqu'à 0,5 mA. Ces conditions expérimentales moins contraignantes que celles nécessaires pour les étalons actuels en GaAs/AlGaAs sont un atout considérable pour la métrologie.

Ces exemples d'application montrent l'intérêt crucial de maîtriser l'obtention de ce matériau lamellaire. La technique dite du « scotch » permet d'obtenir des échantillons de très haute qualité mais de faible surface limitant le passage à grande échelle. La croissance par dépôt chimique en phase vapeur (Chemical Vapor Deposition, CVD) sur métaux est intéressante pour ces grandes surfaces et l'homogénéité des couches obtenues. Cependant, cette technique demande, dans la plupart des cas, une étape de report sur un substrat adapté à la caractérisation ou à l'application visée. Dans le cas de la graphitisation, le graphène est directement généré à partir du substrat de carbure de silicium (SiC), par sublimation des atomes de Si à haute température. L'avantage de cette technique est de pouvoir synthétiser un plan homogène de graphène sur un substrat isolant qui est compatible avec les techniques de lithographie. Désormais, le processus est bien maitrisé sur la face Si du SiC (SiC (0001)) à une pression d'argon de 1 atmosphère et des échantillons de qualité ont été aussi obtenus sous ultravide. Cependant, la croissance sous faible pression d'argon est peu étudiée et aucun travail n'a montré une couche uniforme de graphène synthétisé dans ces conditions.

L'objectif de ma thèse est donc d'optimiser une méthode de croissance sous faible pression d'argon, 10 mbar, permettant la synthèse reproductible et contrôlée des monocouches de graphène par sublimation du SiC (0001) dans un four prototype RTP (Rapid Thermal Processing) – CVD développé par la société montpelliéraine Annealsys.

La croissance par sublimation consiste à chauffer le substrat de SiC à haute température sous une pression contrôlée. **Le SiC** s'organise en bicouche d'atomes silicium et carbone (Si-C). La séquence d'empilement constituée de N bicouches élémentaires définit le polytype. Dans la littérature, on compte plus de 200 polytypes qui ont des propriétés physiques (mécaniques, thermiques) communes mais qui présentent des différences notables de propriétés électroniques. Parmi ces polytypes, seuls trois présentent un intérêt pour les applications microélectroniques : 3C-SiC, 4H-SiC et 6H-SiC. Aujourd'hui, dans ce domaine, le 4H-SiC a supplanté tous les autres polytypes en raison de ses meilleures propriétés électroniques mais aussi en raison de l'amélioration continue de sa qualité cristalline et de l'augmentation régulière de la taille des substrats (150 mm actuellement pour les produits commerciaux). Le SiC présente deux faces de nature différente : une face terminée par un plan d'atomes Si, appelé « face silicium » et une autre terminée par un plan d'atomes C, appelé « face carbone ». Par convention, pour le 4H-SiC, la face Si est indexée par les indices de Miller (0001) et la face C est indexée $(000\bar{1})$. La croissance du graphène sur SiC est fortement dépendante de la surface choisie. Dans cette thèse, nous nous intéressons uniquement à la croissance du graphène sur SiC (0001). **La sublimation du silicium** apparait à des températures plus basses que celle du carbone, laissant alors place aux atomes de carbone pour se réorganiser et former des couches graphitiques. La littérature rapporte qu'environ trois bicouches de Si-C sont nécessaires pour former une couche de graphène. La graphitisation sur SiC nécessite plusieurs étapes qui se distinguent par leurs reconstructions de surface. La première couche de carbone, est une couche tampon (buffer layer), correspondant à une reconstruction de surface $6\sqrt{3}\times6\sqrt{3}$ R30°. Cette interface, présente uniquement sur la face SiC (0001), est constituée d'atomes de carbone arrangés en nid d'abeille. Cette structure est proche de celle du graphène mais un certain nombre d'atomes se lient au substrat par liaison covalente. Par conséquence, les propriétés électroniques de cette couche sont différentes de celles du graphène du fait de l'absence de liaisons π délocalisées. Lors de la croissance, cette couche joue un rôle de modèle pour la graphitisation suivante. Une nouvelle couche se forme entre le substrat et la couche tampon. Cette dernière ne va plus être liée au substrat et formera le graphène.

Le chapitre 1 est consacré à la présentation générale des principales propriétés de la monocouche de graphène, suivie d'un état de l'art sur les méthodes conventionnelles d'élaboration du matériau en précisant les avantages et les limitations de chacune d'entre elles.

De nombreuses techniques sont accessibles au sein du laboratoire pour étudier les propriétés structurales et électroniques du graphène. La microscopie optique, la spectroscopie Raman, la microscopie à force atomique (AFM), et des mesures de transport en champ magnétique ont été principalement utilisées pour avoir un retour sur la qualité et les caractéristiques des échantillons. Ces techniques sont présentées dans **le chapitre 2** et en annexes.

Le chapitre 3 décrit les premières étapes de la croissance du graphène par sublimation sur la face Si sous basse pression d'argon. La croissance de la couche tampon sans graphène est le point de départ de l'optimisation de la synthèse de la monocouche de graphène. Lorsque la température du réacteur dépasse la température de croissance de la couche tampon, on observe l'apparition du graphène sous forme de rubans et de doigts. Nous expliquons les mécanismes de la croissance qui commence en bord de marches et continue sur les terrasses. A plus haute température, 1750°C, on obtient une couche homogène de graphène qui couvre toute la surface. Pour confirmer la présence et la qualité du graphène épitaxié, nous croisons les résultats de plusieurs techniques expérimentales. L'évaluation des propriétés structurales et électroniques est ainsi possible. On obtient par spectroscopie Raman, le rapport $A_{G\text{-graphène}} / A_{G\text{-HOPG}}$ (intensité intégrée de la bande G du graphène, normalisée par celle de la bande G du HOPG (Highly Oriented Pyrolitic Graphite) qui est proche de 3%, valeur attendue pour la monocouche de graphène sur SiC (λ = 532 nm). Les mesures de magnétotransport mettent en évidence un effet Hall quantique à basse température (2 K) sous fort champ magnétique (jusqu'à 13T). La valeur du plateau de résistance de Hall est d'environ 12 kΩ. Ces résultats sont complémentaires et démontrent, sans ambiguïté, la présence d'un film de graphène monocouche continu. Des mesures de topographie par AFM ont permis d'observer la structure de marches de nos échantillons. Des cartographies Raman de la bande 2D montrent également que la couche de graphène est continue. La phase de l'AFM ne montre aucun contraste indiquant une couche uniforme. De plus, le super-réseau 6 × 6 a pu être mis en évidence par STM lors de mesures faites à l'Institut Néel à Grenoble par Clemens Winkelmann. Cette dernière mesure nous permet de confirmer la qualité de la monocouche de graphène obtenue dans nos conditions de croissance. Ces conditions de croissance ont été reproduites plus de 50 fois pendant cette thèse démontrant (i) la possibilité d'obtenir une monocouche de graphène de qualité sous basse pression d'argon, (ii) les performances du four prototype de la société

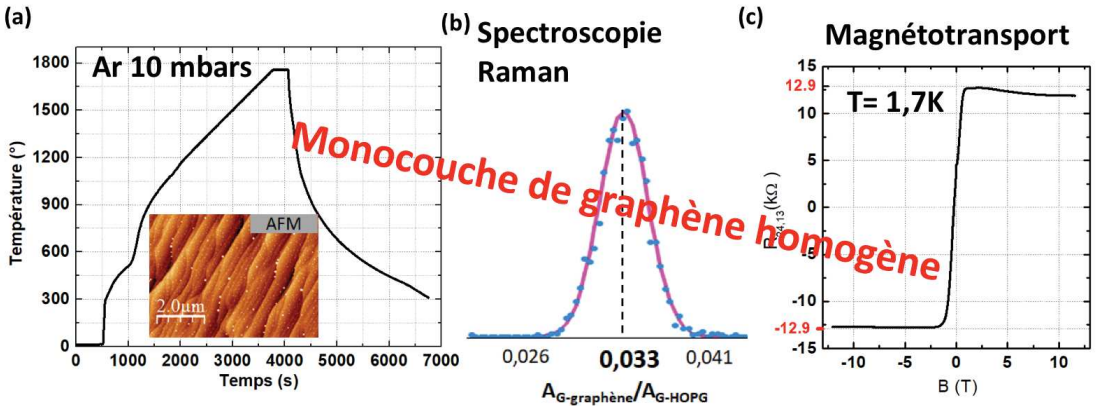

Fig. R.1 Exemples de résultats complémentaires des différentes techniques permettant de démontrer la présence d'une monocouche de graphène sur nos substrats de SiC : (a) par AFM, observation des marches de surface pour la rampe de température adaptée. (b) par spectroscopie Raman, $A_{G\text{-graphène}} / A_{G\text{-HOPG}} \sim 3\%$. (c) par magnéto-transport, la valeur du plateau de la résistance de Hall de l'effet Hall quantique est ~ 12 kΩ.

Annealsys (soulignons que ces résultats ont permis la vente de deux fours par l'industriel) et (iii) la reproductibilité et la robustesse de ce procédé. Suite à l'optimisation de la croissance de monocouche de graphène, nous avons étudié l'impact de certains paramètres de croissance sur les propriétés du graphène. Dans la littérature, des études ont montré l'effet des largeurs de marches et des terrasses sur les propriétés électroniques du graphène. Dans ce sens, des recherches ont été menées pour tenter de contrôler la topographie de surface du SiC en vue d'évaluer l'effet de ce contrôle sur la résistivité, le dopage ou encore la mobilité du graphène. Dans ce travail, nous avons choisi de faire varier la rampe de température pour modifier la hauteur des marches et la largeur des terrasses. Nous avons pu observer, sur une série d'échantillons, des terrasses de plus en plus larges lorsque la rampe de croissance diminuait de 1 à 0,1°C/s. Des largeurs de marches de l'ordre de 10 µm ont pu être obtenues permettant d'envisager des mesures électriques localisées sur une seule marche en s'affranchissant ainsi d'un possible effet d'anisotropie du substrat. Ces échantillons particuliers sont présentés à la fin du chapitre 3. Ils ouvrent des perspectives sur des mesures électriques originales à température ambiante et à basse température - avec ou sans champ magnétique.

La formation d'une couche d'interface, dénommée couche tampon, a un fort impact sur les propriétés électroniques et structurales du graphène épitaxié sur SiC (0001). La littérature est encore limitée dans ce domaine et une meilleure compréhension de la couche tampon permettrait notamment une meilleure compréhension des mécanismes de croissance du graphène. **Le chapitre 4** présente une étude approfondie de cette couche tampon et démontre l'interaction qui existe entre cette couche et le graphène. Ces études sont menées essentiellement à partir d'analyses de spectroscopie Raman qui mettent en évidence l'absence d'une signature unique de la couche tampon dans les très nombreux spectres obtenus. Deux techniques d'exfoliation mécanique du graphène ont été mis en œuvre pour avoir accès à la couche tampon sur SiC sans graphène. Le graphène est exfolié mécaniquement après avoir déposé à sa surface, une couche mince soit de nickel soit d'une colle à base d'époxy. Deux approches sont ainsi testées. Les signatures Raman des couches tampon couvertes ou non de graphène ont ensuite été analysées et comparées. Deux méthodes d'analyse sont utilisées pour cette comparaison : une analyse par ajustement (position, intensité intégrée et largeur à mi-hauteur de quatre pics) et une analyse par intensité intégrée seule (aire de trois régions distinctes). Il est important de pouvoir analyser, sur la même surface de l'échantillon, la couche tampon avant et après l'exfoliation afin d'étudier l'interaction des deux couches. Suite au transfert, des zones de couche tampon sans graphène sont présentes sur le substrat de SiC, le graphène se retrouve en miroir sur le nickel ou la colle. Un repositionnement des échantillons au micron prés, permet de cartographier la même zone avant et après exfoliation par spectroscopie Raman et de l'imager par AFM. Les résultats obtenus sont robustes car ils sont confirmés par les deux méthodes de transfert. Ces résultats donnent des informations importantes sur la couche tampon elle-même et sur l'interaction de cette couche avec le graphène. **Concernant la couche tampon**, l'étude d'un très grand nombre de spectres (étude quasi-statistique sur plus de

15 000 spectres) démontre qu'il n'existe pas une signature unique de celle-ci. Toutefois, nous retrouvons systématiquement, sur toutes les couches tampon étudiées, une bande vers 3000 cm^{-1} en plus des bandes déjà identifiées entre 1200 cm^{-1} et 1800 cm^{-1}. Contrairement à la littérature, nous n'avons pas observé un effet de la température de croissance sur le signal Raman du buffer.

Concernant l'interaction de la couche tampon avec le graphène, un résultat majeur de cette étude est la mise en évidence du couplage qui existe quand la couche tampon est couverte par le graphène :

i. L'apparition de deux pics fins sur le spectre Raman à 1235 cm^{-1} et 1360 cm^{-1}
ii. Un décalage vers les faibles nombres d'onde (down-shift), d'au moins 8 cm^{-1}, la bande dites « G » de la couche tampon.
iii. Une diminution de l'aire globale des bandes entre 1200 cm^{-1} et 1800 cm^{-1} de la couche tampon.

Pour aller plus loin, ces couches tampons ont été également comparées à celle obtenues directement par croissance, c'est-à-dire obtenues dans des conditions de croissance optimisées pour ne pas aller jusqu'à la formation du graphène. On retrouve bien sur ces couches les comportements observés ci-dessus en absence de la couche de graphène.

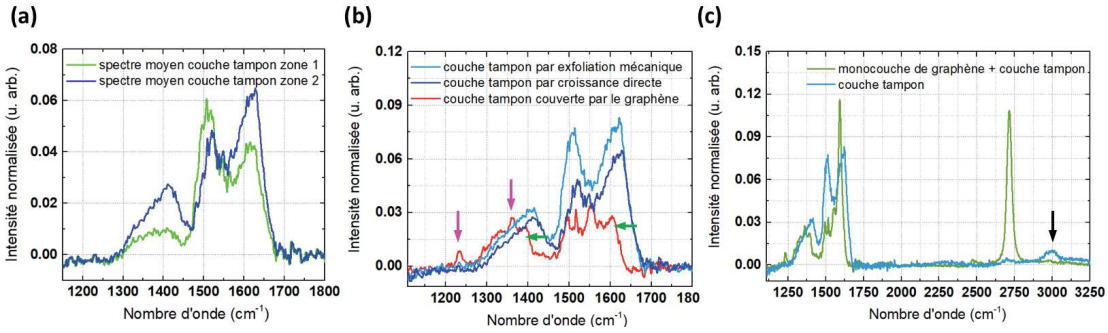

Fig. R.2 Les signatures Raman des couches tampon couvertes ou non de graphène : (a) couche tampon sans graphène obtenues directement par croissance : il n'existe pas de signature unique de cette couche. (b) mise en évidence du couplage qui existe quand la couche tampon est couverte par le graphène : présence de deux pics fins (flèches magenta), décalage vers les faibles nombres d'onde (flèches vertes) et diminution de l'aire globale des bandes de la couche tampon. (c) apparition d'une bande vers 3000 cm^{-1} (flèche noire) pour les couches tampon.

La dernière partie du manuscrit concerne les propriétés électriques des monocouches de graphène sur SiC élaborées pendant la thèse. Contrairement au classique dopage n du graphène épitaxié sur SiC (0001) (~10^{13} cm^{-2}), un dopage résiduel de type-p a été systématiquement mesuré sur nos échantillons (dès la sortie du réacteur) et attribué à un effet de l'environnement. **Le chapitre 5** présente les résultats sur l'évolution du dopage des échantillons sous différentes conditions atmosphériques. En effet, il a été démontré dans la littérature que la présence, à température ambiante, d'impuretés chargées à la surface du graphène faisait varier le niveau de Fermi localement.

Les impuretés chargées présentes à la surface des échantillons pourraient être à l'origine de « flaques » d'électrons et de trous (puddles) réparties à la surface des échantillons et responsables de leur dopage inhomogène. Ces fluctuations de potentiel ont été estimées en ajustant les données expérimentales à partir d'un modèle mettant en jeu deux types de porteurs. La valeur moyenne du désordre ainsi évaluée dans nos échantillons ($s = 27 \pm 10$ meV) est en accord avec celles de la littérature pour du graphène sur SiC. Pour aller plus loin, nous avons pu mettre en évidence un changement de dopage d'un type p à n sous vide et sous illumination ultraviolet (UV). La désorption d'adsorbats chargés pourrait expliquer ce changement. Ces résultats démontrent une possible modulation des propriétés électriques de nos échantillons par un facteur externe. En effet, des mesures STM menées en collaboration avec l'institut Néel à Grenoble et des mesures d'effet Hall sous vide, ont permis de faire passer nos échantillons d'un dopage résiduel p à n illustrant l'effet des adsorbats de l'environnement local du graphène sur son dopage. Une transition progressive du dopage de type-n à type-p après avoir réexposé le graphène à l'air ambiant a pu être mesurée. Cette observation est une preuve directe de l'effet de l'environnement sur nos échantillons. Pour compléter ces données, des mesures de transport ont été effectuées sous un éclairement UV. L'inversion de dopage de type-p à type-n pendant l'éclairement montre l'effet des UV. Un effet de nettoyage de l'échantillon par UV est probable.

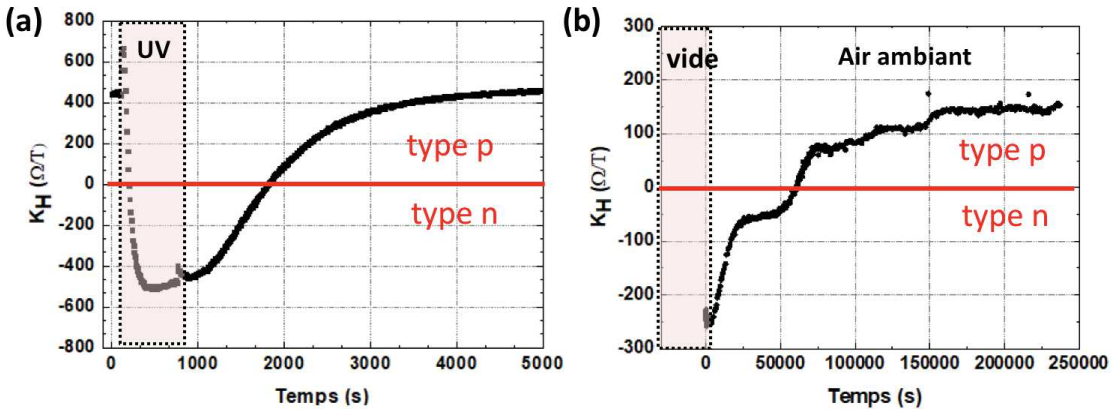

Fig. R.3 Variation du coefficient de Hall $K_H = 1/n_{Hall} \times e$ (n_{Hall}, la concentration de Hall et e, la charge de l'électron) d'un échantillon de graphène en fonction du temps sous clairement UV (a) et sous vide (b). Cette variation montre l'évolution du dopage en fonction de l'environnement et le passage dans les deux cas d'un type n à p.

La sensibilité de nos échantillons permet d'envisager une modulation du dopage de notre graphène. Ce contrôle du dopage est essentiel pour de nombreuses applications, telles que des capteurs de gaz. De multiples perspectives s'offrent à nous afin de contrôler les propriétés électriques de nos échantillons.

Introduction

Graphene, a 2-dimensional material with a unique cone-like band structure, is widely considered to be a promising candidate for the new generation of nanoelectronics. The Nobel Prize in Physics 2010 was awarded jointly to Andre Geim and Konstantin Novoselov *"for groundbreaking experiments regarding the two-dimensional material graphene"* following their published results in 2004. Since this date, a variety of extraordinary properties of graphene have been revealed. For example, its extreme high mobility has attracted interests of electronics community. Besides, the transparency, conductivity, and elasticity of graphene allow the flexible electronics, which challenge the traditionally used indium tin oxide (ITO). Moreover, graphene grown on SiC has been demonstrated as an ideal material for novel quantum resistance standard in metrology thanks to the large spacing of the Landau levels compared to conventional semiconductors and a less critical condition of measurement.

Recent progress in graphene-based applications requires the development in graphene production. Monolayer graphene has been firstly isolated by mechanical exfoliation via adhesive tape. Due to the size limit of the obtained graphene flakes, alternative methods have been then developed. Up to now, wafer-scale uniform graphene films can be achieved by chemical vapor deposition (CVD) or thermal decomposition of silicon carbide (SiC). CVD graphene grown on metal has been largely developed and already used for transparent electrodes applications. However, the transfer process of CVD graphene is still problematic. On the other hand, the sublimation growth of graphene has been known as a promised method to achieve the large-area, homogeneous graphene films, spontaneously forming on a semi-insulating substrate. The advantage of this method is the compatibility with the state-of-the-art nanoelectronic processing which means the graphene transfer process is not necessary. Motivated by the demand of electronic industry, intense researches on epitaxial graphene have been exploding for over a decade. Since 2008/2009, a uniform large-scale monolayer graphene film can be achieved on Si-face of SiC (SiC (0001)) by sublimation under 1 atmospheric (1 ATM) argon (Ar) condition. In the literature, the role of Ar has been justified by a comparison between samples prepared at 1 atm Ar pressure with the samples produced in ultra-high vacuum (UHV) condition. A better uniformity of grown films and controllability of the growth process have been usually found in the former case. However, the graphene growth at a low Ar pressure has been poorly studied in the literature. Moreover, to obtain the films with different but controlled characteristics, i.e. surface morphology, number of layer or doping type, by tuning the growth parameters still remains challenging.

Sublimation is a thermally driven process. Since the silicon has a higher vapor pressure than carbon atoms in the SiC substrate during the heating at high temperature, the Si atoms desorb first from the sample surface while the excess C atoms left behind to reform into graphene layer. Graphene formation happens in a retreating manner as the decomposition of SiC substrate. Sublimation of about three Si-C bilayers is required to

form one graphene layer. The first C-rich layer formed on SiC (0001) is the well-known buffer layer (BL). The carbon atoms arrangement in this layer is similar to that of graphene, i.e. honeycomb structure but there exist C-Si covalent bonds between BL and SiC, which give different electronic properties compared to graphene ones. From the growth point of view, the BL has been considered as the initial stage of graphene growth and acts as a template for subsequent graphene growth. The subsequent carbon layer can be formed between the previous buffer layer and the substrate when more excess C atoms are available transforming the first BL into graphene. Other than the growth mechanism, buffer layer also has an effect on the electronic properties of epitaxial graphene. Indeed, the epitaxial graphene grown on SiC (0001) has been usually found to be n-type doped which is attributed to the presence of buffer layer.

In this thesis, the **objective** is to optimize a **reproducible and controlled** growth process of a **monolayer graphene on SiC (0001)** by sublimation at **low Ar pressure**. i.e. 10 mbar. Meanwhile, we study epitaxial graphene characteristics such as surface morphology, structural and electrical properties as well as the specific interface between graphene and SiC substrate. The growth work is accomplished by using a prototype furnace Zenith 100 fabricated by Annealsys (Montpellier, France). Several growth parameters will be studied. We expect to shed some light on the growth mechanism and characteristics of epitaxial graphene by this growth optimization work.

This manuscript is divided into five chapters.

Chapter 1 discusses the fundamentals and background of graphene. We show the main properties of graphene. We compare the different commonly used techniques for graphene films production: mechanical exfoliation, chemical vapor deposition on different substrates and sublimation method. Then we narrowed down to the sublimation growth of graphene on SiC (0001) and its characteristics. At the end of this chapter, we explain the motivation of this work.

Chapter 2 presents the graphene synthesis equipment and mainly characterization methods used in this work, including Raman spectroscopy, atomic force microscopy, Hall effect transport measurement and scanning tunneling microscopy. We focus on the fundamentals of the techniques and setups are presented in appendix. In the last section of this chapter, we introduce the protocol of samples characterization used in this work.

Chapter 3 details the optimization of monolayer graphene growth by using an intermediate Ar pressure, i.e. 10 mbar. To approach a reproducible growth of graphene in our prototype furnace, starting from the growth of BL, we search step by step the optimum growth window by modifying different parameters (growth time, annealing temperature). The initial stages of monolayer graphene are demonstrated. We analyze the results of characteristic measurements obtained on more than 230 samples. Growth mechanisms are discussed and the reproducibility of this monolayer graphene growth process is confirmed. We also aim to control the sample morphology by tuning the growth parameter (temperature ramp).

Chapter 4 focuses on the interface structure between epitaxial graphene and SiC (0001), i.e. BL. Both the bare BL without graphene covering and the interfacial BL between graphene and SiC substrate have probed in details by Raman spectroscopy. Uncovered BL samples are obtained either by direct growth or by removing the graphene above. We have developed two graphene transfer techniques aiming to mechanically remove graphene layer by depositing then exfoliating the nickel or glue thin layer on the sample surface. More than 15,000 Raman spectra of different types of BL were collected in order to reveal its characteristic. We study the BL synthesized at different temperatures. We compare the Raman signatures of BL with or without graphene covering above. We believe that this study provides new insights on both BL Raman signature and coupling between graphene and BL.

Chapter 5 concerns electrical properties of our monolayer graphene films. The atmospheric effect on the doping characteristics of our samples are revealed by transport measurements under helium condition, in vacuum and at ambient atmosphere. UV illumination influence on electrical properties of graphene will be investigated. These results illustrate the possibility of tuning the electrical properties of our samples by external factors.

.

Chapter 1 Fundamentals and background

Graphene, a single carbon layer material, is arranged in a hexagonal lattice also called honeycomb lattice. In 2004, Andre Geim and Konstantin Novoselov first reported the isolation of graphene by using mechanical exfoliation method. These two scientists were awarded the 2010 Nobel Prize in physic for their pioneering research on two-dimensional graphene. Thanks to the mechanical and thermodynamic stability of the exfoliated graphene flakes, this 2D material has been widely studied. A variety of remarkable properties such as an extremely high mobility reaching 200,000 $cm^2 V^{-1} s^{-1}$ at 5 K, a linear energy dispersion near Dirac points in electronic band structure, an excellent optical transparency, a chemical stability and one of the highest thermal conductivities ever reported has been highlighted [1–5]. Basic properties of monolayer graphene will be discussed in **section 1.1**.

Despite all the interesting properties mentioned for exfoliated graphene, this method to produce graphene can only provide micrometer-sized graphene flakes in a random and uncontrolled way which is obviously unsuitable for industrial purposes. Considering integrating graphene into commercial applications, a scalable and reproducible growth on substrates compatible with devices development is the key requirement. Currently, numbers of production methods have been developed which will be reviewed in **section 1.2**.

The sublimation growth of graphene on Si-face of SiC substrate has been known as one of the most promising option to synthesize the wafer-scale, homogeneous graphene films, which will be described in **section 1.3**. In fact, this process could happen on both polar faces of SiC during the thermal treatment, i.e. Si-face (SiC (0001)) and C-face (SiC $(000\bar{1})$). The growth characteristic on these two polar faces will be compared in this section. Most importantly, the graphene/SiC (0001) interface with the presence of buffer layer has been investigated in the literature due to its great influence on graphene above in terms of growth mechanism and electrical properties. Since the fundamental growth and characteristic investigation by Berger *et al.* [6] in 2004 on 'ultrathin graphite', enormous research works of epitaxial graphene have been done. Back then, the grown epitaxial graphene films obtained under vacuum growth condition were found inhomogeneous in thickness distribution. Later, around 2008-2009, Virojanadara *et al.* [7] and Emtsev *et al.* [8] demonstrated the large-scale and homogeneous monolayer graphene growth on SiC (0001) in a pure argon environment. Both of them have reported the Si sublimation rate can be largely reduced under an atmospheric argon pressure, therefore leading to a better controlled growth process. The

step-terrace morphology which is the result of step-flow growth could be achieved by using argon environment during the graphitization. The graphene growth in vacuum and under argon pressure will be compared in this section. Based on the mentioned fundamentals and background, in **section 1.4**, the motivation of this epitaxial graphene growth work will be discussed.

1.1 Properties of graphene

1.1.1 Electronic band structure of graphene

Graphene sheet consists of one layer of carbon atoms arranged in a hexagonal honeycomb lattice. A unit cell contains two carbon atoms, forming the equivalent sublattices A and B shown in Fig. 1.1 (a). The two lattice vectors can be written as:

$$\vec{a}_1 = \frac{a}{2}(3, \sqrt{3}),\ \vec{a}_2 = \frac{a}{2}(3, -\sqrt{3}) \tag{1.1}$$

where a denotes the carbon-carbon bond length and is about 1.42 Å [9]. Theoretical calculation indicates the lattice parameter of graphene is at 2.461 Å [10,11], which is the same as bulk graphite [12]. The corresponding reciprocal lattice vectors are:

$$\vec{b}_1 = \frac{2\pi}{3a}(1, \sqrt{3}), \vec{b}_2 = \frac{2\pi}{3a}(1, -\sqrt{3}) \tag{1.2}$$

The Brillouin zone (BZ) is shown in Fig. 1.1 (b). The high symmetry points are the **Γ** point at the zone center, the **M** point in the middle of the hexagonal sides, as well as the two inequivalent points **K** and **K′** at corners known as the Dirac points (Fig. 1.1 (c)):

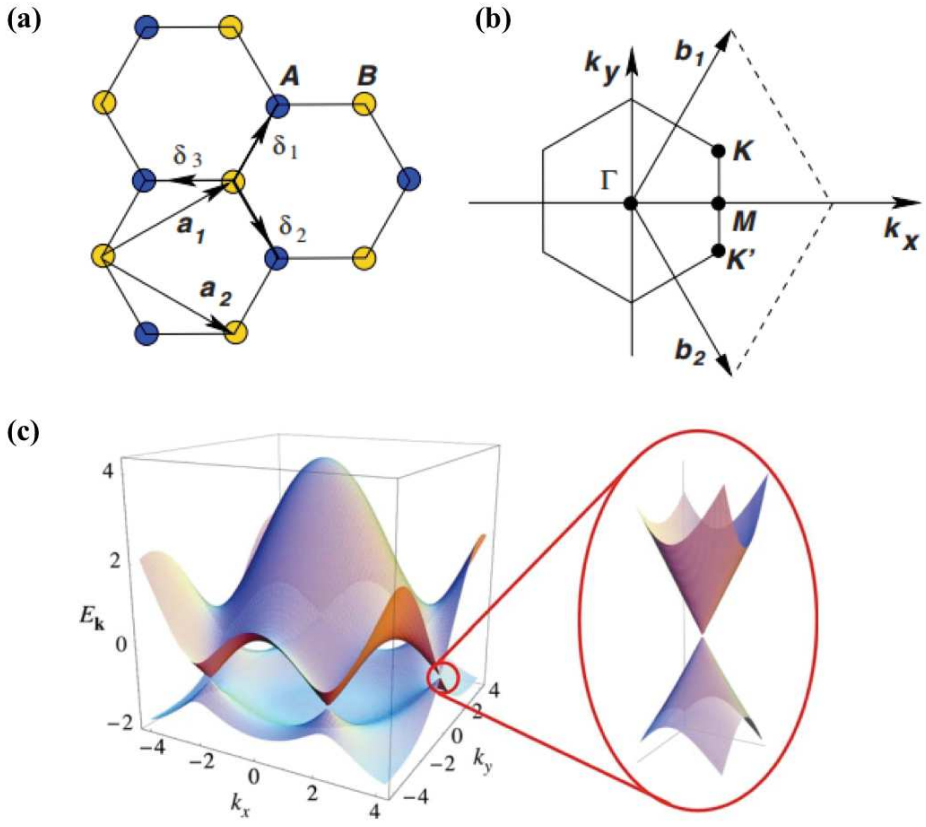

Fig. 1.1 (a) Honeycomb lattice structure of graphene and (b) its Brillouin zone. Taken from [14]. (c) Electronic structure of graphene. The valence band and conduction band touch at K-points of the BZ. Adapted from [9].

$$\boldsymbol{\Gamma} = (0,0), \boldsymbol{K} = \left(\frac{2\pi}{3a}, \frac{2\pi}{3\sqrt{3}a}\right),\ \boldsymbol{K'} = \left(\frac{2\pi}{3a}, -\frac{2\pi}{3\sqrt{3}a}\right), \boldsymbol{M} = \left(\frac{2\pi}{3a}, 0\right) \qquad (1.3)$$

Each atom from sublattice A is surrounded by three atoms from sublattice B, and vice versa. The positions of the three nearest neighbors of each carbon atom are given by the vectors:

$$\vec{\delta}_1 = \frac{a}{2}(1, \sqrt{3}), \vec{\delta}_2 = \frac{a}{2}(1, -\sqrt{3}), \vec{\delta}_3 = a(-1, 0) \qquad (1.4)$$

A single carbon atom has four valence electrons with a ground-state electronic shell configuration of $2s^2 2p^2$. Three electrons in the states of 2s, $2p_x$ and $2p_y$ are hybridized into sp^2 electron states and construct strong in-plane σ-bond. These bonds lead to the extreme mechanical strength of graphene films. The additional $2p_z$ orbital perpendicular to the graphene sheet occupy the π-bond. The overlap of the $2p_z$ between neighboring atoms gives rise to the remarkable electronic properties.

The electronic structure of graphene has been firstly calculated using the tight binding model by P.R. Wallace in 1947 [13]. This calculation only considerate the interaction between the nearest neighbor carbon atoms with hopping energy γ_0. The obtained electronic bands dispersion of graphene are:

$$E_{\pm}(\vec{k}) \approx 3t' \pm \hbar v_F |\boldsymbol{q}| - \left(\frac{9t'a^2}{4} \pm \frac{3ta^2}{8} sin(3\theta_q)\right)|\boldsymbol{q}|^2 \qquad (1.5)$$

where "+" applies to the upper band while "−" the lower band, $v_F = 3ta/2$, $\theta_q = arc\tan^{-1}[q_x/q_y]$, and where t, t' are respectively the nearest-neighbor (i.e. intra-sublattice, A-B) and nearest-neighbor (i.e. intra-sublattice A-A or B-B) hopping amplitudes and $t (\approx 2.5eV) \gg t' (\approx 0.1eV)$ [14].

The conduction and valence bands are connected at the six nonequivalent **K** and **K'** points of the first BZ (Fig. 1.1 (c)). Close to the **K** and **K'** points, where $\vec{k} = \vec{\boldsymbol{K}} + \vec{q}$, the band structure can be approximated as:

$$E_{\pm}(\vec{k}) = \pm\hbar v_F \|\vec{k}\| \qquad (1.6)$$

where v_F is the Fermi velocity ($v_F \approx 1.0\times10^6\ m/s$) and $\vec{k}$ is the wave vector related to one of the points k or k_a'. Equation (1.6) predicts a linear energy dispersion as a function of the wave vector close to the Dirac points, leading to the charge carriers act as relativistic massless Dirac particles. Then the density of states of graphene near the Dirac points is given by:

$$\rho(E) = \frac{g_s g_v |E|}{2\pi\hbar^2 {v_f}^2} \qquad (1.7)$$

where $g_s = 2$ and $g_v = 2$ are the spin and the valley degeneracy, respectively. The density of state of graphene is changing quasi linear with $|E|$ and go to zero at $|E| = 0$, differing with the parabolic electronic structure in other conventional semiconductors. Moreover, the graphene exhibits ambipolar behavior, showing the maximum of resistance at the Dirac point, due to the semi-metal characteristic [2,15]. It allows the possibility to modulate the charge carrier, envisaging the applications such as ambipolar field effect transistor [16]. Further information about the electronic properties of graphene is detailed in reference [9].

1.1.2 Electrical transport properties

Based on the band structure calculation in section 1.1.1, we understand that the conduction and valence bands in graphene touch at one single point, i.e. Dirac point. In neutral graphene (Fig. 1.2 (a)), the Fermi level lays at Dirac point with a fully occupied valence band and empty conduction band, which means that there are no states to occupy and hence no carriers. Consequently, no free carriers could contribute to the electrical transport. We call this undoped graphene as intrinsic graphene. However, in reality, a slight structural disorder, doping or external potential fluctuation will induce carriers in the system, moving the Fermi level away from Dirac point. In Fig 1.2 (b) and (c), the charge transfer to and from graphene are described as electron or hole doping, respectively, with the Fermi level lies within conduction or valence band. When the shift is sufficiently large from zero, one carrier type dominates over the other while the minority carriers could be negligible. This is the so-called extrinsic graphene.

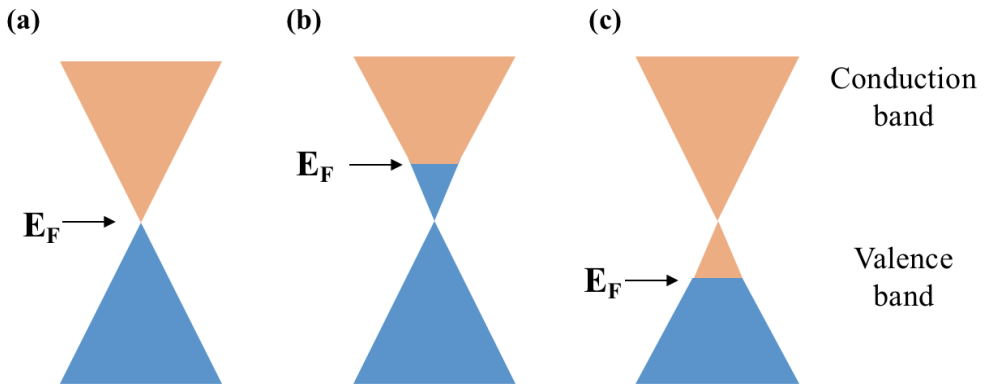

Fig. 1.2 Energy dispersion of graphene around Dirac point, indicating change in Fermi level. Blue indicates levels filled with electrons while red indicates empty levels. (a) Neutral graphene. (b) N-doped graphene. (c) P-doped graphene.

In the famous ambipolar electric field effect, the linear dispersion and zero band gap allow controlling the doping from n-type to p-type through the charge neutral Dirac point by tuning the gate voltage. Besides, the conductivity (σ) increases with increasing the concentrations of electrons or holes. It has been found that the conductivity does not go to zero even with a carrier density vanishes at the Dirac point in extrinsic graphene. It remains a finite value which is referred to minimum conductivity at the neutrality

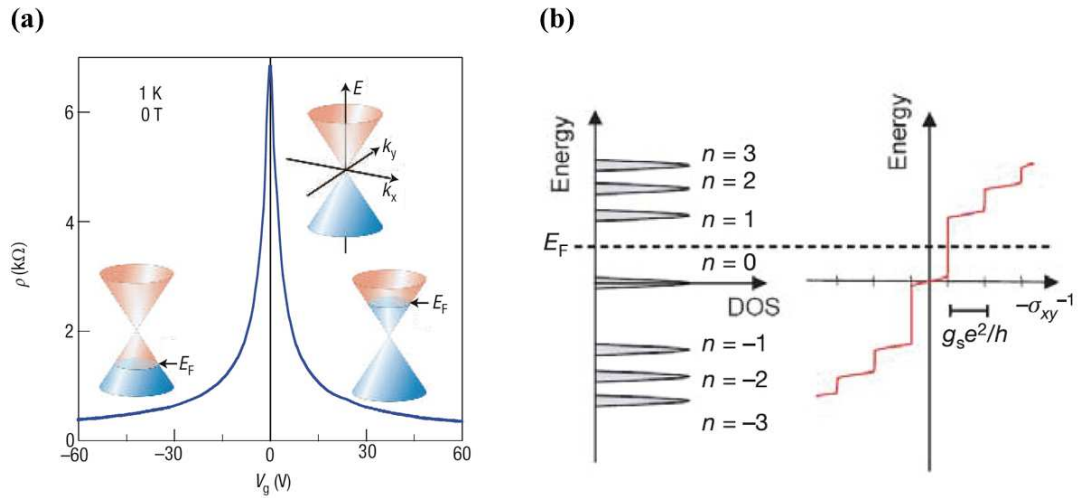

Fig. 1.3 (a) Ambipolar electric field effect in single-layer graphene. The insets indicate the position of the Fermi energy as a function of gate voltages V_g. Positive (negative) V_g induce electrons (holes) in concentrations for field-effect devices with a 300 nm SiO_2 layer used as dielectric. Adapted from [2]. (b) A schematic demonstration of the Landau level density of states and corresponding quantum Hall conductance as a function of energy. The Landau level index n is shown next to the DOS peak [22].

point, as illustrated in Fig. 1.3 (a) [17]. At this point, the density of induced electrons in the conduction band is equal to the density of induced holes in the valence band. The carrier mobility (μ) reflects the scattering mechanism of these induced carriers which is dependent on number of factors, e.g. defects in crystal, impurities or phonons. The mobility can be determined by linear dependence $\sigma\ (V_g)$ and the relationship of $\mu = \frac{\sigma}{ne}$ where e represents the electron charge (1.6×10^{-19} coulombs). The measured mobilities of ~ 15,000 $cm^2\ V^{-1}\ s^{-1}$ under ambient conditions has been exported by Novoselov *et al.* [2]. Furthermore, Morozov *et al.* [18] found the extrinsic disorder could be reduced by depositing graphene on liquid-nitrogen-cooled substrates and the measured intrinsic mobilities of graphene is higher than 200,000 $cm^2\ V^{-1}\ s^{-1}$.

This extremely high mobility has attracted interest of electronics community. Graphene transistor may be expected to play a role in nanoelectronic applications. However, unlike transistor based on conventional semiconductors with a bandgap, the graphene field effect transistors (GFETs) does not turn off completely, i.e. minimum conductivity at Dirac point. In other words, graphene is always conductor. Thus, many efforts aimed at opening a gap in graphene by graphene nanoribbons design [19], bilayer graphene [20], or using boron nitride substrate [21], etc. On the other hand, graphene-based radio-frequency transistors could be realized because the completely switch-off state is not essential for this analog application. In radio-frequency FETs, the cut-off frequency is a most important figure-of-merit for evaluating the performance of devices which describe how quickly a signal can travel from the gate to the drain of the device. To make faster devices, one can either reduce the gate length or use higher mobility

materials. Both of these two parameters could be realized by graphene. Graphene-based FETs have already shown its great performance as we will discuss later in **section 1.2**.

One another unique property of graphene is the unconventional behavior in a high magnetic field at low temperature which is the well-known quantum Hall effect (QHE). With the presence of high magnetic field normal to the graphene plane, charge carriers' motions are quantized into discrete Landau Levels (LLs), as shown in Fig 1.3 (b) [22]. In between two LL, no carrier motion is allowed, thus no increase in carrier density until the next LL is nearly filled. Each LL energies are given by

$$E_n = \pm v_f \sqrt{2e\hbar nB} \tag{1.8}$$

where e and $\hbar$ are electron charge and $\hbar = \mathrm{h}/2\pi$, h is the Planck constant, $v_f = 10^6\ m/s$ is the Fermi velocity, n represents an LL index [22] and + or – represent for electron or holes, respectively. The Hall conductivity:

$$\sigma_{xy} = \pm (n + \frac{1}{2}) g_s g_v \frac{e^2}{h} \tag{1.9}$$

where the $\nu = \pm 4\left(n + \frac{1}{2}\right)$ is the quantized filling factor with a series of $\nu = \pm 2, \pm 6, \pm 10, \ldots$. The value $g_s g_v = 4$ represents the degeneracy considering for spin and valley degrees of freedom. Due to the unique chiral nature of particles in graphene, graphene distinct itself compared to other 2D material by an unconventional quantization condition with a shift of a half integer (the additional 1/2). A shared LL between electrons and holes is present at $\mathrm{E} = 0$. Thus, the 'half-integer' QHE is considered as hallmark of monolayer graphene. Furthermore, graphene is the only material, so far, that shows a QHE at ambient temperature. More details of quantum Hall effect presented in the references [23,24].

The discovery of QHE in graphene draw the attention of the metrological community. The quantum resistance h/e^2 plays an important role in the new quantum International system of units' definition because the former only link to the fixed numerical values such as Planck constant (h), elementary charge (e). Recently, Lafont *et al.* [25] have reported that the relative discrepancy between the quantized Hall resistance in the graphene sample and in a well-known GaAs/AlGaAs heterostructures sample is equal to $(-2 \pm 4) \times 10^{-10}$ at 1.4 K. Moreover, they have demonstrated a quantized Hall resistance over a 9 T-wide magnetic field range with a 10^{-9}-relative standard accuracy. While for GaAs/AlGaAs heterostructures, the quantized plateau does not spread more than 1T for the same accuracy. Thus, graphene has been regarded as better material for resistance standard over conventional GaAs/AlGaAs heterostructures.

1.1.3 Vibrational properties

Fig. 1.4 shows phonon dispersions of monolayer graphene calculated at theoretical lattice [26]. The monolayer graphene with two carbon atoms per unit cell has six normal vibrational modes: three acoustic and three optical vibrational modes. The ZA and ZO modes are two out-of-plane acoustic and optical vibrational mode while the LA and TA modes corresponds the in-plane longitudinal and transverse acoustic vibrational mode, respectively. The LO and TO modes represent the in-plane optical vibrational mode which are degenerated at the Brillouin zone center. The point group of graphene is the D_{6h} group and the lattice vibrations at **Γ** point can be depicted:

$$\Gamma_{lat.vib.} = A_{2u} + B_{2g} + E_{1u} + E_{2g} \tag{1.10}$$

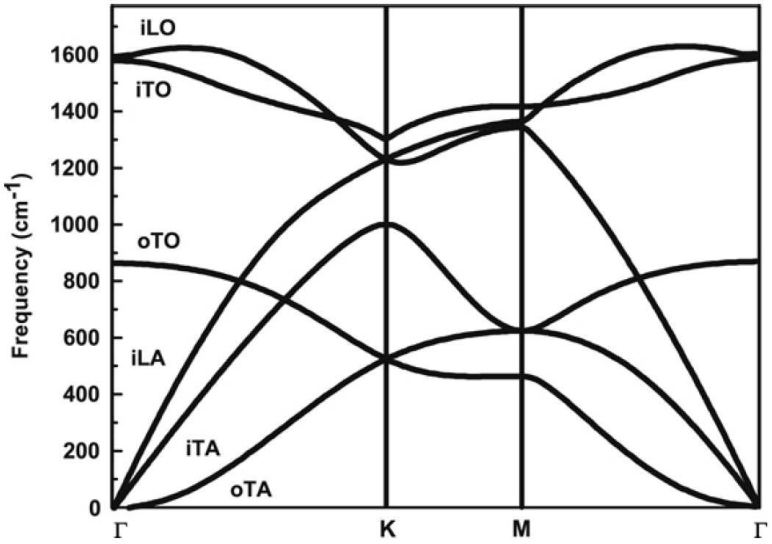

Fig. 1.4 Phonon dispersion of monolayer graphene. Adapted from [26].

The A_{2u} and E_{1u} representations are translations of the plane; the B_{2g} mode is an optical phonon where the carbon atoms move perpendicular to the graphene plane. The E_{2g} is the only Raman-active mode. It corresponds doubly degenerate in-plane optical vibration which describes the graphene sub-lattice A move towards the sub-lattice B. However, the phonon modes far from **Γ** can also be probed by Raman spectroscopy via the double resonant Raman process. More principles of Raman measurement will be detailed in **section 2.2**.

1.1.4 Other properties

The thermal conductivity of graphene has been measured in suspended graphene layers exfoliated from bulk graphite. A high value, exceeding 3000 WmK^{-1}, has been obtained at room temperature [27]. For a comparison, the thermal conductivity of pyrolytic graphite and silver is approximately 2000 WmK^{-1} and 430 WmK^{-1}, respectively. Thanks

to this merit, graphene is often thought to hold advantages over other materials in nanoscale devices application. Although the dissipation from graphene devices are limited by their interfaces, contacts, and surrounding materials, such thermal conductivity is still very high and it exceeds that of silicon and copper [28].

An optical absorption about 2.3% of light in the visible range [3] has been reported for monolayer graphene with a thickness of 3 Å, which is equal to the absorbance of a 5-10 nm thick GaAs film [29]. Adding another layer of graphene increase the amount of white light absorption by approximately the same value of 2.3%. Based on this significant amount of photon absorption, the integration of graphene into photonic devices is promising. For example, photovoltaic cells, light emitting devices, liquid crystal displays, or flexible organic LEDs are devices based on electrodes with high transmission (T > 80%) combined with a low sheet resistance. The advantages of using graphene as photodetector are the wide absorption range, the thinness and the ability to operate at ambient temperature.

Another fascinating property of graphene is its super mechanical properties. The specific carbon structure and geometry in graphene gives rise to an ultimate tensile strength, e.g. Young's modulus about 1TPa [4], compared to A36 structural steel (400 MPa) or Aramid (376 MPa).

Motivated by these interesting properties, great efforts have been done to push graphene-based technologies into the commercial and practical applications. Graphene has been considered as an ideal candidate for the manufacture of ultra-fast and high frequency electronic and optoelectronic devices. In this case, a robust wafer-scale graphene growth process and the reliable processing technique are required. In next section, we will overview the state-of-art of graphene production and its corresponding applications. Commonly used techniques will be compared.

1.2 Production of graphene films

The most famous method of isolating graphene sheets is using adhesive tape to mechanically cleave graphite, which was introduced by Novoselov and Geim in 2004. Indeed, most of the extraordinary properties discovered in graphene were demonstrated on exfoliated graphene flakes. However, the limited sample size (hundred micrometer square) and irregular flake shapes could not fulfill the demand of electronics industry. The success in mechanical cleavage led to an expansion in graphene growth by using a wide variety of production techniques. Here, we stress that the true graphene is only one atomic layer thick (often called a monolayer) which could be floated off the substrate or could be onto another substrate. The other types of graphene containing powder form materials such as graphene oxide, graphene nanoplatelets, and graphene quantum dots, etc., are beyond the scope of this thesis. Regarding the high-quality graphene production for the high-performance electronics, two methods are outstanding: chemical vapor deposition (CVD) and thermal decomposition of silicon carbide (SiC), also called sublimation. For over a decade, these two methods of graphene sheet synthesis have been developed and compared to graphene exfoliation. Since the

graphene quality and performance is strongly dependent on the growth methods, here we briefly review the state-of-art of these growth methods and their corresponding potential applications.

1.2.1 Mechanical exfoliation

The original method to obtain single layer graphene is by mechanical exfoliation of natural graphite or highly oriented pyrolytic graphite (HOPG) with scotch tape. This technique is considered as a fundamental and groundbreaking work reported by Manchester group in 2004 [2,17]. In this method, bulk graphite was rubbed onto scotch tape and sequentially thinned down by repeated peeling, as shown in Fig. 1.5 (a) [30]. The recognition of single layer or thicker flake graphene is simply done by the optical microscope after being transferred to a silicon dioxide layer on Si (Fig. 1.5 (b)). It has been found that a SiO_2 substrate with thickness of 90 or 300 nm could give the most suitable visual contrast in order to identify the graphene flakes [31]. The key reason to choose this method is that the high-quality graphene can be easily accessible at room temperature. A large number of research works have been explored on the exfoliated graphene and various interesting properties have been revealed, as mentioned in **section 1.1**. However, this method is not a well-controlled process since the obtained graphene flakes possess random shape and limited size (at most 100 μm^2) [32]. Thus, this technique could hardly meet the needs for the industrial purposes which require a large-scale and mass production technique. Nevertheless, the obtained graphene films are useful for fundamental studies and a proof of concept waiting for large scale material.

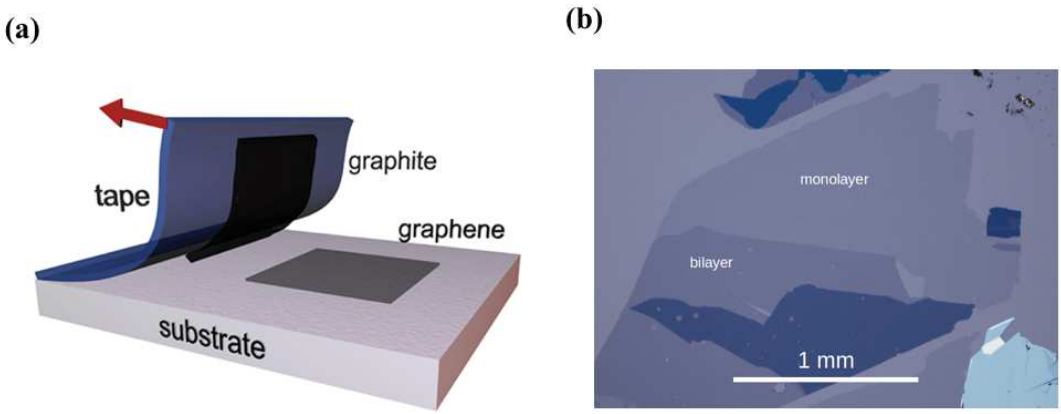

Fig. 1.5 (a) Schematic illustration of graphene exfoliation. Adapted from [30]. (b) Optical image of graphene on SiO_2 [31].

1.2.2 Chemical vapor deposition

The chemical vapor deposition (CVD) growth of graphene has proved to be one of the most promising methods to fabricate wafer-scale graphene layers. Graphene elaboration on a variety of transition metals surfaces, such as Cu [33], Ni [34], Ru [35], and Ir [11,36], has been known for over half a century. In general, the growth process involves

the thermal decomposition of the hydrocarbon sources on a heated substrate, as illustrated in Fig. 1.6 (a). During the process, the precursor gas serving as carbon source, e.g. methane or propanol, is sent into the furnace chamber with the optimized pressure and flow rate. The precursor could react with a catalyst at elevated temperature and forms graphene sheet on the catalyst surface. In fact, the metal substrates not only act as catalyst to lower the energy barrier of the reaction, but also determines the graphene deposition mechanism. In the case of metal possessing high carbon solubility (such as polycrystalline Ni and Fe), the carbon will dissolve into the metal bulk according to the solubility of carbon. During the cooling down, the dissolved carbon will segregate to the surface to form graphene sheets. On the other hand, for metal having low carbon solubility (such as Cu), carbon atoms will nucleus to form graphene domains and expand laterally with decomposition of hydrocarbon at high temperature. The CVD process is usually performed at a growth temperature ranges from several hundred degrees Celsius up to the melting point of the catalyst metal (T~ 1000°C for Cu and Ni). Since Li *et al.* [33] has firstly produced uniform monolayer graphene sheet on Cu foils at low pressure in 2009, Cu has been considered as an ideal substrate. However, the graphene produced by this method is typically polycrystalline with domain sizes varying from a few micrometers to hundreds of micrometers. Here, we define the domain as the area of graphene with same number of layer and crystalline orientation. In the meantime, Reina *et al.* [34] have demonstrated one or two layers of graphene can be grown on Ni surface during atmospheric pressure CVD. They found that the nonuniformity of graphene layers was formed along the boundaries of Ni grain. Indeed, Cu and Ni are most commonly used catalysts due to their low cost, etchability and large grain size. This method is also favorable for future complementary metal-oxide semiconductor (CMOS) technology.

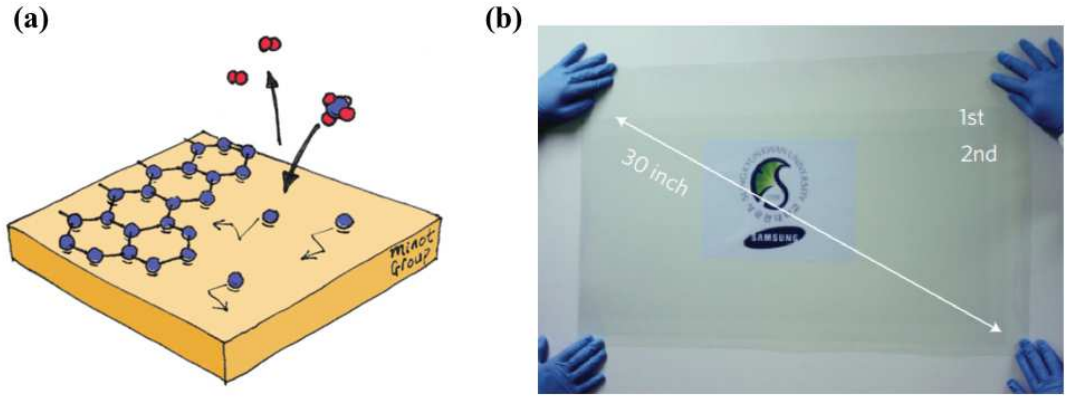

Fig. 1.6 (a) Schematic illustration of CVD method of graphene growth. (b) Transparent ultra large-area graphene film transferred on a 35-inch PET sheet. Adapted from [38].

In spite of the presence of defects or grain boundaries, CVD graphene has been already tentatively used in transparent conductive coating applications. Different from exfoliated graphene, CVD graphene can be scaled up to several inches size (Fig. 1.6 (b))

[37,38]. Sheet resistance of 125 Ω/sq with a transmittance value of 97.4% has been reported for monolayer CVD graphene by a Korea group [38]. This outstanding optoelectronic property represents a good advance for the production of graphene as transparent conductive films, a replacement of indium tin oxide (ITO) [3,38]. However, one of the major challenges of this method is the impurities and wrinkles presented in the obtained films due to the use of metal catalysts. Moreover, the control of thickness and relative crystallographic orientation of the graphene layers are still critical. Besides, since electrical properties cannot be tested on a conductive metal substrate, a process to transfer films on an insulating substrate is followed. This process often affects the graphene quality and performance due to the induced defects and residual of the polymer used to detach graphene from the metal substrates [39]. To overcome these drawbacks, graphene synthesis on insulating substrate has been developed recently.

The metal-catalyst-free synthesis of graphene films on insulating substrate has been reported since 2010. This method avoids the use of metal catalyst as well as the post-transfer process which is also compatible with silicon processing techniques. The first attempt has been performed under argon-propane by Hwang *et al.* at 2010 [40]. They have grown few layers of graphene on sapphire and on C-face of silicon carbide (SiC $(000\bar{1})$) at the temperature ranged from 1350 to 1650°C. Further investigations done by Strupinski *et al.* [41] have demonstrated a monolayer graphene formation under pressures as low as 20 mbar (propane-argon mixture) and temperature as high as 1600°C in a CVD furnace by using argon-propane gas supply. They have shown that by handling the partial pressure of argon (Ar), an Ar boundary layer of gas phase could be established in the vicinity of the surface. Here, it is important to mention that graphene layers can be produced by thermal decomposition of SiC substrate without any external carbon source at a relatively high temperature (> 1650°C). They suggested that with the right growth conditions, one can control the Ar boundary layer thickness which can stop the silicon atoms from evaporating and meanwhile allow the propane passing through and depositing on the substrate. Moreover, graphene grown by this method lies above an interfacial layer which is the well-known buffer layer. This buffer layer is the result of surface reconstruction of SiC, usually reported as the initial step for the sublimation growth of graphene on Si-face of SiC (SiC (0001)). Later, CHREA group (Valbonne, France) has made great efforts to investigate CVD growth of graphene on SiC. Michon *et al.* [42,43] have proposed the use of hydrogen-propane atmosphere during the CVD growth of graphene on SiC (0001) and they investigated the dependence of growth mechanism on the growth pressure and temperature. Two types of graphene structures have been observed under different growth conditions. As we can see in T-P diagram in Fig. 1.7, the in-plane rotational disordered graphene (denoted as IRD) was obtained at high pressure and low temperature. This graphene is normally associated with the growth of graphene on the SiC $(000\bar{1})$ [44] in which different graphene orientation coexist on the same substrate. They explained this observation by the saturation of SiC dangling bonds by hydrogen which prohibits the formation of interfacial reconstruction. The C-rich ($6\sqrt{3}\times6\sqrt{3}$) R30° interfacial reconstructed layer (buffer layer) could act as a template to control the graphene

formation on SiC (0001). We will come back to this point in **section 1.3** in which the buffer layer will be more discussed. Another structure (denoted as $6\sqrt{3}$) was obtained at low pressure and high temperature consisting graphene stacked on buffer layer in same orientation of 30° with respect to SiC. They claimed that both SiC etching by hydrogen and propane supply contribute to the graphene formation and the hydrogenation is suppressed at high temperature. CHREA group has also proposed combining hydrogen and argon gases in which they have obtained good results [45,46]. In this case, the pressure is fixed at 800 mbar while the hydrogen amount in the hydrogen-argon mixture would be altered. Surprisingly, the control of the temperature will not only change the graphene structure (IRD or $6\sqrt{3}$) but also alter the electrical properties. For example, at temperature of 1450°C, one can grow p-type free-standing graphene layer while at temperature of 1550°C, n-type graphene is obtained [46]. Thanks to the high quality of these CVD graphene on SiC, the quantum Hall effect has been observed which led to new achievements in the metrology of resistance standards [25,47]. Hence, CVD direct growth under hydrogen-argon atmosphere seems to be a promising method but whether it is better than sublimation of SiC or not is still questionable.

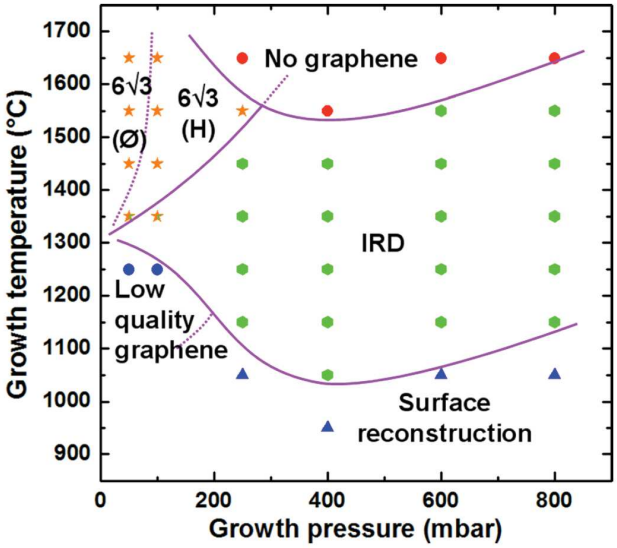

Fig. 1.7 Graphene structure deduced from LEED patterns as a function of pressure and temperature in CVD growth of graphene on SiC. IRD indicates rotational disordered graphene while $6\sqrt{3}$ represents graphene layers with BL underneath. Adapted from [42].

1.2.3 Epitaxial graphene on silicon carbide

One another technique of large-scale production of graphene film is thermal decomposition of SiC (sublimation). Here in this section, we only discuss several points aiming to compare this method to other elaboration techniques. More details of this method will be presented in **section 1.3**. As we known, uniform large-area of graphene films can be grown spontaneously on a SiC substrate by thermal decomposition of silicon carbide (SiC). The graphene grown on SiC by sublimation method is usually

called epitaxial graphene (EG). In fact, as early as 1975, graphite layers were first obtained by annealing the SiC substrate (> 800°C) under ultra-high vacuum (UHV) [48]. However, EG has not attracted much attention until 2004 when the Georgia Tech research group has detected the 2D electron gas behavior by processing a field-effect transistor with ultra-thin graphite layers grown on 6H-SiC (0001) [6]. Since then, the EG grown on SiC has been considered as one of the most viable candidates for the graphene-based nanoelectronic devices fabrication. The growth and characteristics of EG on SiC have been largely investigated. Starke's group (Stuttgart, Germany) [49] have made great efforts in studying the structural and electronic properties of graphene grown on both SiC (0001) and SiC $(000\bar{1})$. They have demonstrated the different surface reconstruction of SiC during the graphene growth on two polar faces. For example, the interfacial reconstructed carbon layer (known as buffer layer) is present between graphene and SiC (0001) but absent for SiC $(000\bar{1})$. Regarding the optimization of growth, IBM [50,51], NTT [52] and other research labs [53–55] have contributed to improving the homogeneity of the grown films. However, the uniform graphene layers were always hard to achieve under UHV growth condition which is consistent with the results of theory calculations [56].

The prominent work concerning the improvement of the uniformity of EG happened around 2008/2009. Virojanadara *et al.* [7] and Emtsev *et al.* [8] have obtained large-scale homogeneous graphene films via sublimation of SiC (0001) by using an argon (Ar) pressure. Both of them have suggested that the growth kinetics under the argon pressure close to atmospheric one (1 atm Ar pressure) is under thermodynamic stability thanks to the reduced Si sublimation rate and a higher growth temperature (> 1650°C). A higher growth temperature can enhance the mobilities of C and Si atoms, leading to an easier surface reconstruction. This growth kinetics has been later supported by theory calculation [56,57]. Most importantly, this method has been largely repeated by other groups and the similar results have been achieved which confirm the reproducibility and controllability of this growth process. Moreover, the uniform monolayer graphene synthesized by this method has shown interesting properties such as quantum Hall effect [52] and improved carrier mobilities [8]. On the other hand, the thickness distribution of graphene grown on $(000\bar{1})$ under Ar pressure is still not easy to control [44] due to a higher surface energy compared to SiC (0001) [58]. Consequently, so far, 1 atm Ar pressure is the most commonly used parameter to produce monolayer graphene on SiC (0001).

Besides, the Georgia Tech research group has developed a confinement-controlled sublimation (CCS) method [59]. During the growth under UHV, they have capsulated the SiC in graphite enclosures. They have shown that by the confined environment surrounding the SiC samples, the growth process is close to equilibrium due to the decelerated Si evaporation rate. Consequently, uniform graphene layers could be produced on both the Si and the C face of SiC. Tromp *et al.* [50] have demonstrated that by using Si background pressure, the Si atoms evaporation could be reduced and the phase transformation of SiC surface could be shifted up by several hundred degrees

Celsius. The strongly improved morphology of graphene can be achieved. The CCS method and Si flux growth method will not be used in current work.

Indeed, the accessibility of wafer-scale and high-quality films, which is also compatible with the CMOS-based electronic devices is the major advantage of the sublimation growth of EG under Ar pressure. Consequently, high-performance devices such as field-effect transistors [60], detectors [61,62] and chemical sensors [63,64] have been developed using the EG. For example, the cut-off frequency in EG-based high-frequency field effect transistors was reported as high as 350 GHz [65]. Even though graphene FETs have significantly outperformed III-V metal-oxide-semiconductor field effect transistors (MOSFETs) which possess a highest measured cut-off frequency of 850 GHz, graphene still has its advantage in terms of downscaling limitation (e.g. 20 nm for INP MOSFET). In addition, thanks to the observation of QHE in EG, one another important application of graphene on SiC regards to the metrological resistance standards, in which these films show advantages over traditional semiconductor heterostructures [66,67]. More potential applications of EG is detailed in reference [68].

1.2.4 Discussion and conclusion

We have discussed the most commonly used techniques to elaborate graphene sheet in **section 1.2.3**. As we can see, each technique has its advantages and limitations.

Exfoliated graphene has unveiled the exceptional properties of graphene such as an extremely high mobility of 100,000 $cm^2\ V^{-1}\ s^{-1}$ at 300 K [18]. This mobility was recorded for encapsulated graphene in boron nitride layers which is a popular research topic today. However, the limited sample size and uncontrolled produce process is the major limitation of this method which makes it not suitable for devices fabrication.

CVD graphene grown on metal is one of the most promising methods to produce large-scale graphene films, especially the preparation of 30-inch rolls of graphene has been realized [38]. The electronic devices such as ITO or FET could be developed due to the development of this technique. However, the ripples and defects in the graphene sheet as well as the following transfer process are still remaining the serious concerns need to be addressed.

CVD graphene grown on SiC has been developed recently. This technique allows a wafer-scale deposition on SiC. The primary advantage of graphene grown on SiC is the compatibility of today's semiconductor processing technique, thus no transfer process is needed.

Similarly, sublimation growth of graphene on SiC has shown comparable properties with CVD graphene on SiC. The uniform and wafer-scale monolayer graphene can be obtained by these two methods and the observation of QHE has evidenced the high quality of the graphene films. The difference between these two methods to produce graphene on SiC is the carbon source and the growth temperature. The CVD requires a temperature lower than sublimation of about several hundred degrees, an appropriate control of gas flow and temperature should be adjusted.

We present in table 1.1 the main properties for each graphene synthesis technique. We also summarize the existing application for each method. The good review and summary of the potential applications of graphene can be found in reference [32].

Table. 1.1 Summarize the main characteristics of the graphene produced by the mentioned techniques.

	Mechanical exfoliation	**CVD on metal**	**CVD on SiC**	**Epitaxial growth on SiC**
Sample size	1 mm^2 [32]	30 inches [38]	Wafer size [69]	Wafer size (76.2 mm) [70]
Mobility at 300 K ($cm^2 V^{-1} s^{-1}$)	2×10^5 [71]	1.6 x 10^4 [72]	9010 [73]	3493 [74]
Applications	Research	Transparent conductive layers [38], sensors, photonics [75], metrological resistance standard [76].	High-frequency transistors and other electronic devices [77], metrological resistance standard [67,78].	

1.3 Epitaxial graphene on SiC

1.3.1 Synthesis of epitaxial graphene by sublimation

In silicon carbide, each Si (or C) atom is bonded to four nearest-neighboring C (or Si) atoms by covalent bonding in tetrahedral coordination. The various stacking and orientation sequences of Si-C bilayer give rise to at least 200 polytypes in the SiC bulk structure. The most common polytypes that are considered for the graphene synthesis are 4H-, 6H- and 3C-SiC, where the number 4 (6 or 3) indicates the number of bilayers per unit cell and H (C) denotes the hexagonal (cubic) symmetry. Each bilayer is composed of a plane of C atoms and a plane of Si atoms with equal atoms number. Fig. 1.8 demonstrates the different stacking bilayers of 3C-SiC (ABCABC), 4H-SiC (ABCBABCB …) and 6H-SiC (ABCACBABCACB …) crystals in the $(11\bar{2}0)$ plane [79]. Despite outstanding properties, 3C-SiC continues to suffer from the lack of good quality bulk substrate while high quality 4H- and 6H-SiC wafers are commercially available for n-type doped or semi-insulating ones. Hexagonal SiC has two non-equivalent polar faces perpendicular to the c-axis, where the Si-face and C-face correspond to the faces with outwards normal in (0001) and the $(000\bar{1})$ surface, respectively. We note that the purchased on-axis wafer generally present a slight misorientation with respect to the basal planes by a miscut towards either $(11\bar{2}0)$ or (1100).

Sublimation is a thermally driven process. Since the silicon atoms have a higher vapor pressure than carbon atoms in the SiC substrate during the heating process at high

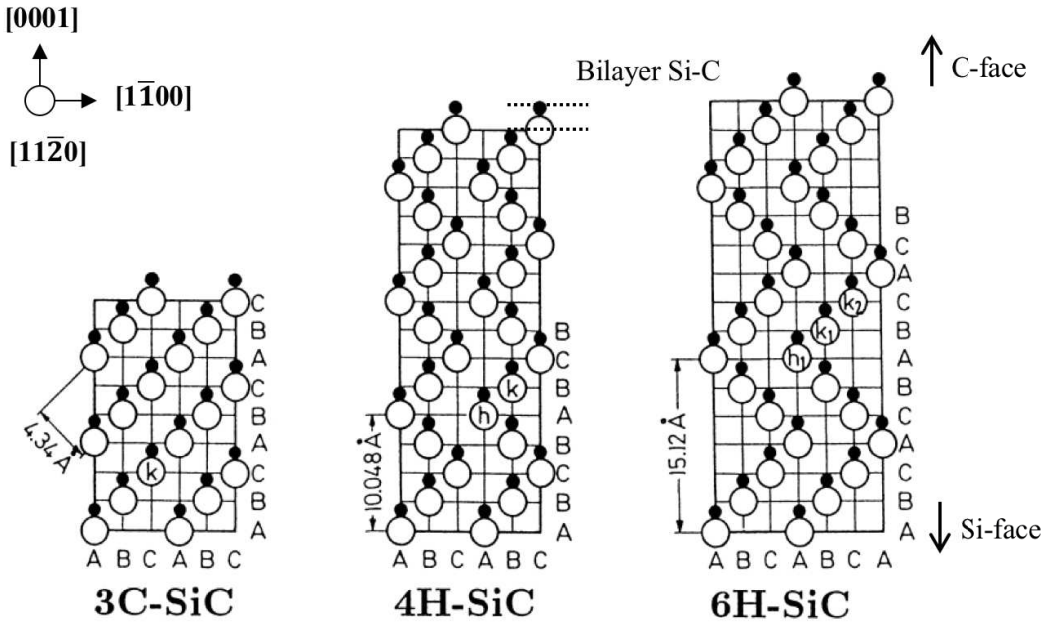

Fig. 1.8 Stacking sequence of bilayer Si-C of the 3C-, 4H- and 6H-SiC polytypes in the $(11\bar{2}0)$ plane and along the c-axis [0001]. Si and C atoms are depicted by open and filled circle, respectively. A, B and C denote the stacking order of the Si-C bilayers. Adapted from [79].

temperature, the Si atoms desorb first from the sample surface [80]. Fig. 1.9 (a) shows the equilibrium pressures of Si-C system at constant pressure. The Si, Si_2, Si_3, SiC, Si_2C, SiC_2, Si_2, C, C_2, C_3 and C_4 are the basic components of SiC evaporation and the solid line represents partial pressure of each component while the dashed line is the total pressure. For example, at 1600°C (vertical dotted line in Fig 1.9 (a)), when the total pressure is about 10^{-6} bar, the vapor pressure of Si atoms is around 10^{-6} bar whereas the C atoms possess a much lower vapor pressure. This means the gaseous Si is more favorable to dominate the system. Therefore, Si atoms accompanied with Si_2C and SiC_2 could be evaporated at high temperature while the excess C atoms left behind on the surface, reform into graphene layer (Fig. 1.9 (b)). Epitaxial growth of graphene has been intensely studied for more than a decade since the remarkable work of Berger *et al*. at 2004, in which they show the possibility to grow thin graphite layers on SiC [6] and the extraordinary properties of the grown film. To date, a large number of research works have been done to understand and control the epitaxial graphene synthesis, in terms of the substrate and growth condition effects. Various experimental techniques such as

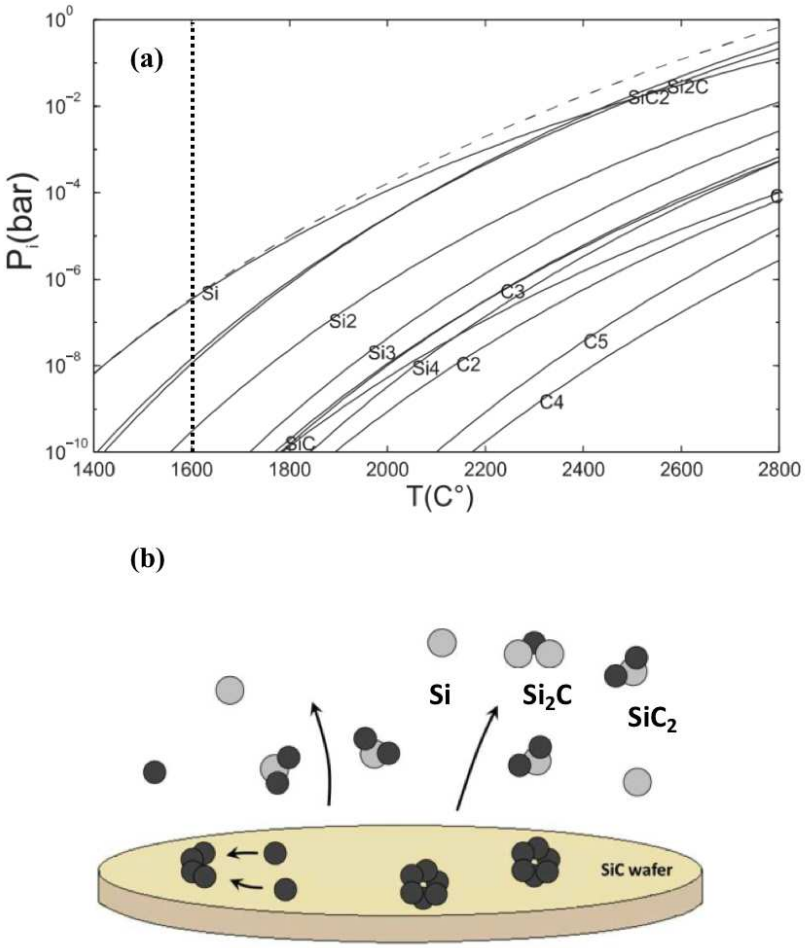

Fig. 1.9 (a) Equilibrium partial pressures at different temperature in SiC system. The solid line and dashed line represent the partial pressure and total pressure respectively. The dotted vertical line highlights the case of 1600°C. Taken from [80]. (b) Schematic illustration of thermal decomposition of SiC. The black and gray solid circles are C and Si atoms. The desorption of Si species leaves behind the excess C atoms on the surface to reform into sp^2 structure.

low-energy electron diffraction (LEED) [48,81], Auger electron spectroscopy (AES) [48], scanning tunneling spectroscopy (STM) [49,82], X-ray diffraction [83], atomic force microscopy (AFM) [53,84,85], Raman spectroscopy [85–88], low-energy electron microscopy (LEEM) and transport measurement [85,89,90], etc., act as the useful tools to investigate the grown films.

1.3.2 Epitaxial graphene on SiC (0001) and SiC (000$\bar{1}$)

During the high temperature heating, the SiC surface undergoes several reconstructions phases before graphene formation, which can be revealed, for instance, by *in-situ* low-energy electron diffraction (LEED) patterns [49,54,91]. It has been demonstrated that the graphene layers can be obtained on both Si-face (denoted SiC (0001)) and C-face (denoted SiC (000$\bar{1}$)) by sublimation of SiC but in the different growth manner, e.g. surface reconstruction and growth kinetics.

Fig. 1.10 illustrates the different stages of graphene growth on SiC (0001) during thermal decomposition process under UHV condition, taken from the reference [81], The pre-treatment of substrate, e.g. annealing under a flux of Si or hydrogen etching, could induce the Si-rich $(3\times3)_{Si}$ surface. The subscript "Si" and "C" denote that this reconstruction is more silicon-rich or carbon-rich. Further increasing annealing temperature leads to the C-rich $(\sqrt{3}\times\sqrt{3})$ R30°-reconstruction. The 'R30°' indicates that the reconstruction is rotated by 30° with respect to the SiC. Later, the C-rich $(6\sqrt{3}\times6\sqrt{3})$ R30° surface reconstruction appears by subsequently annealing at higher

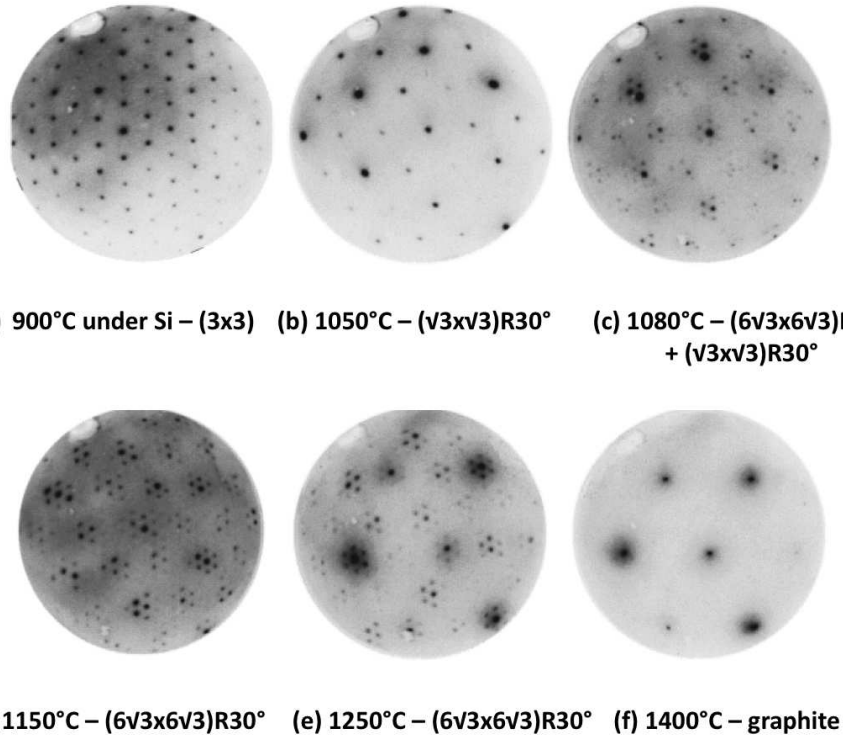

Fig. 1.10 LEED patterns of SiC (0001) upon annealing in UHV obtained on (a) (1 × 1). (b) ($\sqrt{3}\times\sqrt{3}$) R30°. (c) ($\sqrt{3}\times\sqrt{3}$) R30° + ($6\sqrt{3}\times6\sqrt{3}$) R30°. (d and e) $(6\sqrt{3}\times6\sqrt{3})$ R30°. (f) graphite (1×1). Taken from [81].

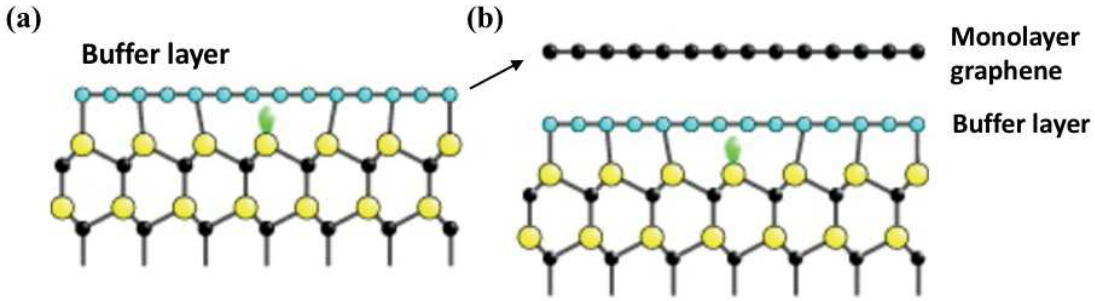

Fig. 1.11 Structure model of epitaxial graphene growth on Si (0001). (a) First carbon layer grown on substrate, so called BL. There exist the C-Si bonds between BL and SiC. (b) New BL grown between substrate and previous BL, transforming the latter into graphene. Taken from [143].

temperature. This reconstructed layer is well known as the first carbon layer grown on SiC (0001), so-called buffer layer (denoted as BL). STM images [92] revealed this BL possesses the same honeycomb lattice as graphene. However, ~ 1/3 of the C atoms are covalently bonded to the Si atoms in SiC, leading to the sp^3 hybridization in these C atoms which differs with sp^2 graphene layer, as we can see from Fig. 1.11 (a). Therefore, this BL shows different electronic properties with graphene, as demonstrated in angle-resolved photoemission spectroscopy (ARPES) measurement in reference [54], e.g. the missing of π-bands. Eventually, further sublimation generates a new carbon layer formed between the previous BL and the SiC substrate [93], meanwhile, the previous BL is detached from the substrate and transforms into the first graphene layer (Fig. 1.11(b)). This described epitaxial graphene growth is a bottom-up growth process. In fact, due to the similar structure between BL and graphene, the BL acts as a template for subsequent graphene formation, therefore the graphene layers are azimuthally aligned with respect to the under-layer substrate. Generally, the stacking order in graphene sheets is commonly found to be hexagonal or AA… stacking, Bernal or AB… stacking, and rhombohedral or ABC… stacking [94] which are demonstrated in Fig. 1.12. In AA stacking, all carbon atoms are directly above each other, while in AB stacking, carbon atoms in layer B are above the center of carbon hexagon in layer A.

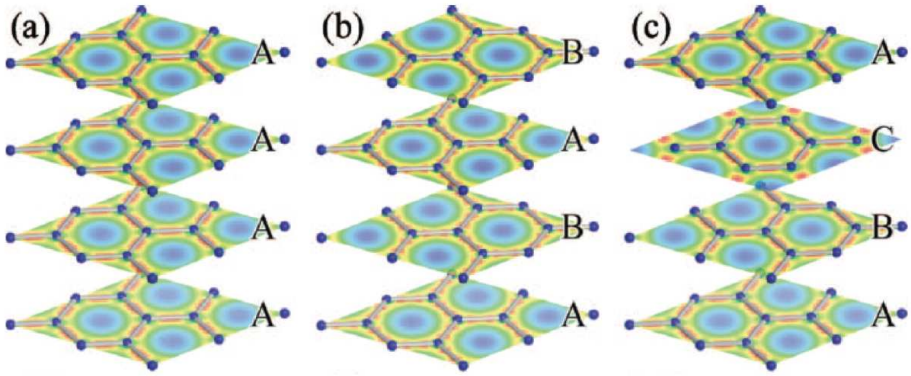

Fig. 1.12 Different stacking in few layers graphene. (a) AA (b) AB (c) ABC stacking [97].

The separation between each layer is about 0.335 nm [95]. Both the calculated and experimental results suggest that the Bernal stacking order in graphene layers grown on SiC (0001) [96] is more energetically favorable [97]. Here, it is important to be clear that we only refer one atomic thick of sp^2 bonded carbon atoms layer to as graphene. Two or three graphene layers are denoted as bilayer or trilayer graphene, respectively.

On the other hand, the surface reconstruction on SiC $(000\bar{1})$ during the heating is completely different compared to SiC (0001). Before seeing the graphene rings in LEED patterns, the presence of the (3×3) has been reported by Starke *et al*. [49] while the (3×3) and C-rich $(2\times2)_C$ reconstructions were demonstrated to be coexisted before the graphene formation [98–101]. Besides, neither of these two reconstructed layers could play a role as a template of growth because there is no simple coincidence between their unit cell size and that of graphene. It is worth noticing that the BL is absent on SiC $(000\bar{1})$, which makes it a specific characteristic of the graphene grown on SiC (0001). Then, further annealing leads to multilayer graphene growth. As evidenced by the multiple $(1\times1)_{graphene}$ diffraction spots and a diffusive ring-like diffraction pattern in LEED measurement, these graphene layers grown on SiC $(000\bar{1})$ do not stack in the Bernal manner, but rather in rotational disorder [48,99]. Multilayer graphene shows a Dirac-like band similar to that of single-layer graphene [102]. This disordered multilayer graphene is sometimes referred to as turbostratic graphene [100].

The graphene growth modes on these two polar faces are quite different in many aspects. Due to the different surface energy of these two polar faces, graphene starts to form at about 1150°C on the SiC $(000\bar{1})$ surface but 1300°C on SiC (0001) surface in UHV [44]. Then, the growth rate of graphene on SiC $(000\bar{1})$ is over an order of magnitude faster than that on the SiC (0001) which can be explained by the different interface structure, e.g. the presence of BL [103]. After the BL formation, the Si sublimation rate could be further reduced since the honeycomb structural arrangement of this BL [104]. Besides, growth on SiC (0001) prefers a lateral growth mode rather than a vertical growth mode in 3-dimension as in the case of growth on SiC $(000\bar{1})$ [44]. For example, for growth under UHV condition, the graphene flake with constant thickness can be over several microns on SiC (0001), whereas the domain size is about only a micron square on SiC $(000\bar{1})$. Therefore, the thickness distribution is more dispersed in the latter case as compared to the former case [44]. Tedesco *et al*. [105] referred to the growth mode on SiC $(000\bar{1})$ as island nucleation and coalescence in which the small grain size is always obtained. From our own experiences of growth on SiC $(000\bar{1})$, taking one sample as an example (Fig. 1.13 (a)), we already observed some few layers graphene islands (white flakes) growing before complete graphene coverage is achieved. On the contrary, the Fig. 1.13 (b) illustrates 1-2 layers graphene grown on SiC (0001) with larger domain size in a relatively homogeneous manner. There is only small portion of bilayer graphene stripes (white contrast) present on the majority monolayer graphene sample surface (blue contrast). Hence, the distinct growth rates and growth

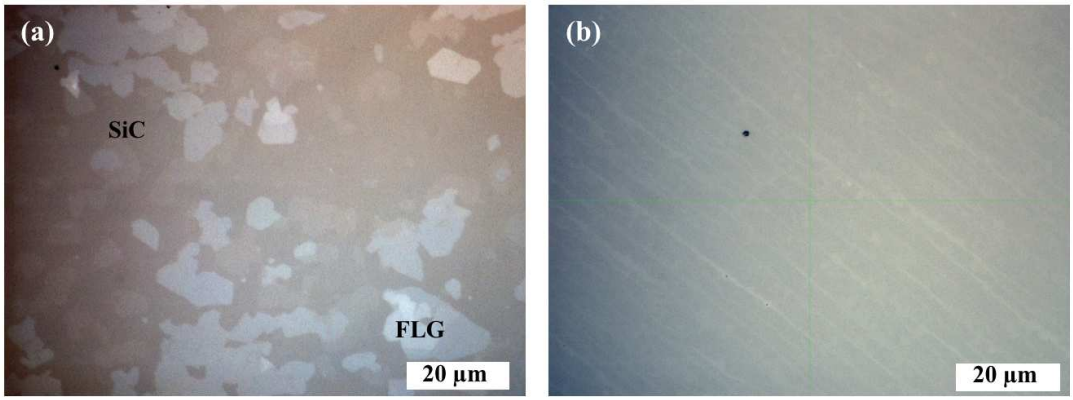

Fig. 1.13 Optical microscope images of the graphene grown (a) on SiC ($000\bar{1}$) and (b) on SiC (0001) in this work. Raman analysis suggest graphene presence in white flakes of sample shown in (a) while only SiC present on gray background. The white stripes in sample shown in (b) are ascribed to the bilayer while the majority blue surface probably consists of monolayer graphene.

temperatures result in the discrepancies in their surface morphology on these two polar faces.

In the literature, the best choice between C-face and Si-face growth is still in conflict until now. In general, the uniform large-scale graphene layers can be achieved on SiC (0001) but the charge transfer between the BL and graphene induces a great effect on the electronic properties of graphene. Degraded carrier mobilities ~ 1000-2000 $cm^2\ V^{-1}\ s^{-1}$ at 300 K [8] is usually obtained. Contrarily, graphene growth on SiC ($000\bar{1}$) has been usually revealed as an uncontrolled growth process while the carrier mobilities of grown graphene show the advantage over the graphene on SiC (0001). More precisely, the decoupling of the adjacent graphene sheets on SiC ($000\bar{1}$) and the weak interaction between graphene and substrate give rise to a higher carrier mobility at room temperature, in the range of 5000 to 15000 $cm^2\ V^{-1}\ s^{-1}$ [89,106]. However, the half-integer QHE is absent for multilayer graphene on SiC ($000\bar{1}$). This half-integer QHE was observed only in monolayer graphene grown on SiC ($000\bar{1}$) and with a very high carrier mobility of 15,000 $cm^2\ V^{-1}\ s^{-1}$ as well as an electron density of $1.27 \times 10^{12}\ cm^{-2}$ [107]. Moreover, the synthesis of large-scale monolayer graphene on SiC ($000\bar{1}$) is still challenging due to the poor controllability.

As mentioned, both growth mode and characteristic of grown film on SiC (0001) are largely related to the particular $(6\sqrt{3}\times6\sqrt{3})$ R30° reconstructed interfacial layer (Fig. 10 (e) and (d)), so called BL. In the following, we review the main research works about this BL. The C atoms of BL are partially bonded to substrate by sp^3 hybridization (Fig.1.11 (a)) which is the first carbon layer grown on SiC (0001) before graphene formation. In the literature, the seemingly conflict theoretical and experimental results were reported for years, for example the LEEM patterns always reveal a $(6\sqrt{3}\times6\sqrt{3})$ R30° reconstruction of this layer whereas the STM images show a (6× 6)

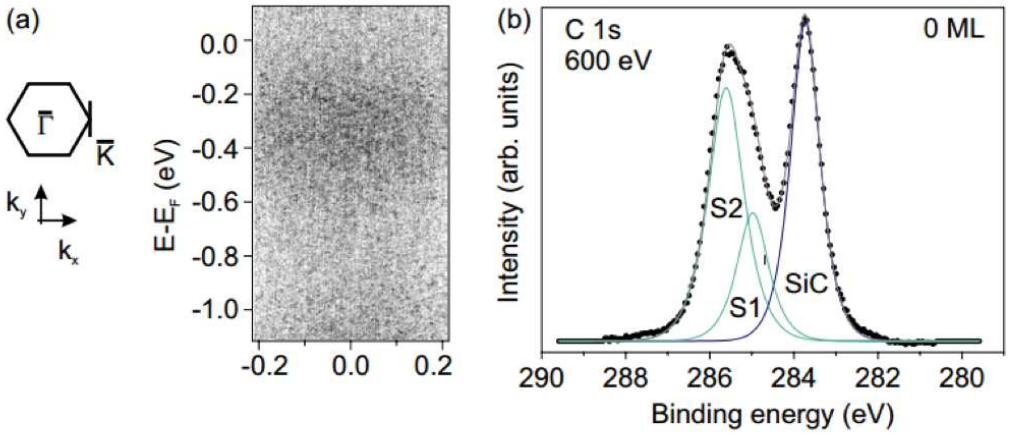

Fig. 1.14. Several experimental analyses of BL in [54]. (a) ARPES measurement showing the band structure. (b) C 1s spectrum in XPS measurement.

reconstruction [82,108]. Recently, it is widely accepted that the (6×6) revealed in STM is the results of the imaging of the interface reconstruction [109]. However, the interpretation of LEED and STM measurements remains an unsolved issue. Furthermore, the electronic properties of BL have been argued. The early ARPES measurement showed a wide gap insulator characteristic of BL [91] while the picture changed and found the BL to be a true semiconductor recently [110]. Despite these confusions, several characteristics of BL are clear. The ARPES measurement highlighted the different electronic properties of this BL compared to that of graphene by the missing of π-bands in the band structure (Fig. 1.14 (a)) which could be attributed to the sp^3 hybridization present in this layer [54]. As evidenced by XPS measurements, two broad components have been detected in this layer (Fig. 1.14 (b)) and attributed to the carbon bonded (S1) and carbon not bonded (S2) to the topmost Si in the SiC substrate [54]. Moreover, it is clear that the atomic arrangement in BL is similar to that of graphene layer as shown in STM images [92]. This argument is also supported by the post-growth treatment of hydrogen intercalation in which we can convert the BL into real graphene layer [111]. The hydrogen is thought to saturate the bonds between the buffer and SiC substrate. Thus, the transform of BL into graphene layer indicate the similar carbon arrangement between these two layers.

Indeed, the presence of BL has both the advantages and disadvantages. On one hand, BL serves as a template to reduce the growth rate and control the growth process which is one of the main reasons for the uniform graphene layer formation. On the other hand, due to the covalent bond between this layer and the substrate, the electronic and structural properties of grown graphene can be largely influenced. As mentioned, it is also well accepted that the degraded mobilities measured in epitaxial graphene layer is the result of this BL effect. Furthermore, the intrinsic n-type doping observed in epitaxial graphene has been reasonably explained by the electrons transfer between the BL and SiC substrate [112]. These mentioned electronic influences have been supported by a hydrogen intercalation treatment. Pallecchi *et al*. have shown the doping level

variation as well as a largely improved mobility after the post-growth hydrogen intercalation treatment [113]. Regarding structural influence, Schumann *et al.* [114] have demonstrated by Grazing-incidence x-ray diffraction measurement that the strain in monolayer graphene is a consequence of the interfacial BL. They suggested that the BL can turn into strain-free graphene layer after the oxygen intercalation treatment. Nevertheless, there still remains considerable works concerning the understanding and control of this graphene/SiC (0001) interface structure since few studies have been done to direct evidence the interaction between the BL and graphene. In this thesis, an exclusive approach to examine this interface and its influence on graphene is presented in **chapter 4**.

1.3.3 Graphene grown on SiC (0001) in vacuum and under argon pressure

Thermal decomposition of SiC was been first performed under UHV condition in 1975. Unfortunately, the graphene growth in this condition is far from the thermodynamic equilibrium, leading to a rapid sublimation rate of Si atoms, thus a poor morphology and disperse thickness distribution. Despite the ultra-thin graphite films can be achieved as shown by Georgia Tech group as early as 2004 [6], the limited grain size considerably affects the continuity and uniformity of the grown films. The control of thickness is crucial because the graphene electronic properties depend strongly on the number of layers. Thus, the inhomogeneous films produced under UHV condition hardly meet the industry demands of large-scale devices fabrication. One of a prominent breakthrough happened around 2008/2009, when two groups [7,8] reported that the large-scale uniform graphene layers can be achieved on SiC (0001) by sublimation under Ar pressure close to 1 bar.

Virojanadara *et al.* [7] have presented a robust method to prepare a homogeneous large-area graphene layer by using an ambient Ar pressure of 1 atm and a temperature of 2000°C [7]. Fig. 1.15 (a) and (b) compared the samples prepared in vacuum and under 1 atm Ar pressure, respectively. In Fig. 1.15 (a), only about half of the surface was

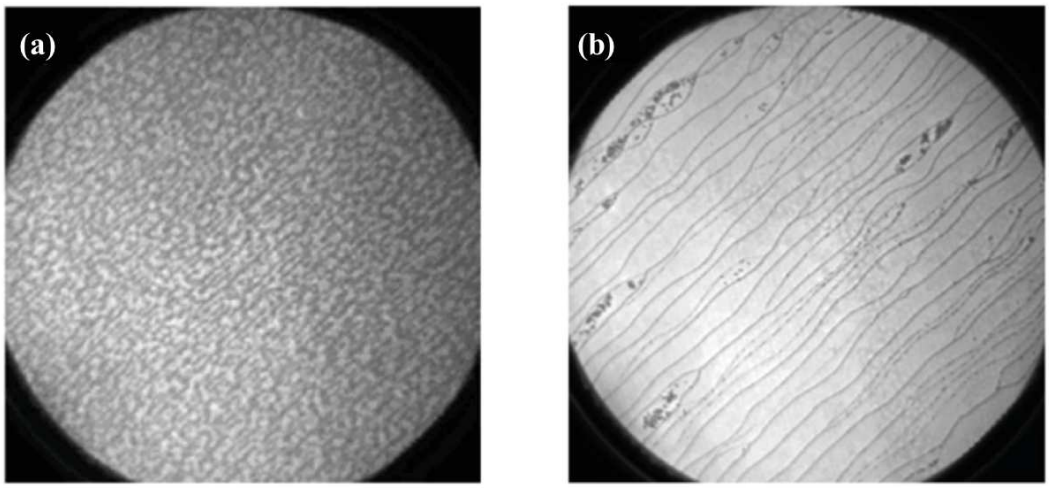

Fig. 1.15 (a) A graphene sample prepared under UHV condition. (b) LEED patterns of a single domain monolayer graphene sheet grown on SiC (0001) under argon pressure. Adapted from [7].

covered by stripe-shape monolayer graphene (dark contrast) in the sample synthesized in vacuum condition. Moreover, the length of these stripes is generally less than 0.1 μm and the distance between these stripes is about 0.18 μm, which is the same as the average terrace width on the substrate surface before the growth. This substrate surface is the typical result of miscut of the substrate during the polishing process. However, in this sample prepared in vacuum condition, the step-bunching process is absent, leading to a limited graphene stripe. In contrast, a homogeneous single domain graphene layer can be achieved on most part of sample synthesized under Ar ambient. In Fig. 1.15 (b), the black lines represent the step edges which are well aligned, implying the presence of step-bunching process. In fact, steps with different surface energies have the different step velocities and therefore the steps are preferable to be bunched together aiming to minimize the total surface energy during the thermal treatment. The authors claimed that the use of Ar pressure here could considerably reduce the Si sublimation rate and consequently increase the growth temperature. The smooth flat surface formation may require an annealing temperature above 1200°C due to a temperature dependent growth kinetics [79]. The atoms diffusion length can be enhanced in high temperature and results in a quasi-equilibrium growth condition. Consequently, the improved surface morphology is expected. The important discrepancies between these two samples suggested that the growth condition is extremely crucial to control the growth process, thus the results of graphene films.

Likewise, Emtsev *et al.* [8] have developed an growth process using an Ar atmosphere close to 1 bar. The monolayer graphene films with large domain sizes were produced on SiC (0001) at 1650°C. Prior to graphene growth, the sample surface has been treated by hydrogen etching and resulted in a uniform flat step-terrace morphology, as shown in Fig. 1.16 (a). Additional graphitization process in UHV condition or Ar atmosphere lead to a different surface morphology of graphene, as demonstrated in Fig. 1.14 (b-f). The AFM and LEEM images in Fig 1.16 (b) and (c) show that the sample prepared in UHV condition (UHV-grown) possess a rough graphene surface with inhomogeneous thickness distribution and irregularly shaped graphene islands. Besides, monolayer graphene areas coexist with the bilayer graphene islands and bare BL areas without graphene covering. Contrarily, the sample prepared using Ar pressure (Ar-grown) shows an improved surface quality. In Fig. 1.16 (d), the macro-steps with an average height of 8-15 nm and terraces widths 5-8 times larger than the original ones (Fig. 1.16 (a)) indicate the occurrence of step-bunching during the graphitization process. Despite the presence of bilayer and trilayer graphene at step edges (indicated in Fig 1.16 (f)), the monolayer graphene domain size is significantly larger than that of the UHV-grown samples which seems only restricted by the step edges. They suggest that the increased annealing temperature is the key factor to achieve the high-quality morphology due to the better crystallization of the C atoms. By the use of Ar surrounding ambient, the Ar atoms act as the diffusion barrier to reduce the Si sublimation rate since desorbed Si atoms would probably be reflected back to the surface by collision with Ar atoms. Thus, the graphitization process does not commence

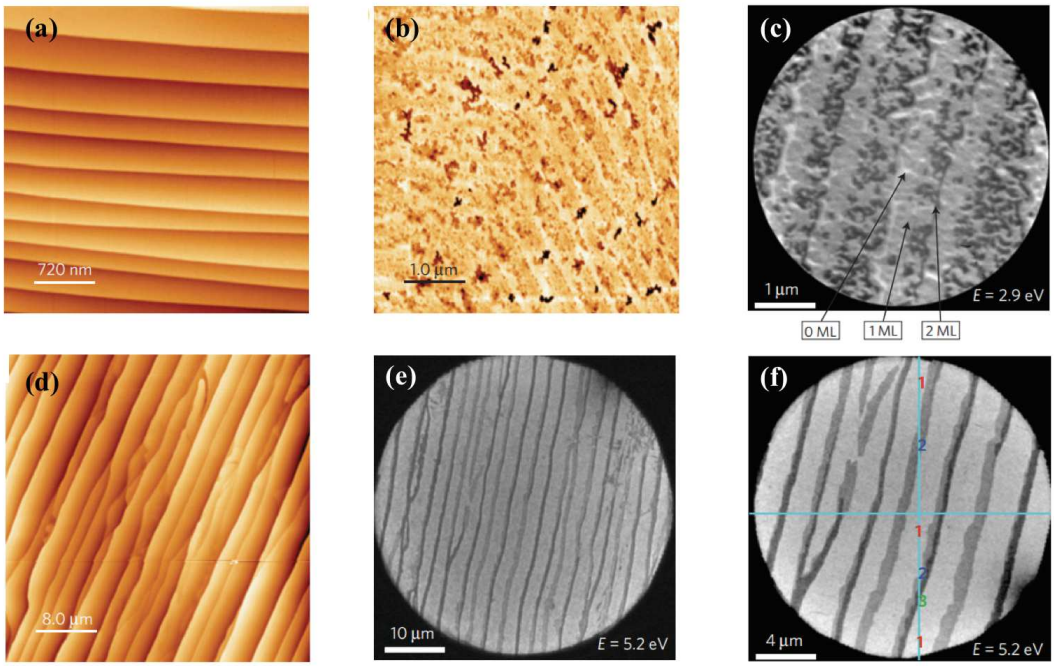

Fig. 1.16 (a) AFM morphology of Si-face after H-etching. (b) AFM image of monolayer graphene formed by annealing at a temperature about 1280°C under UHV condition. (c) LEEM image of a UHV-grown graphene surface. 0-2LG graphene thickness are indicated. (d) AFM image of sample annealed at 1650°C under an argon pressure of 900 mbar. (e) LEEM image of the same sample with that of (d). (f) a zoomed LEEM image of sample produced under argon pressure. 1-3LG graphene thickness have been identified in LEEM image. Taken from [8].

before a temperature attaint to above 1500°C. The surface reconstruction could be completed with step-bunching process before the graphene formation due to the enhanced surface diffusion at high temperature.

More properties of this Ar-grown graphene sample were revealed by LEED, ARPES and Raman spectroscopy, exhibited in the reference [8]. They have suggested that in spite of the improved morphology by using Ar pressure, the other graphene properties such as orientation with respect to the substrate, electronic structure and charge carrier density are similar to the UHV-grown films. The significant improvement in carrier

Table. 1.2 Hall mobilites (scale in $cm^2\ V^{-1}\ s^{-1}$) of UHV-grown and Ar-grown samples, measured in Hall bar and Van der Pauw configuration at room temperature and low temperature in reference [8].

Method	Structure	300 K	27 K
Ar	Hall bar	900	1,850
	Van der Pauw	930	2,000
UHV	Hall bar	470	-
	Van der Pauw	550	710

mobility of Ar-grown films compared to the UHV-grown films is evidenced by Hall effect measurement (Table 1.2), which can be explained by the extension in domain size. However, the typical mobilities at room temperature are generally found to be about 1000-2000 $cm^2 V^{-1} s^{-1}$, which is far from the expected one measured in quasi-free graphene layer and has been understood by the substrate influence as we have mentioned in **section 1.3.2**. The intrinsic n-doping with a carrier concentration of ~ $n = 1\times 10^{13}$ cm^{-2} is detected as a result of interface influence. Consequently, the Fermi level is shifted away from the charge neutrality point relative to the bands below it, i.e. in the valence band regime [87].

Both of these two studies have shown the obvious step-terrace morphology observed in the samples grown on SiC (0001) under Ar pressure. In fact, this characteristic has been known as the specific feature of epitaxial graphene on SiC surface due to the surface reconstruction of the substrate. Despite the on-axis substrate are commonly used in graphene growth, the slight incidental miscut can induce the step arrays on the SiC surface with a tilt angle of θ with respect to the normal c-axis, as illustrated in Fig. 1.17 [115]. Surface energies are different for each SiC bilayer plane in 4H- and 6H-SiC owing to the peculiar stacking sequence. For example, as shown in Fig. 1.18 (right), the 4H-SiC polytype has two different terraces 4H1 (-2.34 meV) and 4H2 (+6.56 meV) while the 6H has three types of decomposition energies 6H1 (-1.33 meV), 6H2 (+6.56 meV) and 6H3 (+2.34 meV) [68]. Steps with different surface energy have differences in step velocities during the high temperature etching or sublimation growth process. Therefore, the steps are preferable to be bunched together aiming to minimize the total surface energy: this phenomenon is called step-bunching. It is responsible for the large steps. In the case of the graphitization of SiC, both the surface reconstruction and step-flow growth at high temperature could generate the giant step-bunching with a step height higher than 10 nm [117,118]. The step-flow growth mode which usually happens when using the Ar pressure [56,119], means that the Si atoms detach firstly from the vicinity of step edges since the Si-C bonding are more active at steps with respect to the terraces. The step retracting follows the direction of basal plane, as indicated by red allows in Fig. 1.15 and Fig 1.18 (right). For instance, based on the

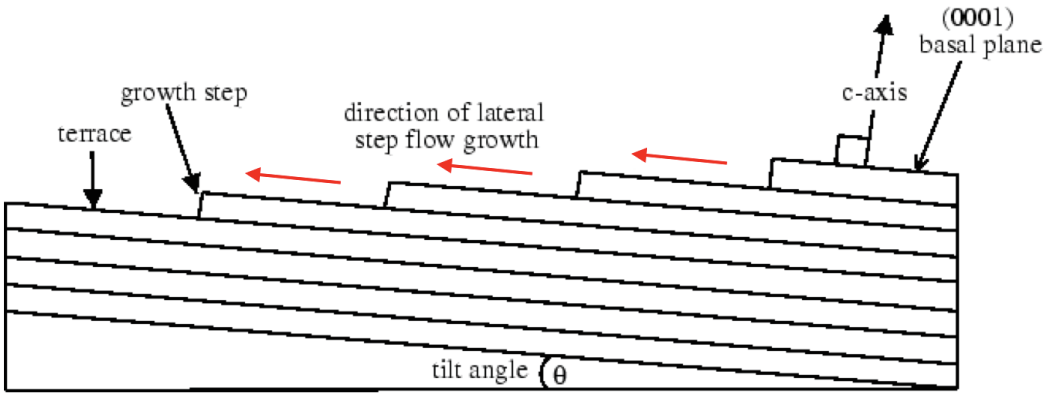

Fig. 1.17 Schematic of ''off-axis'' polished SiC surface [115].

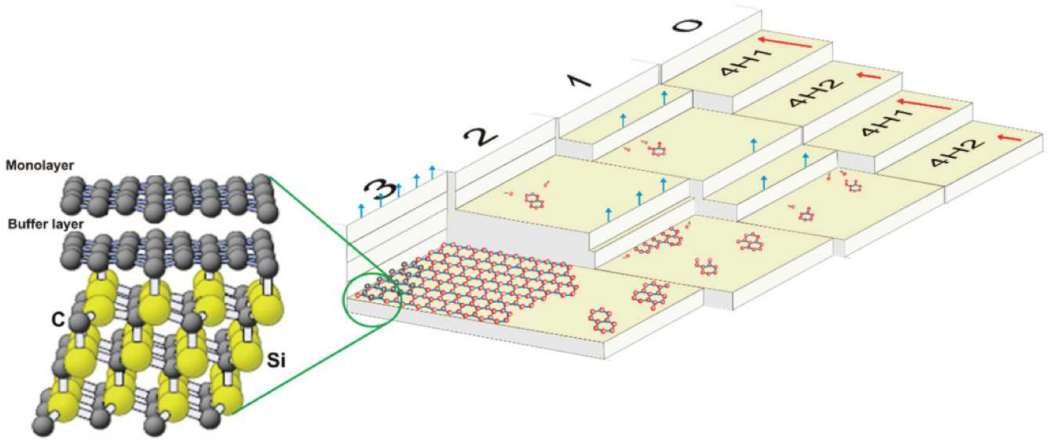

Fig. 1.18 Schematic of the epitaxial graphene growth process on SiC (0001) via sublimation (left). Schematic model of monolayer graphene structure (right). The perpendicular blue arrows with respect to the surface indicate the Si adsorption direction. The large red arrow in stage 0 indicates the step-flow growth direction. The small red arrows in stage 1 and 2 show the C diffusion. Taken from [116].

mentioned terrace energies for 4H-SiC, the 4H1 with a faster step velocity could be completely eroded first and catches up with the slower terrace 4H2 (stage 1 in Fig. 1.18), leading to a newly formed two-SiC bilayer height step (stage 2 in Fig. 1.18). The bunched steps could provide more C atoms and as the Si desorbing from the steps, the released C atoms may emit onto the terrace (Fig. 1.18 (right). These C atoms coalesce and nucleate into graphene islands, which act as the sink sites of subsequently emitted C atoms. Likewise, in the 6H-SiC polytype, the three steps with distinct surface energy are preferable to be bunched together and form three Si-C bilayers steps.

In the literature, there is still a strong disagreement on the understanding and control of the step-bunching process [8,7,120–122]. Various step-bunching degrees have been observed and related to the effect of miscut angle [123], the hydrogen etching [120,122] as well as the growth condition [7,8,121]. Emtsev *et al.* [7,8] have demonstrated that even after a hydrogen etching, the additional step-bunching process occurs during the growth and lead to the macro-steps structure. Oliveira *et al.* [120] have pre-defined the step structure by etching and succeed to suppress the further step bunching during the graphitization process. They suggest that once the substrate surface reaches the minimum total surface energy by pre-treatment, the additional step-bunching during the graphene formation is not an essential process. Kruskopf *et al.* [111] have demonstrated the giant step bunching usually occurs when the hydrogen etching process is performed while the annealing in Ar ambient could result in the sub-nanometer steps. They attributed this difference to the temperature window of the growth of BL. More precisely, the BL formation occurs during the Ar pre-treatment but absent during hydrogen pre-treatment. Once the BL grows, the surface would stabilize and prevent the additional step-bunching during graphene growth. Bao *et al.* have investigated the heating rate influence on the step heights [121]. They have synthesized various samples using the heating rate ranged from 40°C/s to 270°C/s. They found that the step-

bunching degree is dependent on the heating rate based on the argument that the step-bunching stops once the BL fully covers the substrate and graphene starts to grow. Assuming that the graphene formation starts at one fixed temperature, the change in heating rate leads to the time difference to reach this fixed temperature. For example, a slow heating means longer duration before entering the graphene growth phase and therefore the step-bunching process is longer and giant steps could be produced. Dimitrakopoulos *et al.* [123] have revealed the different miscut angle of the substrate could affect the sample morphology. The high miscut angle induces the high density of step edges on which growth nucleates. They argued that the pits formation is the result of the absence of steps.

The reason for such enormous attention on the step-terrace structure is the relationship between the surface morphology and the electronic properties [122–126]. It has been reported that the step orientation and multilayer graphene at step edges could induce an anisotropy in transport measurements [122]. In this argument, the graphene with sub-nanoscale steps has the privilege to the electronic applications over than samples with macro steps. However, several studies indicate that the occurrence of step-bunching would suppress the pit formation, leading to the improved mobilities [123]. Both of these works have demonstrated the morphology dependent electronic properties, which makes possible to alter these properties by controlling the pre-treatment substrate or tuning the graphitization condition. However, more efforts are needed to further understand the relationship between the graphene quality and structural properties as well as the influence of growth condition on these two items.

1.4 Motivation

In this chapter, we have discussed the fascinating properties of graphene due to its honeycomb lattice structure and unique cone-like band structure. Since the isolation of graphene in 2004, there has been a desire to integrate this material into the creation of new nanodevices considering its excellent optical, chemical, mechanical and electrical properties. We have also presented the most commonly used elaboration techniques of graphene films, i.e. mechanical exfoliation, CVD and thermal decomposition of SiC. Due to the lack of scalability, the mechanical exfoliation is limited to the research domain. Considering the other various alternatives, SiC was considered as the most feasible platform for realizing graphene electronics thanks to the compatibility with the state-of-the-art nanoelectronic processing. Graphene on SiC is today widely used in the high-power and high-frequency transistors as well as the metrological resistance standard.

Indeed, the history of research in micro- and nanodevices domain in our group could date back to 2009. We are now equipped with the electronic and optical characteristics measurement set-ups, as well as the techniques for device processing in the clean room. Besides, the growth of graphene on metals by CVD has been already developed in our lab since 2012. We have recently optimized the transfer process via an electrochemical method. However, the transferred films on Si/SiO_2 substrate hardly meet the requires for the electronic researches and applications, which motivated us to start the epitaxial graphene growth on SiC. We expect the obtained graphene films which are compatible with the nanoelectronic techniques will open the route for the fundamental research and further applications. Hence, the work of epitaxial graphene growth on SiC has started in 2015.

Based on the mentioned research studies, we started the graphene growth on SiC (0001) under Ar pressure due to the mentioned advantages in terms of uniformity of the grown films and the controllability of the synthesis process over other growth methods. In the literature, the epitaxial graphene growth under UHV or 1 atm Ar pressure has been largely investigated. However, few studies show a graphene growth process using the low Ar pressure [123,127–129] and none of them have successfully grown homogeneous and high-quality graphene layers. Hence, we expect an optimization work of monolayer graphene growth using an unclassical intermediate Ar pressure, i.e. 10 mbar, could give more insights into the growth and characteristics of epitaxial graphene. In this work, the growth of buffer layer is regarded as a starting point for the further optimization of monolayer graphene growth. Then the effect of growth parameters such as annealing time, annealing temperature, and temperature ramp will be studied while remaining the pressure is remaining 10 mbar. The graphene quality in terms of structural and electrical properties will be probed for samples produced under these various growth conditions. Various techniques will be applied to understand the characteristics of our samples. For example, the Raman spectroscopy will be combined with AFM images to estimate the number of graphene layers. Transport measurement will be performed on the samples of continuous graphene films. Furthermore, STM

images will show the atomic structure of our graphene samples. We expect to reveal the growth mechanism (e.g. step-flow mode or vertical growth) under this unclassical growth condition as well.

As mentioned, the BL, known as specific interface between graphene and SiC (0001), has considerable effects on the monolayer graphene. However, few studies have directly evidenced this interaction. Only few studies compare the bare BL without graphene growth above to the interfacial BL with graphene coverage. Considering the bare BL (first carbon layer growth) and the interfacial BL (second carbon layer growth between graphene and substrate) are different in many aspects, we aim to study the evolution in the same BL flake after mechanical removal of monolayer graphene above. To this purpose, graphene transfer methods have been developed in order to have access to the BL without graphene covering. The uncovered BL is compared to its corresponding interfacial BL examined before transfer experiment. In the meantime, the variety of all the achievable BL under different condition (growth temperature, with or without graphene above) will be investigated and discussed in terms of the homogeneity of their Raman signatures.

Lastly, the electrical properties are crucial for epitaxial graphene grown on SiC considering the potential applications of these films. The control of electrical properties of graphene -based devices is extremely important for further nanoelectronics. In this case, the transport measurements will be performed under various condition such as air ambient, liquid helium temperature, in vacuum or under UV illumination in order to reveal the doping characteristics of our monolayer graphene films. The attempt to control the electrical properties of our films by the UV light exposure will be described.

Chapter 2 Experimental methods

In this chapter, we will show the experimental methods of the epitaxial graphene growth and characterization used in this thesis. More than 230 samples have been produced and analyzed by these techniques, leading to an optimization of graphene growth process. Firstly, in **section 2.1**, a prototype furnace Zenith 100 and the synthesis process will be presented. All the graphene related productions were realized by this furnace fabricated by Annealsys, a company in Montpellier, France. From **section 2.2** to **section 2.4**, the main techniques to characterize our graphene films including Raman spectroscopy, atomic force microscopy, electrical transport measurement will be introduced. These measurements allow both the morphology and electrical properties investigations of our grown films. In **section 2.5**, scanning tunneling microscopy which were performed on several specific samples by our collaborative laboratory Néel Institut (Grenoble, France) will be briefly presented. At the end of this chapter, we will give a protocol of sample characterization procedure and summarize all the properties we can collect from all the mentioned techniques. We note that in this chapter we only focus on the fundamentals of the techniques and the achievable information of the studied samples. The setup details will be presented in **appendixes**.

2.1 Sample preparation in RTP furnace

In the current work, all the studied samples were prepared in our prototype high temperature furnace, Zenith 100 (Fig. 2.1) which was fabricated by the company Annealsys [130], in Montpellier. Annealsys manufactures rapid thermal processing (RTP) and chemical vapor deposition (CVD) systems. The Zenith 100 furnace was made for both high temperature annealing and CVD growth of graphene, belonging to the RTP process category (https://www.annealsys.com/products/annealsys-products/high-temperature-rtp-rtcvd/zenith-100.html). A schematic illustration of the furnace is demonstrated in Fig. 2.2. The low-volume stainless steel reactor chamber, cooled by a water circuit, provides a low memory effect and higher cooling rates (~ 10°C s^{-1}). The heating is performed using the resistive tungsten elements which allow a fast heating (~ 3°C s^{-1}) thanks to a high supply power ~ 36 kW. These stripe-like heaters are positioned at the top and bottom of the chamber. The sample holder coated by graphite and silicon carbide is placed at the center of the chamber and closed to the heating elements which permits an enhanced temperature uniformity. In addition, an easier upscale for large-size substrates up to 4-inch is available due to the design of sample holder. This reactor can sustain a wide range of temperature from room temperature up to 2000°C. Two pyrometers, which positioned at top and bottom of the chamber and pointed close to the center of the sample holder, associated with the fast digital PID controller assure accurate and repeatable thermal control across the temperature range. This furnace is equipped with a standard primary pump for reaching a rough vacuum and a turbo molecular pump for achieving a high-vacuum pressure.

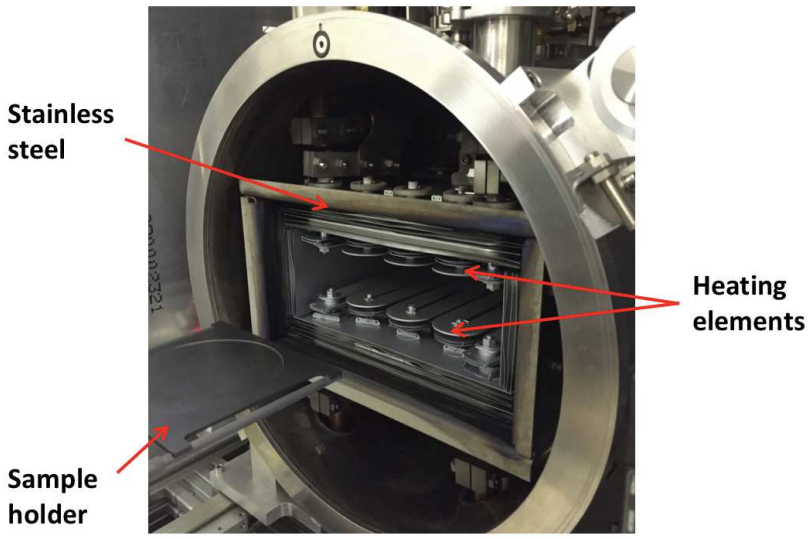

Fig. 2.1 Illustration of furnace Zenith 100, fabricated by Annealsys.

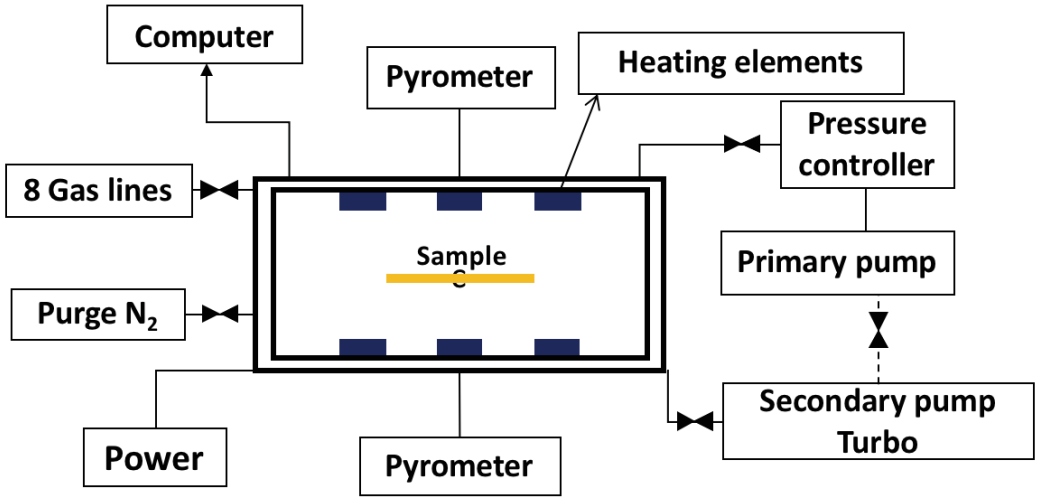

Fig. 2.2 Schematic illustration of furnace Zenith 100.

The pressure can be tuned from atmospheric pressure down to ~10^{-6} mbar at room temperature. In addition, a throttle vacuum valve and gauge allow the automatic adjustment of the pressure within the reactor when a constant inflow of gas is provided. Up to 8 process gas lines with individually digital mass flow controllers enable the different gas entering the reactor. An additional pure gas line is connected to the furnace to allow purging and cleaning of the chamber with nitrogen (N_2). All components of the furnace can be controlled by a computer software developed by Annealsys.

This furnace can realize both high temperatures annealing and CVD growth process. In this thesis, only sublimation process for the graphene growth on SiC was studied. We use the on-axis, semi-insulating 4H-SiC wafers purchased from Tankeblue and polished by NovaSiC (epi-ready). The 3-inch wafers were cut into 6 mm × 6 mm substrates. These substrates were chemically cleaned in acetone for 10 minutes with an ultra-sonic bath in order to remove the grease from the surface followed by sonication in isopropanol for 5 minutes before putting them into the furnace chamber. The

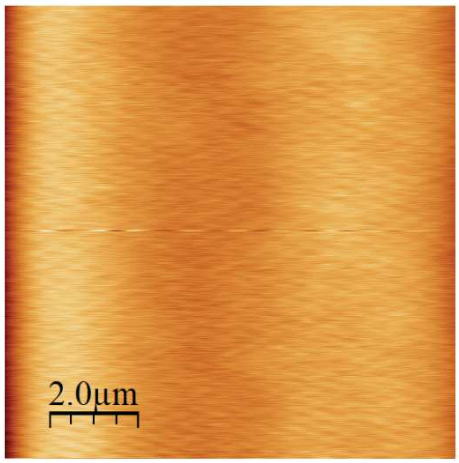

Fig. 2.3 AFM topographic image of SiC substrate before graphitization.

isopropanol can clean the residue of acetone and makes the substrate dry faster. We emphasize that there is no further substrate pre-treatment followed, e.g. no hydrogen etching. Fig. 2.3 demonstrate the substrate surface before graphitization process. We measured by AFM topographic images a root mean square (RMS) roughness around 0.6 nm indicating a relatively flat surface which is the typical result of chemical-mechanical planarization (CMP) of SiC [131].

The Si-face of SiC is deposited towards and at the center of the sample holder. Before each growth procedure, we evacuate all the gases from the chamber using a secondary pumping system until 10^{-6} mbar. This process allows evacuating all the gases in the chamber, thus an identical initial environment is created for each process before starting heating. Then we launch the synthesis by simply starting the pre-designed recipe in software. Several parameters could be defined in this recipe such as growth time, annealing temperature, temperature ramp, pressure, flow rate, etc. In our graphene growth work, the chamber is filled with pure Ar gas (99.995%) with a flow of 800 sccm at a desired pressure, 10 mbar. These two parameters remain constant during the entire growth process as presented in Fig. 2.4. The control valve adjusts to keep the pressure constant. In the meantime, the temperature increases by a power control until a temperature of 1240°C is achieved in order to ensure the thermal stabilization and synchronization of all the elements in the chamber. We have confirmed that the SiC substrate has not yet undergone any surface reconstruction at this temperature. Then the temperature control takes command with a defined temperature ramp and precisely surveillance by pyrometer. Later, the target temperature upholds at desired one for a specific annealing time. When the whole process completes, the heater power turns off. The temperature is left to decrease to room temperature and the pressure keep in a rough vacuum. The reactor is then flushed with N_2 until ambient pressure and the sample is unloaded. The entire process takes about 2h. The full data logging and process historical

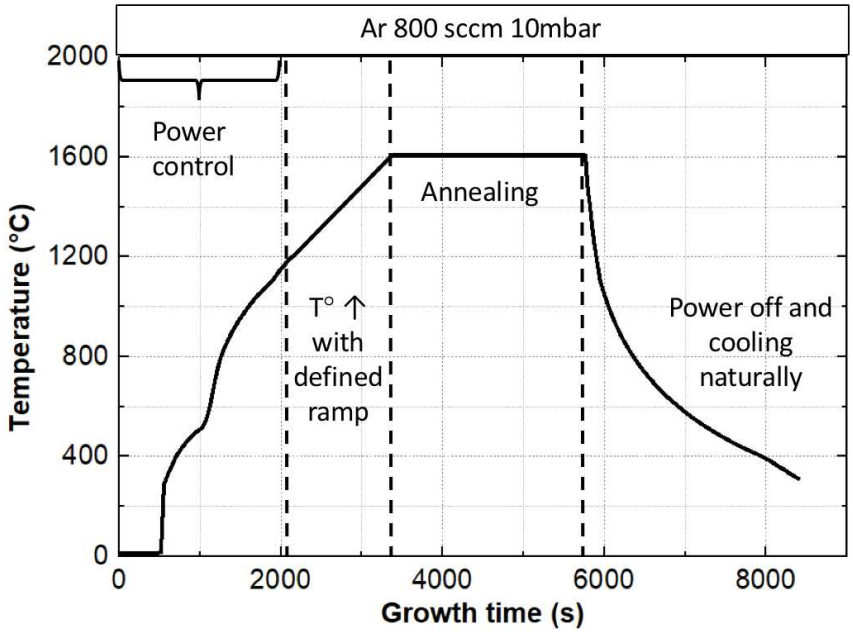

Fig. 2.4 Temperature evolution in one growth process.

is automatically recorded by the software. Before next growth starts, the sample holder is mechanically cleaned by the clean room wipers to ensure the same starting point for each growth. We note that our samples are stored in plastic sample boxes without additional precautions. During my PhD work, more than 230 samples have been produced by the described procedure. We have altered and optimized several parameters such as temperature, temperature ramp, annealing time. All the results presented in the following chapters were obtained by analyzing these samples using diverse characteristic techniques introduced in the following sections.

2.2 Raman spectroscopy

Raman spectroscopy is a widely used tool for the material characterization [132–136] which was discovered in 1928 [137]. In Raman experiments, the sample is illuminated by a monochromatic light and the reflected light is detected after their interaction with the vibrational levels in the sample. Fig. 2.5 presents different light scattering mechanisms when the incident photon excites into a virtual energy state. Besides the elastic process known as Rayleigh scattering, only a small fraction of the photons has undergone inelastic scattering which possesses a different energy than the incident photons. The Raman scattering describes these inelastic scattering by the Raman-active optical phonons in crystals. In this process, a lattice vibration can be excited (Stokes scattering) or annihilated (anti-Stokes scattering). The difference between the emitted photon frequency and the incident light frequency is called Raman shift and is expressed in cm^{-1}.

Since the vibrational states are unique signatures of material structure, Raman spectroscopy is a powerful technique for identification and analysis of material characteristics. For instance, in the case of studying the various forms of the different allotropes of carbon, the sensitive vibrational techniques reveal the geometric structure and bonding within the materials which differs from one to another. In addition, Raman measurements can give insight into the electronic or mechanical properties of materials due to their effect on the band structure of the material. Especially for the study of graphene, Raman spectroscopy provides various information such as the defects, strain and the charge carrier concentration.

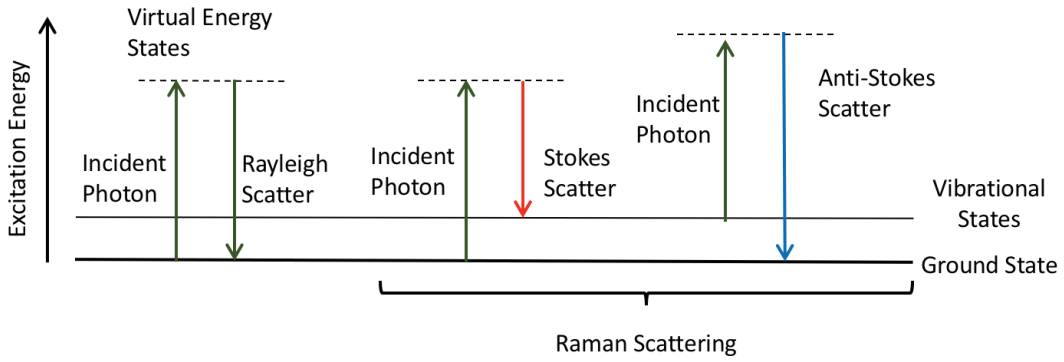

Fig. 2.5 Scattering mechanisms when the sample is excited by a laser source. We consider here the molecule in vibrational energy states.

2.2.1 Raman spectrum of graphene

In **chapter 1**, we have presented the phonon band structure of graphene (Fig. 1.2). Indeed, only few phonon modes are Raman active and can be observed in experiments. The Raman spectrum of graphene is typically dominated by two main peaks: G-peak and 2D-peak at about 1580 cm^{-1} and 2700 cm^{-1}, respectively, for the freestanding graphene measured with an excitation wavelength of 514.5 nm [138]. Fig. 2.6 (a) and (b) shows a Raman spectrum of pristine (defect-free) and defective graphene, respectively. A defective graphene shows significant difference compared to the pristine graphene by presenting several new peaks, e.g. D-peak around 1350 cm^{-1}. Only D-, G- and 2D- peaks are relevant to this work.

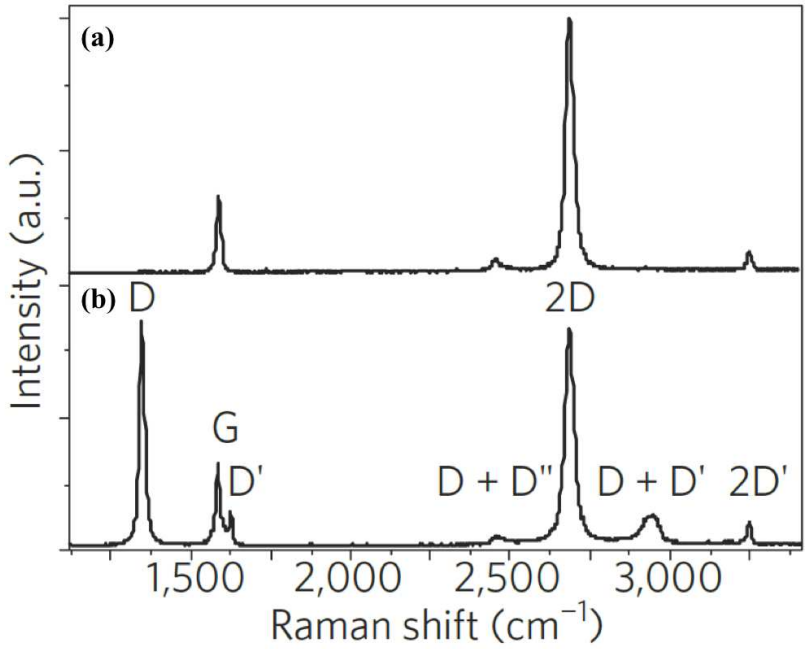

Fig. 2.6 Raman spectra of (a) pristine (defect free) and (b) defected monolayer graphene. Adapted from reference [133].

A real-space and k-space illustrations of the lattice vibration in G mode are shown in Fig. 2.7 (a) left and right, respectively. The G-peak originates from a first-order Raman scattering process corresponding to the bond stretching of all pairs of sp^2 atoms in graphene honeycomb structure. Starting with the excited virtual electron-hole pair created by the incident photon, the electron or the hole can be subsequently scattered by either an iTO (transversal optical) or an iLO (longitudinal optical) phonons which belong to the E_{2g} symmetry at the center of the Brillouin zone, Γ. Then the electron-hole pair re-combines and emits a photon that is shifted by an energy corresponding to that of involved phonon. We note that the G mode is the only Raman-active first-order mode in monolayer graphene.

Another strong peak in graphene is the 2D-peak which is related to the second order Raman process originating from the "breathing mode" of hexagonal carbon rings. The

process consists of two scattering processes and both of them are inelastic involving two near K-point phonons, as described in Fig. 2.7 (b). This double resonant process links the phonon wave to the electronic band structure of the graphene.

The D-peak involves an iTO phonon around the K-point like 2D-peak while the inelastically scattered electron by an iTO phonon to K' point then elastically scatter back to the K point by a defect. This means its activation requires the presence of defects. Thus, the D-peak has been regarded as a signature of defective graphene. In addition, it is found that the D-peak and 2D peaks positions are downshifted with increasing the laser energy. More detailed description of Raman scattering is presented in reference [139].

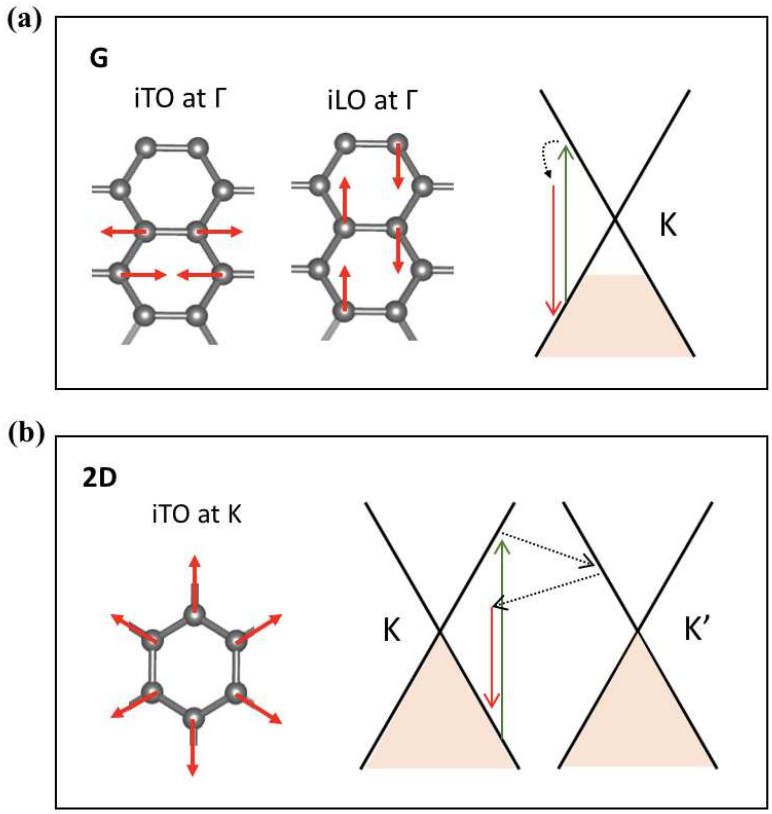

Fig. 2.7 Schematic depictions of the Raman active modes in graphene. (a) Lattice vibration of the G mode in real space (left) and k-space (right). (b) Double resonant scattering of 2D mode, depicted in real space (left) and k-space (right).

2.2.2 Number of layer effect

Raman spectroscopy has been considered as an ideal tool to estimate the number of graphene layers. The FHWM of 2D-peak (denoted as Γ_{2D}) and the ratio of integrated area between 2D- and G- peaks (A_{2D}/A_G) have been commonly used in the literature to distinguish single layer graphene (1LG) with few layer graphene (FLG) [133,140]. It has been reported that the Γ_{2D} increases and the A_{2D}/A_G decreases when FLG grow

compared to the case of 1LG. For instance, the 2D-peak of monolayer graphene can usually be fitted by a single Lorentzian peak with a FHWM about 35 cm^{-1} while four Lorentzian peaks are needed to fit the 2D-peak of the bilayer graphene due to their distinct electronic band structure [138]. Bayle *et al.* (L2C) [141] have demonstrated that these criteria are not always reliable due to the sensibility of the 2D-peak to the stacking order between consecutive graphene layers. They have shown that, in some specific cases, the twisted FLG possess the higher values of the A_{2D}/A_G and narrower 2D-peak widths compared than those measured in 1LG. More precisely, that is when the excitation energy match with a resonance energy, implying a resonance on the G-peak. In addition, several factors such as strain, doping and stacking order have a great chance to alter the shape of 2D-peak. For example, the FLG grown on C-face of SiC shows a symmetric Lorentzian peak [101], which is similar to the monolayer graphene grown on Si-face. Thus, the reliability of the criteria concerning 2D-peak has been questioned. On the other hand, Bayle *et al.* [141] have found that the integrated intensity of G-peak can be used as a criterion to determine the number of layers as proposed in their work. They suggested that the A_G increases step-by-step with the number of layers in the Bernal or rhombohedral stacked FLG [88]. As we know, the absolute Raman intensity is susceptible to experiment conditions (laser power, lens focus, etc.) and cannot be used to directly compare samples. In order to eliminate the influence of experiment condition and further compare the results of different measurements, they use a highly oriented pyrolytic graphite (HOPG) as a reference for the intensity normalization. The HOPG sample is measured in the exact same conditions with studied samples. The number of graphene layers can be estimated by integrated area of G-peak of graphene normalized by that of HOPG reference, denoted as $A_{G\text{-graphene}}/A_{G\text{-HOPG}}$. Taking account of the nature of the substrate and the experimental configuration of the measurement, the $A_{G\text{-graphene}}/A_{G\text{-HOPG}}$ ratio is reported close to 0.03 for the monolayer graphene [142]. In the case of FLG, this ratio value is close to 0.06, 0.09 and 0.12 for bilayer, trilayer and four-layers graphene. It is worth highlighting that this graphene layer estimation method is originated from L2C and has been confirmed as a robust indicator especially for the case of thin graphene films (less than 4 layers) [143]. Despite this, some possible limitations still force us to combine other techniques as a complementary criterion to further confirm the results. In the current study, the Raman maps were commonly combined with AFM images at exact same location to evidence the number of graphene layers. Besides, transport and STM measurements were seldom used to support the obtained results in the case of 1LG.

2.2.3 Raman signature of graphene on SiC

Now we focus on the Raman characteristics of epitaxial graphene (EG) grown on SiC (0001). In Fig 2.8 (a), the black and blue spectra represent the Raman signature of SiC and graphene grown on SiC, respectively. As we see, the second-order signal of SiC substrate overlaps the graphene D- and G-peaks in the Raman shift range of 1000-2000 cm^{-1}. In this case, a subtraction of SiC signal is necessary to reveal the graphene signature. After an appropriate subtraction (appendix 2), we can obtain the Raman signature of EG as illustrated in Fig. 2.8 (c), which allows us to study the D- and G-peaks of graphene. Besides, we observe some broad features between 1100 and 1600 cm^{-1} close to G-peak region. These peculiar features have been reported unique for the graphene grown on SiC (0001) and are absent for the graphene on SiC (000$\bar{1}$) or free-standing graphene, therefore they could be related to the buffer layer (BL) underneath the graphene. Fromm *et al.* [144] have demonstrated the disappearance of these features in free-standing graphene after a hydrogen intercalation process, which largely supports the assignment of these features to the BL contribution. Recently, more and more efforts have been put into the investigation of this BL as we mentioned in

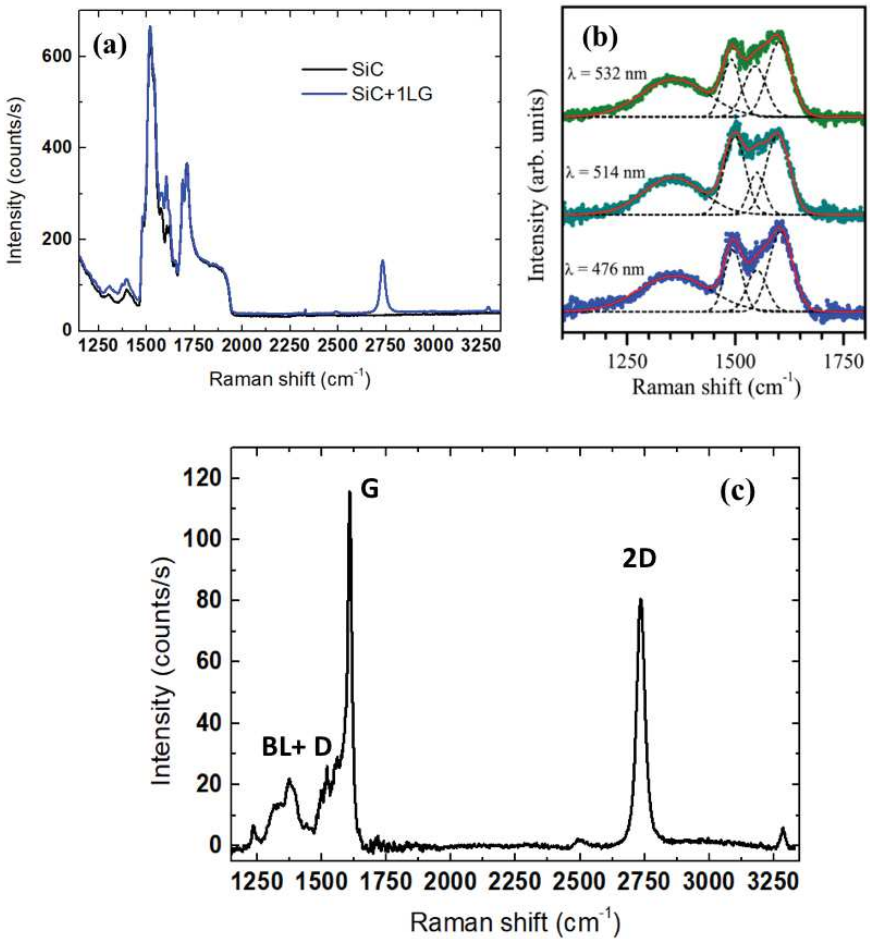

Fig. 2.8 (a) Raman spectrum recorded for a monolayer graphene grown on SiC substrate before subtraction. (b) Raman spectra of bare BL recorded with different laser wavelength. Adapted from [143]. (c) 1LG with the BL underneath on SiC (0001) after SiC subtraction.

chapter 1. Regarding Raman characteristics of BL, numbers of works have reported the observation of its contribution in the Raman spectra of EG but only few works have analyzed its Raman response in detail. For example, Fromm *et al.* [144] have studied the laser energy dependent Raman signature of bare BL without graphene coverage, as demonstrated in Fig. 2.8 (b). Even though different Raman signature of BL compared to graphene has been clearly noticed, the full interpretation of this Raman response of BL is still missing. In addition, a precise recognition of BL contribution in EG Raman spectrum helps us to better study the graphene-related Raman signature, such as the D- and G- peak.

Raman spectroscopy is a non-destructive method to investigate the structural and electronic properties of graphene layer. The defects related D-peak acts as an indicator to estimate the various present defects such as point defects (vacancies, sp^3- hybridized carbon, impurity atoms, etc.…) or edge defects (grain boundaries or domain size) [140]. In this work, due to the presence of BL, the D-peak (when it possesses low intensity) might be obscured by BL contribution in Raman spectrum. When the D-peak has high intensity, it still outstands itself. Furthermore, the electron or hole doping has a major effect on the Raman spectra of graphene in terms of the position or the FWHM of the peaks [136,145]. In the work of Das *et al.* [145], the Raman spectrum variations with doping have been monitored in a top-gated graphene. The electron or hole concentration has been controlled by tuning the applied gate voltage in order to shift the Fermi energy from the Dirac point. It has been reported that the G-peak undergoes a up-shift accompanied with a peak narrowing for both electron and hole doping. The 2D-peak position increases for hole doping while it decreases for electron doping and the FWHM increases for large doping. Besides, the G- and 2D-peaks are sensitive to the strain due to its influence on band structure [146]. It is known that these two peaks will redshift for tensile strain and up-shift for compressive strain. It is also found that the strain effect on 2D-peak is more pronounced by showing a shift twice the shift of G-peak.

EG films grown on SiC (0001) is doped and strained [147], therefore the G-peak and 2D-peak position shift from that of the shift-free and undoped graphene. These shifts are a combination of doping and strain effects. As we have discussed in **chapter 1**, the doping is the results of the presence of BL and external doping source influence. The compressive strain is due to the lattice mismatch (~ 0.2% compressive) and the difference of thermal expansion coefficients between the graphene and SiC substrate (up to ~ 0.8% compressive) [148]. In fact, the independent determination of these two effects is tricky and not feasible by the Raman measurements alone.

2.2.4 Experimental setup of micro-Raman spectroscopy and analysis software

The detailed description with a schematic illustration of our micro-Raman spectrometer setup is presented in appendix 2. Both the individual spectra and Raman mapping have been collected by using this instrument. The whole experimental setup was controlled by a dedicated, home-made Labview application. In addition, the obtained data were

analyzed by a powerful home-made software developed by A.-A. Zahab (L2C). Various data processing tools involved in this thesis are:

- Correction of the laser fluctuations (normalization of Raman map by laser power map).
- Spikes elimination.
- Subtraction of SiC substrate.
- Normalization of the intensity with regard to that of HOPG.
- Peak fitting.
- Correlation between two studied coefficients (intensity, width, integrated area).

These processes above allow the access to the Raman signature of graphene and BL (Fig. 2.8 (c)). With these results, the characteristics of graphene and BL could be analyzed. In addition, with the help of the combined microscopy and a home-made software developed by J.-R. Huntzinger (L2C), the image-tracking can be achieved which allows a repeated imaging of the same area. Consequently, the Raman maps were recorded at retraceable area in order to further combine the AFM technique or reexamine the surface characteristics after some treatment of the samples, e.g. exfoliation of graphene (detail in **chapter 4**).

In this thesis, more than 230 samples synthesized by our furnace have been subsequently analyzed by using this Raman spectroscopy setup. This technique allows a characterization investigation of our grown films in terms of the carbon structure, disorder, the number of graphene layers, etc. These obtained results will be discussed in **chapter 3**. Apart from graphene study, we highlight an BL investigation realized by Raman technique discussed in **chapter 4**. It is also important to mention that our experimental works have made a great contribution to the improvement of our home-made setup and analysis software.

2.3 Atomic force microscopy

Atomic force microscopy (AFM) was used in the current work to reveal the surface morphology of the samples. The AFM technique is based on measuring the force between the probe and the sample surface such as Van de Waals force, mechanical contact, etc. In fact, the force is not measured directly but by detecting the deflection of the cantilever which is induced by the interaction between the tip and the atoms on the sample surface during the scanning of the surface. The detection system consists of a laser beam which is reflected from the cantilever and a position-sensitive photodiode used to detect the deflection. The AFM measurements have three classical modes: contact, non-contact and tapping mode. In this work, the used mode is tapping mode (or intermittent-contact mode). In tapping mode, the cantilever is oscillated at near its resonance frequency. During the scanning, when the tip taps the surface, the repulsive force between the tip and the sample induces a change in the amplitude of the oscillation. The oscillation amplitude of the cantilever is kept constant by adjusting the tip-sample distance using the feedback loop. These adjustments during the scanning are then

converted to a surface profile. The advantage of this mode is the protection of the soft samples such as graphene.

The phase images can be recorded simultaneously with the topographic images. The phase lag of the cantilever oscillation compared to the signal of the piezo driver. The phase contrast is very sensitive to the variations in material properties such as adhesion and viscoelasticity, but also reflects topographic differences which lead to the unambiguous interpretation of the phase shift. Indeed, the phase monitors the energy dissipation involved in the tip-sample interaction. Generally, the hard material gives rise to the elastic interactions which lead to the bright contrast. On the contrary, the soft material induces the inelastic interactions, and thus a more negative phase shift [149]. Despite the complications of interpretation, phase contrast is one of the most powerful techniques to identify the composition characterization of sample surface [150,151].

Regarding the measurements on EG samples, the AFM topographic images are truly useful to reveal the stepped morphology of the sample surface. Besides, the surface quality can be revealed such as the presence of ridges, pits, etc. Fig. 2.9 (a) demonstrates the typical epitaxial graphene surface with the step morphology and pits (white arrows) as well. Furthermore, due to the erosion process during the graphitization, the profile of the sample surface could be used (combined with other techniques) to estimate the number of graphene layers in some occasions [8], especially in the case of step-flow growth of EG layers. More precisely, the carbon content in a single graphene monolayer (38.0 atoms/ nm^2) is very close to that in three Si-C bilayers (36.5 atoms/nm^2) [109]. One single Si-C bilayer constitutes 0.25 nm of height, whereas the separation between graphene monolayers is about 0.335 nm from each other. Thus, one monolayer graphene formation would recede from the top surface by about 0.42 nm ($3 \times 0.25 - 0.33$ nm) [152–154], as illustrated in Fig. 2.10. In this case, the first graphene layer form and extend along the step edges with a relatively lower surface level with respect to the original terraces. This means the graphene surface would be 0.42 nm lower than that of

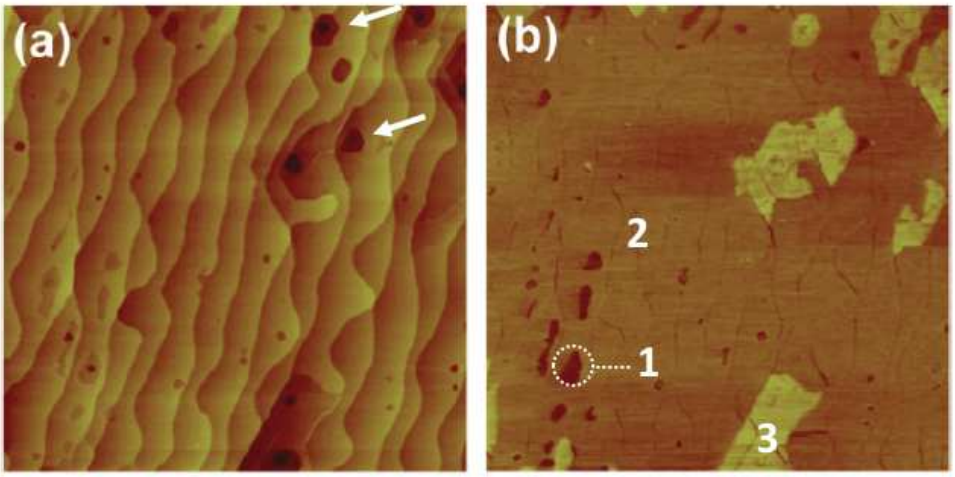

Fig. 2.9 (a) AFM topographic and (b) phase images. The white arrows in (a) indicate the pits. The numbers in (b) imply the number of layers. Taken from [156].

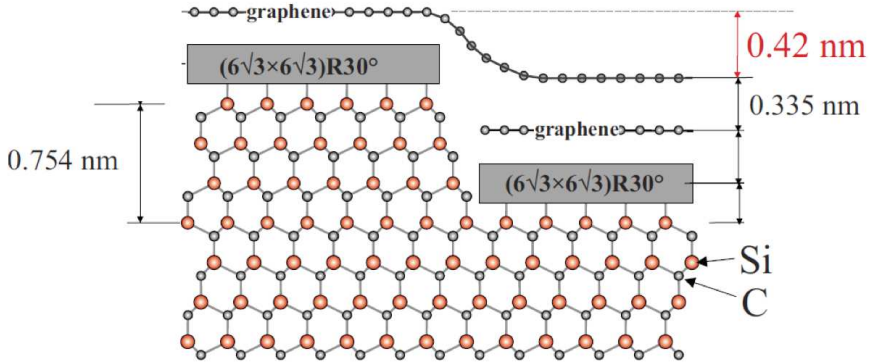

Fig. 2.10 Schematic explanation of the height of depression caused by one graphene layer formation. Adapted from [109].

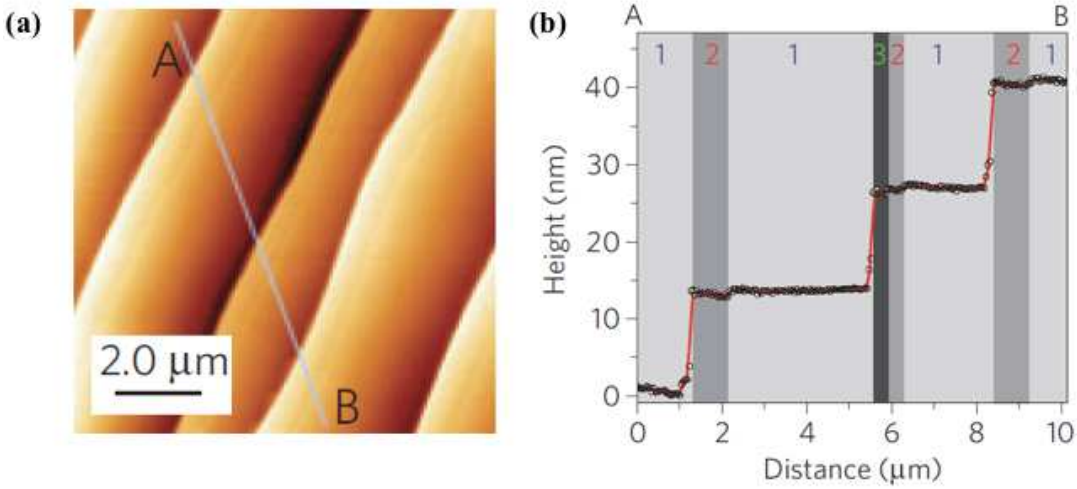

Fig. 2.11 (a) AFM topographic and (b) a profile followed blue line in (a). The depression height of 0.4 and 0.8 nm have been measured at step edges which are attributed to bilayer and trilayer graphene. Taken from [8].

bare BL. After one uniform monolayer graphene forming on the entire terraces, the subsequent graphene growth could follow the same step-flow mechanism. For example, Emtsev *et al.* [8] have used this characteristic to identify the multilayer graphene grown at step edges, as shown in Fig. 2.11. The profile image in Fig. 2.11 (b) show the depression of 0.4 and 0.8 nm at step edges which is the results of bilayer and trilayer graphene growth by sublimation of SiC.

Moreover, the phase contrast has been used as an effective tool to identify the graphene domain, as shown in the reference [155,156]. Both of these works have used the phase images to discriminate areas with different numbers of graphene layers. In Fig. 2.9 (b), Hibino *et al.* [156] have identified 1-3LG by phase contrast while they also stressed the lack of interpretation of the phase phenomenon that they have proposed to understand by adsorbates on the surface. In addition, the sensibility of the phase measurement has

been noticed in this work. They have observed the inverse of the phase contract and attribute it to the different tip condition [156].

In this thesis, the surface morphology of the grown samples was characterized by two AFM system in L2C. Both topographic and phase images could be acquired. The details about these setups are presented in appendix 2. One AFM is equipped with a microscope which allows a precise image-tracking and could be further combined with the Raman experiment. We will show in the following chapters that this combined AFM and Raman technique is a truly useful tool allowing a material identification, the estimation of number of graphene layers and the investigation of the surface morphology, etc. Both topographic and phase data were analyzed with the WSxM software package (v4.0 Beta 8.1) [157].

2.4 Electrical transport measurement

EG offers a high potential for electronic device application [68]. For this purpose, the electrical properties are the critical features of our grown films. Hall effect measurement has been regarded as a straightforward method to probe the electrical transport properties of graphene films. In this thesis, the electrical measurements were mainly employed on the pristine graphene grown on the semi-insulating SiC substrate without any transfer or lithography process. Four-probe Van der Pauw configuration was realized by four silver paint contacts on each corner of the sample, as demonstrated in Fig. 2.12. This enables to avoid the resin effect induced by the lithography processing on properties of our graphene films [39]. The Hall bar devices are occasionally used for specific cases such as measurements under UV illumination (**chapter 5**).

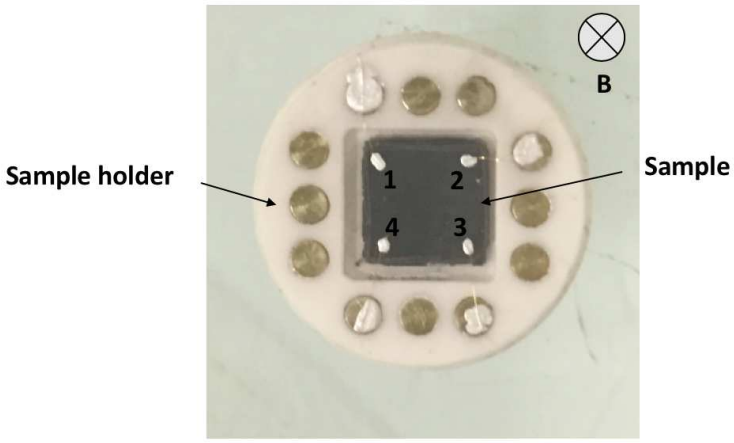

Fig. 2.12 Illustration of the Van der Pauw device in this work. Silver contacts deposited on the sample surface for electrical measurement in Van der Pauw configuration. The contacts at four corners are numbered as 1-4. The magnetic field perpendicularly traverses the sample plane.

2.4.1 Low-field Hall effect measurement

Low field Hall effect measurements were performed in order to study the electrical properties of our samples such as the sheet resistance (R_s, in Ω/sq), charge carrier type (n or p), carrier density (n, in cm^{-2}), and carrier mobility (μ, in $cm^2\ V^{-1}\ s^{-1}$). Aiming to determine all these properties, a combination of a resistivity measurement (without magnetic field) and a Hall effect measurement is needed. The Van der Pauw technique is widely used to probe the resistivity (ρ, in Ω cm) of a uniform 3D sample or the sheet resistance of a uniform 2D sample as graphene layer. For example, we measure the potential difference between points 1 and 2 when a current is injected between points 4 and 3 to obtain the resistance R_{12}. This measurement is repeated four times to get R_{12}, R_{23}, R_{34} and R_{41}. ρ and R_s are calculated as follows:

$$\rho = \frac{\pi d}{ln2} \times \frac{R_{12} + R_{23} + R_{34} + R_{41}}{4} f \tag{2.1}$$

$$R_s = \frac{\pi}{ln2} \times \frac{R_{12} + R_{23} + R_{34} + R_{41}}{4} f \tag{2.2}$$

where d is the film thickness and f a correction factor [158]. Then the sheet resistance R_s for 2D material is obtained by ignoring the thickness. For Hall effect measurement, we apply a magnetic field (0.56 T or 0.5 T dependent on the equipment). The magnetic field perpendicular through the sample will generate a Lorentz force on the sample plane and induce the deviation of the carrier charges, therefore a potential difference (Hall voltage, V_H) can be produced by Hall effect. In our case, if we introduce a current between points 1 and 3, a Hall voltage between points 2 and 4 can be measured and the Hall resistance (R_H) can be obtained. Here, the Hall coefficient (K_H) is calculated as follows:

$$K_H = \frac{V_H}{I \times B} = \frac{R_H}{B} \tag{2.3}$$

This leads us to the carrier density of majority n_{Hall} and the μ:

$$n_{Hall} = \frac{1}{e \times K_H} \tag{2.4}$$

$$\mu = \frac{1}{e \times n_{Hall} \times R_s} \tag{2.5}$$

where e represents the electron charge. Likewise, the current will be injected in points 2 and 4 and the Hall resistance between 1 and 3 is measured. This is to reveal the asymmetries of the sample and eliminate the parasitic resistance effect. The final R_H is the average of these two. Besides, the doping type can be explored by analyzing the slope of the Hall resistance with a consideration of the measurement configuration.

2.4.2 High magnetic field Hall effect measurement

In **chapter 1**, we have briefly introduced the quantum Hall effect (QHE) observed in monolayer graphene, which indicates the electron states are quantized into degenerate energy levels called Landau levels (LL). Indeed, the QHE could be observed during magnetotransport measurements at low temperature in strong perpendicular magnetic fields (B). We remark that this quantum behavior exhibits by the plateau in the Hall resistance of $\nu \frac{e^2}{h}$ and the vanishing in magnetoresistance. Here, in this chapter we focus on the QHE in EG on SiC.

In QHE, the number of states per LL is proportional to B. Usually, when we increase B while maintaining the total carrier density, the separation between each LL (denote as $|E_{n+1} - E_n|$) increases and every single level could accommodate more carriers. The QHE regime occurs when the Fermi level lays between two LLs. Moreover, unlike the conventional semiconductor, LLs in 1LG are not equally separated since $|E_{n+1} - E_n|$ decreases with increasing n. In epitaxial graphene, the charge transfer could widen the quantum Hall plateau in the Hall resistance [159,160]. Thus, the largest separation between the lowest LL $\nu = 2$ is the most prominent and widely observed plateau in 1LG on SiC at high magnetic field. Fig. 2.13 demonstrates the experimental observation of Hall plateau (red curve) and the vanishing in magnetoresistance (green curve) in graphene [25], compared with the QHE observed in GaAs (blue curve). As we can see, with the comparable accuracy, the plateau of graphene seems more promising than GaAs by a wider plateau [25,78]. Besides, the plateau value of Hall resistance of graphene ($\nu = 2$) is close to 12.9 kΩ, which could also be used as a fingerprint for 1LG in this work.

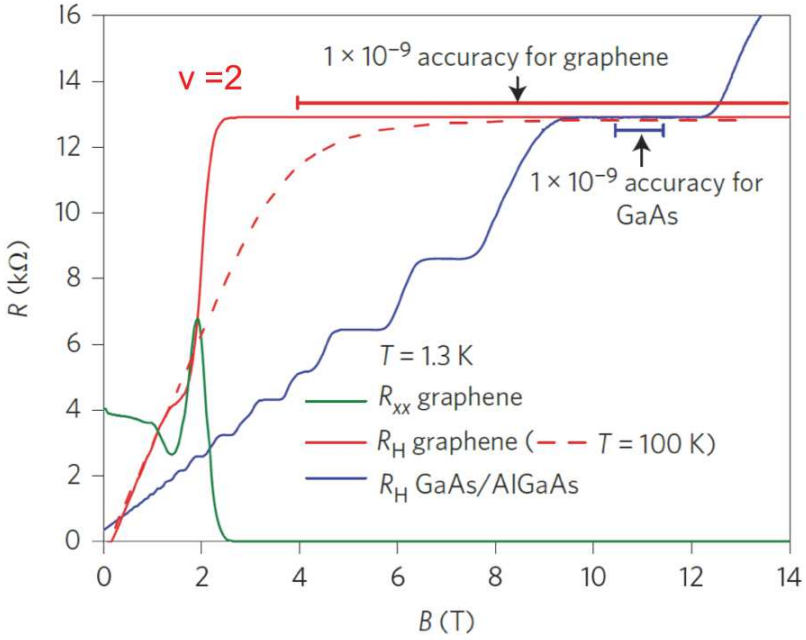

Fig. 2.13 QHE in epitaxial graphene (red for Hall resistance and green for magnetoresistance) and GaAs (blue). Adapted from [25].

2.5 Scanning tunneling microscopy

Scanning tunneling microscopy (STM) is largely used to characterize the surface morphology and local electronic properties of surfaces. It is based on the phenomenon that a tunneling junction could be created when a sharp metallic tip atomically close to a conducting sample surface. As a bias voltage is applied between the two, a tunneling current will flow. The constant current mode is commonly used in STM measurement in which the tip movement is recorded when it raises or lowers by a feedback loop in order to keep the tunneling current constant. The topography image from STM measurement is based on the condition that the tunneling current is very sensitive to the tip-sample separation. Especially when a low bias voltage is used, the atomic surface image could be achieved thanks to an extremely short spacing between sample and tip realized by a reduced tunneling resistance. Furthermore, the STM can be used in the scanning tunneling spectroscopy (STS) mode in order to investigate the local density of states (LDOS) of the samples. In this case, the probe is located at a fixed point in space by turning off the feedback loop and the tunneling current is measured for several different values of voltage. Thus, the signal of derivative of the tunneling current dI_t/dV_{bias} or the tunneling conductance is obtained which is proportional to the LDOS of the sample. More details are presented in the references [82,108].

In the case of 1LG on SiC (0001), the honeycomb lattice has been observed in STM topographic images [108,109]. It also has been found that the presence of (6 × 6) superlattice is the result of BL influence. More precisely, the tunneling transparency of the first graphene layer allows the examination of the structural features of the BL underneath [108]. This characteristic can be used as a fingerprint to distinguish the 1LG

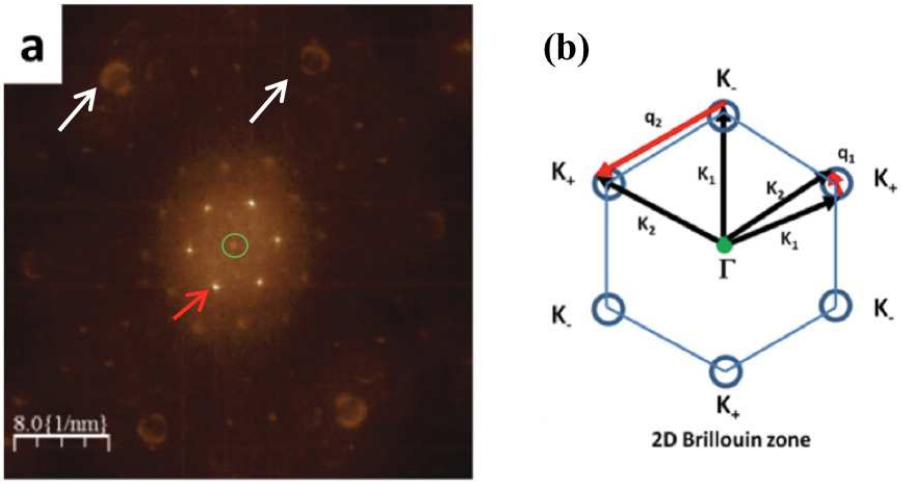

Fig. 2.14 (a) FT-STM image of monolayer graphene on SiC (0001). K points are indicated by white arrows. Green circle highlights Γ point. Red arrow corresponds to the (6 × 6) superlattice. (b) schematic illustration of q-space in graphene. The scattering vectors of intervalley (q_1) and intervalley (q_2) are indicated by red arrows. Taken from [82].

with few layers of graphene. Recently, the electronic properties of 2D material such as graphene, including the energy dispersion, Fermi velocity and chirality of quasiparticles, have been demonstrated by the Fourier transform (FT) of STM/STS technique [161,162]. Fig. 2.14 (a) and (b) show a FT-STM/ STS image obtained from measurements on 1LG on SiC (0001) and a schematic q-space pattern, respectively. In fact, the quasiparticle scattering wave vectors $\bar{q}$ should connect two points of the same Dirac cone (intravalley scattering, q_1), or connect two different valleys between adjacent $\mathbf{K}_+$ and $\mathbf{K}_-$ which are two inequivalent point situated on the corners of the hexagonal Brillouin zone (intervalley scattering, q_2). In Fig. 2.14 (b), the Brillouin zone is highlighted in blue lines and k_1 and k_2 denote the wave vectors of incident and scattered carriers. The green circle at the center indicates the **Γ** point of graphene. In this work, we focus on the q_2 who produce the six circular disks centered at the $\mathbf{K}_+$ or $\mathbf{K}_-$ points as pointed by white arrows in Fig 2.14 (a) and blue circles in Fig 2.14 (b). In fact, the constant-energy contours near E_F cut through the electron or hole conical sheets, resulting in these small circles of radius K. These disks features changed radius as a function of bias voltage because of the dispersion in the graphene electronic states. This could be used to derive the energy dispersion of quasiparticles and estimate the position of Dirac point. In addition, the six bright spots (red arrow) near the center Γ point come from the (6×6) superlattice. Here, we only use this technique as a tool to reveal the atomic structure and estimate the Dirac point. More details of FT-STM technique and quasiparticle interference are in the reference [161,162].

In this thesis, the 1LG sample has been sent to our collaborative laboratory Néel Institute (Grenoble, France), to complete the STM measurement. The measurements have been done by A. De Cecco, H. Courtois and C. Winkelmann. Both the topographic and electronic properties have been investigated and the results will be discussed in **chapter 3**.

2.6 Summary

Here, we present a protocol of the sample characterization and summarize the achievable information considering all the mentioned techniques. After unloading the samples from the furnace, they were stocked in plastic boxes. We started from the optical microscopy (detail in appendix 1) in which we examined the entire surface of 6 mm × 6 mm and some microscale areas of 128 μm × 128 μm situated at sample center and edge. The edge effect, induced by the gradient heating and inhomogeneous sublimation at sample edges, sometimes present in our samples which can be observed in optical images (Fig. A.1 (a)). In addition, the differential interference contrast (DIC) and polarized light were applied to enhance the image contrast (Fig. A. 1 (b)). Consequently, the steps morphology has been clearly seen for the sample with large steps height (higher than 1 nm). After having this first impression of the sample surface, Raman experiments were performed. Raman spectra were acquired from the positions 1 mm, 2 mm and 3 mm distanced from the sample edge. Thanks to a visualization of the step structure by the combined microscope, we were able to acquire Raman spectra close to the step edges and on the terraces for each detected area. Then these spectra were analyzed by the home-made software in order to obtain the information such as the carbon structure, number of graphene layers and the BL contribution, etc. For certain samples, Raman mapping were recorded at the retraceable area with the help of the microscope and the home-made repositioning software. AFM images were collected at a random area or a retraceable area depending on the equipment. The topography and phase images reveal the sample surface characteristic such as step morphology, pit and domains, etc. These results gave an access to study the growth mechanism as well. Next, the transport measurement in a low magnetic field at room temperature was followed for the graphene samples to investigate the electrical properties such as resistivity, carrier density and mobility. High magnetic field measurements were occasionally performed as demands. For instance, the homogeneous 1LG sample confirmed by Raman and AFM measurements or samples with low carrier density and high mobility measured in low magnetic field are worth further measuring at high magnetic field. Note that the QHE could be achievable in the sample with relatively low carrier density (equation 2.6). Later, for several peculiar samples, STM measurements were completed by our collaborative laboratory. We stress that here we only mention the main characterization procedure which has been employed for most of the samples in this thesis. Some special experiments such as the transport measurement under UV illumination or graphene transfer experiments will be presented in corresponding sections.

In the following chapters, we will show that all these tremendously useful techniques enable us to optimize the 1LG growth process and give insight into the understanding of EG growth and characteristics.

Table 2.1 Summary of all the techniques employed in this work and corresponding accessible results.

Techniques	**Results**
Furnace Zenith 100	Sublimation growth of BL, monolayer graphene and multilayer graphene on SiC (0001)
Optical microscopy	Surface cleanness, edge effect, step structure
Raman spectroscopy	Carbon structure, number of graphene layers, morphology by mapping, BL Raman signature
AFM	Step-terrace morphology, number of graphene layers by topographic and phase images
Hall effect transport measurement	Mobility, carrier density, doping type, QHE of 1LG
STM	Atomic topography, LDOS, Dirac point.
Graphene transfer	Access to uncovered BL by mechanical removal of graphene. See chapter 4
UV illumination or vacuum treatment	Doping type transition from p-type to n-type. See chapter 5

Chapter 3 Sublimation growth of graphene on SiC (0001) at low argon pressure

In this chapter, we discuss the growth of epitaxial graphene (EG) on Si (0001) by sublimation at a low argon pressure using our prototype furnace Zenith 100. The part regarding optimization of the monolayer graphene (1LG) growth by tuning growth temperature has been published in the paper "Growth of low doped monolayer graphene on SiC (0001) via sublimation at low argon pressure", *Phys. Chem. Chem. Phys, vol.19, pp.15833, 2017 [85]*, authored by '*P. Landois, T. Wang et al.*

Since the significant breakthrough around 2008/2009, 1 atmospheric (1 atm) argon (Ar) pressure is now commonly used to synthesize 1LG by sublimation of SiC. As we mentioned in **chapter 1**, the role of Ar pressure is to reduce the Si sublimation rate and enhance the growth temperature, therefore leading to a growth process in equilibrium condition. A uniform large-scale 1LG can be obtained at a relatively high temperature (1650°C in [8] and 2000°C in [7]) compared to UHV growth (1400°C in [6]). In the literature, EG growth under UHV or 1 atm Ar pressure has been largely investigated. However, few studies show a graphene growth process using a low Ar pressure [123,127–129] and none of them have successfully grown homogeneous and high-quality graphene layers. We consider that the intermediate argon pressure can reduce the annealing time and/or annealing temperature compared to the case of 1 atm Ar pressure. In addition, obtaining films with different but controlled characteristics, such as the number of graphene layers or the types of doping, by tuning the growth parameters, still remains challenging. Hence, to give more insights into EG growth, we focus on the optimization of 1LG growth by using an intermediate Ar pressure, i.e. 10 mbar.

To approach a reproducible growth of graphene in our prototype furnace, we started searching step by step for the optimum growth window by modifying only one parameter, the temperature, while others remaining fixed. We used a growth time of 300 s, the temperature ramp of 0.33°C/s and most importantly a low Ar pressure of 10 mbar. At the temperature of 1500°C, we have obtained a poor crystallized carbon-rich layer with a large number of disorders grown on the surface. By consequence, we increased the temperature to 1600°C and a sample resembling buffer layer (first carbon layer, denoted as BL) was achieved. The characteristics of this sample will be presented in **section 3.1**. Nevertheless, this sample then served as an initial point allowing us to investigate the growth parameters effects on the further monolayer graphene (second carbon layer) synthesis. We will demonstrate the growth time influence on the graphene synthesis in **section 3.2**. The influence of annealing temperatures will be discussed in

section 3.3. For each growth, we study the structural and electrical characteristics of our grown films following the procedure described in **section 2.6**. The obtained results allow us to progressively get closer to monolayer graphene growth condition. Thanks to this looped work, we have successfully optimized a reproducible process of the uniform large-scale 1LG growth, as will be introduced in **section 3.3** and described in **section 3.4**. More than 50 monolayer graphene samples have been obtained by conducting the same procedure on different wafers (4H-SiC) which confirms the high reproducibility of our growth process. Lastly, as will be demonstrated in **section 3.5**, we aim to control the graphene properties by tuning the temperature ramp. We expect different temperature ramps could lead to the various degrees of step-bunching. Thus, the surface morphology of grown graphene films would be altered. We believe that all these produced samples (more than 230) during this PhD work could give us essential insight into the growth of the EG on SiC (0001).

3.1 Starting with BL-like sample growth

As we mentioned in **chapter 1**, the first carbon layer grown on SiC (0001) by sublimation method is the so-called buffer layer (BL) which possess different properties compared to graphene. This difference could be explained by the covalent bonding between this layer and substrate. In this thesis, the growth of BL sample has been considered as a starting point of our graphene growth work. To this purpose, a sample has been produced at a growth temperature of 1600°C with a temperature ramp of 0.33°C/s and an annealing time of 300 s under a low Ar pressure of 10 mbar. We emphasize that back to the time when we produced this sample, we regarded this sample as a true BL based on the comparison of its Raman signature with the literature [163,164]. However, our recent results suggest that this sample is more alike with a carbon structure between the buffer layer phase and amorphous carbon phase [165]. We note that this sample was synthesized at very beginning of this growth work. Thus, we related the results of this sample to the unoptimized growth process. More detail of the identification of this sample will be introduced in **section 4.4**. Indeed, this misunderstanding of this sample only has a minor influence on the main results of this work. In this manuscript, we still consider this sample in this section as the starting point for the further optimization of growth parameters and denote this sample as BL-like sample. Different techniques, i.e. Raman and AFM experiments, will be used to reveal the characteristics of this layer. Here, the objective is to show the initial growth stages prior to 1LG formation. The detailed discussion of BL will be shown in **chapter 4**.

Fig. 3.1 (a) shows the Raman map of the integrated intensity of 2D-peak (denoted as A_{2D} map) of the sample produced using the parameters described above. The average spectrum of this map, shown in red spectrum in Fig. 3.1 (c) after a subtraction of SiC background, evidences there is neither sharp G-peak nor 2D-peak present. The lack of 2D mode is a signature that no or only small portion of well-crystallized honeycomb structure is formed on this sample. Indeed, the lineshape of this spectrum is very comparable to the spectra reported for the BL in the literature [144,163,166,167], as we discussed in **section 2.2** (Fig. 2.8 (b)). Most of the BL peaks are situated between the region of 1100 and 1700 cm^{-1} (outlined in red dashed rectangular in Fig. 3.1 (c)) with some low broad bands around 2D-peak region. Our red spectrum can be fitted by four Gaussian functions, centered at 1333, 1420, 1490 and 1578 cm^{-1}, as shown in red, green, orange and brown peaks, respectively, in Fig. 3.1 (d). The black and magenta lines represent the raw data and total fit, respectively. Moreover, each individual Raman spectrum in this map is almost identical except some minor discrepancies in 2D-peak intensity, evidenced by two types of contrasts in A_{2D} map. We then calculated the average spectra of all the yellow/green areas and navy-blue areas and the spectra are shown in Fig 3.1 (c) in dark yellow and navy-blue spectra, respectively. We excluded the spectra situated at the boundary of areas in order to acquire only pure signature of each domain. Evidenced by the slight 2D-peak in the dark yellow spectrum, the small organized carbon patches could be responsible for this yellow/green contrast.

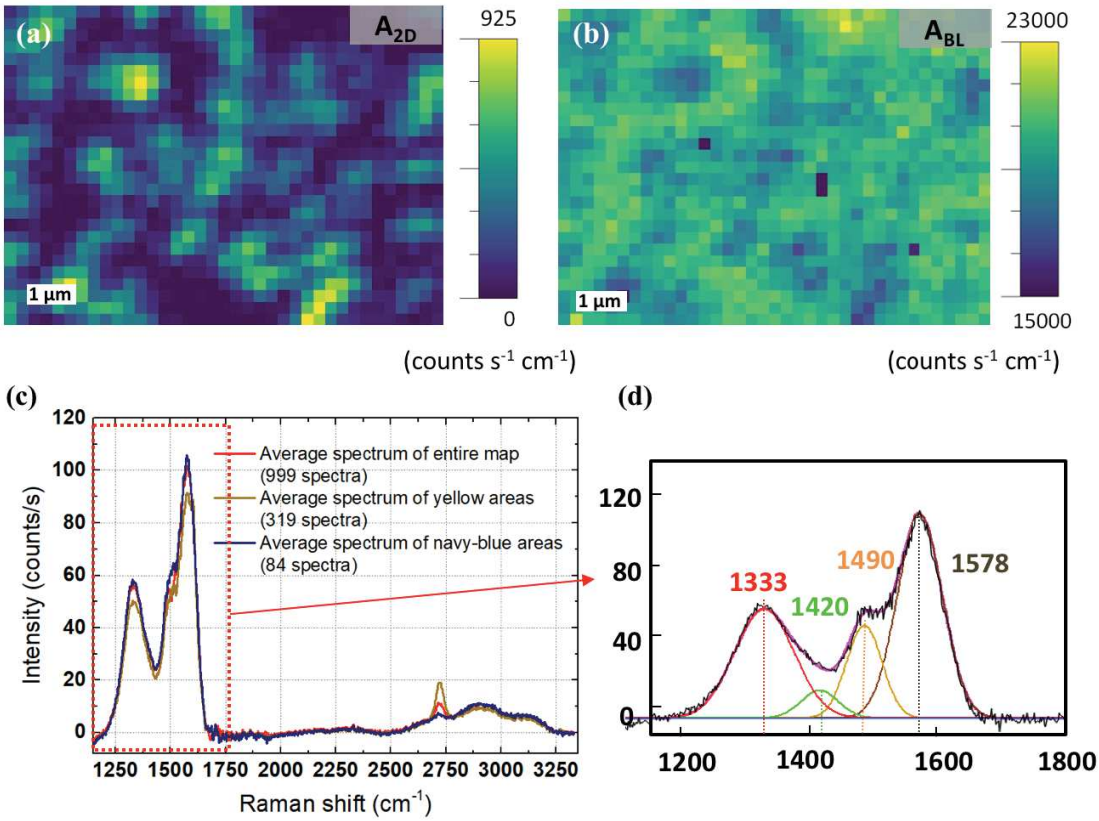

Fig. 3.1 Raman analyses of sample 1600°C, 300 s. (a) Raman map of integrated intensity of the 2D-peak from 2650 to 2800 cm^{-1}, A_{2D} map. (b) Raman map of integrated intensity of BL signal from 1100 to 1800 cm^{-1}, A_{BL} map. (c) Average Raman spectrum of the Raman map in (a) is shown in red curve; Average spectra of the yellow/green and navy-blue areas of Raman A_{2D} map are shown in dark yellow and navy-blue spectrum, respectively. (d) Average spectrum of entire map (red spectrum in (c)) is fitted by four Gaussian functions. Four Gaussian peaks are shown in red, green, orange, and brown. The black and magenta lines represent the raw data and total fit, respectively.

Nevertheless, as demonstrated in the map of integrated intensity between 1100 and 1800 cm^{-1} (denoted A_{BL} map, Fig. 3.1 (b)), this sample is covered by a homogeneous BL-like carbon structure.

The corresponding AFM phase image of this sample (Fig. 3.2 (a)) was recorded at exact same zone as Raman map. The location of the Raman map is outlined by the red dashed square. As introduced in **section 2.3**, this phase contrast is sensitive to material properties (SiC, BL or graphene). Regarding this sample, on the majority gray-blue surface, we observe some dark blue areas with a relatively lower phase value situated close to step edges (highest phase contrast shown by white lines). We then overlay this phase image with the corresponding Raman A_{2D} map, as shown in Fig. 3.2 (b). We note that the contrasts of these two overlapped images have been changed in order to give a better visualization. Obviously, the dark blue areas in phase image are exactly overlapped by the yellow/green patches of A_{2D} map where we observed a weak 2D signal in Raman analysis. As so, it is reasonable to attribute these dark blue zones to the

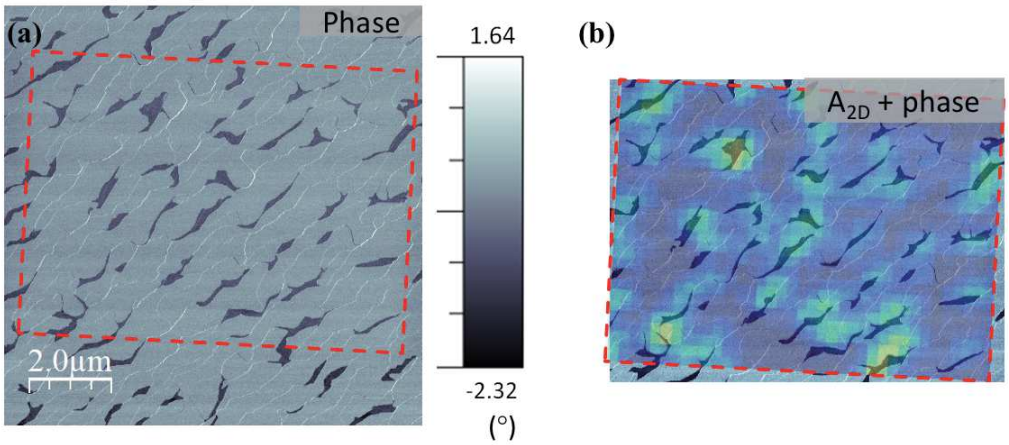

Fig. 3.2 (a) AFM phase image recorded at the same area as Raman map in Fig 3.1 (a). The red rectangle indicates the Raman map position. (b) The overlying AFM phase image and Raman A_{2D} map.

presence of small organized carbon structures on the BL-like layer, demonstrating the first step of the graphene growth. The location of these patches indicates that the graphene formation starts at step edges where the Si atoms can be easier detached from the SiC bulk [119,168,169]. It is an implication of step-flow growth mechanism based on the fundamentals presented in **chapter 1**.

The corresponding topographic image (Fig. 3.3 (a)) reveals a step-terrace morphology in which the step direction and terrace width were determined by incidental miscut of the SiC wafers, as we discussed in **chapter 1**. The step height and the terrace width are around 1~3 nm and 1 µm respectively, as shown in the profile (Fig. 3.3 (b)). This signifies the presence of the step bunching process of the SiC substrate during heating. This process has happened during the substrate heating under the Ar environment which is consistent with the observation of Emtsev *et al* [8]. However, the difference between our study and that of Emtsev *et al.* is the used Ar pressure, i.e. 10 mbar (this work) vs. 1 atm Ar pressure in theirs. At this point, we highlight a relatively smooth surface has been achieved in our work, evidenced by the absence of ridges on the regular stepped structure. Only several crayon shaped pits are presented closed to step edges (pointed by the white arrow in Fig 3.3 (a)) which is the result of different retracting rate of each terrace during the step-bunching [51]. The similar studies using a relatively low Ar pressure usually produce a morphology with a large number of pits, islands and ridges [123,128,129] due to the limited diffusion length and rapid Si desorption rate [57,127,128]. Sun *et al.* calculated the Si atoms diffusion barrier in UHV and Ar growth condition [57]. They found that the growth in UHV lead to a Si atoms diffusion-limited regime, therefore the diffusion toward step edges is preferred pathway for Si out-diffusion. By consequence, the pits could be largely produced in order to release Si atoms. Hibino *et al.* demonstrated the BL formation process in UHV results in a considerably rough surface with densely steps on the terraces [52]. They stated that the

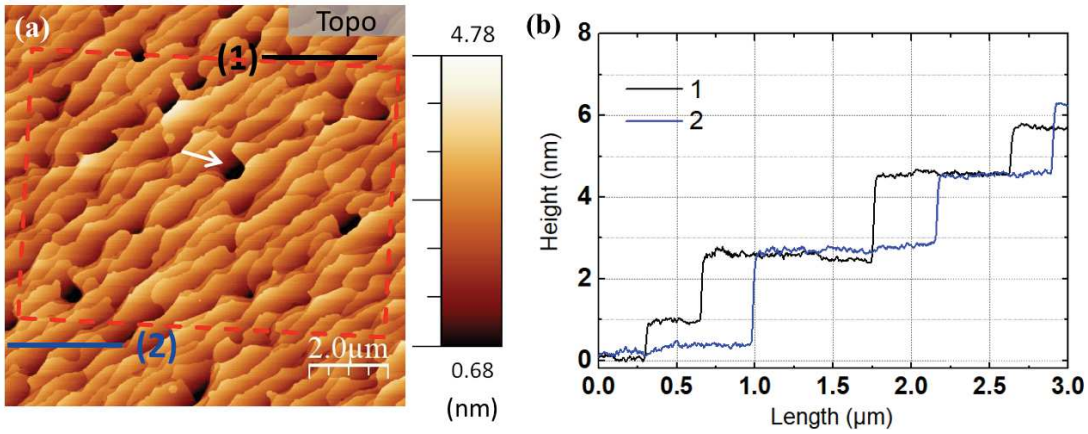

Fig. 3.3 (a) AFM topographic image recorded at the same area as Raman map in Fig 3.1 (a). The red rectangle indicates the Raman map position. The white arrow points at one canyon shape pit. (b) The extracted height profiles from black line (1) and blue line (2) in (a).

surface could recover regular smooth step-terrace morphology after bilayer graphene growth because the topmost graphene layers can stabilize the Si sublimation rate. Both of these two studies have argued that the use of 1 atm Ar pressure can improve the uniformity of the graphene films. Our observation illustrates a smooth BL-like sample surface without pits formation could be synthesized under an intermediate Ar pressure.

3.2 Growth time effect: from BL-like structure to multilayer graphene growth

Based on the previous BL-like sample, we first altered the growth time by prolonging it from 300 s to 2400 s and keep an annealing temperature of 1600°C. An extended growth time aims to sublimate more Si atoms and thus more C atoms available to form into graphene layer. Fig 3.4 (a) is a Raman $A_{G\text{-graphene}}/A_{G\text{-HOPG}}$ ratio (integrated intensity of G-peak in graphene, normalized by that of HOPG) map collected from this sample. We note that sharp G-peak and 2D-peak are continuously present within the sample, indicating the full coverage of graphene. Besides, the broad bands (between 1200 and 1800 cm^{-1}) close to G-peak could be recognized as BL contribution [85,144,164]. At first glance of $A_{G\text{-graphene}}/A_{G\text{-HOPG}}$ ratio map, we roughly identify two zones, green/blue and yellow/green contrast. The ratio of former and latter are ranged from 0.045 to 0.055 and from 0.065 to 0.08, respectively. Here, we emphasize that we again eliminate all the spectrum situated at the boundary of these two types of zone, considering they could be the result of the mixture of two zones. The average spectra of the green/blue and yellow/green areas are shown in Fig. 3.4 (b) in green and yellow spectra, respectively. In chapter 2, we have introduced a method to estimate the number of graphene layer by using the $A_{G\text{-graphene}}/A_{G\text{-HOPG}}$ ratio in Raman experiments (**section 2.2**). Here, the calculated $A_{G\text{-graphene}}/A_{G\text{-HOPG}}$ ratio (after subtracting of BL contribution) suggests that the graphene is thicker than 1LG in the green/blue zones since all the spectra show a value higher than 0.03 [88]. However, the value of ratio is also lower than that of 2LG (0.06). Thus, we assume 1LG/2LG could probably present in these areas. On the other

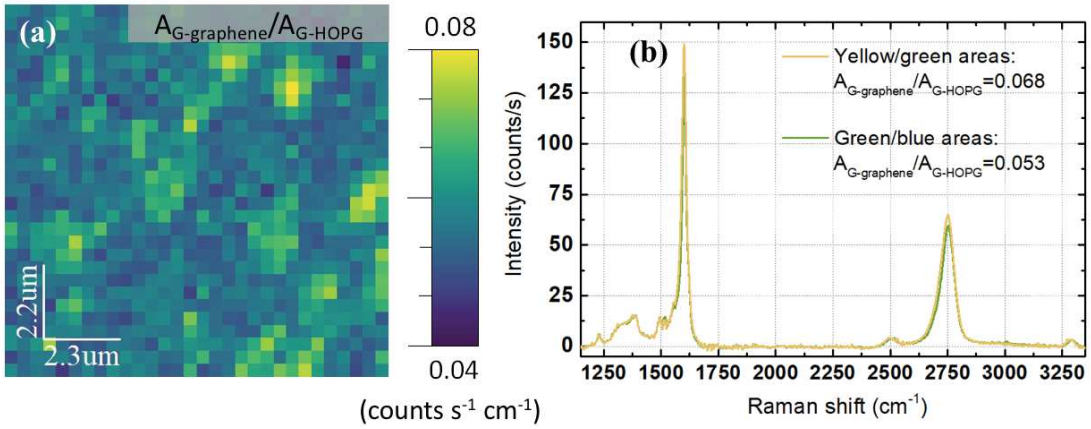

Fig. 3.4 Raman analyses of sample 1600°C, 2400 s. (a) Raman map of $A_{G\text{-graphene}}/A_{G\text{-HOPG}}$ ratio. (b) representative spectra of yellow/green and green/blue zones in map (a).

hand, in yellow/green areas, the $A_{G\text{-graphene}}/A_{G\text{-HOPG}}$ ratio is slightly higher than the expected value for 2LG (0.06). We suppose the 3LG could be seldom shown in these areas. Moreover, no obvious D-peak displayed in every spectrum of this map, signifying a well-crystallized graphene structure. Hence, comparing to the previous BL-like sample, an easy expansion of the annealing time could grow graphene layers from the initial stage of graphitization.

Fig 3.5 (a) and (b) show the AFM topographic and phase images collected at the same position as Raman map in Fig 3.4 (a). The Raman map area is highlighted by white dashed square. As we can see, the yellow/green zones in Raman map can be overlapped by darker flakes in topographic image. Considering the sublimation growth is an eroding process which will induce a surface depression after the graphene growth, the lower surface height could be related to a thicker graphene layer. This observation is consistent with the previous Raman analysis. Then, we observed numbers of white spots with a height of few nm and few hundreds of diameters distributed on the sample

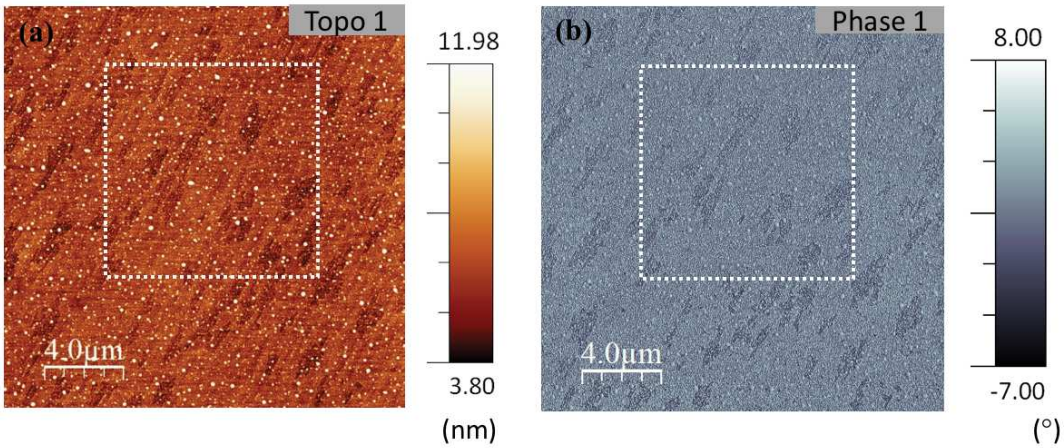

Fig. 3.5 (a and b) Topographic and phase AFM images of sample 1600°C, 2400 s, acquired from the same zone as Raman map in Fig 3.4 (a). The white dashed square shows the Raman map location.

surface. In the following, we denote these white spots observed in AFM image as nanoparticles. In fact, the presence of these white spots makes difficult to precisely measure the surface height difference for the thickness estimation. Regarding the phase image, the blue (relatively low phase value) and gray-blue (relatively high phase value) contrast correspond to the yellow/green and green/blue areas in Raman A_{2D} map, respectively. This observation shows that the phase image could identify the areas with different number of graphene layers. Since we have attributed green/blue and yellow green areas in earlier Raman analysis to 1LG/2LG and 2LG/3LG, respectively, it is thus puzzling to see only one type of phase contrast in gray-blue and blue areas in Fig. 3.5 (b). One explanation might be related to the presence of nanoparticles which could largely reduce the quality of the image. When scanning the small domains, it is difficult to identify them because the nanometer height particles could reduce the sensibility of the tips. In any case, the Raman and AFM techniques show the comparable surface characteristics which exhibit the advantage to combine these two techniques.

Another zone of this sample has been probed by AFM measurement. In Fig. 3.6 (a), the topographic image shows a step morphology with a terrace width of less than 1 μm, which is similar to the previous BL-like sample annealed at the same temperature for 300 s. Besides, the nanoparticles are present again in this zone but seem possess different size compared with that of Fig. 3.5. These nanoparticles could be possibly related to the growth process or the post-growth adsorption from environment. We note the AFM image in Fig. 3.5 were acquired recently, almost two years after the growth of the sample while the AFM image in Fig. 3.6 were collected one month after the sample growth. Thus, these nanoparticles seem to have a time evolution which supports the assumption of the post-growth adsorption. Until now, it is still not feasible to determine the growth effect and post-growth effect separately because these two images were probed at different locations and comparable geometry of these nanoparticles are present in these two images. We rather assume both of these two factors lead to their occurrence. Despite the origin of these nanoparticles is unclear for now, at this moment we would like to briefly highlight several observations. With the help of the statistical

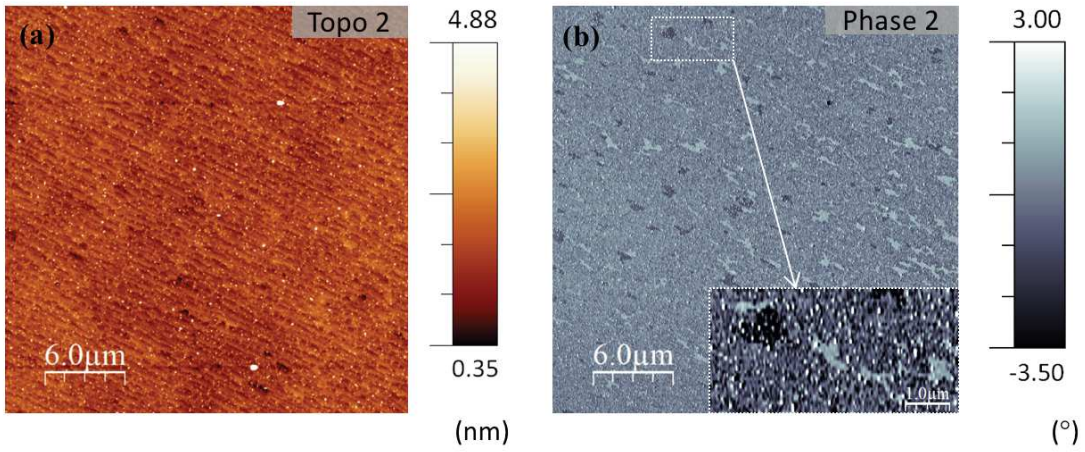

Fig. 3.6 (a and b) Topographic and phase AFM images of sample 1600°C, 2400 s. The inset image of (b) indicate the dark blue, blue and light blue areas observed in phase contrast.

analysis of the AFM image, we have identified the radius sizes of the nanoparticle present in this area with a variation between ~20 nm to ~200 nm and their height between ~ 0.67 nm and ~ 10 nm. The size variation of the nanoparticles indicates a different degree of the cluster. Moreover, these nanoparticles are absent in some samples which implies that they are probably not related to the contamination of the furnace environment. Indeed, these nanoparticles could degrade the AFM image quality as well as the cleanness of sample surface. For this reason, growth parameters were altered aiming to suppress their presence. Further discussion about these nanoparticles will be continued in **section 3.3**.

Then, the AFM phase image shows three types of contrast as illustrated in the inset image of Fig. 3.6 (b). The surface is majority covered by blue contrast while gray-blue with highest phase value and dark blue with lowest phase value are occasionally shown in island shapes. Since the Raman experiment has not been performed at this position, we could not precisely identify the number of graphene layers. In the early observation, we have shown that the AFM phase image could be used to distinguish the domains with different number of graphene layers. In this case, we might attribute these phase contrast to the three types of graphene thickness which indicate the ununiformed graphene distribution of this sample. In addition, seeing less intense of nanoparticles and the detection of small graphene flakes (inset of Fig 3.6 (b)), we highlight that even the small domains that possess different thickness could be clearly recognized in AFM phase images.

Hence, by increasing the graphitization time, we are able to fully cover the sample surface by multilayer graphene (FLG). However, the homogeneous monolayer graphene formation is probably hard to achieve at this temperature since graphene with different number of layers coexist on the sample surface with relatively small domain size, which signifies a low surface energy at this growth condition. Thus, increasing the annealing temperature is one of the solutions to enhance the surface energy and we will tune this parameter in **section 3.3**.

3.3 Growth temperature effect: optimization of monolayer graphene growth

Based on the initial BL-like sample growth, in this section, we will study the growth temperature effect which is a vital factor to control the graphene growth process. We will show that the graphene ribbons could be obtained at an annealing temperature of 1700°C with the same annealing time (300 s). Most importantly, the monolayer graphene is optimized by using a temperature of 1750°C (300 s). Besides, the FLG samples can also be achieved at the annealing temperature of 1700°C and a longer annealing time (1200 s).

By annealing SiC at 1700°C for 300 s, obvious ribbon-like features revealed by the yellow contrast appear in Raman 2D map (Fig. 3.7 (a)). In this case, two types of zones have been identified: navy-blue areas and yellow/green ribbons areas. We collected two representative spectra from each zone, as shown in Fig. 3.7 (b). Comparing to the literature [144,167], the navy-blue spectrum taken from navy-blue zone can be

identified as a BL spectrum. In Fig. 3.7 (c), we fit this spectrum by 4 Gaussian functions situated at 1367, 1504, 1563 and 1618 cm^{-1} and its lineshape is close to the one reported in [144,167]. On the other hand, in the yellow spectrum collected from the yellow ribbon zone, we observe the sharp G-peak and 2D-peak situated at 1611 cm^{-1} and 2740 cm^{-1}, respectively, indicating the presence of graphene. These two peaks have undergone an up-shift in comparison to undoped and unstrained graphene [138], which is typically observed in graphene grown on SiC [86], as we discussed in **section 2.2**. Moreover, the BL contribution has been identified in the wavenumber region between 1200 cm^{-1} and 1800 cm^{-1}. Its lineshape is quite similar to the ones reported in the literature [144,164] and in Fig. 2. 8 (c). We can fit this BL contribution and G-peak

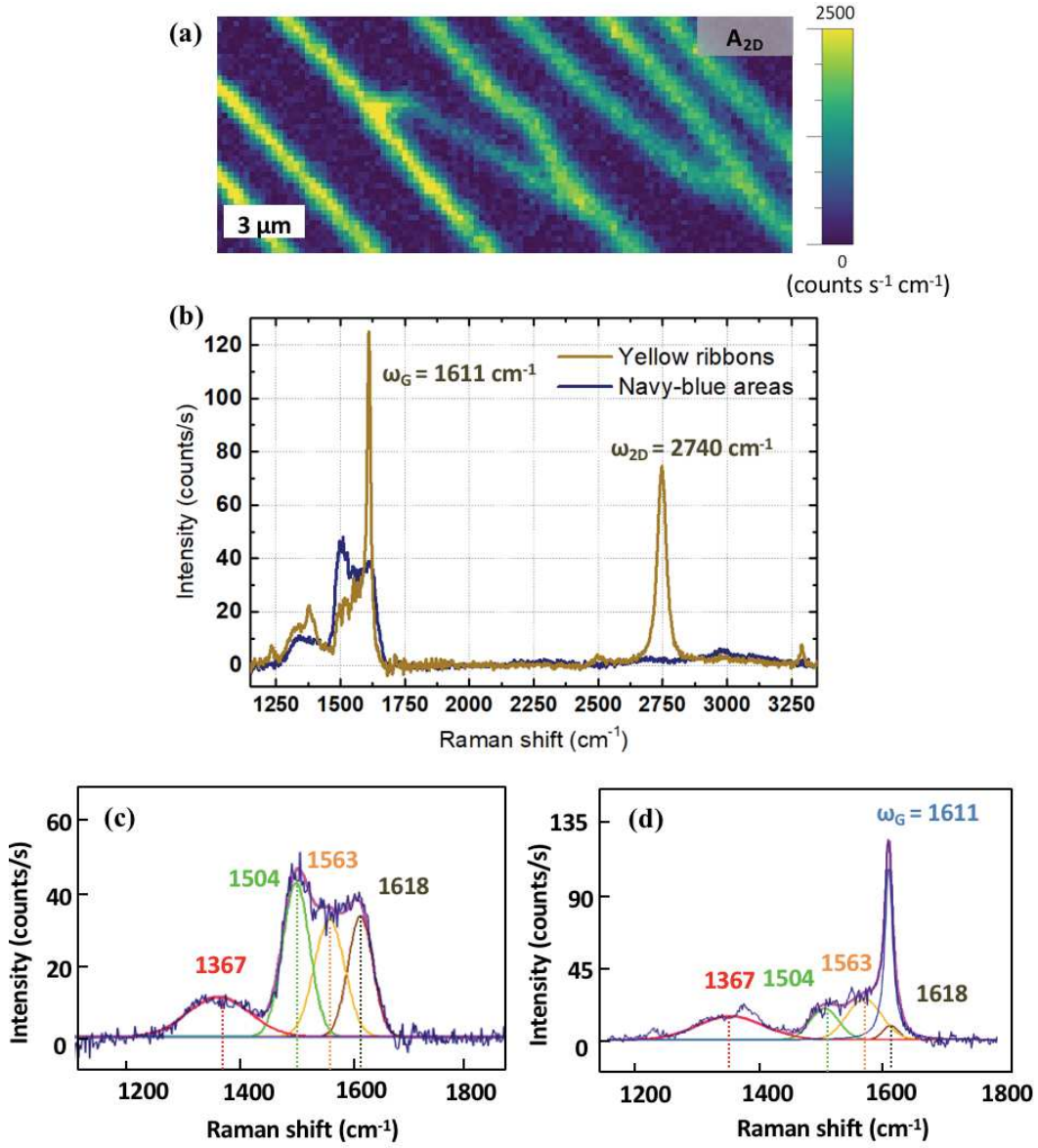

Fig. 3.7 Raman analyses of sample 1700°C, 300 s. (a) Raman 2D-peak map. (b) Representative spectra of yellow stripes and navy-blue areas in map shown in (a), respectively. (c) Representative Raman spectra of navy-blue zones fitted with four Gaussian functions. (d) Representative Raman spectrum of yellow stripes zones fitted by four Gaussian functions and G-peak fitted with a Lorentzian function. The peak positions are indicated.

situated by 4 Gaussian functions and a Lorentzian function, respectively, as shown in Fig. 3.7 (d). So far, one might notice the discrepancies of BL contribution in Raman spectrum dependent on samples and zones as well as the graphene coverage. For example, the BL contribution undergone an intensity change after the graphene coverage. If we compare the BL in Fig. 3.7 (c) with (d), we notice a decrease in intensity of peak at 1618 cm^{-1}. Variety of BL will be discussed in **chapter 4**. Then, the D band, which is a signature of the presence of defects in the graphene layer, is rarely observed, proving well-structured graphene ribbons. Regarding the thickness of graphene, we calculated the ratio of $A_{G\text{-graphene}}/A_{G\text{-HOPG}}$ in several spectra taken from the middle of the ribbon areas. The obtained average value ~ 0.031 suggests the presence of monolayer graphene ribbons [88]. However, it is important to take laser spot size and ribbon width into consideration. To precisely measure the width of ribbons, AFM images are completed as follows.

Fig. 3.8 (a) and Fig. 3.9 (a) display the corresponding AFM topographic and phase images of this sample which was collected at the exact same area as Raman map shown in Fig. 3.7 (a). A giant step height more than 10 nm and large terrace width about 10 µm are measured from the profile of blue line in topographic image and shown in Fig. 3.8 (b). This high step is the results of the large step-bunching process [121]. It is worth emphasizing that the macro-steps in our sample are the result of growth process without a hydrogen-etching pretreatment. Here, we take advantage of this observation to question the role of hydrogen etching used in other works. A few research have

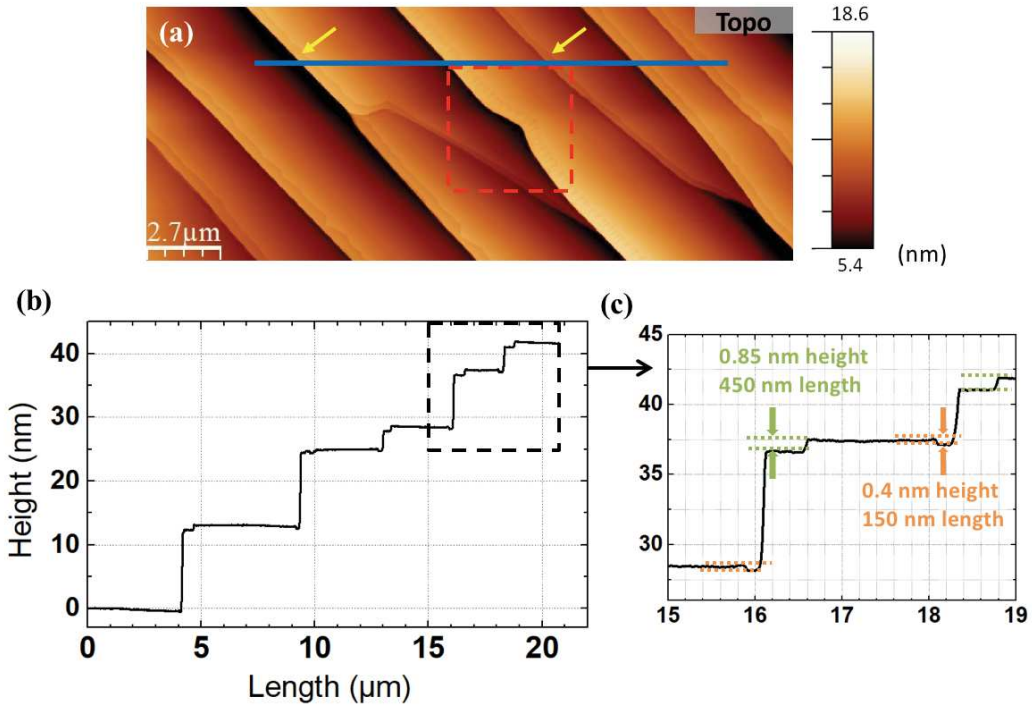

Fig. 3.8 AFM analyses of sample 1700°C, 300 s. (a) Topographic AFM image of the same area as the Raman map in Fig. 3.7 (a). (b) A profile extracted from blue line in (a). (c) A zoomed profile of dashed squared in (b). The depressions underlined by dashed horizontal green and orange lines are observed on upper and lower sides of steps.

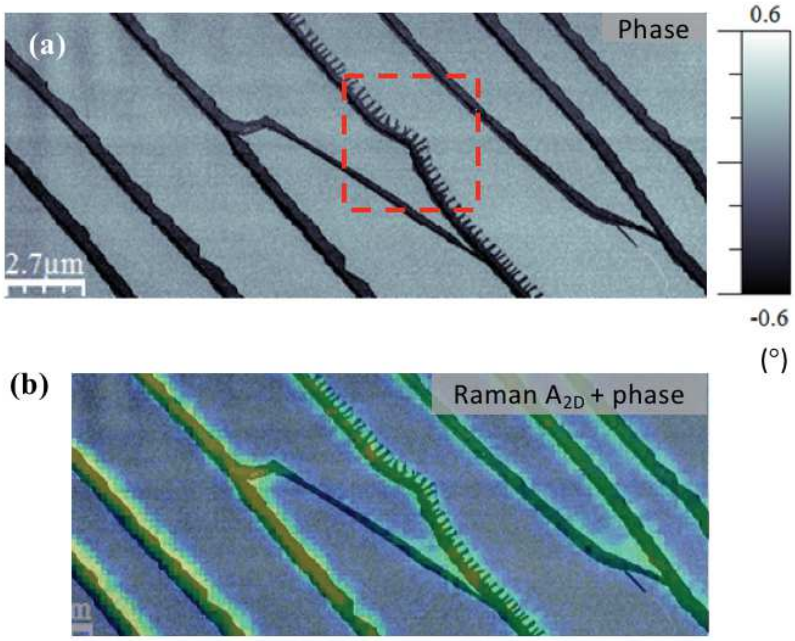

Fig. 3.9 AFM analyses of sample 1700°C, 300 s. (a) AFM phase image of the same area as the Raman map in Fig. 3.7 (a), evidenced by (b), a superposed AFM phase image to Raman A_{2D} map.

stressed the importance of the hydrogen etching process to obtain these macro steps [120,122,170] and uniform step distribution [171]. They argued that the graphitization process in Ar environment could only result in the steps with a height of 1-2 nm [8]. Based on our results, we suggest that the step-bunching process could also present under Ar condition without H_2. It would be probably not necessary to perform the cumbersome hydrogen etching process before the graphitization to obtain such morphology. The growth parameter and the substrate effect on the surface morphology will be discussed in **section 3.5**. Here, it is important to highlight the smooth step-terrace structure shown on this sample surface in which the pits and ridges are rarely seen.

The sub-nanometer depth depression stripes are observed along each step edge on their upper and the lower sides (e.g. yellow arrows in Fig. 3.8 (a)). Evidenced by the profile in Fig. 3.8 (b)) and a zoomed profile of the area outlined by the dashed black line (Fig 3.8 (c)), we found a broader depression with a width of 450 nm present on the upper side of step (e.g. green horizontal dashed lines in zoom image) while a narrower one about 150 nm (e.g. orange horizontal dashed lines) is observed on the lower sides. Furthermore, the same level of dark blue contrast shown in phase image on both sides of step edges (Fig. 3.9 (a)) while a different gray-blue contrast with a relatively higher phase value shown on the terraces. Since the AFM phase contrast could differ the material with different dissipation, we assume that all the dark blue ribbons (depressions in topographic image) consist of the same material which is different with the one on the terrace. Moreover, we can overlay the dark blue ribbons in phase image to the yellow/green ribbons observed in Raman A_{2D} map thanks to the same location of these

three images, as demonstrated in Fig. 3.9 (b). In Raman analysis, we have identified the ribbons as graphene and the off-ribbons zones as BL. Thus, we believe that the graphene ribbons and BL caused the dark blue and gray-blue phase contrast, respectively. Moreover, since the sublimation growth of graphene is an erosion process, additional Si atoms evaporate for the second carbon layer growth. Therefore, it is reasonable that the relatively lower surface height (depressions) shown in graphene areas compared to that of BL areas in AFM topographic image (Fig. 3.8 (a)). Thus, all the evidence agrees with each other, driving to a conclusion that the graphene ribbons start to form at each step edges in two directions. This suggests a step-flow growth mechanism. As we discussed in **chapter 1**, this step-flow growth usually happens for the graphene growth on SiC (0001) under Ar pressure since the Ar environment helps to reduce the Si atom sublimation rate. Under this condition, the Si atoms detach firstly from the vicinity of step edges because the Si-C bonding is more active at steps with respect to the terraces. In the meantime, the increased annealing temperature could enhance the C atom diffusion rate. It has been argued that the step-flow growth usually produces a high-quality graphene layer [8,169] because the growth condition is in an thermodynamic equilibrium. The poor surface morphology of the graphene grown under UHV is due to the non-equilibrium growth condition. Hence, we highlight this step-flow growth mechanism happened in our growth condition of low Ar pressure.

Until now, we have already identified the graphene ribbons at step edges and bare BL areas on the terrace by the combined Raman and AFM analysis. As we mentioned in Raman analysis, the graphene ribbon has been estimated as 1LG by calculating the $A_{G\text{-graphene}}/A_{G\text{-HOPG}}$ ratio. However, another technique is required to support our Raman results due to the limit width of these ribbon features. In the current case, AFM topographic image can be helpful with the analysis of the different surface height between graphene and BL as shown in the follows.

Firstly, we focus on the lower side of the steps where the measured the depressions height in the topographic image is 0.4 ± 0.05 nm between the eroded zone and the terrace (Fig. 3.8 (c)). As mentioned in **chapter 1** and in the schematic illustration of Fig. 3.10 (a), from a stoichiometric point of view, it causes a depression of ~ 0.42 nm (3 × 0.25 – 0.33 nm) in height to grow monolayer graphene in the case of sublimation [152–154]. More precisely, the 0.25 nm is the thickness of one Si-C bilayer in SiC substrate and 0.33 nm represent the thickness of single graphene layer [109]. Considering three Si-C bilayers are required to grow one single layer graphene in sublimation growth, the calculated 0.42 nm corresponds to the surface height change in the 1LG growth case. Here, we consider the BL surface as initial zero height surface. In other words, the 1LG surface would be 0.42 nm lower than the BL surface which is in a great agreement with our observation in AFM image thus support our Raman analysis about the number of graphene layers.

Likewise, we do the same measurement for the upper side steps (Fig. 3.8 (c)). The measured higher depression of 0.85 ± 0.05 nm could be attributed to:

i) the formation of 1LG with two additional SiC bilayers (0.42 + 2 × 0.25 nm) sublimation, as depicted in Fig. 3.9 (b). In this case, the released carbon atoms in two SiC bilayers are not enough to form the second layer of graphene. or;

ii) the formation of bilayer graphene (0.42 nm × 2) as illustrated in Fig 3.10 (c).

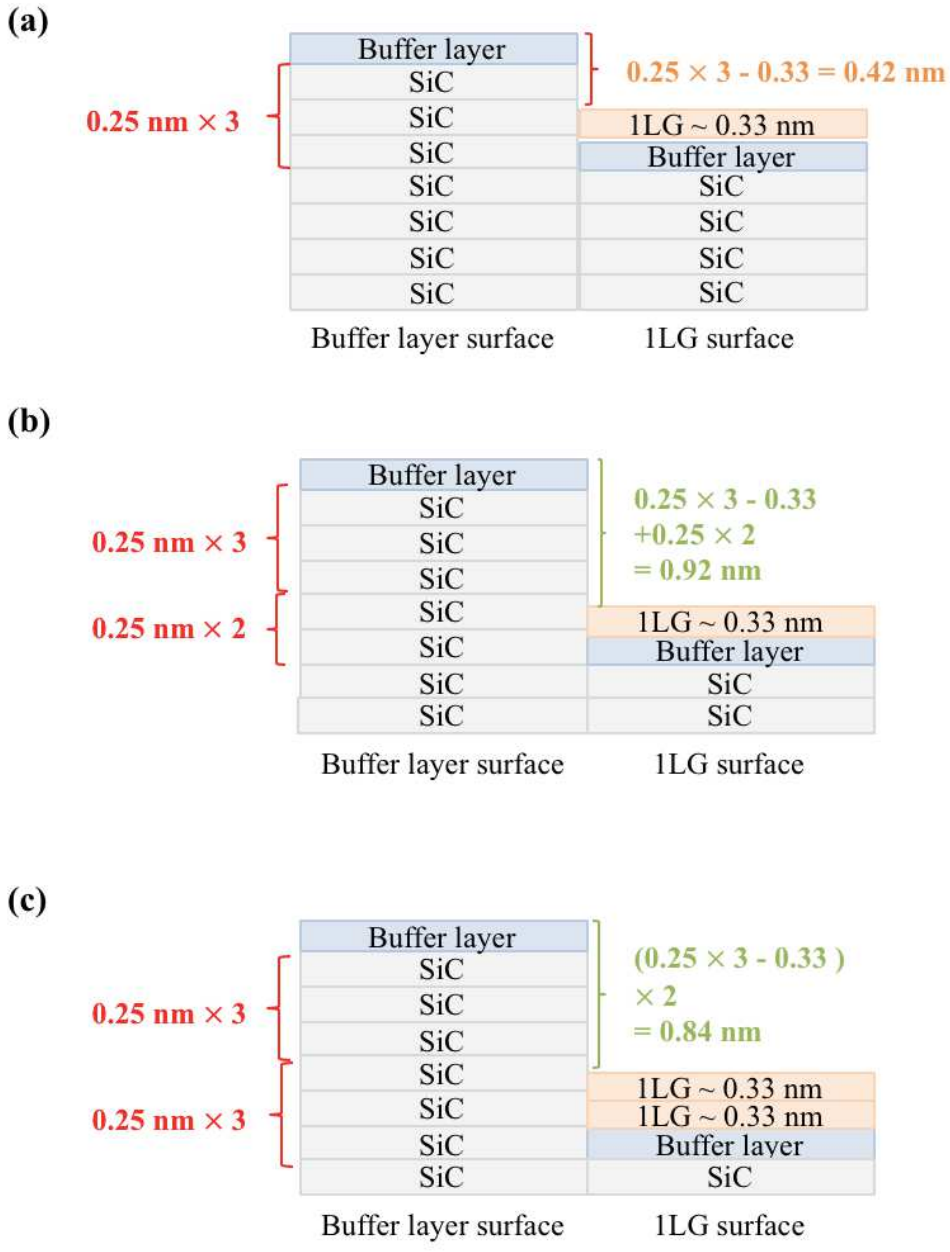

Fig. 3.10 Schematic illustrations of the formation of the depression at step edges. (a) Demonstration of the measured 0.4 nm depression on lower side of step edges. After BL growth, further 1LG formation requires three Si-C bilayer erosion and then 1LG deposited on the surface. (b) First possibility of the measured 0.85 nm depression on upper side of step edges. After 1LG formation, two additional Si-C bilayers were eroded. (c) Second possibility of the measured 0.85 nm depression on upper side of step edges. Two layers graphene were formed.

At this stage, the phase contrast and Raman analysis could be useful to rule out one possibility. First, the phase contrast of the ribbons in our measurement shows no obvious difference on both sides of the steps which is in the error bar of noise (0.1°). Kazakova *et al.* describe a phase contrast higher than 1° between the bilayer and monolayer graphene [172]. Second, as mentioned in Raman analysis, the ratio of $A_{G\text{-graphene}}/A_{G\text{-HOPG}}$ is about 0.03 which is close to the reported value for 1LG. The total width of graphene ribbons (> 600 nm) is comparable to the laser spot full width at $1/e^2$ and its width on the upper side of the steps represents 2/3 of the total width. These two pieces of evidence strongly suggest that the formation of bilayer graphene is unlikely. Therefore, it is largely plausible that 1LG ribbons are grown at each step edges. In addition, we would like to highlight that the first graphene layer growth starts on both upper and lower side of the step edges. This indicates a two direction of growth but with different growth rate, i.e. 450 nm width on upper side and 150 nm on lower side. This is consistent with the results of Robinson *et al.* [171] but different with that of Emtsev *et al* [8] and Ohta *et al.* [31] in which they only observed the growth on one side of the step edges. Considering the two latter studies used an Ar pressure closed to the atmospheric one and the former used the UHV growth condition, the pressure could be one possibility to understand the different growth method. One supposition is that, at relatively lower pressure, the Si sublimation rate could be enhanced and more free carbon atoms could migrate towards both sides of steps. However, the reason for different growth rate at two sides is still uncertain for now but we assume that the SiC substrate plays a role in this growth method.

Besides these regular ribbon features with the straight-line borders, irregular finger-like shape ribbons are occasionally observed. The finger-like shape features (highlighted in dashed red square in Fig. 3.8 (a) and Fig. 3.9 (a)) are zoomed in Fig. 3.11 (a) and (b). We denote three areas as zone I, II, and III. Considering the earlier Raman and AFM discussion, the zone I with the relatively lowest phase value (navy-blue) is attributed to graphene and zone II and III with a relatively higher phase value (blue) to BL. Then we acquired the height profile of this structure along the blue line in Fig. 3.11 (a) and shown in Fig. 3.11 (c) and (d). The different zones are highlighted by different colored background with the indicated corresponding number I, II, III in Fig. 3.11 (c) and (d). The graphene area (zone I) is 0.8 nm lower than the terrace (zone III). Region between fingers, zone II, is 0.25 nm lower than the terrace (zone III), corresponding to a single SiC bilayer height. A diffusion front clearly marks the limit between zone III and II as demonstrated in the inset image in Fig. 3.11 (a) and (b), showing the step erosion edge which is perpendicular to the finger-like structure growth direction. In addition, it is worth to notice that this finger-like shape is only situated at the upper side of the step edges but not at lower sides. The presence of these two different types of the eroded structure, i.e. straight or finger-like growth front, reflects the different growth energy and rate at each step. These finger-like shapes were seldom observed during the first graphene layer formation in the literature [53,55,174]. Borovikov *et al.* [55] have explained the finger-like step edges by a competition between capillary smoothing and a curvature-drive mechanism for step edge roughening. They have calculated the step

edges stability regions taking the factors of temperature and pressure into account. They argued that the instability window is largest for the growth under vacuum based on the calculation results which could be one possibility of their presence in our samples. Ohta *et al.* [173] have explained that these finger-like features could be related to the single bilayer or two Si-C bilayer step height in which the number of emitted carbon atoms is not equal to the number of carbon atoms required to form monolayer graphene.

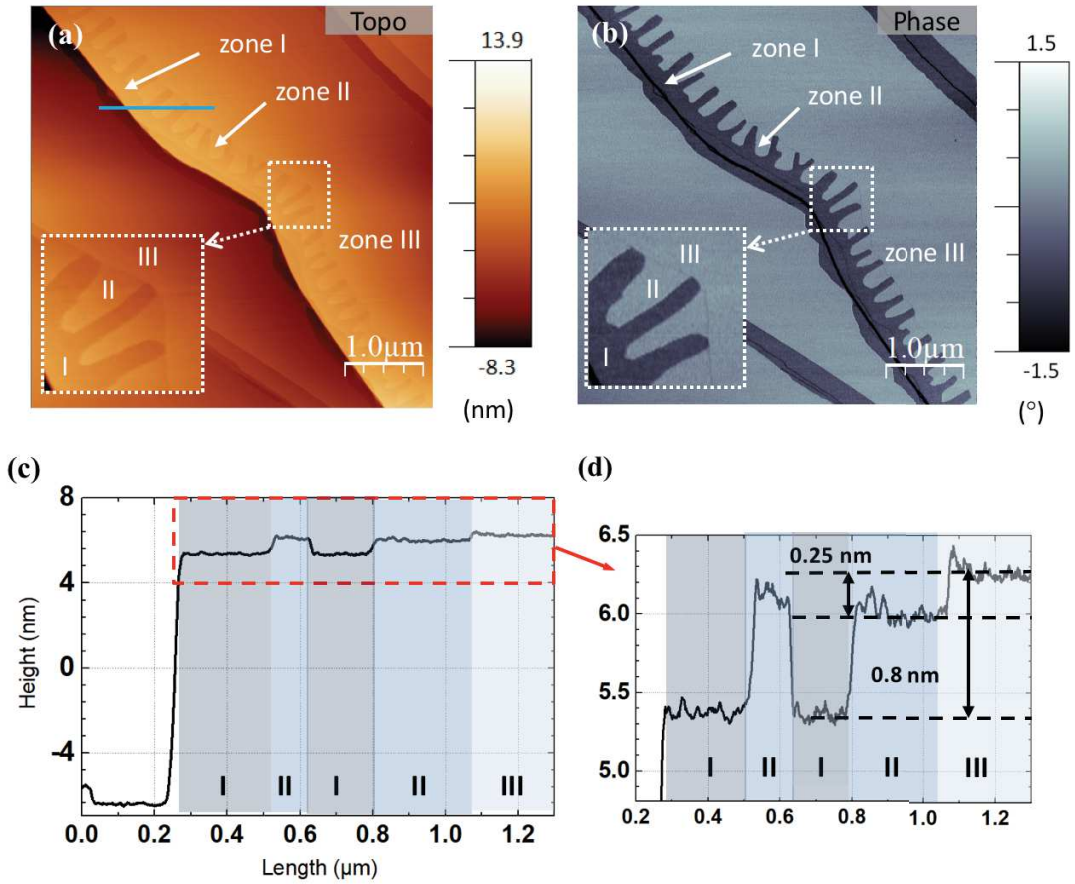

Fig. 3.11 (a and b) Topographic and phase AFM images of finger-like shapes in sample graphene ribbons. (c) height profile corresponding to the blue line in (a). Zone I refer to finger shape areas, zone II refers to regions between fingers and zone III corresponds to the terraces. (d) A zoomed profile acquired from red dashed rectangular region in (c), corresponding the fingerlike structure area on upper side of step.

Finger-like shapes were observed in other samples. Raman signatures of this type of sample always show a relatively lower G-peak intensity and a large portion of BL contribution, indicating a surface partially covered by graphene layer. Regarding the AFM topographic and phase images, one example is illustrated in Fig. 3.12 (a) and (b), respectively. The gray blue region in phase contrast corresponds to the relatively higher surface height in topographic images. Thus, we attribute gray-blue and dark blue areas in phase image to BL and graphene, respectively. In fact, this sample can strengthen several early observations of finger-like features:

i) We confirm that the finger-like growth mainly happens at the one side of the step edges. The growth front generally remains straight at the lower sides while few finger-likes shapes were observed at the upper side of step edges. Most of the finger growth front is perpendicular to their initial step edges.

ii) In the zoom images (Fig. 3.12 (c) and (d)) of white square in Fig. 3.12 (a) and (b), the region between the fingers (denoted as zone II) which has similar phase value to

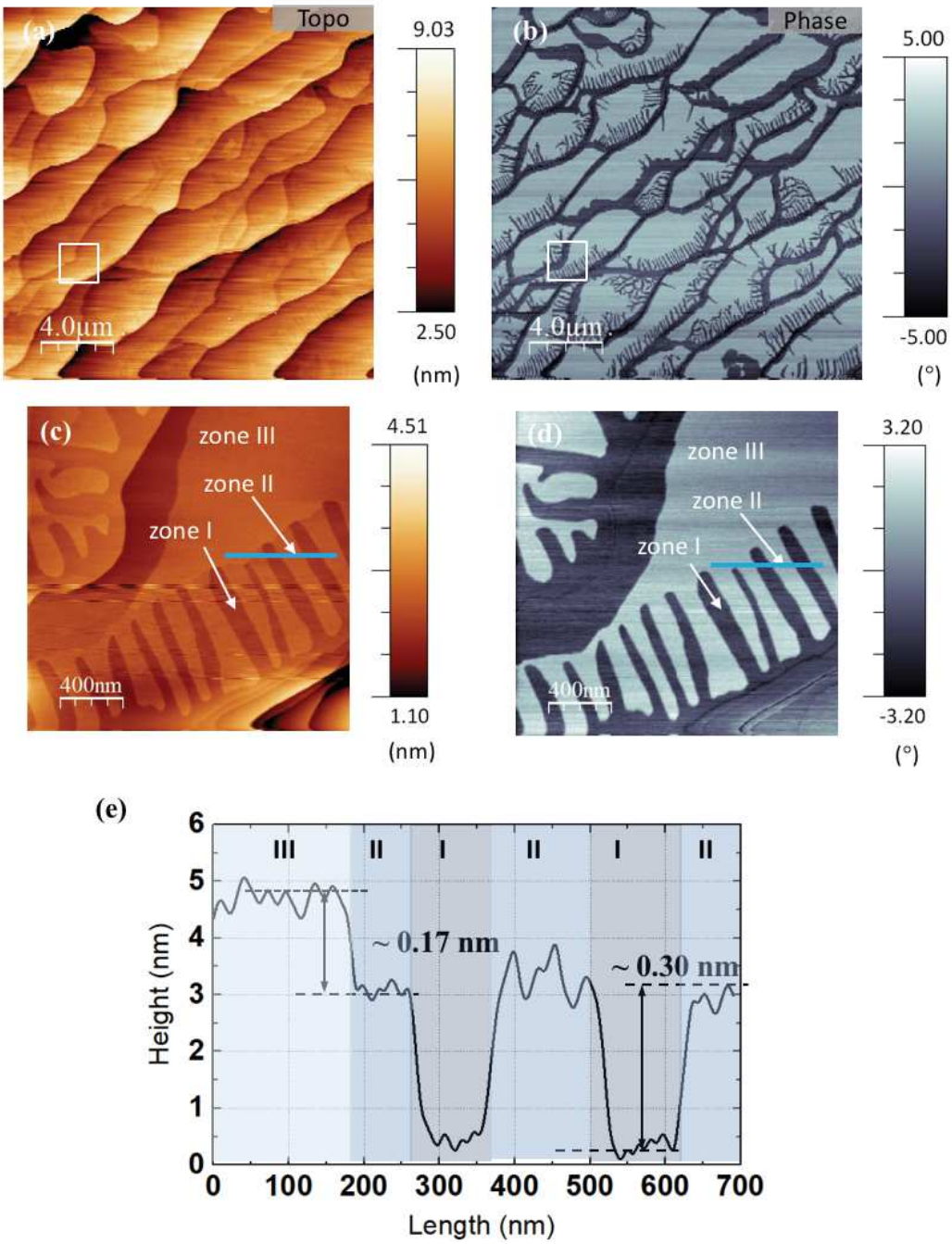

Fig. 3.12 (a and b) Topographic and phase AFM images of the finger-like shapes. (c and d) A zoomed image of white square in (a and b). Zone I refer to finger shape areas, zone II refers to regions between fingers and zone III corresponds to the terraces. (e) Profile of blue line in (c).

that of terraces (zone III) are identified as BL. A surface height of these regions between the fingers is lower than that of terrace surface of about 0.17 nm, as demonstrated in the zoomed image in Fig. 3.12 (c) and the profile along the blue line shown in Fig. 3.12 (e). The retracting front of zone II is obviously shown in the topographic image, which is parallel to the step edges and perpendicular to the growth front of graphene in finger-like shapes. The relative lower surface height compared to the terraces indicates an additional SiC bilayer sublimation compared to the terrace. On the other hand, the finger shapes (zone I) possess a surface height ~ 0.30 nm lower than the zone II areas and thus ~ 0.47 nm (0.3 nm + 0.17 nm) lower than zone III. This value could be related to the single layer graphene growth, consistent with the observations in the previous sample.

However, the finger-like features are more intensely present in this sample which could be related to wafer effect or different growth condition. From growth mechanism point of view, the growth condition and substrate structure [55,57,174] both play the vital role in the growth kinetics. Kageshima *et al.* [56] have stated based on their calculation of step stability that the finger-like shapes are generally seen under low temperature growth condition while the smooth surface can be optimized by using a higher temperature or a higher Si pressure. Ohta *et al.* [174] have stressed the effect of BL morphology on the growth mechanism. They have argued that the growth of high-quality large-area graphene most likely arises from etching pre-existing triple bilayer SiC graphene. Because the C atoms emitted by SiC sublimation is quantitatively equal to the required number in graphene growth. The single or double Si-C bilayer leads to an unstable step edges, e.g. creation of finger-like features. While, the opposed conclusion has been raised by Hupalo *et al.* [154]. They claimed a single Si-C bilayer steps have the advantage for the finer control of the Si evaporation rate as well as the graphene nucleation and the growth. In any case, the growth condition of these samples is not in thermodynamic stabilization, leading to the inadequate carbon supply. We remark that the graphene ribbons with straight or finger-like step edges are reproducible in the specific growth condition (e.g. 1700°C, 300 s). To optimize the homogeneous graphene coverage, higher temperature or longer annealing time is needed.

Then, we have extended the growth time and remain the temperature at 1700°C aiming to continuously grow graphene layer fully covered the entire terraces at this temperature. Fig. 3.13 (a) is a Raman $A_{G\text{-graphene}}/A_{G\text{-HOPG}}$ ratio map collected from the sample annealed at 1700°C for 1200 s. The continued presence of 2D-peak in all the spectra in Raman map suggests that the surface is fully covered by graphene. As expected, a longer growth time compared to that of graphene ribbons growth condition (300 s) indeed gives rise to the continued graphene layer formation. From the Raman $A_{G\text{-graphene}}/A_{G\text{-HOPG}}$ ratio map, we can identify three types of contrast: navy-blue, green and yellow contrast. The average spectra of these three types of area are shown in Fig. 3.13 (b). More precisely, the $A_{G\text{-graphene}}/A_{G\text{-HOPG}}$ ratio calculated from navy-blue zones (e.g. in blue dashed circles) exhibit a value close to 0.06 (~2LG) and the yellow zones (e.g. in yellow dashed circles) show a ratio higher than 0.109 (~4LG). The green zones possess a ratio value is ranged between 0.085-0.107, implying the existence of

3LG/4LG mixture. Here, we would like to underline the almost superposed 2D-peak of these three average spectra which signify that the FWHM (61, 68 and 69 cm^{-1} respectively) of 2D-peak might not be a reliable indicator to analyze the number of graphene layers.

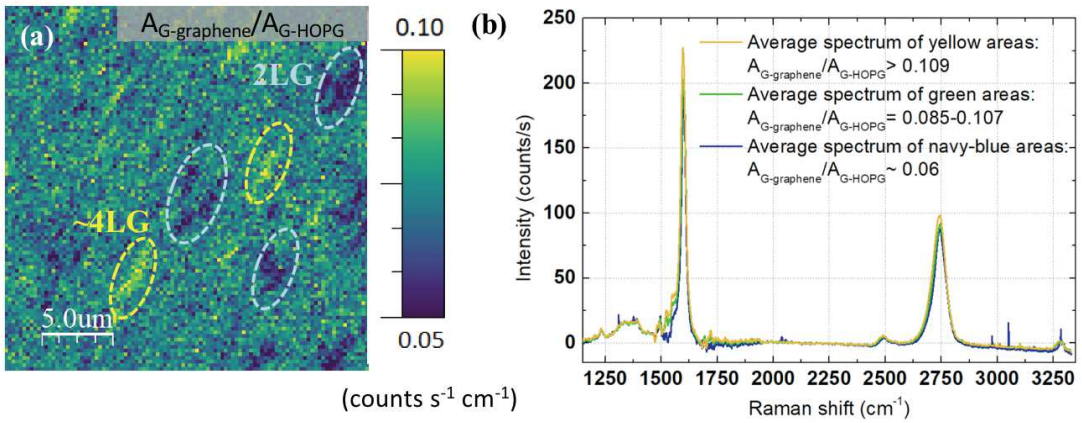

Fig. 3.13 Raman analyses of sample 1700°C, 1200 s. (a) Raman map of $A_{G\text{-}graphene}/A_{G\text{-}HOPG}$ ratio. The yellow and navy-blue dashed circles indicate the areas with $A_{G\text{-}graphene}/A_{G\text{-}HOPG}$ value about 0.109 (4LG) and 0.06 (2LG), respectively. (b) Average spectra and the corresponding $A_{G\text{-}graphene}/A_{G\text{-}HOPG}$ ratio of yellow, green and navy-blue zones in map (a) are shown in yellow, green and blue spectra, respectively.

The corresponding AFM phase image (Fig. 3.14 (b)) shows gray-blue, blue and dark blue contrast which can be perfectly superposed by the navy-blue, green and yellow zones in Raman $A_{G\text{-}graphene}/A_{G\text{-}HOPG}$ ratio map respectively. The corresponded zones are indicated by the same color dashed circle as in Raman map (Fig. 3.13 (a)) and AFM images (Fig. 3.14 (a) and (b)). At first glance, the blue contrast majority covered the surface seems homogeneous. However, if we zoom one area including gray-blue and blue contrast (e.g. green square in Fig. 3.14 (a) and (b)), we identify three types of contrast instead of two. On the gray-blue zone, without surprise, only one contrast present, superposing by the navy-blue zone in Raman (~2LG). On the other hand, the majority blue contrast, superposing by green area in Raman map, possess plenty of stripe-shape of dark blue patterns. We recall that we have determined a thickness more than 3LG of the green zone in Raman $A_{G\text{-}graphene}/A_{G\text{-}HOPG}$ ratio map. Thus, we attribute the blue contrast and the dark blue stripes shape to the 3LG and 4LG respectively. Because of the Raman measurement resolution limited by laser spot, these stripes could not be distinguished in Raman map. Regarding the AFM topographic image, the thicker graphene possesses a relatively lower phase contrast value who corresponds to the highest Raman $A_{G\text{-}graphene}/A_{G\text{-}HOPG}$ ratio. Hence, we found our Raman and AFM analyses are in a great agreement and support each other as a reliable technique to identify the material and determine the number of graphene layers.

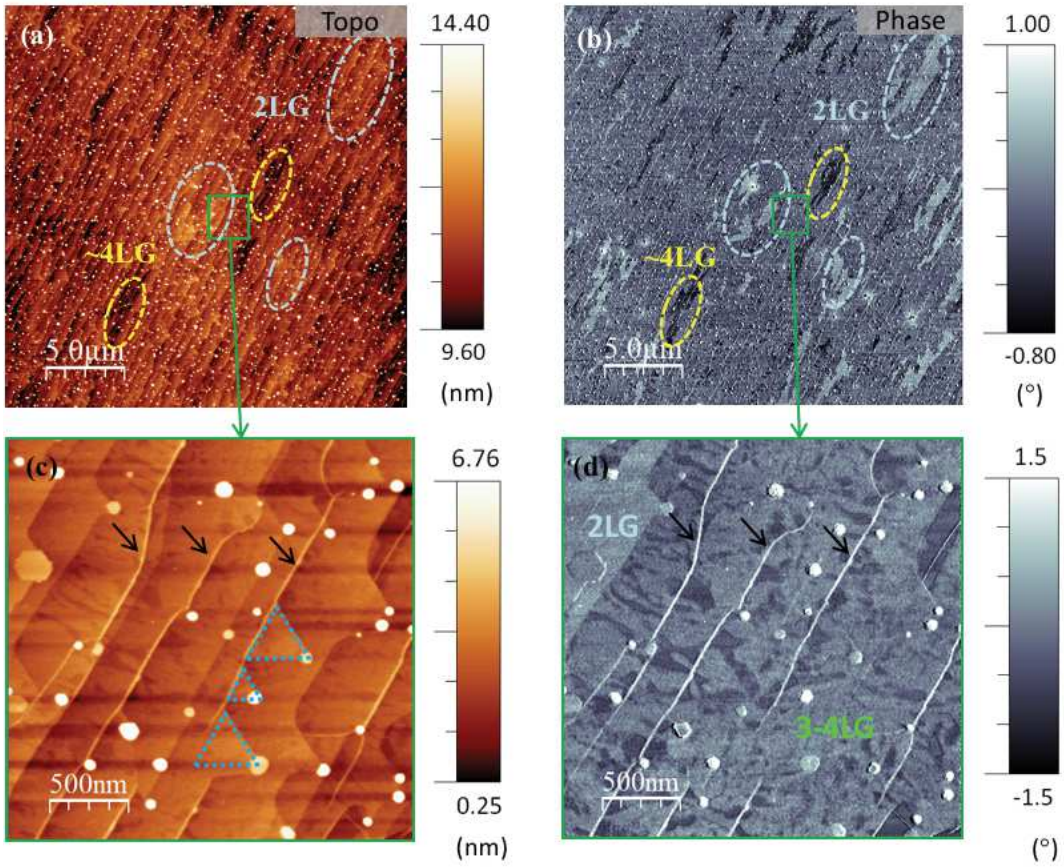

Fig. 3.14 AFM analyses of sample 1700°C, 1200 s. (a and b) Topographic and phase AFM images recorded at same location as Raman map in Fig. 3.13 (a). The light blue and dark blue contrast in phase outlined by orange and purple dashed circles, corresponding to navy-blue (~2LG) and yellow (~4LG) areas respectively; (c and d) High resolution AFM images of one area highlighted in green square in (a and b). The red arrows indicate the cracks and the blue dashed triangles highlight the pits with triangle shapes.

As demonstrated in AFM topographic images (Fig. 3.14 (a) and (c)), the terrace width is measured about 0.5 μm. Besides, the nanoscale ridges are obviously seen on the terrace (black arrows in Fig. 3.14 (c) and (d)). The ridges and cracks are commonly known as a result of bending and buckling to relieve the compressive strain when the multilayer graphene grown on SiC [175]. In addition, the white nanoparticles again are clearly visible on the surface of this sample. With the help of the AFM surface analysis, we roughly measured radius ranged from 20 nm to about 60 nm. The height of these nanoparticles is between 1 nm and 8 nm. In addition, the high resolute AFM images in Fig. 3.14 (c and d) allow us to identify the nanoparticles shapes as circle or hexagonal which are often located at step edges where there exist the dangling bonds. Interestingly, several nanoparticles are situated at one angle of the triangle shaped step front as highlighted by the blue dashed triangles in Fig. 3.14 (c). These step front could be related to the SiC substrate who possesses this shape of stacking faults [176]. During the thermal treatment of SiC, these defect locations might expose several dangling bonds where the adsorption and desorption could be more active. Hence, the behavior

of these nanoparticles situated at step edges is likely related to the growth process, e.g. excess C atoms or Si atoms. Both the too high temperature or the too long growth time could lead to a non-equilibrium growth process in which the excess carbon atoms could plausibly present. Due to the limited diffuse length, these carbon atoms could not travel for a long distance, therefore they aggregate into cluster. In this case, the size and density of these carbon or Si clusters are largely dependent on the growth parameters and substrates. On the other hand, if we consider the nanoparticles present in multilayer graphene sample synthesized at 1600°C (**section 3.2**), we found there is no clear preference of location of those nanoparticles in that case which could differ themselves with these ones shown in this sample. However, we still could not rule out the post-growth adsorption effect on the current sample. In addition, the nanoparticle is occasionally seen on the sample produced by the other growth conditions which usually concern a too long growth time or too high temperature growth condition. Besides, after we change the SiC wafer, these features are more commonly seen. As we discussed in **section 3.2**, we could basically rule out the possibility of furnace contamination. However, the growth process effect or post-growth effect on their existence is still under investigation. To identify its chemical composition, we have performed SEM (scanning electronic microscopy) but this measurement could not provide useful information. Likewise, our nanoparticles are limited in size for the energy-dispersive X-ray spectroscopy measurement. In this case, the identification of these nanoparticles remains a future work. For now, regardless of its chemical composition, our objective in this thesis is to suppress its formation by tuning the growth parameters.

If we take a look at the multilayer samples discussed in **section 3.2 and 3.3** in which we used a temperature of 1600°C and 1700°C and a long growth time (2400 s and 1200 s respectively), we found that their growth method does not respect the layer-by-layer growth mechanism. For example, 4LG flakes are started to form on the terrace when there is still 2LG remain. Nevertheless, comparing these two samples, the step width in sample 1700°C appears to be wider than that of the sample produced at 1600°C, i.e. more than ~500 nm vs. ~ 400 nm. Moreover, one 2LG flake of sample 1700°C is able to cover more than three neighboring steps as indicated in blue circles in Fig. 3.14 (a) and (b). This phenomenon is consistent with the results in the reference [118,119] which could be understood by the enhanced perpendicular growth rate. As the carbon atoms could move a longer distance along the steps or perpendicular to the steps, the coalescence of graphene stripes leads to the larger graphene islands [118]. On the other hand, the domains in sample 1600°C seem to be limited at one terrace, inducing the smaller domain size and higher density of islands. Nevertheless, the inhomogeneous distribution of graphene might signify that the Si desorption and C diffusion rate are limited in both of these two samples by surface energy. Therefore, two likely solutions could be proposed here: to increase the annealing temperature in order to accelerate the diffusion rate, or to increase the Ar pressure as to suppress the Si evaporation and C release rate. In contrast with the results of Bolen *et al.* [53], we found that a higher growth temperature seems to be the key point to improve thickness distribution and the surface morphology [118,119,171]. To this end, we then altered the temperature to

1750°C while remaining the pressure at 10 mbar and the annealing time of 300 s. We will show with a detailed analysis in **section 3.4**, that an optimized monolayer graphene growth process was achieved. We would like to highlight firstly that by only altering the temperature, we have successfully controlled the initial stages of 1LG formation: from BL-like layer via graphene ribbons to 1LG.

3.4 Structural and electrical properties of monolayer graphene

Previously, we started from a BL-like sample production obtained by annealing the SiC substrate at 1600°C for 300 s. Then we investigated the growth time and temperature effects in which we are able to obtain the graphene ribbons started to grow at step edges and the multilayer graphene as well. Naturally, we expect that the 1LG could homogeneously cover the sample surface if we properly tune these two parameters. To this purpose, in this section, we show the growth results of samples synthesized at 1750°C for a same growth time of 300 s. We fixed pressure and the temperature ramp at 10 mbar and 0.33°C/s, respectively. With this growth condition, we have successfully optimized the reproducible 1LG growth process, confirmed by repeating more than 50 samples with comparable results. The characteristic measurements were performed on each sample following the protocol presented in **section 2.5**. Next, we will show the representative results to demonstrate the general properties of our monolayer samples.

3.4.1 Structural characteristics of monolayer graphene

The Raman A_{2D} map (999 spectra) of the sample annealed at 1750°C for 300 s shows a quite uniform surface (Fig. 3.15 (a)), indicating continuous graphene layer fully covered the surface. The average spectrum of this map (Fig. 3.15 (b)) shows the shape G-peak and 2D-peak situated at 1607 cm^{-1} and 2735 cm^{-1}, respectively. Moreover, the BL contribution has been recognized in the region between 1200 and 1800 cm^{-1}. Besides, the D-peak is rarely present, showing a well-crystallized carbon structure. The $A_{G\text{-graphene}}/A_{G\text{-HOPG}}$ ratio has been calculated for whole map (Fig. 3.15 (c)) and the distribution can be perfectly fitted by one Gaussian function centered at 0.033 as shown in Fig. 3.15 (d). The highest value (133 counts) of this distribution means the $A_{G\text{-graphene}}/A_{\text{-HOPG}}$ ratio in these 133 spectra is 0.033, which is close to the experimental value reported in monolayer graphene [88]. In addition, the majority of the spectra (94.5%) fall into the value region between 0.026 and 0.041 which indicate the number of layers is ~1LG in most of the spectra. The ratio value barely drops into the region lower than 0.026 or higher than 0.041, signifying the homogeneous 1LG surface. Therefore, the sample synthesized at 1750°C is plausibly covered by 1LG and a BL underneath according to the Raman analysis.

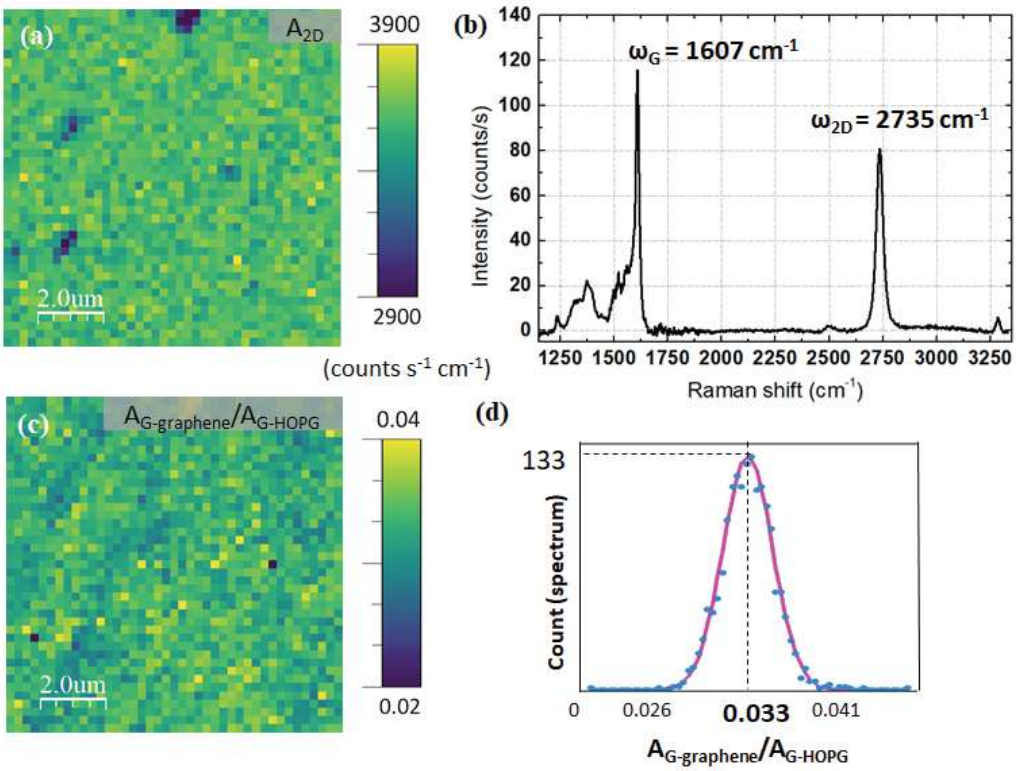

Fig. 3.15 Raman analyses of sample 1750°C, 300 s. (a) Raman map of integrated intensity of the 2D-peak from 2650 to 2800 cm^{-1}, A_{2D} map. (b) Average Raman spectra of the map in (a). (c) Raman map of the $A_{G\text{-graphene}}/A_{G\text{-HOPG}}$ ratio. (d) Gaussian fit of the $A_{G\text{-graphene}}/A_{G\text{-HOPG}}$ ratio distribution, centered at 0.033.

The AFM topographic and phase images are recorded as illustrated in Fig. 3.16 (a) and (b), respectively. Fig. 3.16 (c) shows a profile acquired from the blue line in topographic image and the step height and terrace widths were measured around 0.5-3 nm and 0.3-2 μm, respectively. We remark that these values of step and terraces are the typical values for graphene growth under Ar pressure [8,117]. A smooth surface without pits and ridges with regular straight step-edges shape was obtained by our non-classical growth condition, similar to that of the samples grown under 1 atm Ar pressure. Unlike the understanding of other works of low Ar pressure growth [127,128], we show that a smooth graphene surface can be achieved in this condition. Furthermore, no obvious phase contrast was visible suggesting a homogeneous film formation.

Fig. 3.17 shows the topographic scanning tunneling microscope (STM) images of the sample produced under this condition recorded at low temperature of 200 mK. A relatively low bias voltage of 30 mV is applied to obtain the high resolute STM images, as demonstrated in Fig. 3.17 (a). The low bias voltage was used to reduce the tunneling resistance, therefore the tip could be closed to the sample surface in order to precisely identify the surface with an atomic roughness during the scanning. Then, the (6 × 6) superlattice with a periodicity of ~ 1.9 nm is evidenced in a relatively large image collected at 100 mV and shown in Fig. 3.17 (b). One (6 × 6) cell is outlined by the white lines.

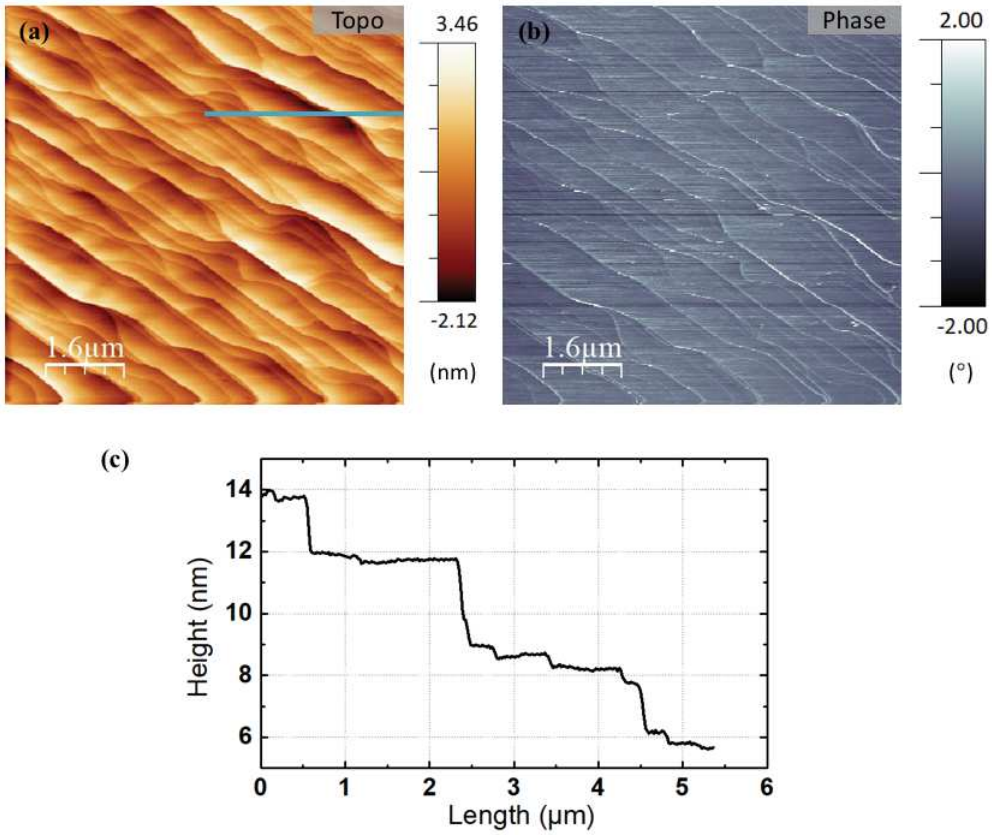

Fig. 3.16 AFM analyses of sample 1750°C, 300 s. (a) Topographic and (b) phase AFM images. (c) Height profile corresponding to the blue line in (a).

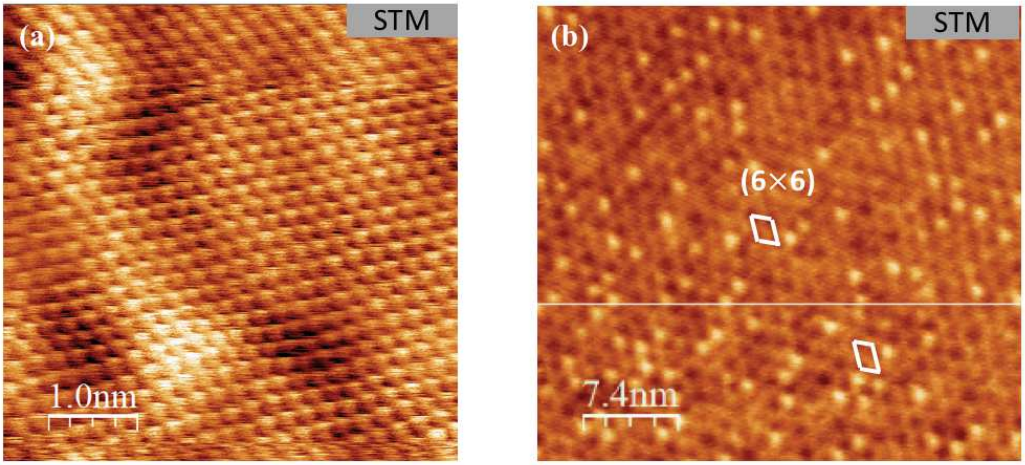

Fig. 3.17 STM images of sample 1750°C, 300 s recorded at bias voltage of (a) 30 mV and (b) 100 mV. The atomic resolution has been revealed in (a). The (6×6) superlattice was observed in (b). A unit cell is highlighted in white diamond shapes.

Furthermore, the spectroscopic local density of states (LDOS) maps was probed from the area shown in Fig. 3.18 (a) and analyzed by 2D Fourier transform (FT). The resulting pattern is shown in Fig. 3.18 (b) and compare to a schematic FT map in Fig. 3.18 (c) which indicates the reciprocal space of epitaxial monolayer graphene. The features present in FT-LDOS maps of our sample have clearly indicated the (6 × 6) superlattice by 6 spots (6 corners of red hexagonal shape) surrounding the center **Γ** point (central point) of the graphene [152]. Besides, the rings around the **K** and **K'** point (green circles) are the signature of the Dirac cones. Rutter *et al.* [108] have demonstrated that the observation of this the (6 × 6) superlattice can be used as a fingerprint to distinguish the single-layer graphene with few layer graphene [108] since this superlattice is caused by the SiC interfacial reconstruction (BL). The tunneling transparency of the first graphene layer allows the examination of the structural features of the BL underneath [82,109]. Thus, this supplementary measurement could further confirm the well-crystallized 1LG growth with the presence of BL underneath in the sample produced by using our optimized growth process, consistent with our Raman and AFM analysis.

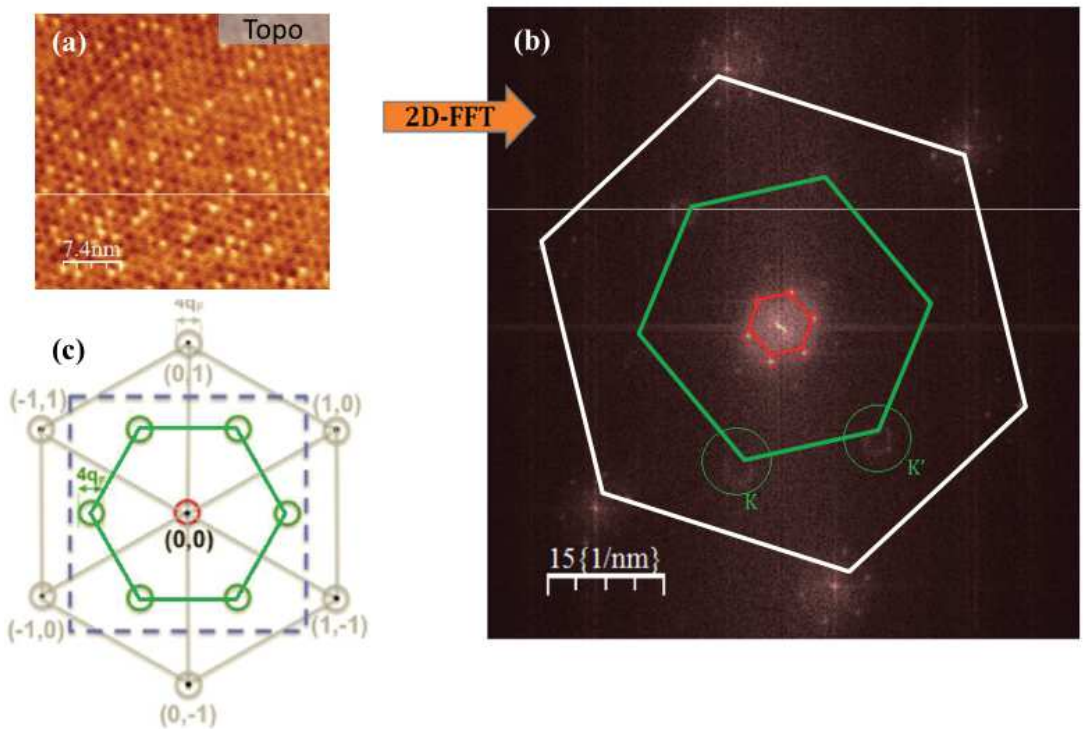

Fig. 3.18 (a) The probed area for the LDOS analysis. (b) FT-LDOS patterns of area in (a). The different order of (6×6) superlattice is identified by red circles in the center. (c) A schematic demonstration of the expected two-dimensional Fourier transform map of the LDOS.

Regarding the growth mechanism, the step-flow growth method is achievable under our non-classical growth condition, i.e. low Ar pressure of 10 mbar. Fig. 3.19 (a) and (b) show the AFM topographic and phase images, respectively, of one graphene sample. The number of graphene layers has been estimated by the Raman spectra collected from

this sample (not shown). $A_{G\text{-graphene}}/A_{G\text{-HOPG}}$ ratio indicates that the sample surface is mostly covered by 1LG while small portion of 2LG is also present. In the phase image of Fig. 3.19 (b), we generally observe two types of contrast, gray-blue and dark blue. We notice that some of the dark blue contrast is located at step edges where the surface height is relatively lower than terraces as indicated in corresponding topographic image in Fig. 3.19 (a). Based on our previous results, it suggests that the dark blue stripes located at the steps edges in phase image are corresponding to 2LG. Thus, the 2LG has started growing at step edges. This is a strong evidence of step-flow growth mode. In addition, we found that the dark blue areas situate on both upper and lower sides of the steps. This implies a two-direction growth method which is consistent with our earlier results in graphene ribbons sample (Fig. 3.8 and Fig. 3.9). However, we also observe several pits present on the terraces as demonstrated in Fig. 3.19. Indeed, these pits could be catalogued into four types: triangle shape, hexagonal shape, round shape and irregular stripe-shape pits, highlighted in blue, purple, red and green dashed circles. The triangle and round shape pits, with a depression height measured about 0.5 nm, show no phase contrast in phase image (indicated by blue and red dashed circles in Fig. 3.19 (b)) compared to terraces. It suggests no difference in number of layers compared to terraces. These triangle and round pits shapes are usually seen in epitaxial graphene due to the dislocations or defects of SiC bulk [53,121]. Besides, majority of these triangle pits show a clear crystallographic direction in the way that at least one edge parallel aligned with the step-edge orientation. This observation is in agreement with the description in [53] that the mechanism which drives pit erosion appears to be the same for terrace erosion. Moreover, comparing the topographic and phase images, we found that the hexagonal shape pits show a phase contrast compared to the terraces. On the other hand, the stripe-shape pit is the most common shape seen on the terrace. These stripe-shape pits are largely present on the terrace with various length and depressed height (from 0.1 nm to 1 nm). Some of these stripe-shape pits could cause a phase difference with the respect to the terrace and some of them not, indicating that these stripes could be either monolayer or bilayer graphene. And their depressed height

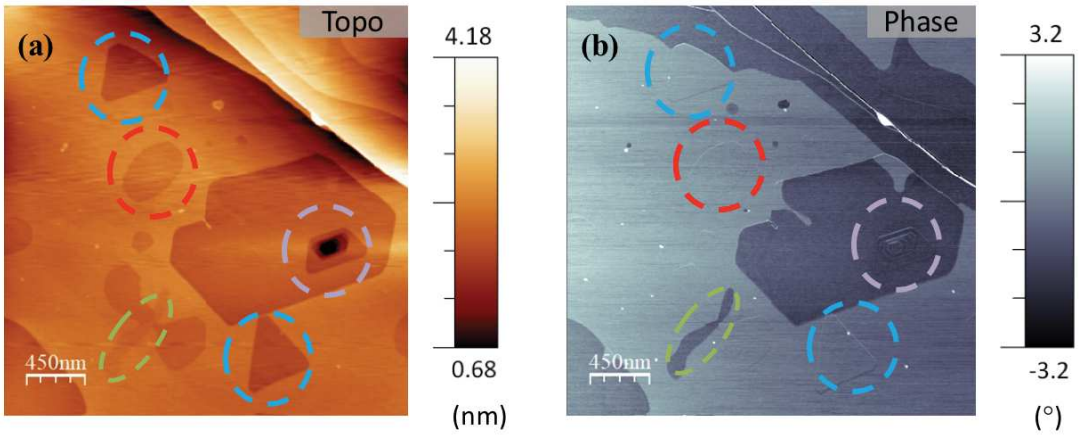

Fig. 3.19 (a and b) Topographic and phase AFM images of a majority 1LG sample. The dashed blue, purple, red and green circles outline the triangle, hexagonal, round and stripes shape pits on the terrace, respectively.

seems to be irrelevant with the graphene thickness. In addition, there is no particular crystallographic direction of these stripes at first glance, making the interpretation difficult.

Hence, in this section, we have probed the structural properties of our 1LG samples obtained in this thesis. Based on the obtained results, we have shown the step-flow growth of graphene has been achieved and the 1LG with stepped morphology has been obtained. These characteristics are comparable with the 1LG grown under 1 atm Ar pressure. Besides, a small portion of 2LG is present on our samples. However, we with a good control of the growth parameter, we improve the surface morphology of graphene layers. An investigation of the surface control was carried out in this work and will be discussed in **section 3.5**.

3.4.2 Transport properties of monolayer graphene

Hall effect measurements were performed on our 1LG samples in order to determine their electrical properties. The van der Pauw configuration was generally used and four silver paints were deposited at four corners of 6 mm × 6 mm samples as demonstrated in **chapter 2**. This allows protecting the original properties of our as-grown samples from the lithography influence [39]. The measurement can be performed at room temperature (RT) or at low temperature down to 1.7 K. In this section, we only show main results concerning the quantum Hall effect (QHE) as well as the mobilities and carrier densities detected in our 1LG samples. More discussion on the electrical properties of our films will be continued in chapter 5.

Fig. 3.20 demonstrates the results of the Hall effect measurement as a function of magnetic field at low temperature of 1.7 K in helium (He) cryostat. As shown in the curves, we observe the QHE in our samples: there are plateau in Hall resistance (Fig. 3.20 (a)) accompanied with the vanishing in magnetoresistances (Fig. 3.20 (b)) at high magnetic field. The basic concept of this phenomenon is detailed in **chapter 2**.

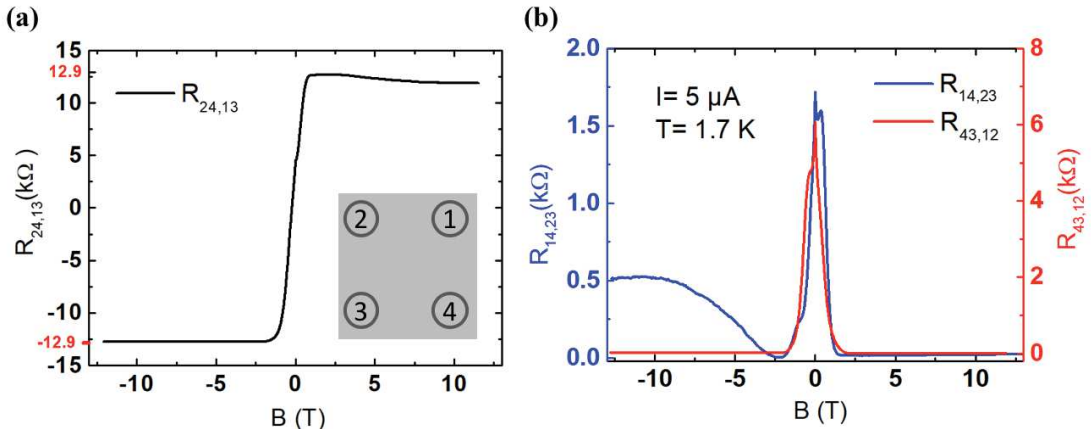

Fig. 3.20 Transport measurement of sample 1750°C, 300 s. (a) The transverse magnetoresistance $R_{24,13}$ show clear evidence of quantum Hall effect at T = 1.7 K, with a quantum plateau at $R_H \simeq 12{,}900\ \Omega$. An illustration of the sample with the labels of the contacts is shown in the inset of (a). (b) The two van der Pauw magnetoresistances $R_{14,23}$ (blue) and $R_{43,12}$ (red).

Here, we emphasize the plateau value observed in our measurement ~12 kΩ is close to the calculated value for the monolayer graphene corresponding to the filling factor $\nu = 2$ [22,106]. Thus, the presence of QHE in our sample produced by the optimized 1LG growth process is another strong evidence to validate this process.

In addition, due to the low carrier densities of the samples, QHE plateau can be observed already from about 2 T (see description in chapter 2). Furthermore, by the slope of the Hall resistance (based on the configuration of our setup), we have identified the p-type doping in the measured samples. The observation of the p-type doping is an unusual result considering the presence of the BL in epitaxial graphene [54,112]. We attribute the measured low p-type residual concentration to the atmospheric doping effect [177]. A detailed study of this specific doping characteristic will be presented in chapter 5.

The sequential measurements on several 1LG samples have been done under low magnetic field at 1.7 K confirm a low residual hole concentration of the order of few 10^{10} cm^{-2} up to few 10^{11} cm^{-2} depending on the experimental conditions. The results of three representative samples were detailed in table 3.1. For example, two successive cooldowns (at different rate) of sample S45 and S37 lead to different carrier concentrations, varying by one order of magnitude. This discrepancy in two measurements performed in the same sample could support the assumption of the atmospheric influence on our samples. We assume that the amount of the adsorbates varied between these two measurements when we exposed the samples again in the air. In addition, different cooling down process leads to the different kinetic of these contaminations on the graphene surface [178]. Furthermore, mobility at low temperature is strongly dependent on the residual concentration. Higher mobilites (more than 10,000 cm^2 V^{-1} s^{-1}) were achieved with a doping closed to the charge neutrality point ($p < 10^{11}$ cm^{-2}). For this moment, we assume the inhomogeneous doping is the main cause for the low doping level. In fact, the charged impurities on the sample surface or the structural corrugations indeed could shift locally the relative position of

Table. 3.1 Hall concentrations and mobilities at T = 1.7 K (He cryostat) and at 300 K (ambient) measured in studied 1LG samples. Two successive experiments were performed at 1.7 K on sample S37 and S45.

	Measurement in cryostat at 1.7 K		Measurement in ambient at RT	
	p_{Hall} (10^{11} cm^{-2})	**μ (cm^2 V^{-1} s^{-1})**	**p_{Hall} (10^{11} cm^{-2})**	**μ (cm^2 V^{-1} s^{-1})**
S45	1.87 0.9	3390 12497	12	1770
S37	0.16 1.62	27830 3651	16	1100
S50	3.77	2770	24	805

Dirac point with respect to the Fermi level and induce electron-hole puddles [179]. This phenomenon is reported in the literature and several models have been proposed to estimate the disorder level. In our group, a precise study of this doping characteristic by using an adapted model has been done and will be presented in **chapter 5** [180].

The Hall effect measurements at room temperature have been completed on these samples and the results are summarized in table 3.1. The measurements have confirmed a p-type doping about $p_{Hall} \sim 10^{12}$ cm^{-2} at room temperature. The carrier mobility ranges from 800 to 2000 cm^2 V^{-1} s^{-1}. As we discussed in **chapter 1**, the mobilities in epitaxial graphene are largely depressed by the presence of BL. The mobilities achieved in our samples are similar to the ones found in homogeneous graphene produced under 1 atm Ar pressure by sublimation [8,106]. This confirms that our non-classical growth process could also yield the graphene samples with a comparable quality with samples produced under 1atm Ar pressure, validating our synthesis method. More electrical properties of our monolayer samples will be revealed in **chapter 5**.

3.5 Temperature ramp effect: surface morphology control of graphene

Previously, we have observed the step-terrace structure in our 1LG films which are the typical results for the epitaxial graphene grown on SiC. The step height value higher than that of one single Si-C bilayer is the evidence of the presence of step-bunching process. Based on our results, we stress again that the step-bunching process could happen under a low Ar pressure and without a hydrogen etching treatment. However, as we can see, various degree of step-bunching has been identified by different step height (from ~ 1 nm to more than 10 nm) and step density. Based on our observations of these samples, the surface morphology is dependent on the growth temperature, growth time and the number of graphene layer as well. In fact, the graphene surface morphology has a great influence on the epitaxial graphene quality in terms of the electrical properties. For example, bilayer graphene at step edges could induce an anisotropic Quantum Hall effect in 1LG [181]. Besides, a degradation of conductance was found at the 1LG/2LG junctions [182]. Moreover, Eriksson *et al.* [124] have studied the terrace width effect on the doping characteristics. They show that when the terrace width increases from 300 nm to 1200 nm, the n-type carrier reduces by 8×10^{12} cm^{-2}. To this end, numbers of groups aim to design the surface structure by etching the substrate or tuning the graphene growth parameter [120,121]. Oliveria *et al.* [120] have pre-defined the stepped structure by hydrogen etching. They stated that if the steps were already achieved a stable status, the further graphitization process would barely change the surface, which means the step-bunching will not occur. In this case, they can pre-define the sample morphology by pre-treatment of substrate before graphene growth. On the other hand, Bao *et al.* [121] have observed the presence of small steps (1.5 nm height) after the hydrogen etching and argued that the high steps (more than 10 nm height) can be still achieved during the graphitization process by controlling the temperature ramp. They showed that a faster heating (270°C/min compared to 40°C/min) led to a higher step density. However, the kinetic of step-terrace arrangement and its relationship with graphene growth is still unclear because the *in-*

situ atomic scale experimental investigation is difficult to be done during high temperature graphitization process. In current study, since no hydrogen etching process has been performed, we aim to alter and control the step morphology during the heating treatment under low Ar pressure by tuning the temperature ramp. Based on our optimized 1LG growth process, all the parameters remain the same with the 1LG growth process (1750°C, 300 s, 10 mbar) except the temperature ramp. This parameter is chosen because we believe the different heating rate acts as an extrinsic kinetic effect which could alter the step moving rate during surface reconstruction.

Two groups of samples A and B have been produced using varied temperature ramp ranged from 0.1°C/s up to 1°C/s. These two groups of samples were synthesized by using two wafers. They are both 4H-SiC but undergone independent polishing process. In this case, the unintentional miscut angle might be different. Before examining the surface morphology, all the samples were measured by Raman spectroscopy. The constant presence of 2D-peak in Raman spectra indicate that all the samples are fully covered by graphene, except for one sample in group B (1°C/s). The $A_{G\text{-graphene}}/A_{G\text{-HOPG}}$ ratio calculated in the acquired spectra estimate the number of layers of 1-2LG. Typically, the 1LG is majority covered while 2LG ribbons are occasionally detected near the step edges. Therefore, we assume the comparable results in terms of number of graphene layers are shown in all the studied samples.

Now we focus on the step-terrace structure of these samples. Fig. 3.21 (a-d) demonstrates the AFM topographic images of four samples in group A and their corresponding profiles, synthesized with a temperature ramp of 0.1°C/s, 0.33°C/s, 0.8°C/s and 1°C/s, respectively. The large terraces with the width of more than 2 μm have been achieved in first three samples. These large steps with a height larger than one-unit cell of the 4H-SiC signify the occurrence of a large degree of step-bunching process. If we now look at their surface more closely, we found that the sample with longer heating process shows the wider terraces and higher steps. Most importantly, the terrace width as large as 10 μm has commonly seen in sample produced by a heating rate of 0.1°C/s. We highlight this large terrace width obtained here which allows the perspective of specific transport measurement on this sample. For example, a Hall bar could be fabricated on single terrace in order to investigate the step influence on the electronic properties of graphene. Moreover, the step height measured following the blue solid line in topographic images decreases with the increase of temperature ramp (Fig. 3.21 (b, d, f and h)). On the other hand, the surface morphology in sample 1°C/s is obviously different compared to the others. Unlike the straight step edges revealed in three earlier samples, the steps with zigzag step edges are present in this sample. This instability in the step edges has been explained by an insufficient step-bunching during the step retreating. In other words, the largely reduced step-bunching process lead to small terraces and high step density.

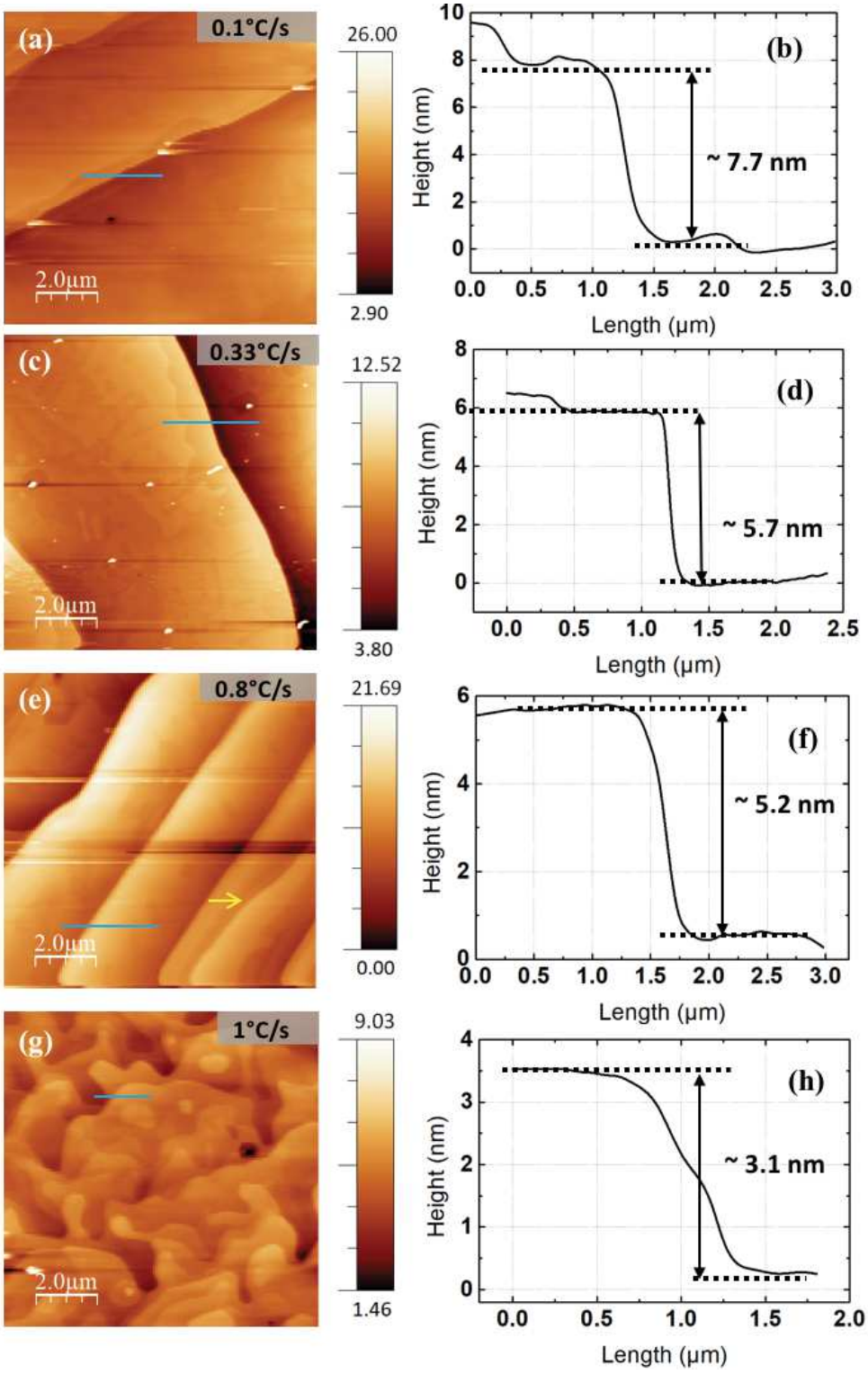

Fig. 3.21 AFM topographic images of samples of group A using 4H-SiC wafer 1. Scale bar in nm. All the samples were produced with a temperature of 1750°C and growth time of 300 s. (a, c, e, and g). Topographic images of samples with various temperature ramp of 0.1°C/s, 0.33°C/s, 0.8°C/s and 1°C/s, respectively. (b, d, f, and h) Profiles of blue lines in corresponding topographic images.

These various step characteristics give us insights into the step-bunching mechanism. Bao *et al.* [121] have argued that once the BL has fully covered the sample surface, the step-bunching does not occur anymore. In other words, the step-bunching only happens before the graphene formation. At this stage, we consider a time period started from the beginning of the step reconstruction until the beginning of the graphene formation and denote it as the step-bunching window. The surface morphology which is related to the step-bunching degree, depends on the duration of this window. For instance, in sample 1°C/s, due to the rapid heating, the step bunching window is largely reduced. This results in an unstable step edges with non-equilibrium surface energy. Thus, the zigzag step-edges shapes have been obtained. Besides, the small terraces located beside the large steps in sample 0.8°C/s (highlighted by yellow arrows in Fig 3.21 (e)) is an indicator of the inhomogeneous step-bunching process which means the surface energy is different at each step. On the contrary, in sample 0.1°C/s, because of the long heating process, the surface energy minimization could be achieved by the large step-bunching process, leading to a relatively homogeneous distributed wide terrace. In any case, we have demonstrated that by controlling the temperature ramp, we can alter the step-bunching degree, therefore the control of the step morphology in graphene samples is feasible.

However, samples of group B show different results. We first focus on the three former samples because the sample 1°C/s has not been fully covered by graphene according to Raman analysis. As we can see in Fig. 3.22 (a-c), unlike the observation in samples of

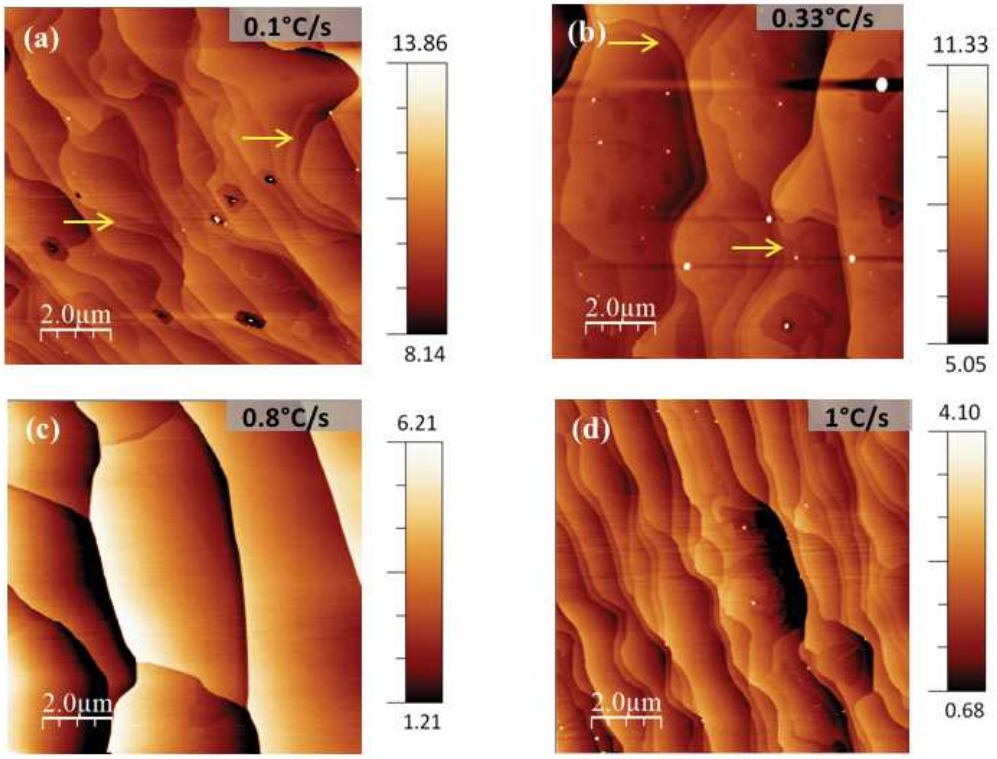

Fig. 3.22 AFM topographic images of samples of group B using 4H-SiC wafer 2. Scale bar in nm. All the samples were produced with a temperature of 1750°C and growth time of 300s. Various temperature ramp of 0.1°C/s, 0.33°C/s, 0.8°C/s and 1°C/s were investigated and shown in (a-d).

group A, the wave-shaped step edges were generally present. Except the quite smooth surface obtained in sample 0.8°C/s, the small steps with sub-nanometer height (0.2-0.5 nm) usually appear nearby the relatively large steps in sample 0.1°C/s and 0.33°C/s, as indicated by yellow arrows. These sub-nanometer height steps could be related to the results of the step-bunching, implying the different surface energy and erosion rate at each terrace. Thus, the wave-shaped step-edges is not totally unexpected. However, we emphasize that the step structure is still clearly discernable, which is different with the canyon shapes observed in sample 1°C/s of group A. On the other hand, the sample 0.8°C/s shows a relative straight step-edges and homogeneous terrace width. The measured step height is between 2-5 nm with a terrace width larger than 2 μm. The smooth surface is supported by in the topographic image and the lack of contrast in phase image (not shown), confirming the homogeneity of this sample. According to Raman analysis, this sample is covered by monolayer graphene, indicating that the growth has happened in an equilibrium thermodynamic condition. Then, we pay attention to the sample 1°C/s in which the first graphene layer is not yet fully covered the surface. We found the sub-nanometer steps next to the large terraces and wave shape step-edges in this sample, likely indicating step-bunching in progress. This observation is consistent with our earlier analysis that a surface energy minimization could not be achieved with a rapid heating process. On the contrary to sample group A, no clear temperature ramp effect is observed in these samples. The terrace width seems irrelevant with the temperature ramp and the large terrace is absent in sample using 0.1°C/s. Indeed, the miscut of our wafer is about $\pm$ 0.2°. Considering this large error bar and the absence of hydrogen etching in our growth process, we attribute the different results of group A and B to the wafer effect (miscut angle).

The results of group A indeed show the temperature ramp effect on the sample morphology, which inspired us to further optimize this parameter. We stress that the sample group B were produced on another wafer which highlights the importance of wafer properties on graphene morphology. In order to suppress the substrate effect, a hydrogen etching treatment could be considered in this experiment. In the near further, we propose to tune the heating rate in a larger range, i.e. up to 5°C/s or down to 0.01°C/s, incorporating with the optimization monolayer graphene growth by tuning other parameters, e.g. growth time. Considering the perspective of 10 μm wide terrace, more efforts are needed until a full control of the step morphology by growth parameter.

3.6 Summary

In this chapter, starting from the growth of BL, we have further studied the growth time, growth temperature and temperature ramp effect. The main results are presented in Fig. 3.23. Most importantly, the initial stages of monolayer graphene growth, i.e. BL-like layer, BL, graphene ribbons, were demonstrated in samples synthesized using different growth parameters.

At 1600°C: we are able to grow a BL-like sample. Some small well-structured carbon patches are visualized around step edges, signifying the first step of graphene growth. However, the multilayer graphene sample produced at this temperature indicated an inhomogeneity in graphene distribution.

At 1700°C, the graphene microscale ribbons grown on both lower and upper sides of the step edges where the Si detachment and sublimation are easier. We observed a step-flow growth method which is the main growth method achieved in this thesis by using a low Ar pressure. On the other hand, the sample with fully graphene coverage synthesized at this temperature show the relatively small graphene domains, indicating a limited carbon diffusion.

At 1750°C, the 1LG growth is completed by a step-flow growth mechanism. Regarding the structural properties, the Raman map and AFM phase images demonstrate a homogenous and continuous single graphene layer formation. And the topographic AFM images reveal a regular step-terrace structure, similar to the graphene grown under 1atm Ar pressure. The STM images reveal a (6×6) superlattice, evidencing the presence of both monolayer graphene and BL. Then, the quantum Hall effect was observed and the plateau value in Hall resistance at high magnetic field can further confirm the number of layers. The transport measurements show a low doping in the order of few 10^{10} cm^{-2} up to few 10^{11} cm^{-2} at low temperature of our monolayer graphene samples. It is worth emphasizing that all the characteristic techniques show the consistent results which validate not only our optimized monolayer graphene growth method but also the methodology of our sample analysis.

In addition, we would like to highlight the extremely reproducibility and controllability of our growth process. We have repeated the 1LG growth process more than 50 times. Even if changing the SiC wafer, the optimized temperature for the 1LG formation slightly shifts within 10°C. Both the Raman spectroscopy, AFM and transport measurements have been performed on these monolayer samples and showing the similar morphology and electrical properties. Hence, we have achieved a reproducible and controlled process of the monolayer graphene growth in this thesis. Based on this robust production, the graphene/SiC (0001) interface and epitaxial graphene properties could be further studied as we will present in the following chapters.

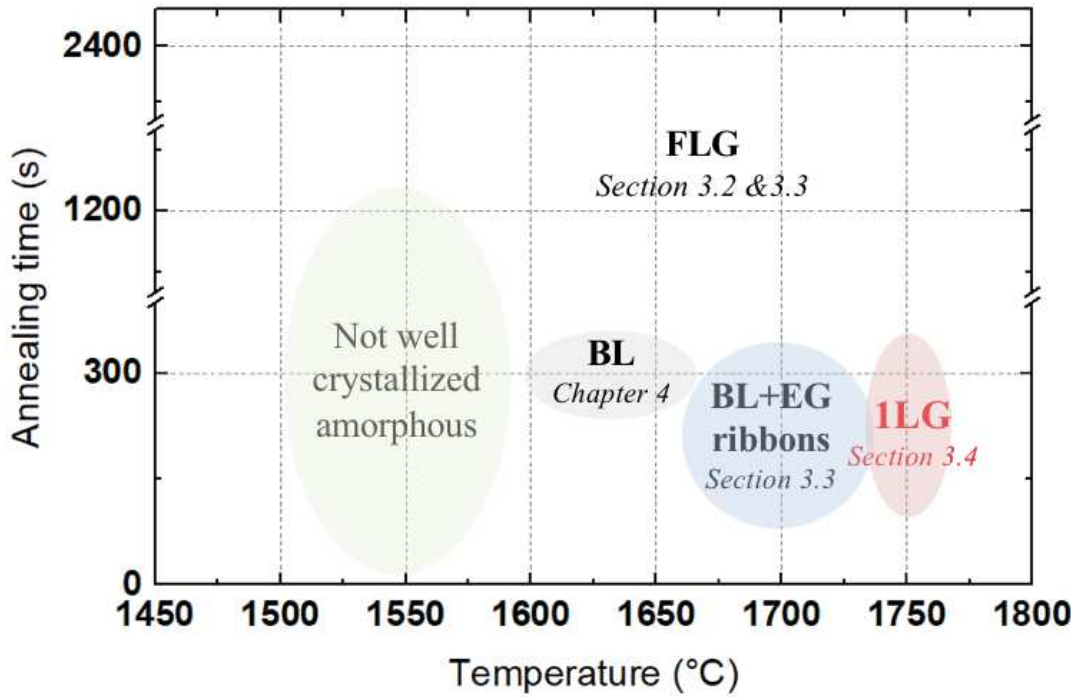

Fig. 3.23 Conclusion of achievable and reproducible samples in this thesis. The number indicate the sections and chapters where these samples are mentioned.

Chapter 4 Epitaxial graphene and SiC (0001) interface

In **chapter 1**, we have introduced the interface structure between epitaxial graphene and SiC (0001), which is the well-known buffer layer (so called BL). As mentioned, BL has considerable influences on mechanical and electronic properties of graphene. In **chapter 3**, we took a glance at the Raman spectrum of BL in our samples. Both the bare BL without graphene covering and the interfacial BL laying between monolayer graphene (1LG) and SiC substrate have been probed by Raman spectroscopy. In **chapter 4**, our objective is to explore characteristics of BL as well as coupling between 1LG and BL. In the literature, several works studied this coupling by comparing the bare BL prior to graphene growth (denoted as BL_0) with the interfacial BL (BL_{1LG}) laying at the interface of graphene/SiC [114,164,183]. The schematic representation of these two types of BL is shown in Fig. 4.1. Schumann *et al.* [114] have measured the different lattice constant and corrugation in these two types of BLs by the grazing-incidence X-ray diffraction and found that the BL_0 possesses a larger lattice (2.467 Å) compared to BL_{1LG} (2.463 Å). They attributed this decrease in the lattice constant of BL after covering by graphene to the lowering of out-of-plane corrugations. Similarly, Conrad *et al.* [183] have observed that the vertical corrugation of the BL_{1LG} is smaller than that of BL_0 by the X-ray standing wave and X-ray reflectivity measurements. They explained this result by a larger strain in BL_{1LG} compared to BL_0. Regarding Raman analyses, Tiberj *et al.* [164] have observed a decreased Raman intensity of BL with a ratio of 3 after the growth of the 1LG. At this stage, it is extremely important to clarify that the BL_0 and the BL_{1LG} differ in several aspects. First, the BL_0 is the first carbon layer which grows at the Ar-SiC interface whereas the BL_{1LG} is the second carbon layer grown between the 1LG and SiC substrate. Then, the growth temperatures might be different for these two BLs. The bare BL, as the first carbon layer grown on SiC (0001), is formed prior to the interfacial BL growth, which possibly corresponds to a lower growth temperature. Thus, the graphene coverage is not the only difference between the BL_0 and BL_{1LG}. To evidence the coupling between 1LG and BL more directly, we come

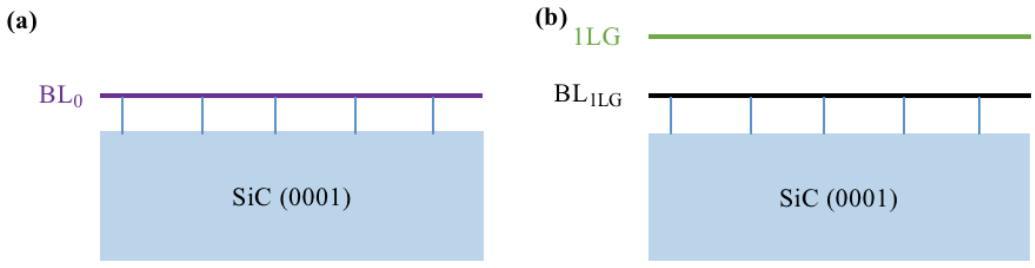

Fig. 4.1 Schematic illustration of two types of BL: (a) BL_0 and (b) BL_{1LG}.

up with an idea of mechanically removing the graphene layer above the BL_{1LG} at room temperature in order to have access to the BL_{1LG} without graphene covering (uncovered BL_{1LG}). This transfer experiment allows not only a study of coupling between 1LG and BL revealed by the evolution in BL after the removal of graphene, but also an investigation of characteristics of different types of BL: i) direct growth BL_0 samples; ii) BL_{1LG} covered by graphene, and iii) uncovered BL_{1LG} obtained by mechanical removal of graphene.

In order to facilitate the lecture, we list all the types of mentioned BLs:

BL_0	bare BL obtain from direct growth, prior to 1LG growth
covered BL_{1LG}	interfacial BL covered with graphene above
uncovered BL_{1LG}	interfacial BL after mechanical removal of 1LG
covered $BL_{1LGminusG}$	interfacial BL covered with 1LG but we subtract the contribution of 1LG in Raman analysis

Indeed, the debate on BL regarding its structural and electronic properties has lasted for years in the literature. Numbers of techniques has been used to study this layer including STM, XPS, ARPES, and Raman spectroscopy, etc. Concerning our own experiences, Raman signatures of BL have been presented in **chapter 3**. At that moment, we have noticed the variety of BL Raman signature in terms of peak integrated intensity and position in the studied samples. In the literature, despite Raman signature of BL being reported and the inhomogeneity of these spectra having been noticed [122,144,163,164], a systematic and statistical analysis of BL characteristic is still missing. Moreover, only few works have investigated the coupling between graphene and BL by Raman technique. Indeed, our previous observation of Raman signature of BL as well as the work of Tiberj *et al.* [164] have inspired us to continue the BL investigation by Raman spectroscopy which is largely used to study the structural and electronic properties of carbon structure. Besides, our micro-Raman spectroscopy setup and home-made repositioning software allow a retraceable map collection, therefore the exact same BL flakes with or without graphene coverage can be compared.

The exfoliation of graphene can be achieved by depositing and sequentially removing a thin epoxy-based glue layer or Nickel (Ni) layer, as will be presented in **section 4.1**. The validation of graphene exfoliation will be demonstrated by two example samples. Later, in **section 4.2**, we introduce the four-component fitting which is generally used to study the Raman signature of BL in the literature and 3-region analysis method. Next, the effect of growth temperature on BL_0 will be discussed in **section 4.3**. We have also reidentify our BL-like sample (section 3.1) in this section. In **section 4.4**, the excitation wavelength dependent Raman experiments were employed for the purpose to better understand the physical origin of these Raman peaks. Lastly, the BL_{1LG} Raman signatures before and after the graphene removal process were compared in **section 4.5**, showing the evolution of BL in these two cases. We believe this evolution could shed some light on the interaction between the BL and graphene as well as BL characteristics.

4.1 Mechanical exfoliation of graphene layer by thin layer deposition

The graphene exfoliation experiments have been performed on our 1LG samples which were produced by the optimized growth process presented in chapter 3. The transfer of graphene was inspired by two works [37,184] in which they used a thin epoxy-based glue layer and Ni layer, respectively, to mechanically exfoliate graphene layer. The process is illustrated in Fig. 4.2. More experimental details concerning the preparation of glue layer, the control of the thin glue (or Ni) layer deposition as well as the removal of this glue (or Ni) layer are presented in appendix 4. The main processes are as follows. Firstly, a very thin epoxy-based glue layer or Ni layer has been deposited on the whole

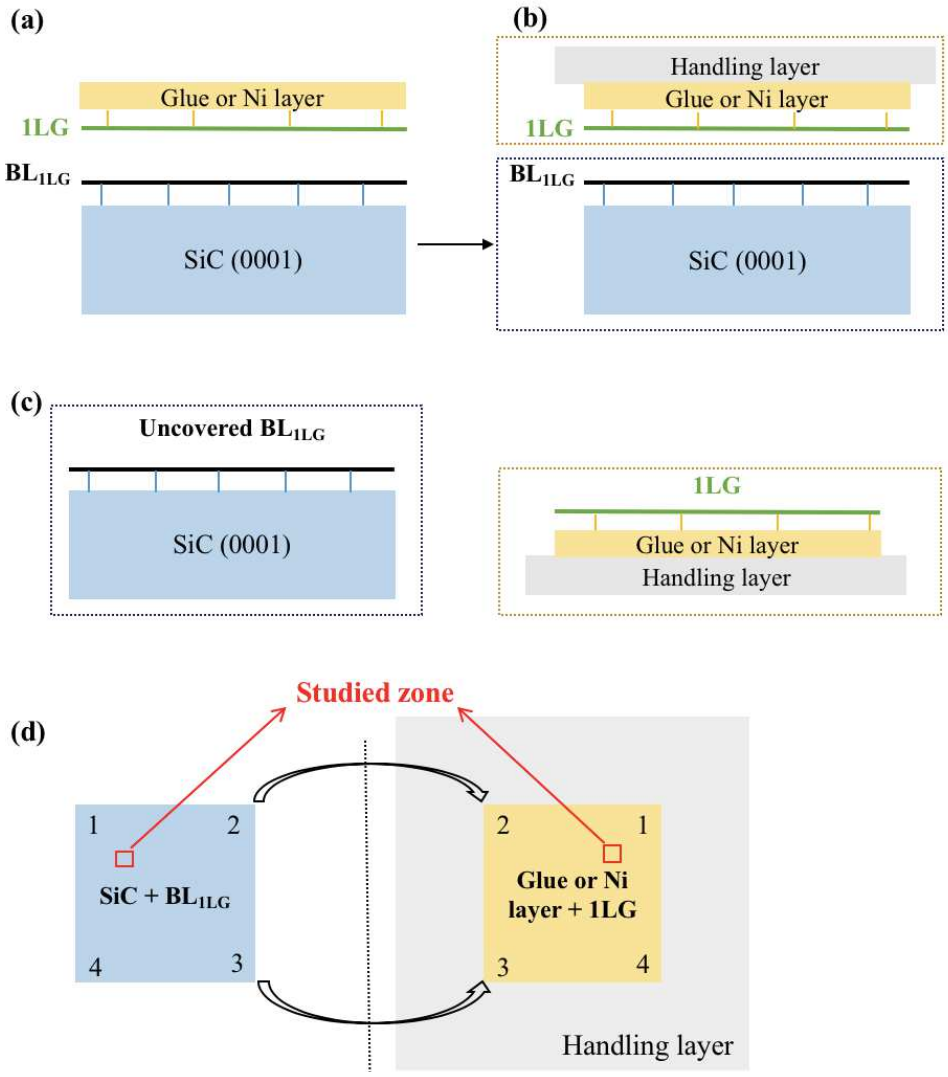

Fig. 4.2 Schematic illustration of graphene exfoliation process achieved by a thin epoxy-based glue layer or Ni layer deposition. Cross section views of (a) the deposition of thin layer. (b) a handling layer which was deposited in order to mechanically remove the glue or Ni layer. (c) Left: the uncovered BL_{1LG}. Right: the glue or Ni layer as well as 1LG which was released with the removal of handling layer. (d) Vertical view of the transferred glue or Ni layer which was situated on handling layer as a mirror-reversal of sample surface across a vertical axis. The red squares show an example of the position of one studied zone on SiC surface (left) and its corresponding position on thin glue or Ni layer (right).

sample surface (Fig. 4.2 (a)). Then, due to the higher binding energy at the interface of glue (or Ni) layer and graphene compared with that of the graphene and BL [37,184], the graphene layer can be mechanically exfoliated when we remove the deposited layer via a handling layer (Fig. 4.2 (b)). Therefore, only uncovered BL_{1LG} was left on the SiC substrate while the graphene layer was transferred onto the deposited thin epoxy-based glue or Ni layer (Fig. 4.2 (c)). Since the deposited layer had covered the entire sample surface, after its release, this layer can be easily recognized on the handling layer by the same shape of graphene sample, i.e. 6 mm × 6 mm square (Fig. 4.2. (d) and Fig. A4.1 in appendix 4). It is worth mentioning that we have performed the graphene transfer experiments on more than 6 samples by both glue and Ni deposition and exfoliation in order to validate our techniques and results. During this process, the removal of the graphene layer was confirmed by comparing the Raman maps collected before and after the experiments at the exact same position. The AFM and optical images are combined as the supplementary evidence. The comparable results obtained from all the studied samples highlight the reproducibility of this experiment. Next, we will show the results of two representative samples in order to demonstrate our validation process.

Fig. 4.3 (a) demonstrates the Raman mapping (975 spectra) of the integrated intensity of 2D-peak (denoted as A_{2D} map) of a studied sample **before** the exfoliation experiment. The well-defined G-peak and 2D-peak are constantly detected in all the spectra, showing the presence of a continuous graphene layer. Besides, we found some broad features between 1200 and 1800 cm^{-1} close to G-peak region which could be identified as BL_{1LG} signature based on the early analyses in **chapter 3**. At first glance, two contrasts can be identified in this A_{2D} map: green zones and yellow stripes. We then estimate the number of graphene layers by appropriately calculating the corresponding $A_{G\text{-graphene}}/A_{G\text{-HOPG}}$ ratio based on the method presented in **section 2.2**. Here, the $A_{G\text{-graphene}}/A_{G\text{-HOPG}}$ ratio was calculated after a subtraction of BL contribution following the process introduced in appendix 2. We only consider the spectra situated at the center of each domain, ignoring the spectra at the boundary of two domains. For spectra in green areas, the $A_{G\text{-graphene}}/A_{G\text{-HOPG}}$ ratio ranged from 0.025 to 0.040 (402 spectra) in a Gaussian distribution centered at 0.033. This value indicates that most of the spectra in green areas could be attributed to 1LG. We remark that few spectra with an $A_{G\text{-graphene}}/A_{G\text{-HOPG}}$ ratio lower than 0.025 (5 spectra) have not been taken into consideration because of a bad subtraction of SiC. On the other hand, the spectra in yellow contrast areas possess an $A_{G\text{-graphene}}/A_{G\text{-HOPG}}$ ratio ranged from 0.044 to 0.063. The corresponding distribution centered at 0.054 by Gaussian function, close to the expected value for 2LG (0.06). The average spectra of these two types of areas are presented in green and yellow spectrum, respectively, in Fig. 4.3 (b). We note that the individual spectra were normalized by dividing the value of the integrated intensity of G-peak of corresponding HOPG reference ($A_{G\text{-HOPG}}$) allowing the comparison between maps.

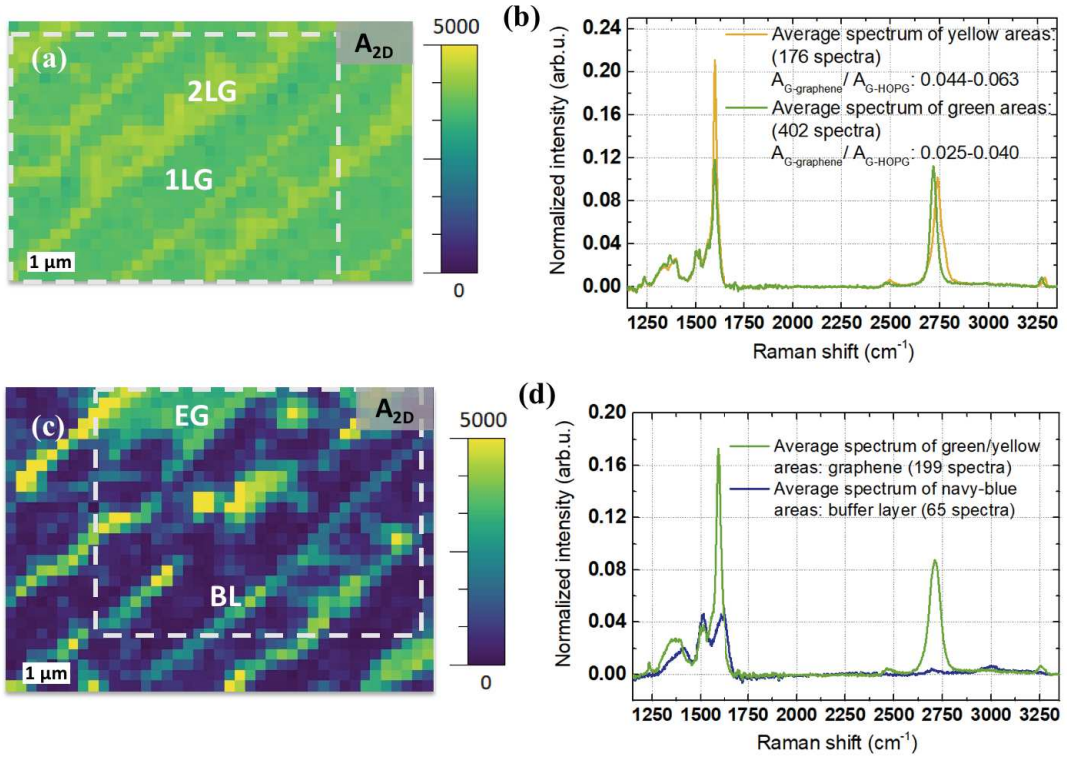

Fig. 4.3 Raman analysis of a sample on which we have performed a glue layer deposition experiment to transfer the graphene layer. Two Raman A_{2D} map (a) before and (c) after the graphene transfer, unit in counts s^{-1} cm^{-1}. Different domains have been indicated in images: BL, 1LG, 2LG and EG. The dashed rectangles highlight the common area of these two maps. (b) and (d) demonstrate the average spectrum of each analyzed zone. The scanning steps of both x and y directions are 0.5 µm in these two maps.

Fig. 4.3 (c) is the A_{2D} map (1305 spectra) of this sample **after** the deposition and removal of the thin epoxy-based glue layer (called glue layer deposition method). We stress that this Raman map was recorded at the exact same position as the one collected before the graphene transfer experiment (Fig. 4.3 (a)). The intersection area is outlined by the dashed white rectangle in each map. After releasing the deposited glue layer, we observed that the 2D signal dropped to quasi-zero in some areas (navy-blue contrast in Fig. 4.3 (c)). In **chapter 3**, we have used the A_{2D} as an indicator to distinguish the graphene with BL zones, because this value shows a considerable difference in the BL spectrum (below 150 counts s^{-1} cm^{-1}) compared to that of graphene spectra (more than 2800 counts s^{-1} cm^{-1}). On the other hand, the G-peak or $A_{G\text{-graphene}}/A_{G\text{-HOPG}}$ ratio could not be used for this purpose due to the broad peaks of BL in Raman spectrum around G-mode region. Thus, we consider an A_{2D} value below 150 counts s^{-1} cm^{-1} as an indicator to distinguish BL from graphene. The choice of the value 150 count s^{-1}. cm^{-1} will be justified later in this section. Meanwhile, we ignore all the spectra with the A_{2D} between 150 and 2800 counts s^{-1} cm^{-1}, considering they could be the mixture of BL/1LG. The average spectrum of navy-blue areas (A_{2D} < 150 counts s^{-1} cm^{-1}) is shown

in navy-blue curve in Fig. 4.3 (d). As expected, the well-defined G-peak and 2D-peak are absent in this average spectrum of navy-blue areas but several intense and broad bands in the spectral region of 1200 - 1800 cm^{-1} have been revealed. Besides, a few low-intensity bumps extending from 2600 cm^{-1} to 3000 cm^{-1} are visible. Thus, we naturally relate these navy-blue areas to the BL since the spectra acquired from these areas hold all the characteristics of the Raman signature reported for the BL [85,144,163,164]. Next, we average all spectra of the green/yellow areas in Fig. 4.3 (c) where we have an intense 2D peak (A_{2D} above 2800 counts s^{-1} cm^{-1}) and the spectrum is shown in green curve in Fig. 4.3 (d). As expected, the G- and 2D- peaks as well as the BL fingerprint can be identified, indicating the presence of graphene and interfacial BL_{1LG}. Comparing these two A_{2D} maps in Fig. 4.3 (a) and (c), we believe that the graphene flakes have been mechanically removed by the glue deposition method in the navy-blue areas in Fig. 4.3 (c), thereby leaving the uncovered BL_{1LG} on the SiC surface. Furthermore, we notice that most of the uncovered BL_{1LG} zones were situated on the terraces. The graphene close to step edges are generally left on the surface.

The removal of the graphene flakes has been further validated by checking the thin epoxy-based glue layer since the exfoliated graphene flakes were expected to be transferred to this deposited glue layer, as illustrated in Fig. 4.2 (d). First, we have recognized the thin glue layer situated on handling layer by searching the 6 mm × 6 mm square shape (Fig. A4.1 in appendix 4). Based on the mirror reversal relationship between the glue surface and sample surface, we then retrace, on glue surface, the specific zone corresponding to where we recorded the Raman maps from the sample surface. An optical image of this retraced zone on glue surface is shown in Fig. 4.4 (a) with a dashed white rectangle highlighting the Raman map corresponded zone. Generally, we observe the white flakes on the green background. In Fig. 4.4 (b), the shape of these white patches can be perfectly superposed by the navy-blue areas in Raman A_{2D} map while the green areas are correlated to the yellow/green regions. Earlier in Fig. 4.3 (c), we have observed that the graphene has been removed, in the meantime, the uncovered BL_{1LG} has been left on the navy-blue areas. Correspondingly, we acquired several spectra from the white flakes at the positions marked by c-i. We subtract the spectrum acquired from the green area from all the spectra of the white flakes since we assumed the white flakes could be related to graphene while the green area is corresponding to the glue layer. The results after this subtraction are shown in Fig. 4.4 (c). The intense G-peak (1589 ~ 1598 cm^{-1}) and 2D peaks (2675 ~ 2690 cm^{-1}) are displayed in all of the spectra, indicating the presence of graphene in these white flakes. Besides, the BL contribution is absent in all these spectra. This result is foreseen and consistent with early analyses of sample surface. Thus, we have confirmed that graphene transfer process can be achieved by the deposition and removal of the glue layer. Furthermore, no visible D-peak presents in the whole set of spectra which indicate not only a well-structured graphene layer growth but also a successful graphene transfer process.

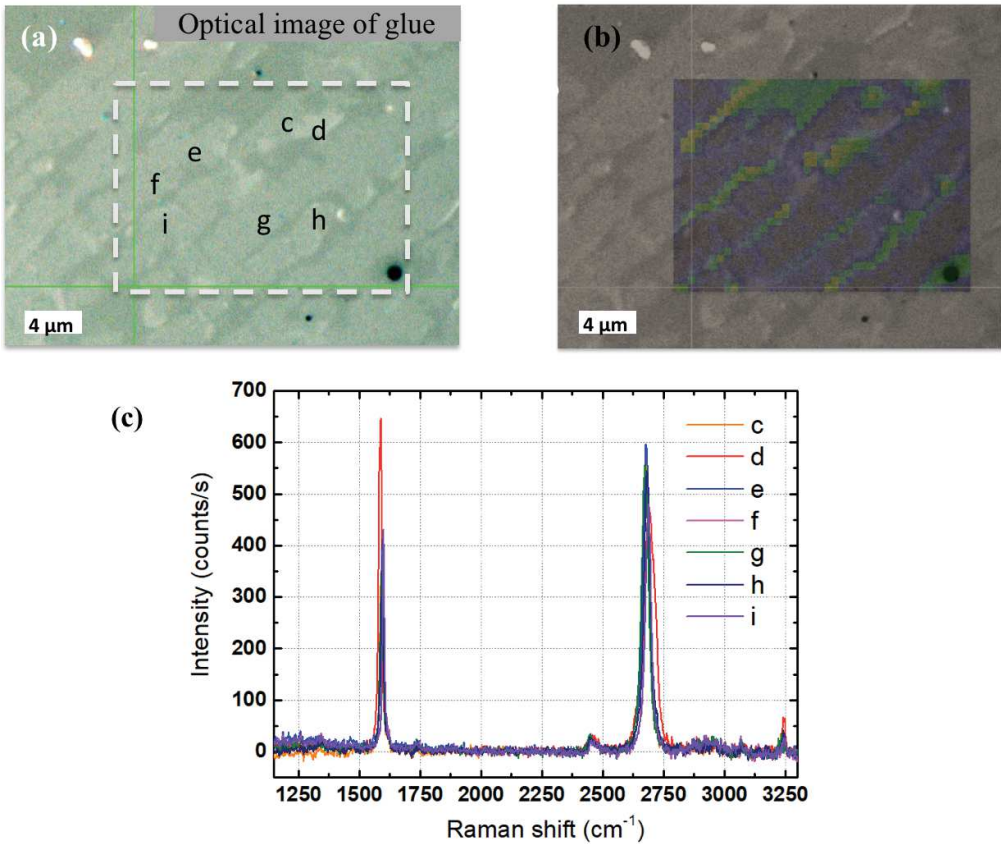

Fig. 4.4 (a) Optical image of the deposited glue layer surface. c-i indicate the positions of the acquired Raman spectra in (c). Dashed white rectangle highlight the Raman map position. (b) The superposed Raman A_{2D} map (blue/yellow) and optical image. (c) Raman spectra at position c-i in (a).

Regarding the case of graphene removed by depositing and exfoliating the Ni layer (Ni layer deposition method), the main procedure to validate the accomplishment of graphene transfer by the Raman technique is similar to that of glue layer deposition case. The Raman A_{2D} map **before** (900 spectra) and **after** the transfer process (1085 spectra) are presented in Fig. 4.5 (a) and (c), respectively. The position of the former is outlined by dashed white rectangle in the latter. In the similar manner as before, we first confirm the continuity of the graphene by examining every spectrum in A_{2D} map in Fig 4.5 (a). Then the $A_{G\text{-graphene}}/A_{G\text{-HOPG}}$ ratio has been calculated for green and yellow areas. In green areas, the $A_{G\text{-graphene}}/A_{G\text{-HOPG}}$ ratio ranged from 0.028 to 0.038 (374 spectra) in a Gaussian distribution centered at 0.036 which could be attributed to 1LG. On the other hand, we calculated the yellow areas possess the $A_{G\text{-graphene}}/A_{G\text{-HOPG}}$ ratio between 0.039 and 0.050. This could indicate the presence of both 2LG and 1LG in these areas which results in an $A_{G\text{-graphene}}/A_{G\text{-HOPG}}$ ratio higher than the value expected for 1LG but lower than that of 2LG. The average spectra of green and yellow areas are shown in Fig. 4.5 (b) by green and yellow spectra, respectively. Likewise, in the A_{2D} map after releasing the deposited layer (Fig. 4.5 (c)), the spectra collected from green/yellow ($A_{2D} > 2800$ counts s^{-1} cm^{-1}) and navy-blue areas ($A_{2D} < 150$ counts s^{-1} cm^{-1}) can be identified as

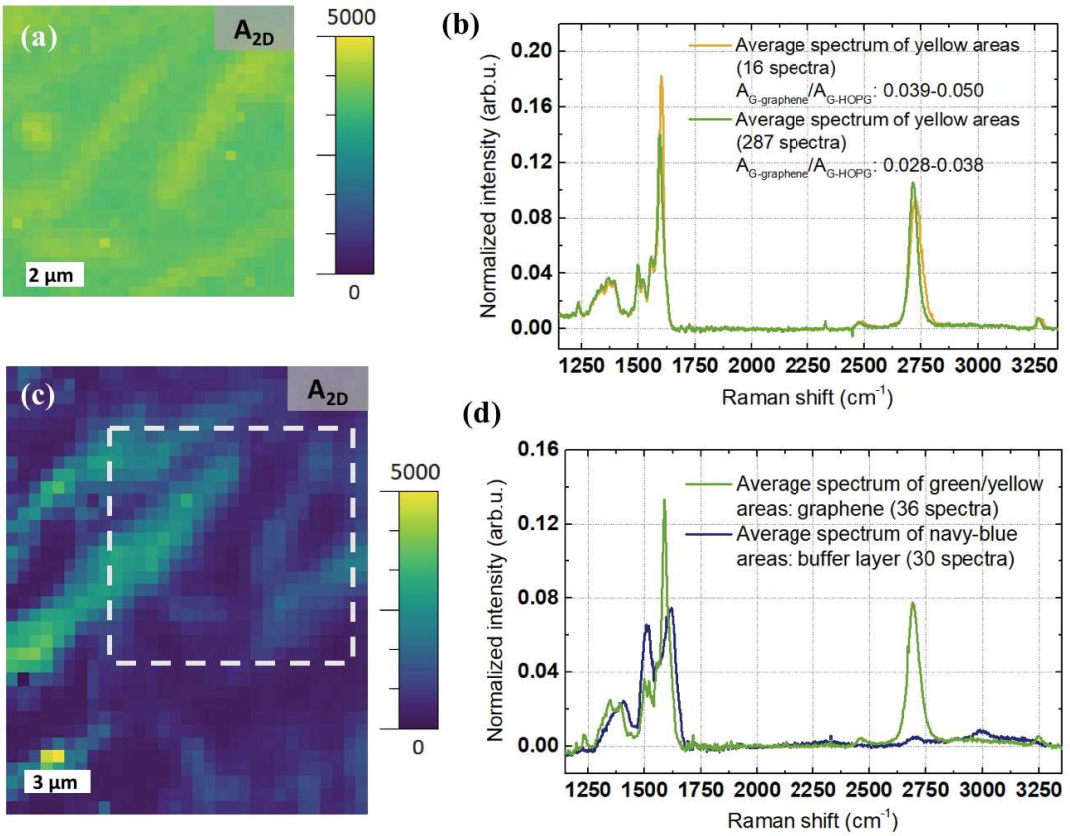

Fig. 4.5 Raman analysis of a sample in which we performed a Ni layer deposition experiment to transfer the graphene layer. Two Raman A_{2D} map (a) before and (c) after the graphene transfer at exact same position, unit in counts s^{-1} cm^{-1}. Dashed white rectangle in (c) highlight the position of (a). (b) and (d) demonstrate the average spectrum of the analyzed zones. The scanning steps of both x and y directions are 0.5 µm in these two maps.

graphene and BL spectrum, respectively. However, most of the spectra in this map have an A_{2D} value between 150 and 2800 counts s^{-1} cm^{-1} which could be attributed to the mixture of 1LG/BL. We assume a large number of small 1LG patches could be left on the sample surface after transfer experiments. Nevertheless, we can still find pure BL areas with relatively large domain size (several μm^2). Then the average spectra taken from these two types of areas are presented in green and navy-blue curves, respectively in Fig. 4.5 (d). In this case, Raman analysis after removing the Ni layer implies a successful graphene exfoliation by this method.

In the Ni layer deposition case, only several black lines and spots are visible in optical image of Ni surface after the exfoliation process (Fig. 4.6 (a)). Due to the lack of optical contrast of graphene deposited on Ni layer, the retracing of the Raman map corresponded position on the sample surface is difficult to achieve. Nevertheless, the randomly acquired spectra from the Ni surface obviously show the Raman signature of graphene with the presence of G-peak (1610 cm^{-1}) and 2D-peak (2695 cm^{-1}), as illustrated in Fig. 4.6 (b). Different areas were probed and show comparable Raman spectrum. We also remark the absence of BL contribution as well as the D-peak in these

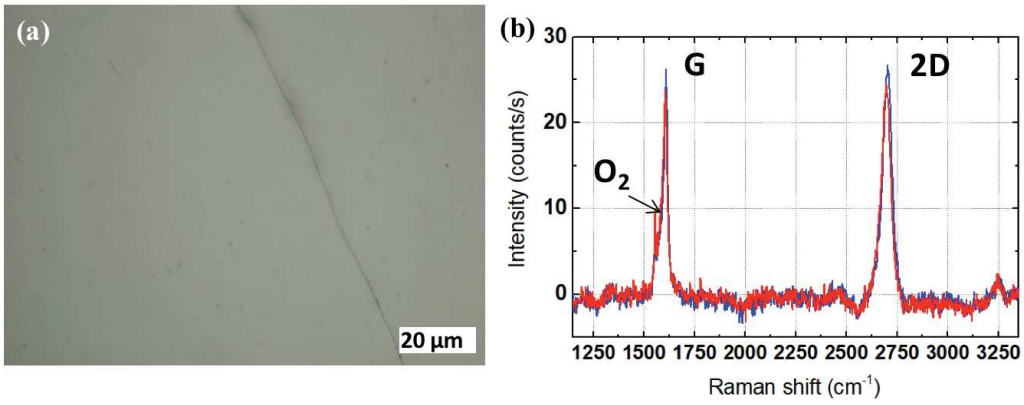

Fig. 4.6 (a) Optical image of Ni layer surface. (b) Two representative spectra acquired from the Ni surface after the graphene transfer process.

spectra. Furthermore, a fine peak situated at 1556 cm^{-1} is observed in all the spectra, which could be related to the presence of oxygen [185]

Then, in the Ni layer deposition case, the AFM images have been collected on the sample after graphene transfer experiment as a complementary information. The AFM topographic and phase images were recorded at the position corresponding to the Raman map in Fig. 4.5 (c). In Fig. 4.7 (a) and (b), the Raman map position is outlined by the dashed white rectangles. In **chapter 3**, we have demonstrated that AFM technique is a useful tool to identify different material when combining with Raman map analysis. Here, we have generally seen three types of contrast in AFM phase image, refer as to gray-blue, blue and dark blue contrast (from the highest to lowest phase value). More precisely, the gray-blue contrast is majority observed on the sample surface with several blue contrast stripes located both on terrace and step. The dark blue contrast refers to the small patches surrounded by blue contrast or situated at step edges, as one example pointed by black arrow in Fig. 4.7 (a). Combing with the corresponding Raman map in Fig. 4.5 (c), the gray-blue phase areas in Fig. 4.7 (a) can be superposed to the BL areas while the blue and dark blue phase contrast corresponds to the graphene areas. Because of the limited domain size of dark blue phase areas, these zones are not distinguishable from the blue areas in Raman analysis. Besides, small blue patches (graphene) are largely present in majority gray-blue terraces (BL). This is consistent with the previous result of Raman analyses where we have identified the 1LG/BL mixture in most of the spectra. Regarding the topographic image in Fig. 4.7 (b), we observed a sample surface after the transfer without external adsorption or cracks in sample surface, indicating a clean transfer method.

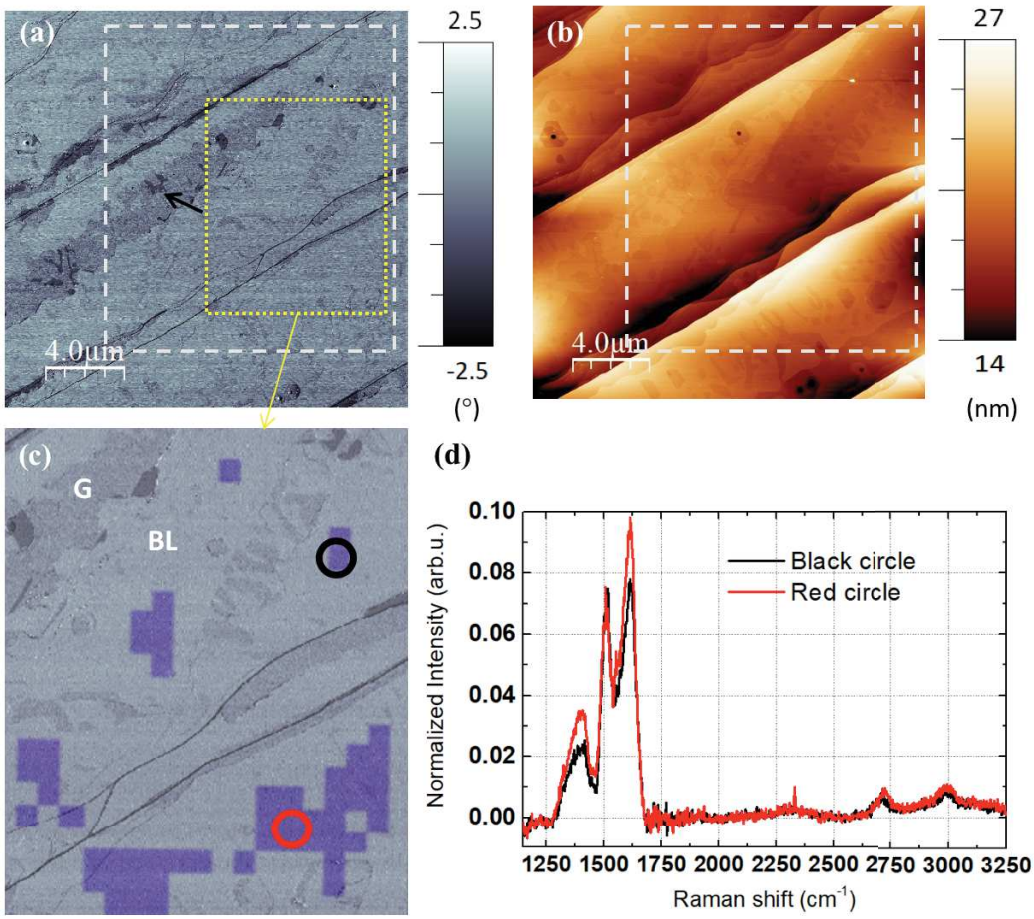

Fig. 4.7 AFM (a) phase and (b) topographic images corresponded to the Raman map shown in Fig. 4.5 (c). The latter is highlighted by dashed white rectangle. (c) A zoomed phase image of yellow square in (a), overlapped by a Raman 2D mask in which the spectra with an intensity less than 300 counts s^{-1} cm^{-1} were selected. (d) Two spectra collected at the position of red and black circles in (c).

Then, we take advantage of the resolution of AFM images to further validate our criteria for BL areas selection in Raman analysis. As we mentioned before, we have used the A_{2D} to distinguish the graphene and BL areas due to the considerable difference shown in these two cases. However, small patches of graphene could still possibly present in our identified BL area selected by using our A_{2D} criteria ($A_{2D} < 150$ counts s^{-1} cm^{-1})? In other words, by using our criteria, can we appropriately select the pure BL areas without small graphene patches? Fig 4.7 (c) is a zoomed AFM phase image of yellow rectangle zone in Fig. 4.7 (a), superposed by Raman mask (in purple) in which we selected the spectra with an A_{2D} lower than 300 counts cm^{-1} s^{-1} of Raman map shown in Fig. 4.5 (c). As we can see, all the selected spectra are situated in the homogeneous areas with only gray-blue contrast in phase. No graphene patches (blue) were found at these locations which means the acquired Raman spectra from these areas are truly pure BL fingerprint. Thus, we have confirmed our criteria for the selection of BL spectrum. To be cautious,

we usually set a value lower than 300 counts cm^{-1} s^{-1}, i.e. 150 counts cm^{-1}. s^{-1} for all the studied map.

Then we compared our uncovered BL_{1LG} obtained by graphene removal with BL_0 samples produced by growth in this work aiming to have a first impression about their lineshape. In Fig. 4.8, blue spectra represent two spectra of samples in which we mechanically removed the graphene. The red and orange spectra are two spectra collected from a BL_0 sample achieved by direct growth. These four spectra are comparable in terms of lineshape. The discrepancies mainly concerning the clearly observed Raman intensity will be discussed in the following section. Moreover, the well-defined second-order Raman peaks (e.g. 2D-peak) is absent for all the BL spectra. In this case, this similarity between these two types of BLs could further confirm the success of graphene removal experiments.

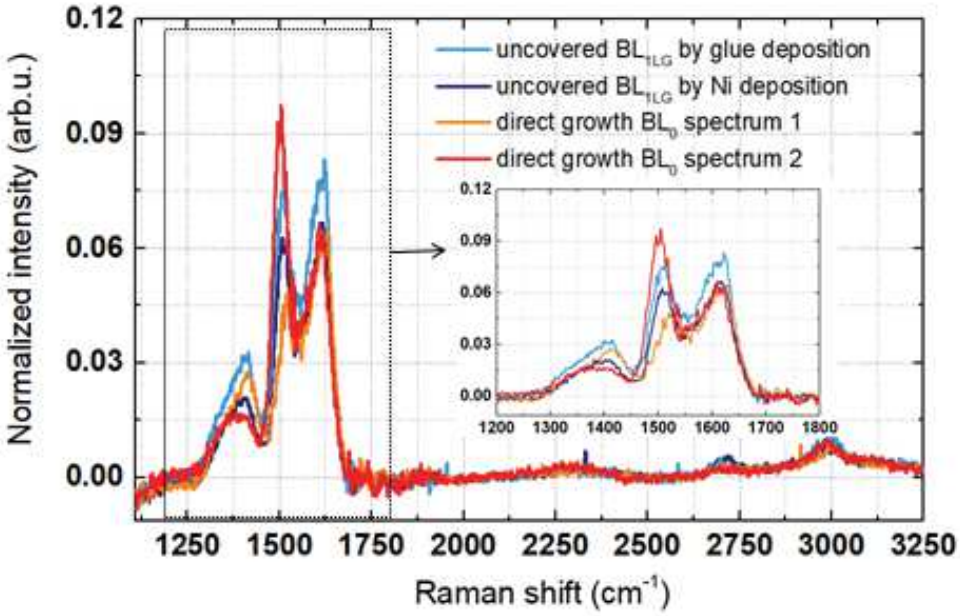

Fig. 4.8 Raman spectra of uncovered BL_{1LG} samples achieved by Ni (light blue) or glue (navy-blue) layer deposition methods and BL_0 samples obtained by direct growth (green).

Hence, we have successfully developed the graphene removal methods by depositing and mechanically exfoliating a deposited thin epoxy-based glue layer or Ni layer. The BL_{1LG} without graphene covering is achievable by this experiment. In the meantime, we show again that the repositioning software acts as an indispensable tool in this study, especially in the case of the discovery of the interest zone on thin glue layer surface. It is worth mentioning that both the BL and the graphene could be remained intact without considerable modification after the exfoliation experiment, evidenced by Raman signature. For example, no obvious D-peak is observed in the transferred graphene spectrum. We highlight the reproducibility of this experiment by the similar results obtained in more than 6 samples.

4.2 4-component fitting vs. 3-region method

So far, the graphene exfoliation experiment has been validated by the analyses of Raman spectroscopy, AFM and optical microscopy. We have now access to different BL under various conditions: i) BL_0 synthesized by different growth process; ii) BL_{1LG} covered by monolayer graphene and iii) uncovered BL_{1LG}. Next, we focus on the Raman technique to study our obtained BL. Before starting to examine the Raman spectra, we first need to consider the methodology of Raman analysis by using our home-made software. Indeed, we have already shown the fitting of the BL-like and BL_0 spectra as well as the BL_{1LG} spectrum by 4-component (Gaussian functions) in **chapter 3** (Fig. 3.1 and 3.7). In the literature, Fromm *et al.* [144] have fitted their BL spectrum by 4 Gaussians functions centered at 1364, 1490, 1544, and 1600 cm^{-1} respectively. Similarly, Kruskopf *et al.* [167] have suggested 4 peaks to fit the spectra which located at 1370, 1492, 1543, and 1595 cm^{-1}, respectively . Even though the 4-component fitting has been largely used, the explicit assignment of each peak is not available considering the phonon modes of buffer layer in each frequency region has not yet been clarified. Fromm *et al.* [144] have reported ab initio calculations of BL in which they show significant flatter phonon bands with respect to that of graphene. They suggested a large number of Raman active modes could plausibly exist, leading to the difficulty in peak assignment. Nevertheless, the 4-component fitting allows a higher R-square value which indicates the goodness of fitting (> 0.96) with respect to 2- or 3-component fitting (< 0.95). Especially in 3-component fitting, we have set the peak position at around 1390, 1510, and 1610 cm^{-1} according to the three evident broad band observed in Raman spectrum. However, residue is obviously seen around the wavenumber of 1560 cm^{-1} (appendix 2). For this reason, we have added one another peak at about 1560 cm^{-1}, thus leading to our 4-component fitting.

The 4-component fitting can be accomplished manually or automatically by our home-made software. We usually fit the individual spectrum manually. As illustrated in Fig. 4.9 (a), the black and magenta curves show the raw and fitting data, respectively. Four Gaussian peaks are exhibited in red, green, yellow and brown and refer to peak 1-4 respectively. Table. 4.1 show fitting results of this example spectrum in terms of the position (ω), full-width half maximum (FWHM) and the integrated areas of each peak (A). The Gaussian peaks are centered at 1392, 1509, 1565 and 1619 cm^{-1}, respectively. We notice that our four peaks are up shifted compared to works of Fromm *et al.* and Kruskopf *et al.* using same laser wavelength of 532 nm [144,167]. The intensity shown in figure and integrated areas shown in table 4.1 have been normalized by the intensity area of G-peak in HOPG reference measured in the same condition in order to normalize the difference between measurement conditions (e.g. laser power, acquisition time or experimental environment). Obviously, our BL spectrum could be fitted by 4 Gaussian functions with a high accuracy, evidenced by quasi-zero residue (blue curve in Fig. 4.9 (a)). In the case of automatic fitting, constraints of parameter should be appropriately chosen. Due to the lack of physical interpretation of each peak, we could only roughly set the constraints for fitting parameters with a relatively large range during the

automatic fitting of whole Raman map. For example, the four peak positions were set at 1390 ± 20 cm^{-1}, 1510 ± 20 cm^{-1}, 1560 ± 20 cm^{-1} and 1610 ± 20 cm^{-1}, respectively. Nevertheless, the obtained fitting results generally show a relative high R-square value (> 0.96).

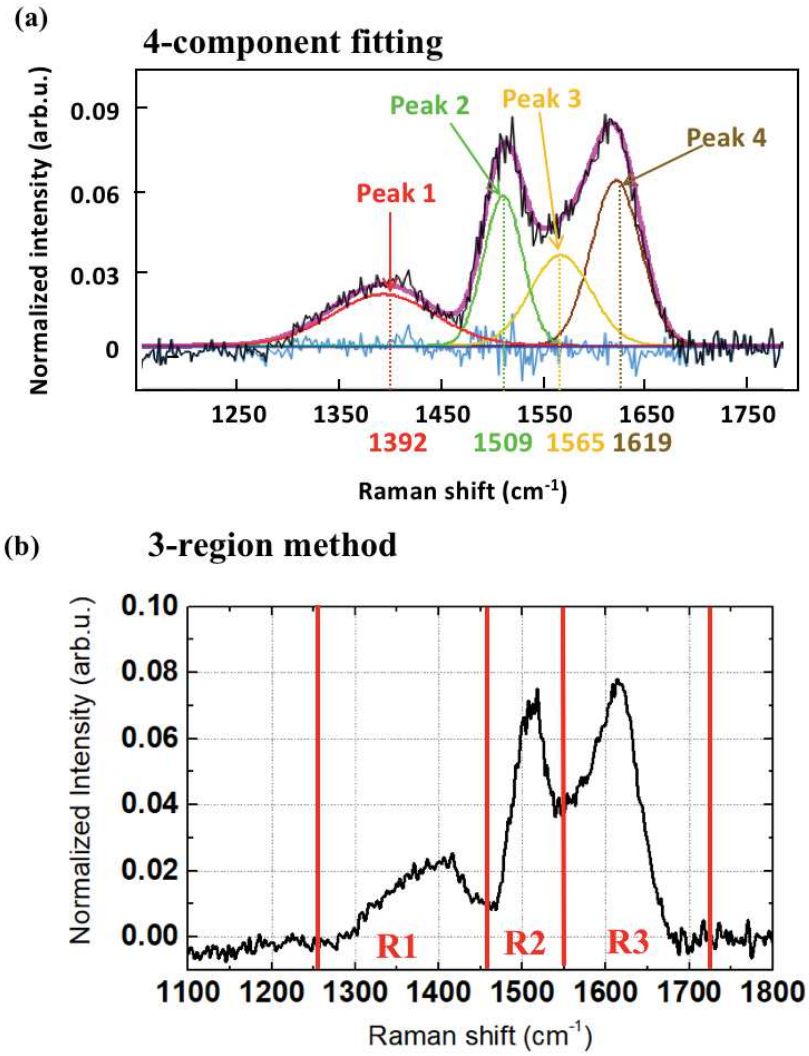

Fig. 4.9 Two methods of Raman analyses. (a) 4-component fitting and (b) 3-region method, in frequency region ranged from 1260 to 1710 cm^{-1} of BL spectra.

Table. 4.1 Fitting results of spectrum shown in Fig. 4.9 by using 4-componenet fitting. The peak 1-4 indicate the used four Gaussian functions. In each cell, three values correspond to the peak position (cm^{-1}), FHWH (cm^{-1}) and percentage of normalized integrate areas (by HOPG reference).

4-component	**Peak 1** $(\omega, FWHM, A\times 100/A_{G-HOPG})$	**Peak 2** $(\omega, FWHM, A\times 100/A_{G-HOPG})$	**Peak 3** $(\omega, FWHM, A\times 100/A_{G-HOPG})$	**Peak 4** $(\omega, FWHM, A\times 100/A_{G-HOPG})$
spectrum	1392, 120, 2.0	1509, 44, 2.2	1565, 70, 2.1	1619, 56, 3.1

Table. 4.2 The analysis result of 3-region method analysis of spectrum in Fig. 4.9. In each cell, integrated intensity has been calculated for corresponding frequency region (normalized by HOPG reference).

3-region	**R1** $(\mathbf{A\times 100/A_{G-HOPG}})$	**R2** $(\mathbf{A\times 100/A_{G-HOPG}})$	**R3** $(\mathbf{A\times 100/A_{G-HOPG}})$
spectrum	2.4	3.9	5.8

For the efficient analysis, we will also use a 3-region method as an alternative way to investigate our BL. Taking the same example as the one shown in Fig. 4.9 (a), we straightforwardly divide the BL contribution in the frequency region between 1260 cm^{-1} and 1710 cm^{-1} into three parts (Fig. 4.9 (b)): i) 1260 to 1460 cm^{-1}; ii) 1460 to 1550 cm^{-1}; iii) 1550 to 1710 cm^{-1}, denoted as R1, R2 and R3. This division is based on three broad bands situated at about 1390, 1510 and 1610 cm^{-1}. We emphasize that each region represents the totality of contributed Raman mode. Then the integrated areas of each region of this spectrum are calculated and the results are shown in table 4.2. At the moment, we do not remove the baseline here. As the consequence, the results of total integrated areas in 3-region method are generally different with respect to that of 4-component fitting. Nevertheless, for each of these two independent analysis methods, we always follow the identical protocol for all the studied samples.

4.3 Inhomogeneity of buffer layer Raman signature

We then examine BL samples by using our two analysis methods presented in **section 4.2**. In Fig. 4.8, we have already a first impression of the inhomogeneity of Raman signature of BL. Here, we further examine this characteristic of BL. First, Fig. 4.10 (a) shows the Raman A_{2D} map of a direct growth BL sample (denoted as DG1, zone A) without graphene transfer experiment. Based on the previous analyses, we identify that graphene ribbons are shown in green/yellow areas while the navy-blue contrasts represent the BL_0. By comparing with the corresponding optical image (not shown) of this area, we found that graphene ribbons are located close to step edges and there is only BL_0 grown on the terraces. We now denote the terrace at left and right side as terrace 1 and terrace 2, respectively. Fig. 4.10 (b) illustrates the average spectra of these two terraces. Comparing these two spectra, we found that their general lineshape are similar. However, the difference between these two average spectra collected from two neighboring terraces is obvious. The divergences between them mainly refer to the relative intensity (or integrated area) of each peak, as evidenced by 4-component fitting results in table. 4.3. For example, the $A/A_{G\text{-}HOPG}$ value of each peak 1, peak 3 and peak 4 of spectrum terrace 2 are both more intense compared with that of terrace 1. The opposite result is found for peak 2. In 3-region method (table. 4.4), we found A_{R1} and A_{R3} of terrace 2 are higher than that of terrace 1 while A_{R2} show the opposite result.

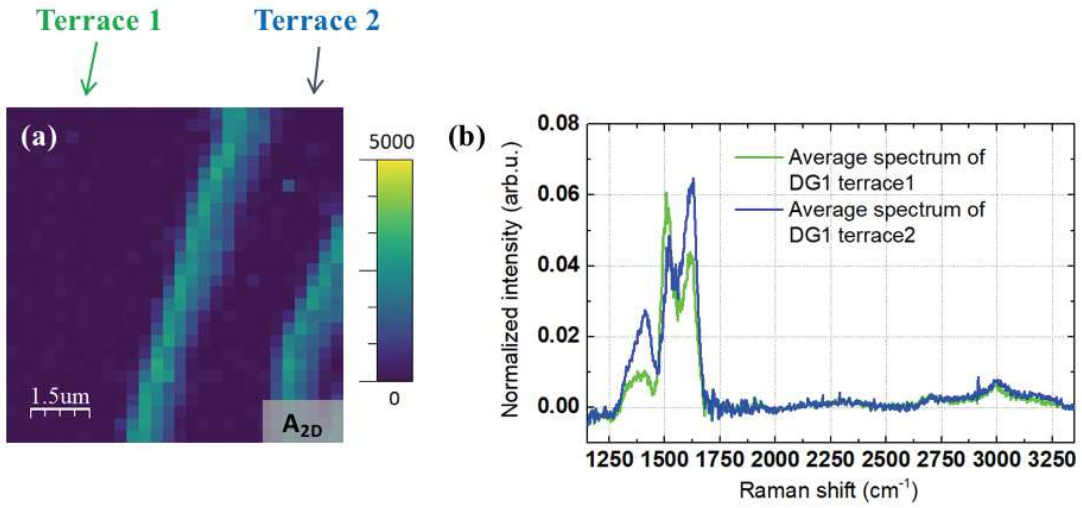

Fig. 4.10 Raman analysis of graphene stripes sample DG1, unit in counts s^{-1} cm^{-1}. (a) Raman A_{2D} map. Navy-blue areas represent the BL on the terraces (1 on left and 2 on right) while the monolayer of graphene is shown in green/yellow contrast. (b) Average spectra of terrace 1 and 2 are shown in green and blue spectra, respectively.

Table. 4.3 4-component fitting results of two average spectra shown in Fig. 4.10 (b). The peak 1-4 indicate the used four Gaussian functions. In each cell, three values correspond to the peak position (cm^{-1}), FHWH (cm^{-1}) and percentage of normalized integrate areas (by HOPG reference).

4-component	**Peak 1** **(ω, FWHM, A× $100/A_{G-HOPG}$)**	**Peak 2** **(ω, FWHM, A× $100/A_{G-HOPG}$)**	**Peak 3** **(ω, FWHM, A× $100/A_{G-HOPG}$)**	**Peak 4** **(ω, FWHM, A× $100/A_{G-HOPG}$)**
terrace1	1387, 127, 1.6	1506, 47, 2.6	1553, 58, 1.6	1619, 63, 2.8
terrace2	1400, 127, 3.5	1514, 44, 1.6	1565, 68, 2.5	1622, 56, 3.6

Table. 4.4 3-region method analysis of two average spectra in Fig. 4.10 (b). In each cell, integrated intensity has been calculated for corresponding frequency region (normalized by HOPG reference).

3-regions	**R1** **(A×100/ A_{G-HOPG})**	**R2** **(A×100/ A_{G-HOPG})**	**R3** **(A×100/ A_{G-HOPG})**	**Total** **(A×100/ A_{G-HOPG})**
terrace1	0.89	3.0	3.2	7.09
terrace2	2.4	2.4	4.7	9.5

Considering there is not yet explicit physical assignment for each fitted peak, we now rather continue the analysis by 3-region method for the efficiency of analysis. Inspired by the observation of two average spectra in Fig. 4.10 (b), now we plot the relationship between A_{R1} and A_{R3} of all the BL spectra in this Raman map (Fig. 4.10 (a)). The results are shown in green and blue open circles in Fig 4.11 (a). Interestingly, the spectra of terrace 1 (green open circles) are mainly dropped into the left side while the spectra of terrace 2 (blue open circles) fall into right side. In other words, the spectrum from terrace 2 possesses a higher A_{R1} and A_{3R} in comparison with terrace 1. This is consistent with our previous result obtained from two average spectra. This observation could indicate the inhomogeneity in Raman signature of BL dependent on sample topology. Indeed, due to the step bunching process, the surface energy of each terrace could be different. Thus, during the graphitization, different stages of graphene formation could give rise to the variety of BL characteristic. Strupinski *et al.* have reported a lower contribution of sp^2 hybridization (1%) at step edges against terraces (10%) [163]. They related the lower sp^2 hybridization to a higher G-peak position. Furthermore, we

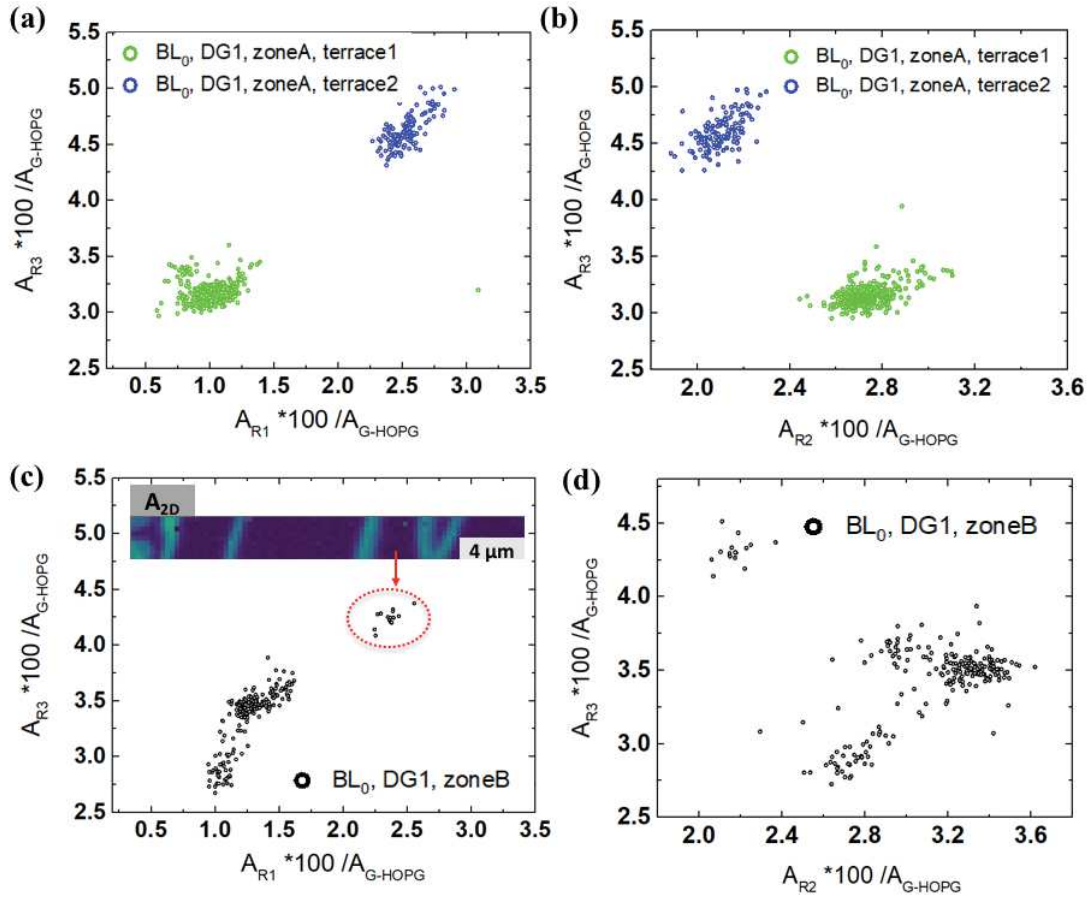

Fig. 4.11 (a and b) 3-region method analyses of BL_0 sample DG1, zone A. (a) Relationship between A_{R3} and A_{R1} (b) between A_{R2} and A_{R3} of all the spectra in Raman map shown in Fig. 4.9 (a). (c and d) 3-region method analyses of BL_0 sample DG1, zone B. (c) Relationship between A_{R3} and A_{R1} (d) between A_{R3} and A_{R2} of all the spectra in Raman map shown in inset of Fig. 4.11 (c). The inset of Fig. 4.9 (c) show a Raman A_{2D} map collected from the sample DG1, zone B, unit in counts s^{-1}. cm^{-1}.

highlight that the A_{R1} and A_{R3} value of spectra acquired from same terrace seems quite comparable, revealed by relative narrow variation range of these two terms. For example, the $A_{R1}/A_{G\text{-}HOPG}$ value of terrace 1 is about 1 ± 0.5% and about 2.7 ± 0.5% for terrace 2. On the other hand, the relationship between A_{R2} and A_{R3} show a negative correlation dependent on sample topology, as shown in Fig. 4.11 (b).

Then, to confirm these observations, we have studied another zone of this sample (DG1, zone B). The inset image of Fig. 4.11 (c) demonstrates the Raman A_{2D} map of this zone. Likewise, the navy-blue and green/yellow contrast represent the BL and graphene, respectively. Comparing with optical image (not shown), we note that there are several terraces in this area. The black open circles in Fig. 4.11 (c) represent the relationship between A_{R1} and A_{R3} of spectra collected from this area. As we see, a great number of data possess similar results with that of terrace 1 of zone A (low A_{R1} and low A_{R3}) while only few data are comparable to that of terrace 2 of zone A (high A_{R1} and high A_{R3}). We then found that the latter belongs to one single terrace (indicated by red arrow and circle in Fig. 4.11 (c)). This implies the topology effect on the BL characteristics which support our previous observation. On the other hand, the plot of A_{R2} as a function of A_{R3} show more dispersed data (Fig. 4.11 (d)) which is inconsistent with the previous results of zone A.

Next, to further elucidate the dependence between A_{R1}, A_{R2}, and A_{R3}, more samples have been studied (Fig. 4.12). The results of three other direct growth BL_0 samples (named as DG2, DG3 and DG4) are shown in light blue, light yellow and magenta open circles, respectively. Both A_{R1} and A_{R3} value of each sample is relatively homogeneous, evidenced by a narrow range of distribution in plotted data. We remark that these four BL_0 samples were produced by different annealing temperature (varied from 1640 to 1750°C). Thus, no clear temperature dependence is observed here and more detailed discussion of the temperature effect will be presented in **section 4.4**. Besides these BL_0 samples, we have also studied the uncovered BL_{1lG} samples obtained by graphene exfoliation experiments. Except for the data in orange squares which are for sample (TG1), achieved by Ni layer deposition transfer method the data in dark yellow, purple, olive, red, and dark red are the results of the samples (TG2) obtained by glue layer deposition transfer method. As we see, A_{R1} and A_{R3} show a positive linear correlation in these uncovered BL_{1lG} samples which indicates that the mentioned topology effect is not the only factor that alter the BL signature. For example, the olive rectangle represents the data collected from one area of $3\ \mu m \times 3\ \mu m$ (zone A4). We have compared the Raman map with optical image and found that there are no visible steps more than 1 nm in this studied area. Thus, we believe another factor different from the step-terrace effect could be responsible for the linear correlation between A_{R1} and A_{R3}. One supposition is related to our graphene exfoliation experiment in which the BL could be altered considering a large linear relationship is only present in uncovered BL_{1LG}. For example, the bonding between buffer layer and substrate might be affected during our experiments. Nevertheless, we cannot rule out the topology effect in the case of

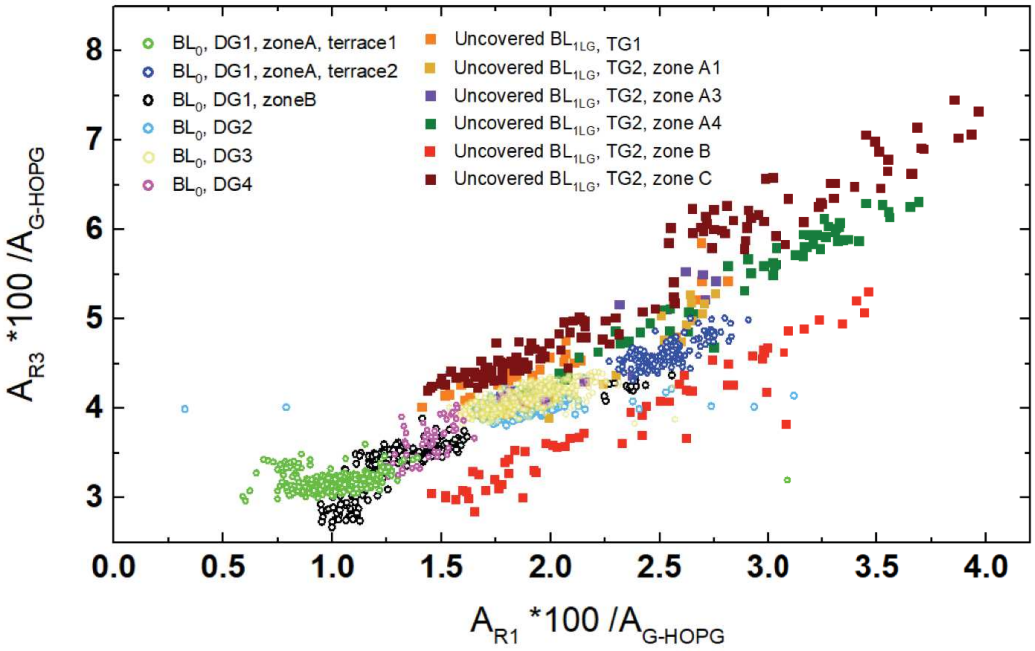

Fig. 4.12 Relationship between A_{R1} and A_{R3} of all the studied spectra. The open circles are data of BL_0 while solid squares are data of uncovered BL_{1LG}. Various colors represent the different studied zones: green and blue (sample DG1, zone A); black (sample DG1, zone B); light blue (DG2); light yellow (DG3); magenta (DG4); orange (sample TG1), yellow, purple, olive (sample TG2, zone A); red (sample TG2, zone B); dark red (TG2, zone C).

uncovered BL_{1LG} samples as well. Regarding the relationship between A_{R2}, and A_{R3} or A_{R2} and A_{R1}, we have plotted the results of all the studied samples (appendix 5). However, no clear relationship is obviously observed for this moment.

Hence, considering these two regions R1 and R3 are situated in the similar frequency region with D-peak and G-peak of graphene, their consistent behavior and relationship to graphene require more investigations. Nevertheless, the inhomogeneity of buffer layer has been highlighted by the analyses based on a large number of spectra. This variation of buffer layer might be related to the buffer layer structure or its doping characteristic. For example, one idea is to change the doping of BL_0 by ions projections realized by corona discharges. ARPES measurement will be combined to study the surface and electronic properties before and after the ion projection experiment.

4.4 Temperature dependence of buffer layer

In **chapter 3**, we have demonstrated the Raman signature of the samples synthesized at 1600°C and 1700°C for 300 s (Fig. 3.1 and 3.7, respectively). After comparing their Raman spectra with the literature, we have identified these two samples as buffer layer sample (now we reidentify 1600°C sample as BL-like sample) and a graphene ribbons sample with BL_0 on terraces, respectively. Indeed, the BLs of these two samples considerably differs in Raman signature. At that time, we attributed this difference to

crystallinities of carbon structure. Concerning the temperature effect on buffer layer, Kruskopf *et al.* have described a BL formation by the polymer-assisted sublimation growth [167]. The deposited polymer adsorbates have undergone several phases from amorphous carbon to nanocrystalline graphite until the final stage of the BL as a function of growth temperature ranging from 450°C to 1500°C. The temperature dependence of BL was clearly reported in their study by showing the corresponding Raman spectra. For example, the sample of 1400°C and 1500°C show different relative intensity of peaks at about 1500 and 1600 cm^{-1}. In this section, our objective is to investigate the BL samples synthesized under different growth temperature by Raman spectroscopy in order to shed some light on the temperature effect on the BL Raman signature. In addition, we have also reidentified the sample discussed in **section 3.1** (1600°C, 300 s) as a BL-like sample, based on the results of this study. Before this temperature study, we have identified that sample as true BL sample. However, the contrary results obtained here allow as to correct this misunderstanding as we will present in this section.

First, we consecutively produced BL_0 samples with an annealing temperature from 1720°C to 1600°C by using same wafer and other parameters are fixed (300 s, 0.33°C/s, 10 mbar). Fig. 4.13 compares these Raman spectra of BL_0 samples and all spectra generally show a similar lineshape. The 3-region analysis is shown in table. 4.5. The total integrated intensity in the frequency region from 1260 to 1710 cm^{-1} are quite similar for all the studied sample. The discrepancies, e.g. the difference in A_{R1} value, could not be related to the temperature effect but rather the inhomogeneity of buffer layer based on our discussion in last section. In our case, the variation in A_{R2} seems to

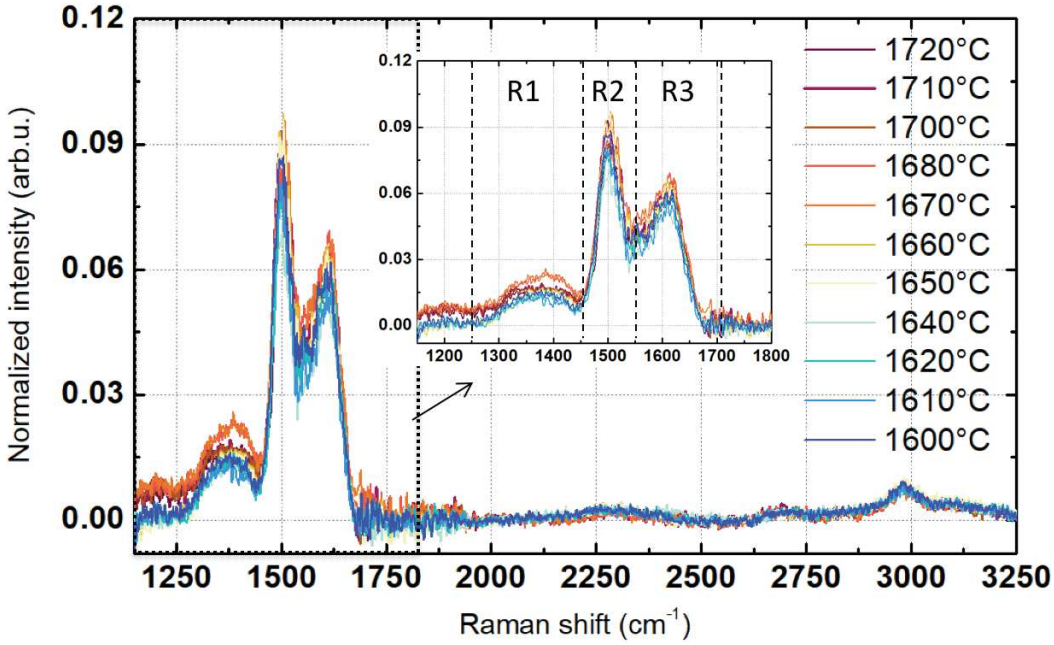

Fig. 4.13 Raman spectra of BL_0 produced at different annealing temperature ranged from 1600 up to 1720°C on wafer TK. Inset image show frequency region between 1150 to 1800 cm^{-1}. Dashed vertical lines in inset image separate different frequency region R1, R2 and R3.

Table. 4.5 3-region method analysis of all the spectra shown in Fig. 4.13, as a function of growth temperature. In each cell, integrated intensity has been calculated for corresponding frequency region (normalized by HOPG reference).

3-region	R1 ($A\times100/A_{G-HOPG}$)	R2 ($A\times100/A_{G-HOPG}$)	R3 ($A\times100/A_{G-HOPG}$)	Total ($A\times100/A_{G-HOPG}$)
1720°C	2.5	4.6	5.0	12.1
1710°C	2.7	5.3	5.2	13.2
1700°C	2.7	4.9	4.9	12.5
1680°C	3.4	5.1	5.7	14.2
1670°C	3.4	5.5	5.8	14.7
1660°C	2.2	5.2	5.0	12.4
1650°C	2.0	5.0	4.9	11.9
1640°C	1.7	4.0	4.1	9.1
1620°C	1.8	4.3	4.8	10.9
1610°C	1.7	4.5	4.3	10.5
1600°C	2.4	5.5	5.4	13.3
1600°C _W34	4.0	5.9	7.1	17.0

disagree with the study of Conrad *et al.* [186]. They have reported that the peak around 1490 cm^{-1} has firstly increased and then appears suppressed once monolayer begins as a function of growth temperature. For this reason, they attribute this peak to the BL associated feature. Here, we doubt the SiC subtraction method in their Raman analysis seeing negative value around the frequency region of 2000 cm^{-1}. Based on our own experiences, the Raman mode around wavenumber of 1500 cm^{-1} is sensitive to SiC subtraction method. One example of intentional bad subtraction who induce a negative value is demonstrated in appendix 2. Thus, we question their argument about temperature effect on Raman response of BL. As far as our knowledge, BL samples produced at a temperature above 1600°C show comparable Raman signature independent of growth temperature.

Then we notice that samples synthesized at 1600°C show different lineshape with the one presented in chapter 3 (Fig. 3.1). To facilitate the discussion, we replot the Raman spectrum of the sample presented in **section 3.1** in black spectrum of Fig. 4.14. This sample will be called as W34_s023 in the following. In fact, the lineshape of this black

spectrum which is dominated by two main peaks situated around 1333 cm^{-1} and 1578 $cm^{-1}$is resembling the that of the sample produced at 1300°C in the work of Kruskopf *et al.* [167]. In the literature, this lineshape of Raman spectrum has been observed and attributed to buffer layer [163,164]. The two main peaks have been referred to as D-like and G-like peak considering their peak positions. In addition, the similar Raman fingerprint has been reported for the disordered graphene in reference [187]. They have intentionally introduced the disorder into the graphene by the ion bombardment and control the disorder level by the different dose. By increasing the dose from 10^{11} Ar^{+}/cm^2 to 10^{15} Ar^{+}/cm^2, they have observed the boost of D-peak and the broaden of G-peak. The Raman spectrum of the sample with a 10^{14} Ar^{+}/cm^2 dose is quite comparable with our black spectrum of W34_s023 sample and they describe their Raman spectrum as a carbon layer consisting of graphitic clusters with a significant portion of sp^3 hybridization.

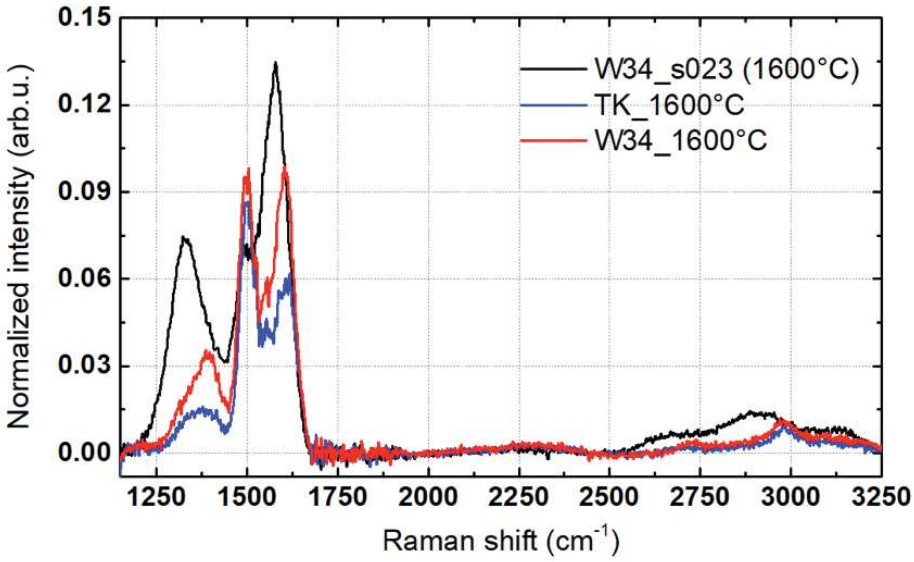

Fig. 4.14 Three BL_0 samples produced with an annealing temperature of 1600 °C on two wafers W34 (red) and TK (blue) and BL-like sample presented in chapter 3 (black).

The recently grown sample (denoted as TK_1600°C) by using the same growth parameters with W34_s023 is shown in blue spectrum in Fig. 4.14. We could easily notice the difference in spectrum lineshape between blue and black spectra. Considering these two samples were grown on different wafers, we have produced another sample (denoted as W34_1600°C) using the same wafer with W34_s023 and its Raman spectrum is shown in red curve in Fig. 4.14. Both of these wafers are 4H-SiC of Tanke blue but independent polishing processes have been performed. As we see, the red spectrum is largely different with black spectrum even though the same growth parameters and SiC wafer were used in these two samples. In fact, the red spectrum is more comparable to the blue spectrum. For example, the Raman integrated intensity of frequency region between 1200 and 1800 cm^{-1} as well as a group of broad bumps from 2400 to 3000 cm^{-1} could differ the black spectrum from the other two spectra. It is a

strong evidence of the existence of distorted sixfold rings [188] in sample W34_023. On the other hand, the blue spectrum and red spectrum could be well superposed at high frequency region while the black spectrum possesses a larger Raman intensity. Furthermore, Raman spectra of these two recent samples (red and blue spectra) are comparable with that of sample produced at a relatively higher temperature (>1400°C) in the work of Kruskopf *et al.* [167]. We stress that the sample W34_s023 was produced before the optimization growth work, therefore it is not totally surprising that it is not reproducible. Thus, considering the carbon bonding and disorder influence on the shape of the Raman spectra, we believe a large disorder present in our W34_s023 sample produced at 1600°C. We rather attributed the sample with the Raman signature similar with that of W34_s023 to a largely disordered carbon structure or a BL-like carbon structure. The other two recently produced samples are attributed to BL samples. This conclusion is contrary to the work of [163,164] based on the large number of spectra acquired in this work.

Hence, as we argued, no detectable temperature dependence is observed in our BL_0 samples produced at a temperature ranged from 1600°C to 1720°C by Raman spectroscopy. In addition, since the W34_s023 e sample is not reproducible and almost all the other direct growth buffer layer samples show different lineshape, we attribute this sample as BL-like sample. We stress again that even though we had misunderstood this sample at the beginning of this growth work, there is a minor influence on the further optimization of growth as we shown in **chapter 3**.

4.5 Excitation laser wavelength dependence of buffer layer Raman response

As we know, the phonon dispersion relation in graphene can be revealed in Raman experiment by changing the excitation laser energy [134]. The behavior of each peak (i.e. D-peak, G-peak or 2D-peak) as a function of laser energy differ due to the different responsible phonon mode for each peak. For example, Cançado *et al.* have reported that A_D and A_{2D} shown no laser wavelength dependence while A_G was found to be dispersed with the laser energy [134]. To shed some light on the physical origin of Raman signature of BL, the excitation wavelength dependent measurements have been probed on the uncovered BL_{1LG} samples as follows. In the current study, three laser wavelengths have been used: 457 nm (2.7 eV), 532 nm (2.33 eV), 633 nm (1.96 eV). Firstly, by analyzing the Raman A_{2D} map recorded with a laser wavelength of 532 nm, we first identify the graphene and BL areas on a sample after the graphene transfer experiment (Fig. 4.15 (a)). Then, we collected the individual spectra by using different laser energies in the uncovered BL_{1LG} areas. All the acquired spectra using these three laser energies were normalized by their corresponding HOPG reference collected in the same experimental condition. Two samples have been studied. We found the results obtained from these two samples are not totally consistent with each other. Thus, we only discuss the common observations of these two samples which could be possibly related to laser energy effect. The results of one of these samples are shown as follows and the results of another sample will be shown in appendix 5. Uncovered BL_{1LG} spectra were compared in Fig. 4.15 (b) as well as analyzed by 3-region method (table. 4.6) and

fitted by 4-component fitting (table. 4.7). We remark that the studied spectra were not acquired at the exact same position for each laser wavelength due to the difficulty of repositioning the exact location for the individual spectra measurement. Therefore, we should take the inhomogeneity of BL into consideration during the comparison, especially the Raman intensities, based on the previous analyses. The blue, green and red spectra in Fig 4.15 (b) represent the spectra acquired at the position closed to red circle on in Fig 4.15 (a) by using excitation laser wavelength of 457 nm, 532 nm and 633 nm, respectively. Comparing these collected spectra by three laser energies, we found that these spectra possess similar lineshape in general. Shown by 3-region analysis results, the total integrated intensities of the BL contribution collected at laser wavelength of 457 nm and 633 nm are comparable (table. 4.6) which is different with that of 532 nm. In this case, we could basically rule out the laser energy effect on the total integrated intensity of Raman spectrum while other factor (e.g. inhomogeneity) should be responsible for the relatively high value of 532 nm.

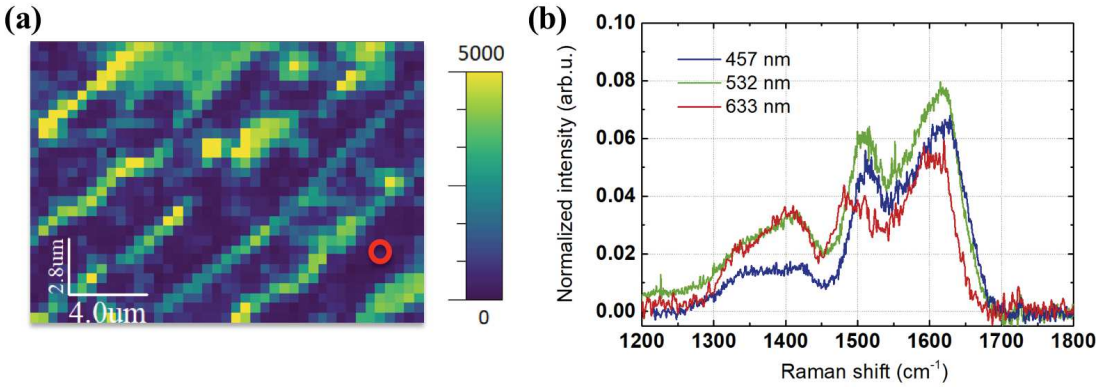

Fig. 4.15 (a) A Raman A_{2D} map (532 nm) of one studied sample in which we identify the BL and graphene areas, unit in counts s^{-1} cm^{-1}. (b) Blue, green and red spectra were collected by laser wavelength of 457 nm (blue curve), green curve (532 nm) and 633 nm (red curve) close to the position of red circle in (a) of uncovered BL_{1LG} sample, respectively.

Table. 4.6 3-region method analysis of all the spectra shown in Fig. 4.15 (b). In each cell, integrated intensity has been calculated for corresponding frequency region (normalized by HOPG reference).

3-region	R1 ($A\times100/A_{G-HOPG}$)	R2 ($A\times100/A_{G-HOPG}$)	R3 ($A\times100/A_{G-HOPG}$)	Total ($A\times100/A_{G-HOPG}$)
BL_{1LG} 457 nm	2.1	3.1	6.0	11.2
BL_{1LG} 532 nm	4.4	4.1	6.6	15.1
BL_{1LG} 632 nm	4.1	3.0	4.3	11.3

Regarding the results of 4-component fitting (table. 4.7), the position shift in peak 1 has already been seen in previous analyses. For example, the peak 1 of two average spectra shown in Fig. 4.10 has been fitted and the results are demonstrated in table. 4.3. The shift in peak1 could be as large as 13 cm^{-1} between those two spectra. Thus, the discrepancy in peak1 of these three spectra here could not be totally related to dispersion with laser energy. On the contrary, an obvious position shift in peak 2 and 4 has been noticed which is absent from earlier results. More precisely, the peak2 and peak4 of red curve downshifted about 15 cm^{-1} and 13 cm^{-1} to lower frequency, respectively, compared to that of blue curve. The dispersion of this peak with laser energies could be responsible for this large shift. Cançado *et al.* have reported a G-peak position dispersion in disordered carbons. They observed an increase in G-peak position as the excitation wavelength decreases which is in an agreement with the behavior of our peak 2 and peak 4 [134]. However, the explicit relationship between peak 2 and peak 4 and to the G-peak in graphene is still under investigation. It is important to emphasize again that these four peaks in 4-component fitting represent a combination of Raman modes of each frequency area. Thus, the shift of the peak could be related to the intensity or position variation of one or several Raman modes. We remark this shift has been observed in another studied sample as demonstrated in Fig. A5.2 in appendix 5. Nevertheless, our observation here is in contrast with the work of Fromm *et al.* [144] in which the authors have reported the constant frequency of each peak independent on laser energy at different laser wavelength as well (532 nm, 514 nm, 476 nm).

Table. 4.7 4-component fitting results of all spectra shown in Fig. 4.15 (b). The peak 1-4 indicate the used four Gaussian functions. In each cell, three values correspond to the peak position (cm^{-1}), FHWH (cm^{-1}) and percentage of normalized integrate areas (by HOPG reference).

4-component	**Peak 1 (ω, FWHM, A× $100/A_{G-HOPG}$)**	**Peak 2 (ω, FWHM, A× $100/A_{G-HOPG}$)**	**Peak 3 (ω, FWHM, A× $100/A_{G-HOPG}$)**	**Peak 4 (ω, FWHM, A× $100/A_{G-HOPG}$)**
BL_{1LG} 457 nm	1387, 150, 2.6	1509, 45, 2.0	1565, 66, 2.6	1624, 63, 4.1
BL_{1LG} 532 nm	1394, 155, 4.6	1506, 42, 1.9	1565, 78, 3.7	1620, 61, 4.0
BL_{1LG} 632 nm	1392, 120, 3.8	1494, 52, 1.7	1562, 68, 2.2	1611, 54, 2.6

4.6 Interfacial buffer layer with or without graphene layer covering

Until now, we have exhibited the varied Raman fingerprint of BL dependent on the surface topology and other factors. Besides, the graphene coverage seems to alter the Raman signature of BL as well which has been poorly investigated in the literature [85,114,164,183]. For example, Tiberj *et al.* have found the BL signature chute in intensity after graphene grown above [164]. Inspired by this work, we believe that the investigation of graphene coverage effect on the BL might evidence the coupling between 1LG and BL. Based on the previous discussion, we should distinguish the BL_0

with BL_{1LG} in terms of growth condition. Moreover, we found that even though the samples were produced by using the same growth parameters, the present BL could possess different Raman signatures. Thus, our idea is to compare the exact same BL flake with and without monolayer graphene above. We consider the variation of BL by other factors (temperature, sample topology, etc.) could be maximally suppressed in this way which means the only considerable difference could be narrowed down to the coverage of graphene. To reach this, we have performed the graphene transfer experiment presented in **section 4.1** on our 1LG samples in order to have access to the uncovered BL_{1LG}. We expect this comparison study could shed some light on this peculiar interface of graphene/SiC.

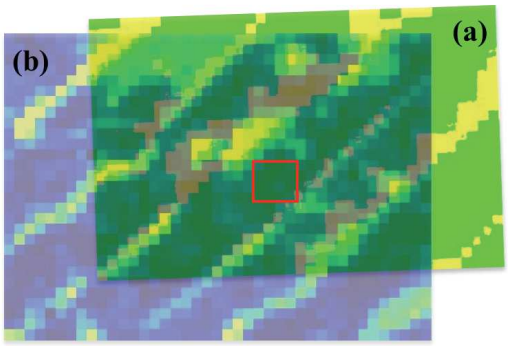

Fig. 4.16 Two superposed 2D maps collected before (a) and after (b) the graphene transfer, respectively. The red square underlines the studied zone where we have removed the 1LG by thin epoxy-based glue layer.

The analysis process is as follows. We firstly choose a zone by comparing two recorded A_{2D} maps, i.e. before and after the graphene transfer experiment. For instance, Fig. 4.15 demonstrates two superposed Raman A_{2D} maps before (Fig. 4.16 (a)) and after (Fig. 4.16 (b)) the graphene transfer process. Based on the previous analyses, we recognize the green contrast areas in map before transfer experiment corresponds to the 1LG with BL underneath while the navy-blue contrast areas in map after transfer experiment represent the uncovered BL. Thus, the studied zone is outlined by a red square in which we had exfoliated monolayer graphene. During this selection process, the number of graphene layers before graphene transfer has been determined by fitting both the G-peak of graphene and BL contributions. This is aiming to avoid an over-estimation of G-peak because the G-peak region is overlapped by BL signature. The integrated intensity of G-peak corresponds to that of monolayer graphene ($A_{G\text{-}graphene}/A_{G\text{-}HOPG}$~0.03). We calculated average spectra of this studied zone in two Raman maps, as shown by green and navy-blue spectra in Fig. 4.17. Then we further subtracted the contribution of G-peak from the spectrum obtained before transfer experiment (green spectrum) and the residual is shown in orange spectrum in Fig. 4.17. This orange spectrum supposed to represent only the BL contribution without considering the graphene contribution (denoted as covered $BL_{1LGminusG}$) in the frequency range between 1200 cm^{-1} and 1800 cm^{-1} of epitaxial graphene. After all, we can compare the uncovered

BL_{1LG} spectrum (after transfer) with the covered $BL_{1LGminusG}$ spectrum (before transfer). We emphasize that several samples have been produced and studied. In the following, we only illustrate the results of two representative samples obtained by both Ni and glue layer deposition methods but the discussion and conclusion are based on the results of all the studied samples.

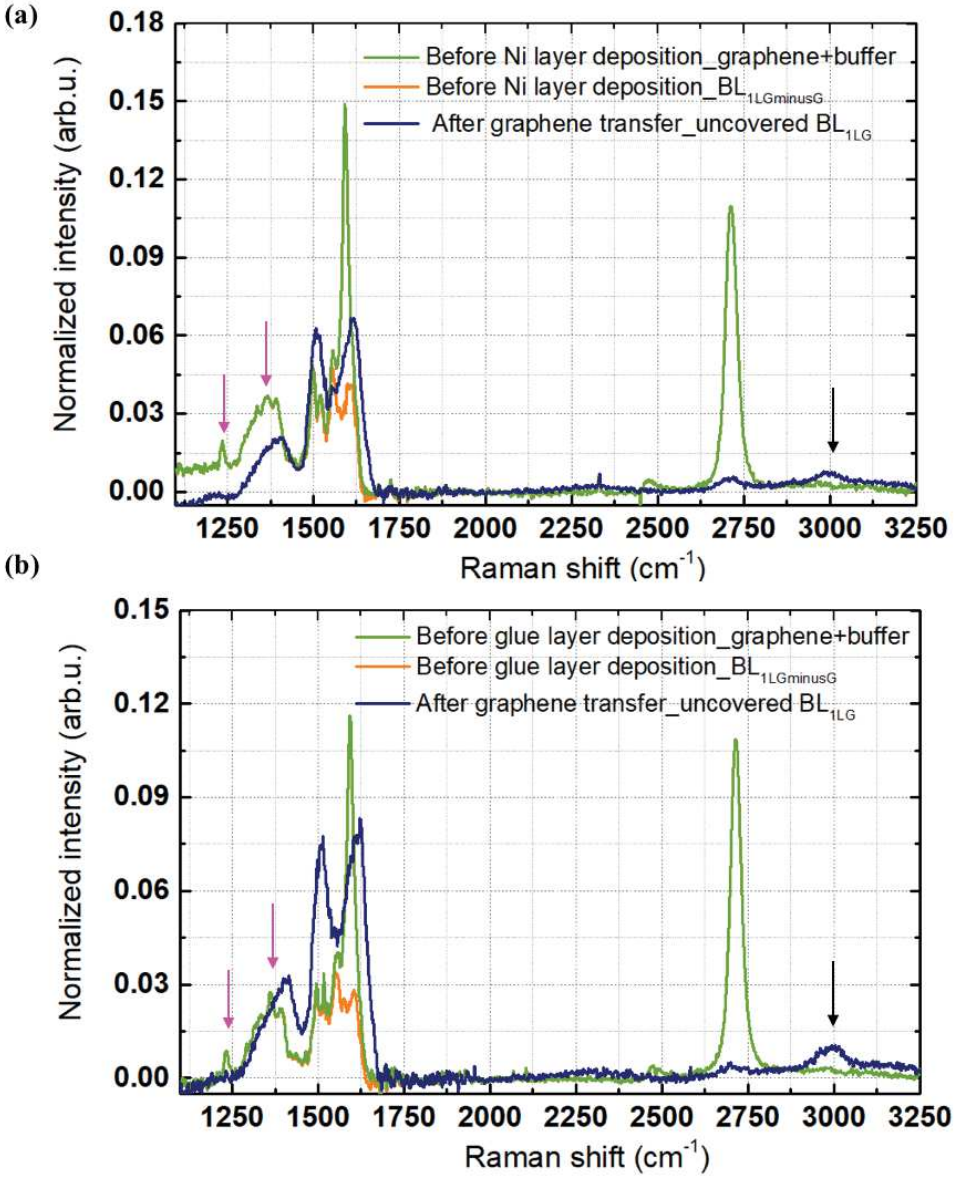

Fig. 4.17 The comparison of uncovered BL_{1LG} (navy-blue), the corresponding 1LG+BL (green) and $BL_{1LGminusG}$ (orange) spectra of samples in which we performed a (a) Ni layer deposition or (b) glue layer deposition methods to mechanically remove the graphene. The magenta arrows point the two fine peaks situated at about 1235 cm^{-1} and 1360 cm^{-1}. The black arrow indicates the broad peak around 3000 cm^{-1}

Fig. 4.17 (a) and (b) show the results of two representative samples in which we have performed the Ni layer and a glue layer deposition experiments to obtain the uncovered BL_{1LG}, respectively. In Fig. 4.18, we show a comparison between the covered

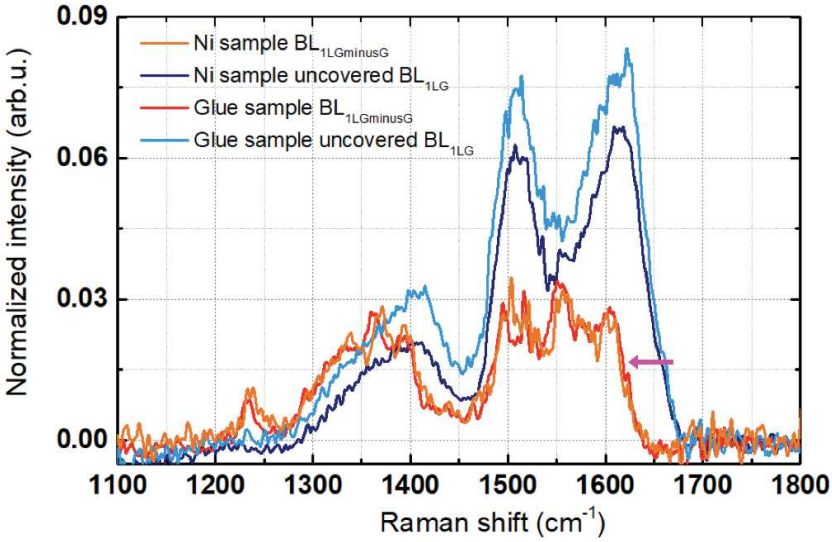

Fig. 4.18 Representative $BL_{1LGminusG}$ spectrum spectra in frequency region between 1200 cm^{-1} and 1800 cm^{-1} collected before Ni (orange) or glue (red) layer deposition. Representative uncovered BL_0 obtained by Ni layer or glue layer deposition methods, shown in navy-blue and light blue, respectively. The magenta arrow indicates the peak 4 shift.

$BL_{1LGminusG}$ spectrum (red and orange) with the uncovered BL_{1LG} (navy-blue and light-blue). The fitting results of each spectrum using 4-component fitting and the analyses of 3-region method are detailed in the table. 4.8 and table. 4.9, respectively.

Based on the results, we can highlight several observations by comparing these two kinds of BL spectra of all the studied samples as follows.

i) We remark two fine peaks at the wavenumbers of about 1235 cm^{-1} and 1360 cm^{-1} observed in the covered BL_{1LG} spectra, indicated by magenta arrows in Fig. 4.17. We notice that these two peaks are commonly shown in almost all the 1LG spectrum with the presence of BL_{1LG} but absent in uncovered BL_{1LG} and BL_0 as well as the transferred graphene. Kruskopf *et al.* have observed the similar peaks at about 1230 cm^{-1} and 1350 cm^{-1} and they attributed them to the vibrational density of states of the BL and the D-peak related peak, respectively [167]. Unlike their analyses, we rather attribute these two peaks to the interaction of BL and 1LG, because of their absence in uncovered BL_{1LG} or the transferred graphene. For example, the peak of 1350 cm^{-1} disappear in the spectra of our transferred graphene even it was present in epitaxial graphene before transfer, therefore it is hard to relate it to the D-peak of graphene. However, the physical assignment of these two peaks is still under discussion since barely no Raman mode of graphene or SiC is reported active around these wavenumbers except the D-peak of graphene. Nevertheless, the identification of these two new peaks is important because of their peculiar position making difficult to pinpoint the D-peak.

ii) We highlight a low broad peak in uncovered BL_{1LG} at the wavenumber of about 3000 cm^{-1}, as marked by black arrows in Fig. 4. 17 (a) and (b). This peak seems absent in our epitaxial graphene spectrum (green spectra). Its peak position is close to the D+D'

peak of graphene (~ 2900 cm^{-1}) which is a disorder-related mode. Moreover, this peak is also present in all the BL_0 spectra, e.g. Fig. 4.13. Thus, we attribute it to BL characteristic.

iii) The integrated intensity of BL contribution between 1200 cm^{-1} and 1800 cm^{-1} generally decreases after the coverage of monolayer graphene. At first glance of Fig. 4.18, the orange and red spectra ($BL_{1LGminusG}$) seems to possess a lower signal in this frequency region compared with that of light blue and navy-blue spectrum (uncovered BL_{1LG}). This integrated intensity between 1200 cm^{-1} and 1800 cm^{-1} has been estimated by both 4-component fitting and 3-region method as seen in last column of table 4.8 and 4.9, respectively. For example, in 4-component fitting analysis (table 4.8), this value has decreased to 56% (= 6.3/11.2) of its initial value after graphene coverage in glue deposition sample while decreased to 66% (= 6.1/9.3) of its initial value in Ni deposition sample. Except for this studied zone, all the other studied zones indicated a decrease in Raman integrated area of BL after graphene coverage. Most of the BL samples decrease its Raman signal to 50% and 70% of their initial values after graphene coverage, estimated by 4-component fitting. In 3-region analysis, this decreased value is between 42 and 73% for all the studied samples. In spite of this discrepancy between these two analysis results, the decrease of Raman integrated intensity of BL after graphene coverage is consistently seen. This result is observed in all the studied samples and agrees with the early study of Tiberj *et al.* [164] in which they observed a BL intensity decrease after graphene coverage. However, they reported a signal decrease by a ratio of 3 after the graphene growth which is larger than our results. One possibility of this evolution in intensity would be the surface flatness change after the growth of graphene layer, which indicates a strain effect between graphene and BL [114,146]. It has been reported that the vertical corrugation of BL gets smaller after graphene growth.

Table. 4.8 4-component fitting results of all spectra shown in Fig. 4.18. The peak 1-4 indicate the used four Gaussian functions. In each cell, three values correspond to the peak position (cm^{-1}), FHWH (cm^{-1}) and percentage of normalized integrate areas (by HOPG reference). The total integrated intensities of four peaks (normalized) is shown in last column.

4-component	Peak 1 (ω, FWHM, A× $100/A_{G-HOPG}$)	Peak 2 (ω, FWHM, A× $100/A_{G-HOPG}$)	Peak 3 (ω, FWHM, A× $100/A_{G-HOPG}$)	Peak 4 (ω, FWHM, A× $100/A_{G-HOPG}$)	Total (A×100 $/A_{G-HOPG}$
Uncovered BL_{1LG} (Ni)	1391, 115, 2.1	1508, 45, 2.3	1560, 47, 1.4	1615, 59, 3.5	9.3
$BL_{1LGminusG}$ (Ni)	1364, 105, 2.7	1510, 58, 1.6	1564, 33, 0.9	1603, 35, 0.9	6.1
Uncovered BL_{1LG} (Glue)	1395, 124, 3.1	1510, 49, 2.5	1563, 49, 1.3	1617, 63, 4.3	11.2
$BL_{1LGminusG}$ (Glue)	1363, 110, 2.8	1507, 45, 1.4	1563, 44, 1.4	1607, 30, 0.7	6.3

Table. 4.9 3-region method analyses of all the spectra shown in Fig. 4.18. In each cell, integrated intensity has been calculated for corresponding frequency region (normalized by HOPG reference).

3-region	R1 ($A\times100/A_{G-HOPG}$)	R2 ($A\times100/A_{G-HOPG}$)	R3 ($A\times100/A_{G-HOPG}$)	Total ($A\times100/A_{G-HOPG}$)
Uncovered BL_{1LG} (Ni)	2.1	3.5	5.2	11.8
$BL_{1LGminusG}$ (Ni)	2.7	1.7	1.7	6.4
Uncovered BL_{1LG} (Glue)	3.4	4.6	6.4	14.4
$BL_{1LGminusG}$ (Glue)	2.7	1.7	1.7	6.4

iv) We found peak position shifts between the uncovered BL_{1LG} an covered $BL_{1LGminusG}$ samples indicated by magenta arrow in Fig. 4.18. Based on the 4-component fitting results in table 4.8, we remark a considerable down-shift of peak 4 in $BL_{1LGminusG}$ with respect to that of uncovered BL_{1LG}, i.e. more than 8 cm^{-1}. Even though the variation of peak 4 has been highlighted in previous sections, no such shift has been noticed. For example, in Fig. 4.8, we have compared the uncovered BL_{1LG} with BL_0 to reveal the inhomogeneity of BL. However, the shift in peak 4 is not visible seeing a good overlap of these spectra at wavenumber from 1650 to 1700 cm^{-1} (right-tail of the peak 4). In this case, we attribute this down-shift in peak 4 of uncovered BL_{1LG} compared with that of the $BL_{1LGminusG}$ samples to the graphene coverage effect. In the literature, the position shift is commonly related to doping or strain effect [135,139]. Schumann *et al.* have attributed the compressive strain in 1LG to the presence of interfacial BL [181]. They have measured the BL_0 possesses a larger lattice (2.467 Å) compared to BL_{1LG} (2.463 Å) which means the BL suffers a compressive strain after graphene growth. Their result is contrary to our results because our down-shift in frequency after the graphene coverage corresponds to the relaxation of compressive strain or tensile stress [86,139]. Another possible explanation of this down-shift is related to the doping effect on buffer layer. An investigation of the doping effect on Raman signature of BL is ongoing at this moment.

Considering the graphene coverage is the most remarkable difference between covered BL_{1LG} and uncovered BL_{1LG}, we attribute these mentioned evolutions i, iii and iv to the coupling between BL and graphene while the observation ii is related to the BL characteristic. We believe our results could provide a direct evidence of this coupling between graphene and BL. However, the missing knowledge of phonon mode of BL is the main obstacle for a further understanding of the revealed BL evolution while the current results are truly motivating for the further studies on the BL by this method.

4.7 Summary

Three types of buffer layer have been investigated by Raman spectroscopy in this chapter: i) bare buffer layer BL_0 obtained directly by growth; ii) interfacial buffer layer lying BL_{1LG} between graphene and SiC substrate; and iii) uncovered interfacial buffer layer, uncovered BL_{1LG}. The last one is achieved by two graphene transfer techniques in which we can mechanically remove the graphene and leave behind the uncovered BL. We highlight the reproducibility and robustness of these graphene transfer experiments, allowing the investigation of uncovered interfacial BL_{1LG}. The different types of BL have been probed by Raman spectroscopy, aiming to better understand its characteristics. 4-component fitting and 3-region method have been used to analyze the BL contribution in Raman spectra. Due to the incomplete knowledge on the BL band structure and its phonon modes, we stress that each peak or frequency region represents the combination of Raman modes in their regions. In the literature, the Raman signature of BL has been largely reported by several groups and discrepancies of results, e.g. lineshape of spectrum, could be noticed. However, until now, no statistical study on buffer layer has been done to further reveal these discrepancies. Considering the week signal of BL in Raman measurement, this is indeed a time-consuming research work. In this case, we highlight our investigation by the number of studied BL samples (more than 20 samples) and Raman spectra (more than 15,000 spectra). Based on all the measurement and analysis, we remark the inhomogeneous Raman response dependent on the sample topology, growth condition, graphene coverage and some unknown factors. There are several observations that worth mentioning as follows:

Firstly, both BL_0 and uncovered BL_{1LG} has been studied to reveal the inhomogeneity of buffer layer. The integrated intensity of two peaks situated close to the D- and G-mode (~ 1390 cm^{-1} and 1610 cm^{-1}) of graphene clearly show a correlation in uncovered BL_{1LG} samples. On the other hand, the bare BL_0 samples obtained by direct growth show relatively homogeneous Raman signature on one single terrace. Thus, the variation of Raman signal in these two types of BL samples has been highlighted.

Then, we found the temperature effect on Raman spectra of BL_0 seems to be negligible for the samples produced at temperature ranged from 1600°C to 1720°C. This disagreed with the works of Kruskopf *et al.* [167] and Conrad *et al.* [186] in which they found the temperature indeed has an effect on the lineshape of BL Raman spectra.

Later, the excitation laser energy dependent Raman experiment seems to suggest the comparable behavior of peaks around 1610 cm^{-1} to the G-peak in graphene. The peak position shift at wavenumber of 1500 cm^{-1} depending on laser energy has been revealed as well. However, we stress the difficulty of reposition during the individual spectrum collection. For this reason, laser energy dependent Raman maps will be required.

Lastly, we compare the Raman fingerprint of the exact same BL flake with and without monolayer graphene above. The results revealed that the BL contribution in Raman spectrum decreases after the graphene growth evidenced by Raman integrated intensity at frequency region between 1200 to 1800 cm^{-1}. Furthermore, two fine peaks situated at ~1235 and 1360 cm^{-1} are present in epitaxial monolayer spectrum while absent in that of BL and transferred graphene, which might be related to the interface. We believe this is a direct evidence of coupling between graphene and BL. In the meantime, the peak around 1610 cm^{-1} would undergo a down-shift (> 8 cm^{-1}) after graphene coverage. These evolutions could be plausibly explained by change in BL between these two conditions, e.g. doping effect. Moreover, we highlight a low peak at Raman shift about 3000 cm^{-1} which has been generally seen in BL_0 and uncovered BL_{1LG} Raman spectra. We attributed this peak to the buffer layer characteristic.

Hence, considering the great BL influence on graphene, we believe our systematic study of buffer layer could contribute valuable results to the understanding of graphene/SiC interface.

Chapter 5 Study and tuning the electrical properties of graphene on SiC (0001)

In **chapter 3**, we have presented a monolayer graphene growth process by sublimation at low Ar pressure and main characteristics of these 1LG samples. Regarding electrical properties, we have briefly shown the results obtained from Hall effect measurements in van der Pauw configuration under various experimental conditions (magnetic field, temperature). The quantum Hall effect (QHE) observed in high magnetic field at low temperature has confirmed the presence of 1LG, therefore validating our growth process. Besides, one unusual characteristic of our sample is the low residual p-type doping (few 10^{10} cm^{-2} to 10^{11} cm^{-2} at 1.7 K) measured in low magnetic field. As we mentioned, the epitaxial graphene grown on SiC (0001) is generally reported to be n-type doped (~ 10^{13} cm^{-2}) in the literature due to the presence of buffer layer (BL) [54]. In our case, we attribute our unusual low p-type doping characteristic to the unintended charge impurities deposited on the sample surface. We have understood the low residual doping as the results of the compensation between the external atmospheric doping effect and the intrinsic doping effect induced by substrate. In this chapter, more results and evidence will be provided to support this argument. In **section 5.1**, the inhomogeneous doping characteristic induced by the charged impurities on our 1LG sample surface will be further studied by an analytical model. This model calculation assumes the existence of the electron-hole puddles, thus two charge carriers are active and the doping disorder could be estimated by a temperature-dependent Hall transport measurement. In **section 5.2**, we will show that the n-type doping can be restored by vacuum treatment. The local STM/STS measurement and Hall effect measurement in Van der Pauw configuration is carried out under vacuum condition consistently indicated a n-type doping. After exposure to the air, interestingly, a transition from n-type to p-type doping with the time evolution strongly evidence the charged impurities effect on our sample surface. In **section 5.3**, the Hall effect measurement will be performed on $6\ mm \times 6\ mm$ sample and on microscale Hall bar devices under ultra violet (UV) illumination. An inversion of doping type is also observed under UV illumination. We believe that the sample surface could be 'cleaned' by the UV light. All these obtained results are consistent and support our argument of atmospheric doping. A summary of this chapter and perspectives will be presented in **section 5.4**.

5.1 Transport in two charge carrier system: electron-hole puddles

A low p-type concentration is generally shown in our grown 1LG films. This residual hole concentration measured at low temperature (1.7 K) is about a few 10^{10} cm^{-2} up to few 10^{11} cm^{-2}. We have attributed this doping characteristic to the atmospheric effects, such as oxygen, water etc. [177]. In fact, the charged adsorbates unintendedly deposited on the graphene surface or between the graphene and substrate could induce a local chemical potential variation and thus lead to a shift of the local Fermi level (E_F). As a result, the graphene surface is inhomogeneously doped with the presence of large fluctuating potentials (V(**r**)) and the system splits into hole-rich and electron-rich puddles at the charge neutrality point (CNP), as schematically demonstrated in Fig. 5.1 (a). Indeed, the local electronic potential fluctuates randomly about its average value across the surface of the graphene sheet. By assuming that the value of the potential at any given point follows a Gaussian distribution, the large spatial fluctuation in E_F can be characterized by parameter $s = V_{rms}$ (the root-mean square fluctuation or the standard deviation in V(**r**) about the average potential). Indeed, the deposited adsorbates and topographical ripples in graphene layer are the two main causes of the electron-hole puddles. The existence of puddles has been evidenced by STM mapping of the

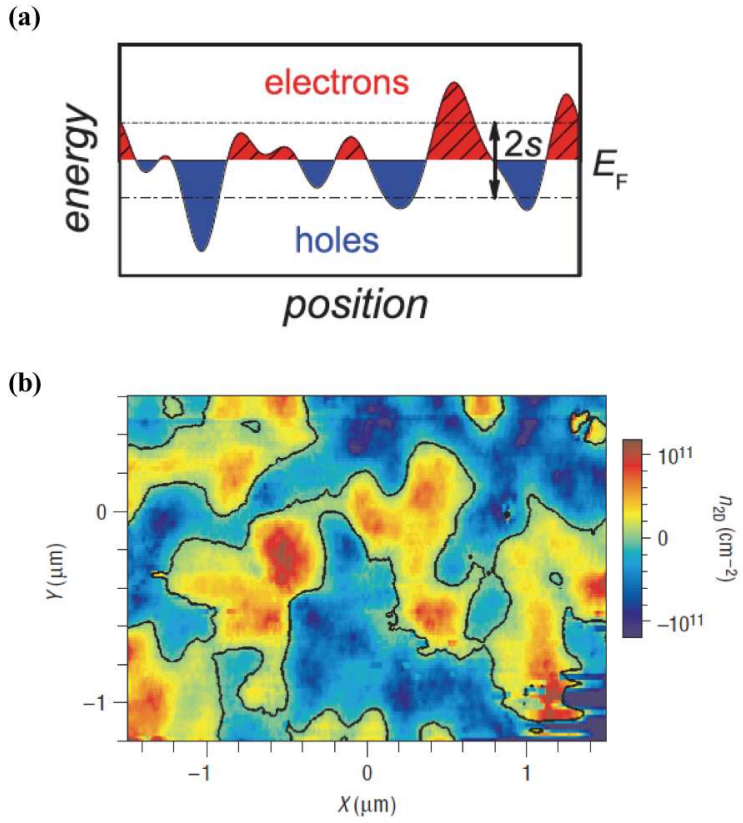

Fig. 5.1 (a) Sketch of the random potential fluctuations in the sample yielding a broadened effective density of states. Red and blue bumps represent the puddles and s is the amplitude of potential fluctuations. Adapted from reference [192]. (b) Color map of the spatial density variations in graphene flakes when the average carrier density is zero. The blue regions correspond to holes and the red regions to electrons. The black contour marks the zero-density contour. [190].

transferred graphene on Si/SiO_2 [189,190] in which the local Dirac point map was spatially pictured. In Fig. 5.1 (b), the color map clearly indicates the spatial density variation zero average carrier density showing the landscape of charge puddles, i.e. blue regions for holes and red regions for electrons. Indeed, with the presence of electron-hole puddles, at finite temperatures and at not too high densities, both electrons and holes would contribute to the conductivity. Consequently, the classical Drude model which considerate only one type of charge carrier is failed to estimate the true density of electrons and holes. Thus, an analytical model based on the theory calculation of Li *et al.* [191] has been proposed in our group to adapt our case. The detail of this model is presented in [180]. Here, we take advantage of this model to estimate the amplitude of potential fluctuations in our 1LG samples. This estimation has been done by fitting the temperature-dependent effective carrier density obtained by Hall effect measurement.

The charged impurities could be located near the graphene, creating a local electrostatic potential. The potential fluctuations are assumed to be described by a statistical distribution function $P(V)$, where $V(\boldsymbol{r})$ is the fluctuating potential energy at the point $\boldsymbol{r} \equiv (x, y)$ in the graphene plane. Thus, $P(V)dV$ is the probability of finding the local electronic potential within a range dV, supposed to have a Gaussian form:

$$P(V) = \frac{1}{\sqrt{2\pi s^2}} exp(-\frac{V^2}{2s^2}), \tag{5.1}$$

where s is the standard deviation of the disorder or the strength of potential fluctuation. Indeed, both the amplitude and the sign of the term $V - E_F$ determine the characteristics of the puddles, i.e., a negative (positive) indicates an electron (hole) region. Due to the electron-hole symmetry in the problem, we only provide the equations for the electronlike carriers and the hole part can be obtained by changing E to -E.

We then model the electron density of states (DOS) in 1LG with the presence of electron-hole puddles by:

$$D_e = D_1 \int_{-\infty}^{E} (E - V) P(V) dV, \tag{5.2}$$

where $D_1 = g_s g_v / 2\pi(\hbar v_F)^2$, g_s, g_v are the spin and valley degeneracies respectively, v_F is the Fermi velocity.

Combining equation 5.1 and 5.2, we obtain the analytical formula of the electron density as following:

$$\begin{aligned} D_e(E) &= \int_{-\infty}^{E} \frac{g_s g_v\,(E - V)}{2\pi(\hbar v_F)^2} p\,(V) dV \\ &= D_1 \left[\frac{E}{2} erfc\,\left(-\frac{E}{\sqrt{2}s}\right) + \frac{s}{\sqrt{2}s} exp\,(-\frac{E^2}{2s^2}) \right], \end{aligned} \tag{5.3}$$

where $erfc\ (x)$ is the error function:

$$erfc\ (x) = \frac{2}{\sqrt{\pi}} \int_x^{\infty} e^{-t^2} dt, \tag{5.4}$$

A similar equation can be used for the hole density of states D_h. Based on the calculation of density of states, the carrier density can be estimated taking account of two charge carriers, i.e. the electrons (n_e) and holes (n_h). In Fig. 5.2, we show the normalized DOS as a function of energy. Obviously, in the case of $s = 0$ (homogenous doping), the density of states is $D_e(E) = D_1 E$. The orange and blue curves represent the system without potential fluctuation. Thus, at $E_F = 0$ and $T = 0$, there is no carrier density.

When the charged impurities present ($s \neq 0$), the density of states at CNP is non-zero, as demonstrated in yellow and purple curves in Fig. 5.2. Based on the equation 5.3, the density of electrons and holes are $D_e\ (E) = D_h\ (E) = D_1 s/\sqrt{2\pi}$ at $E = 0$ and close to $D_1 E$ at high-energy. As plotted in in Fig. 5.2, the coexistence of electrons and holes around Fermi level leads to an effective DOS around the CNP.

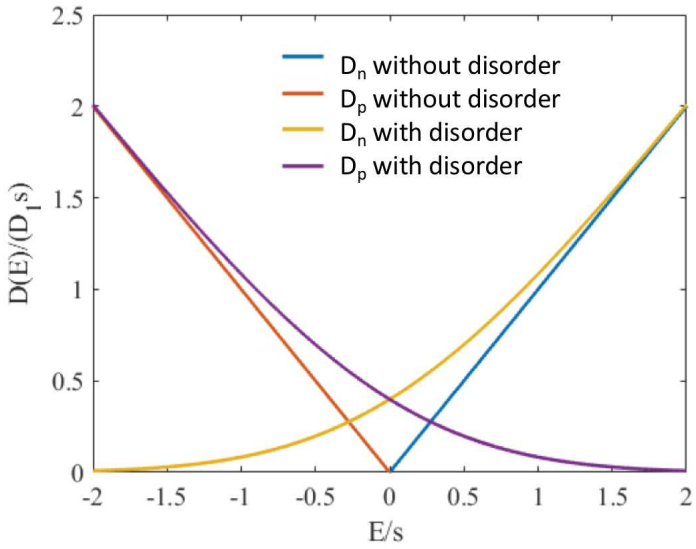

Fig. 5.2 Normalized density of states for both electron and holes in graphene. The orange and blue curves are for the DOS in homogeneous system $s = 0$ while the yellow and purple curves are the DOS in inhomogeneous system $s \neq 0$.

In 1LG, the temperature dependence of density of electrons can be calculated by:

$$n_e = \int_{-\infty}^{\infty} D_e(E) f_e(E)\, dE, \tag{5.5}$$

where $f_e = \frac{1}{1+e^{\beta(E-\mu_{ch})}}$ is the Fermi distribution, $\beta = 1/k_B T$ with k_B the Boltzmann constant and μ_{ch} the chemical potential. The density of hole can be calculated by the same equation.

In the case of epitaxial graphene, a finite doping is usually found. Thus, in the following, we only discuss the case of $E_F \neq 0$. For a given disorder and a Fermi energy E_F, it is reported that the excited electron density increases quartically rather than quadratically at low temperature while at high temperature the quadratic relationship is obtained [191]. Thus, the charge density depends on both temperature and disorder, s.

The presence of electron-hole puddles does not induce any additional charge in the 1LG system, thus, we assume a temperature independent charge concentration $n_e - n_h$. Then the finite-temperature chemical potential μ_{ch}(T) changes as a function of both temperature and the strength of potential fluctuation s with the relationship:

$$n\,(T=0) = \int_{-\infty}^{E_F} D_e(E) f_e(E)\,dE - \int_{E_F}^{\infty} D_h(E) f_h(E)\,dE \tag{5.6}$$

Based on the Drude model of two types of charges, we numerically recalculate the thermally activated Hall concentration:

$$n_{Hall}(T) = \frac{(n_e\mu_e + n_h\mu_h)^2}{(n_e{\mu_e}^2 - n_h{\mu_h}^2)} \tag{5.7}$$

where $n_{e(h)}$ and $\mu_{e(h)}$ are the electron (hole) concentration and mobility respectively. We remark that the measured Hall concentration n_{Hall} depend on mobility and density of electrons and holes. Thus, the measured value could not represent the real density of states in the samples. Nevertheless, the measured $n_{Hall}(T)$ as a function of 3 parameters: s, E_F and the mobility ratio μ_e/μ_h can be used to estimate the potential fluctuation in sample.

Fig. 5.3 illustrates the temperature dependence of carrier density in our 1LG samples S37, S45 and S50. This strong dependence indicates a thermally activated carrier concentration above T = 100 K, where electrons and holes must be present. We take advantage of the proximity of the Fermi level with the charge neutrality in our 1LG samples, aiming to estimate the sample disorder by the adapted model. The results of the fit for three 1LG samples is reported in Fig. 5.3. The obtained average value of the disorder is $s = 27 \pm 9$ meV, with E_F ranging from -4 to -5.5 meV and $\mu_e/\mu_h \simeq 1$. The disorder amplitudes are close to those reported in [179] for graphene on SiC (10 – 30 meV). With respect to references [179,192] in which their model are established for the case of $E_F = 0$, the inclusion of E_F as an additional parameter enhances largely the quality of the fits.

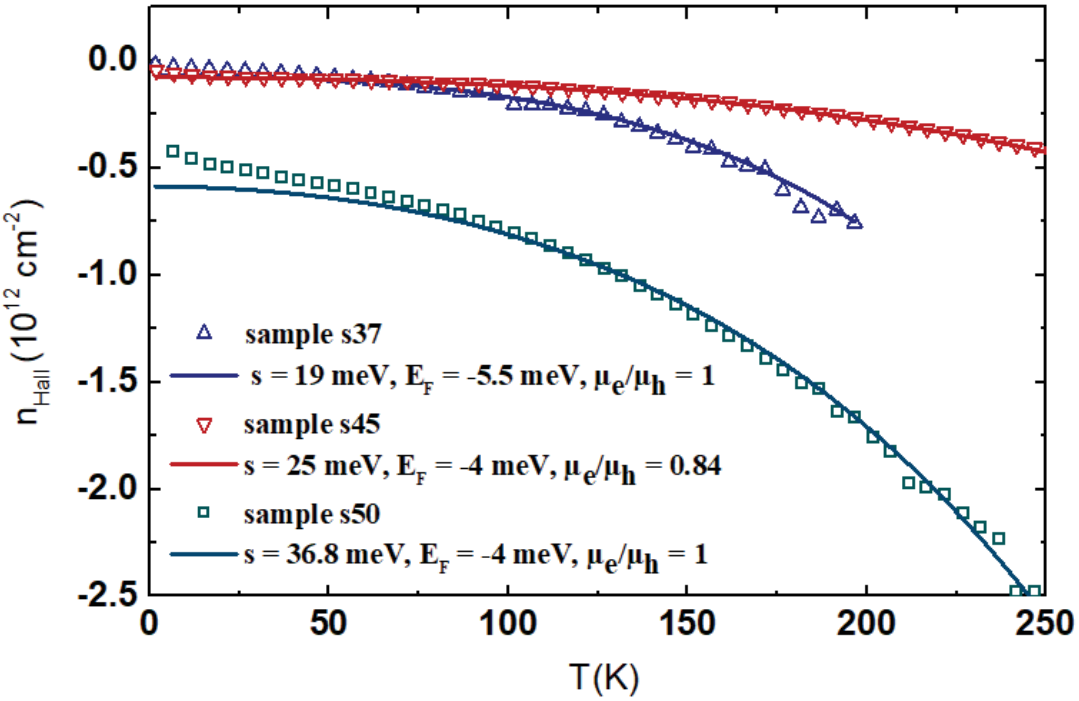

Fig. 5.3 Temperature dependence of the Hall concentration for three 1LG samples. S37, S45 and S50. The experimental data are shown in dashed color lines while fit data are in solid lines. The disorder potential s, the Fermi level E_F and the mobility ratio μ_e/μ_h are extracted from the fitting.

Therefore, we have estimated the doping disorder of our graphene film by an analytical model calculation. The well fitted experimental data has strengthened our assumption of the existence of two charge carrier system in our samples. In the literature, the epitaxial graphene is usually reported as a n-doped system. Contrarily, the activation of two charge carrier in our case could be induced by the adsorbates on graphene surface. Thus, the relatively low residual hole doping could be reasonably explained by the atmospheric doping effect on graphene films. More experimental evidence will be completed in the following sections. Nevertheless, the low doping achieved after the air exposure is still puzzling because of this nearly perfect compensation. The precise

doping mechanism and direct evidence of the existence of electron-hole puddles still remain to be clarified and requires more efforts.

5.2 Transport measurement in vacuum

Until now, all the transport measurements were carried out under air ambient or helium environment without a precise control of the sample surrounding condition. We argue that the inhomogeneous doping (electron-hole puddles) induced by charged impurities could be responsible for the low p-type doping observed in our samples. Since we attributed our unique doping characteristic to the atmospheric effect, we wonder if a simple pumping of sample surrounding environment could alter the doping of epitaxial graphene by the desorption of the adsorbates. In the reference [193]. Pallecchi *et al.* [193] have studied an original low n-type doped (9×10^{11}) oxygen-adsorbed epitaxial graphene. After a vacuum annealing, they found the doping level shift to a higher doping of 10^{13} cm^{-2} which is the typical value for the epitaxial graphene [54]. They attribute this change in doping level to the desorption of oxygen molecules during the vacuum treatment. In this section, two transport experiments have been done in vacuum condition: STM/STS measurement and Hall effect measurement in Van der Pauw configuration.

5.2.1 Scanning tunneling microscopy and spectroscopy measurement

STM/STS measurements have been done on 1LG samples under vacuum at low temperature of 200 mK by our collaborative laboratory, Institut Néel (Grenoble, France). The sample was produced by using our optimized growth process for 1LG (1750°C, 300 s, 10 mbar). The atomic structure of our 1LG samples has been demonstrated in **chapter 3** (Fig. 3.17). In Fig. 3.18, the K and K'- points disks of Dirac cone have been revealed in two dimensional Fourier transformed (FT) pattern measured at fixed bias voltage, as replotted in Fig. 5.4 (a). In this section, the conductance has been measured at different bias voltage for the studied zone and the corresponding rings at K and K'-points have been extracted in FT patterns, as illustrated in Fig. 5.4 (b). The diameter of these rings is equal to $4k_F$ (Fermi wave vector) which allows a calculation of Fermi velocity. By measuring the average radial of these rings, the dispersion relation E (k) has been evaluated (Fig. 5.4 (c)). The linear fit yields to an estimation of the Dirac energy which is about -393 meV in this study. More details of the fundamental and model to evidence the quasiparticle dispersion of graphene in the vicinity of the Fermi level is presented in reference [194]. Here, we only focus on the most important result extracted from this analysis which is the estimation of Dirac point situated at -393 meV. This n-type doping is in contrary with our earlier results of Hall effect measurement in which we highlight the low p-type doping characteristic. However, considering the different experimental conditions, the discrepancy between these two results can be understood by the desorption of deposited charged impurities in vacuum condition. We believe that the pumping process before the measurement could evacuate the gas surrounding sample surface, therefore there is a great chance that the oxygen and water

deposited on the sample surface could be desorbed during the vacuum treatment. Consequently, the 'clean' epitaxial graphene samples were achieved in this STM experiment. We highlight that this measurement providing the characteristic of the intrinsic properties of our graphene films which is also a supplementary technique to our transport measurement (**section 5.2.2**).

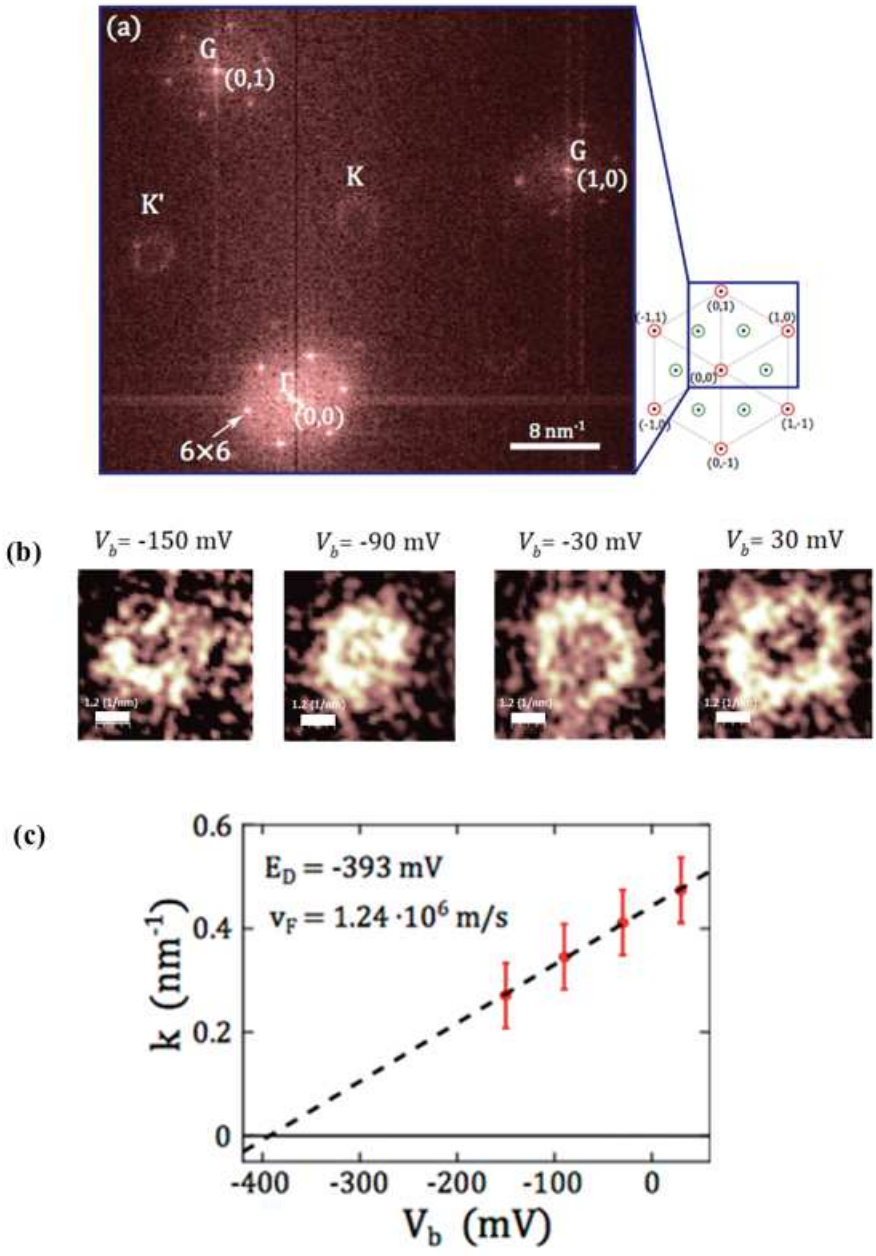

Fig. 5.4 (a) STS-FT image of 1LG sample at fixed bias voltage. (b) Sample-bias dependence of rings at K points in the FT-LDOS maps. The scale bar is 1.2 (1/nm). (c) Dispersion relation extracted from the radial average of the rings shown in (a).

5.2.2 Hall effect measurement

Hall effect measurement has been performed at liquid helium temperature under vacuum on the same sample studied by STM in **section 5.2.1**. STM measurement is a local probing technique while the Hall effect measurement has been done on entire sample surface which provides the global transport properties of our samples. Before putting the sample into cryostat system, the sample has been measured in air ambient. The p-type carrier concentration about 2.6×10^{12} cm^{-2} and resistivity about 4800 Ω are obtained. Then, the sample was loaded into the sample chamber. The chamber has been evacuated overnight until a pressure of 10^{-6} mbar. Later, the sample has been inserted into the cryostat system and the Hall effect measurements have been performed in magnetic field under vacuum condition. We measured firstly at a temperature of 176 K. We have obtained a n-type doping of 2.6×10^{12} cm^{-2} and a dropped resistivity of 2100 Ω. Next, after the system has been cooled down to 1.7 K, a n-type doping of 2.3×10^{12} cm^{-2} and a resistivity of 1800 Ω were measured. To facilitate the comparison, the experimental process and the results have been summarized in table 5.1. In addition, the Hall resistance has been measured as a function of magnetic field (B), as shown in Fig. 5.5. Considering the configuration of the setup and the slope of Hall resistance, we have determined the doping characteristic in this experiment as n-type doping which is consistent with the results obtained in low magnetic field measurement. However, QHE was absent in this measurement due to the relatively high concentration (few 10^{12} cm^{-2}) and a maximum magnetic field applied equal to 13 T.

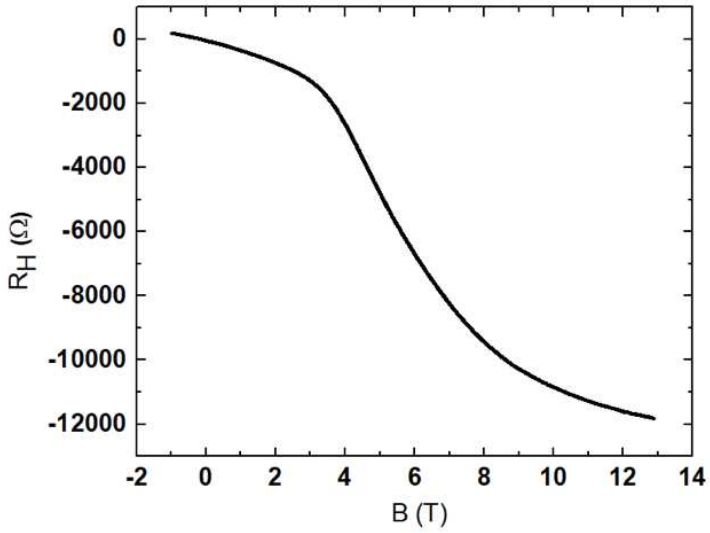

Fig. 5.5 Hall resistance as a function of magnetic field at liquid helium temperature under vacuum condition.

Regarding the doping type, we highlight the n-type doping measured under vacuum condition compared to the low p-type observed in helium or air environment in early magneto-transport measurements in **chapter 3**. Besides, the results collected at 176 K have already shown the n-type doping which could rule out the temperature effect on the doping type in some respects. We remark that no significant difference in electrical

properties was observed between these two temperatures of 176 K and 1.7 K. Especially, the carrier concentration remained nearly the same at these two temperatures. Compared to the large temperature dependent carrier density observed in early measurement (Fig. 5.3), this temperature independent feature might indicate the different scattering mechanisms of samples in air or vacuum which worth further investigations. Thus, the vacuum treatment indeed can alter the surface condition of the samples which is consistent with the results in STM measurement in **section 5.2.1** in which the similar vacuum condition has been used. Hence, we remark that the doping level could recover to the intrinsic values under vacuum treatment.

Table. 5.1 Experimental condition and Hall effect measurement results obtained on 1LG sample. The measurements have been done before (first row), under (second and third rows) and after vacuum treatment (last row).

T (K)	P	Resistivity (Ω)	Carrier density (cm^{-2})
300	Ambient	4800	p-type 10^{12}
176	Vacuum	2100	n-type ~10^{12}
1.7	Vacuum	1800	n-type ~10^{12}
300	Ambient	From 2800 to 3900	from n-type 10^{12} to p-type 10^{12}

Next, the subsequent Hall effect experiments after unloading the sample from cryostat were carried out in air ambient. After exposure to air, the Hall coefficient (K_H) and resistivity of the sample has been monitored with the evolution of time, as illustrated in Fig. 5.6. We note that the K_H is inversely proportional to carrier density ($n \propto 1/K_H$) in the case of high carrier density and the negative and positive sign indicate the n- and p-type doping, respectively (equation 2.4). However, when the electron-hole puddles present at charge neutrality point, the carrier concentration failed to be estimated by the equation 2.4 because only majority charge carrier has been taken into account in that equation [195]. In this case, we use K_H only to describe the doping type. At the beginning, the sample still showed a similar n-type doping (10^{12} cm^{-2}) compared to that measured in vacuum. Interestingly, the transition from n-type to p-type doping happened after ~17 hours exposure to the air. Then ~66 hours later, the sample finally stabilized at a p-type residual concentration of few 10^{12} cm^{-2}. This observation can be regarded as a direct evidence of atmospheric doping phenomenon which strongly strengthens our assumption. On the other hand, the resistivity returned back to its initial value more rapid than that of carrier density. We highlight a reversible doping mechanism of deposited impurities.

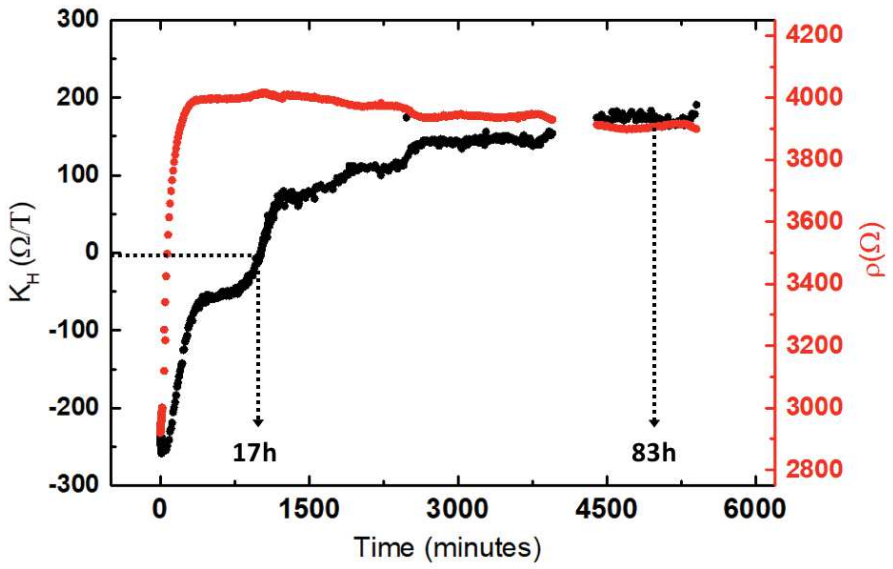

Fig. 5.6 Hall coefficient evolution as a function of time after exposure to air from vacuum condition. The measurement was performed at room temperature but without temperature control.

Hence, these two transport measurements employed under vacuum condition have revealed the n-type doping characteristic which is different with to our early observation of low p-type doping. We emphasize that the vacuum treatment indeed has an effect on surface condition of samples by 'cleaning' the deposited charge impurities. In this case, we have not only supported our argument of atmospheric doping effect, but also demonstrated the possibility of tuning the doping type in our 1LG samples. The inversion of doping type could be explained by the low doping level in our graphene films. It is worth mentioning that we have not heated the samples during the vacuum treatments. Contrarily, Pallecchi *et al.* have stressed the importance of annealing during the pumping to desorb oxygen adsorbates [193]. However, they attributed the difficulty of desorption of oxygen to a deposited PMMA layer on the sample surface.

5.3 Transport measurement under UV illumination

In the previous analysis, we highlight the sensibility of our 1LG samples to the atmosphere (ambient or vacuum) and the possibilities of controlling the doping characteristic. One another source which could modify the doping characteristic is the ultraviolet (UV) light [196–198]. To this purpose, we have first *ex-situ* examined the UV illumination effect on the doping characteristic of our graphene film by Hall effect measurement in Van der Pauw configuration. Before the UV treatment, a residual p-type Hall concentration has been measured. Then, the carrier density has been probed 5 minutes after the UV light exposure and the n-type doping has been observed. The doping level gradually changed back to p-type doping after the experiment. This result motivates us to develop an *in-situ* setup. To achieve this, we combine a Hall effect measurement equipment with a UV source (wavelength 335-385 nm, power intensity 10 mW cm^{-2}), allowing a monitor of electrical properties of our sample under the UV

illumination. The magnetic field is generated by a magnetic coil and the measurement is piloted by home-made program (P. Charlier, Master student). The tests of this experiment were performed on several graphene samples in which we search for the propitiated parameters in terms of UV source and transport measurement. For example, the circular current and the duration of the illumination are well set in order to avoid the heating of the sample. This experiment has been performed both on Van der Pauw device and on Hall bar device of our 1LG samples in Van der Pauw configurations. We emphasize that a test with light filters ensure that only the UV light (wavelength 335-385 nm in our case) has an effect on the electrical properties of our sample as shown in the following.

5.3.1 Van der Pauw device ($6\ mm \times 6\ mm$)

Before the UV treatment, the 1LG sample has been studied. Fig. 5.7 (a) exhibit the results of Hall resistance (R_H) and resistivity (ρ) as a function of magnetic field. The Hall coefficient (K_H) as well as the Hall concentration (p_{Hall} or n_{Hall} for p or n type residual carrier density) and the Hall mobility (μ) could be estimated as demonstrated in Fig. 5.7 (a). We note that the p-type residual Hall concentration about 10^{12} cm^{-2} and the resistivity about $\rho \sim 4000\ \Omega$ are measured.

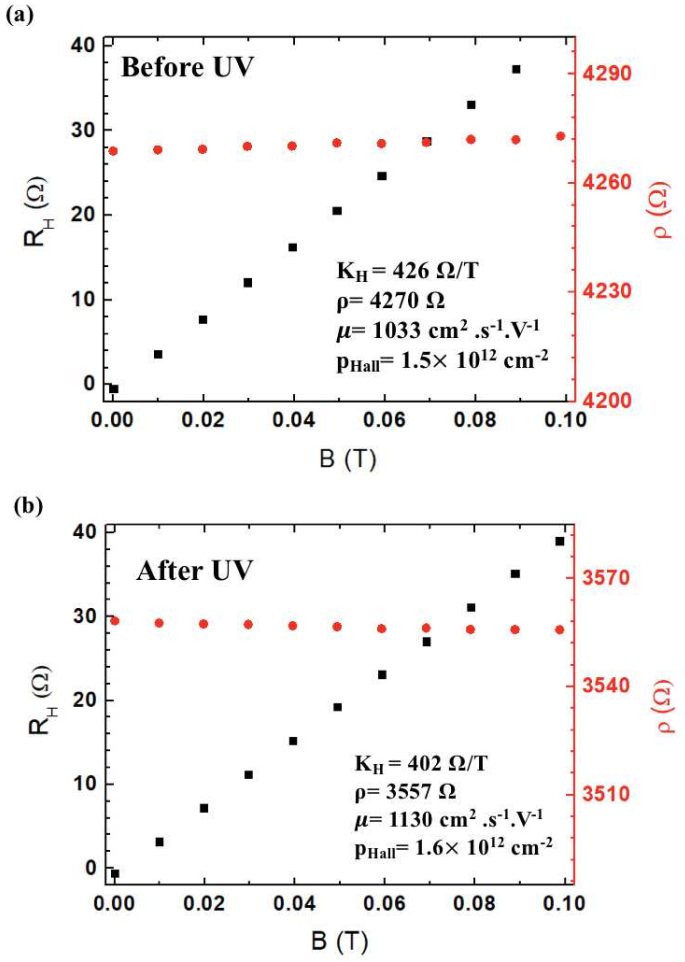

Fig. 5.7 R_H (Ω) and ρ (Ω) as a function of magnetic field of one 1LG sample (a) before and (b) after UV illumination on 1LG sample measured in Van der Pauw device.

Then the transport measurement has been done at fixed magnetic field. Fig. 5.8 (a) shows the K_H and ρ measured before, during and after the first UV illumination in air ambient at room temperature. We note that the K_H which is inversely proportional to carrier density indicates the type of doping as we mentioned in last section: the positive and negative K_H signifies the p-type and n-type doping, respectively. Obviously, the UV has an effect on the electrical properties of our graphene samples. Before the UV treatment, the graphene sample was p-type doped ~ 10^{12} cm^{-2} and possessed a ρ ~ 4270 Ω. Then the UV light has been turned on for 10 mins and turned off. The inset image of Fig. 5.8 is the zoom image of time region during the UV illumination. The illumination windows are highlighted in yellow background. When the UV light was

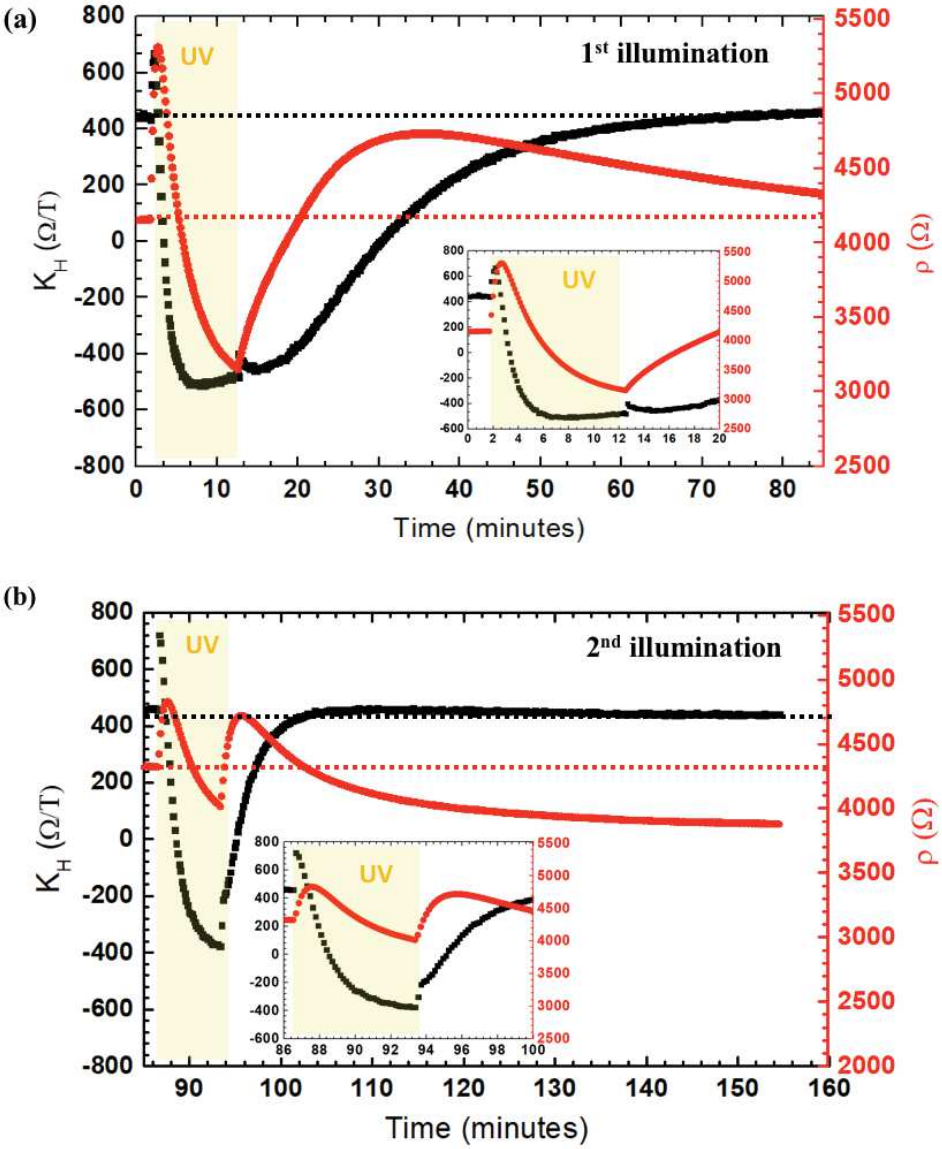

Fig. 5.8 Evolution of K_H (Ω/T) and ρ (Ω) as a function of time, before, during, and after the (a) first and (b) second UV treatments on 1LG sample in Van der Pauw device. Inset images are the zoom of UV light treatment regions. The UV illumination windows are highlighted by yellow background. The dashed horizontal black and red lines represent the initial values of K_H (Ω/T) and ρ (Ω), respectively, for facilitate the comparison.

turned on, the K_H has firstly increased to a higher value then decreased abruptly from a positive value (p ~10^{12} cm^{-2}) to a negative one (n ~10^{12} cm^{-2}) in few minutes. After the treatment, the doping level gradually recovers to its original value. Then about 85 mins after turning off the UV light, it stabilized at the original value. On the other hand, the ρ has undergone a rapid increase from 4200 Ω up to 5300 Ω and then decreased down to 3200 Ω during the illumination. After the UV light treatment, this value increased to a higher one (4600 Ω) compared to its initial value and then decreased back to the initial one. The black and red dashed horizontal lines show the initial values of K_H and ρ, respectively, to facilitate the comparison.

After 85 mins, both the K_H and ρ have nearly returned back to their initial values. We started the second UV treatment (7 minutes) as shown in Fig. 5.8 (b). The x-axis is shown as a prolongation of Fig 5.8 (a). Likewise, the K_H has firstly increased to a higher value then decreased abruptly from a positive value to a negative value (n ~10^{12} cm^{-2}). On the other hand, the ρ increased and then decreased during few minutes UV light treatment. However, if we compare these two experiments more carefully, we found several discrepancies:

i) During the second illumination, the ρ decreased to a minimum value about 4000 Ω which is higher compared with that of first experiment (3200 Ω).
ii) After the second illumination, both the ρ and K_H recover faster than the first experiment (e.g. 15 mins vs. 85 mins for K_H).
iii) After the second illumination, the ρ increased and then decreased as the first UV illumination. Surprisingly, it did not stop decreasing after it achieving its original value (at ~ 105 mins). It drops to a value about 3900 Ω afterwards (150 mins).

Indeed, the different behaviors of our sample in these two illuminations is still under investigation. We assume the faster response to UV light in second illumination might be related to a shorter impurities' adsorption time, i.e. 85 mins between two experiments. In this case, the surface state before these two illuminations could be different, i.e. different adsorptions.

Later, after one-night stabilization, we measured again the R_H and ρ as a function of magnetic field (Fig. 5.7 (b)) and obtained p_{Hall} ~10^{12} cm^{-2} and ρ ~3570 Ω, respectively. This indicates that the doping level has returned back to its original state while the ρ is slightly lower than the original value. Nevertheless, the reversibility of the UV treatment could be highlighted. Indeed, the similar UV treatment has been performed on variety of samples produced using different growth conditions. Almost all the samples show a reversible variation in doping level under the UV effect.

5.3.2 Hall bar device

The UV light treatment has also been done on the Hall bar devices of 1LG sample. The Hall bar has been prepared by lithography process, developed in L2C and CTM (Centre de Technologie en Mirco et Nanoélectronique) in Montpellier by C. Roblin and S. Nanot. Then, we will focus on measurements on a 160 μm × 20 μm size Hall bar similar results were also observed on others Hall bar devices. We note that after the lithography process, we have measured n-type doping in our samples with a K_H value of about -1000 Ω/T. This is a normal result considering the influence of resin on doping characteristic of graphene [199]. Fig. 5.9 and Fig. 5.10 shows the evolution of K_H before, during and after four consecutive cycles of UV illumination (UV-1 to UV-4) which are highlighted by yellow background. In UV-1, we have quickly exposed the sample upon UV light. The change in K_H has been observed as clearly shown in inset image of Fig. 5.9. More precisely, the K_H has varied from -1000 to -400 Ω/T. After about 200 mins of relaxation, K_H has been returned back to its initial value and that is when we started UV-2. We note that the UV-2 was a long duration UV illumination (100 mins). We have observed that K_H firstly abruptly changed to -400 Ω/T at the moment when we turned on the UV light and then returned back to around -1000 Ω/T gradually even during the illumination. We assume that UV light could probably 'clean' the residue of resin [199,200] and the sample surface condition has been varied during these two illuminations. Then, as we turned off the UV light at the time of about 330 mins (Fig. 5.9), the K_H has progressively changed from negative to positive value,

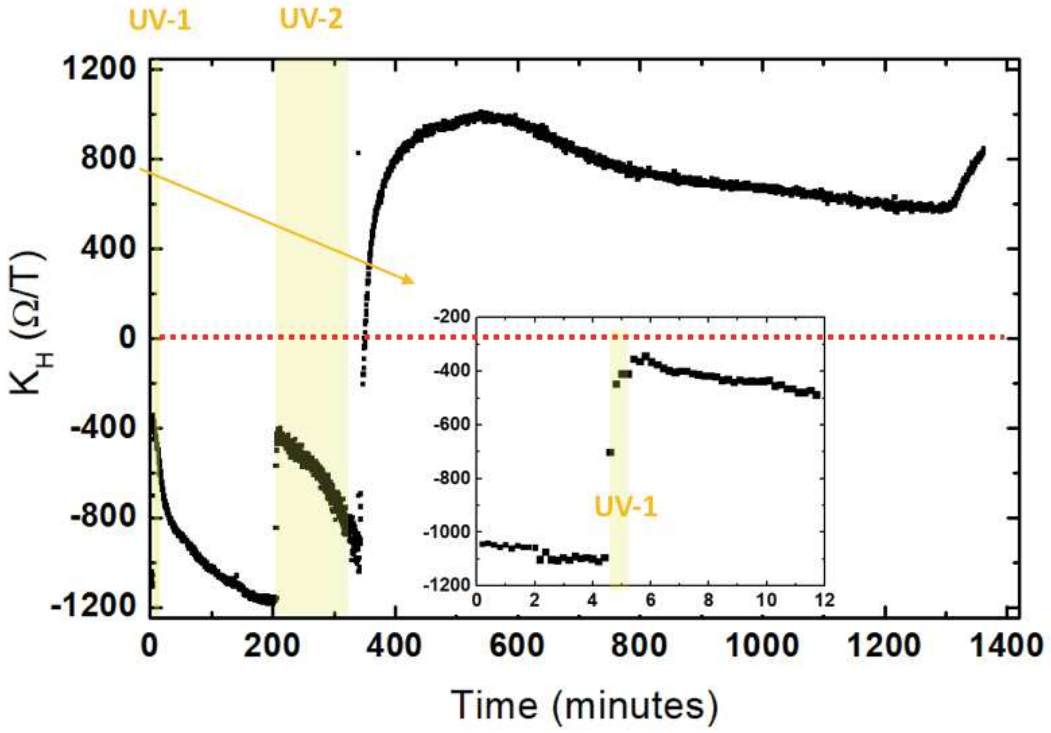

Fig. 5.9 Evolution of K_H (Ω/T) and ρ (Ω) as a function of time, before, during, and after the (a) first and (b) second UV treatments on 1LG sample in Hall bar devices. Inset images are the zoom of UV-1. The UV illumination windows are highlighted by yellow background. The zero level of doping is shown in red horizontal dashed line.

indicating a transition of doping type from n-type to p-type. We believe this transition is due to the atmospheric doping effect on graphene sample considering the previous results. In this case, these first two UV treatments could probably reduce the resin effect on our samples [200]. Besides, we note that abrupt increase around 1330 mins is due to an unintentional experimental environment changes (air circulation).

Then, after the K_H is relatively stable at a value of 1000 Ω/T, we turned on the UV light for the third time (UV-3). The results are shown in Fig. 5.10 (a) and the zoom image Fig. 5.10 (b). As we see, the K_H change from positive to negative value during UV exposure and gradually returned back to positive afterward. This observation supports that the resin effect has been largely suppressed after UV-1 and UV-2. The UV-4 has been performed after the sample regain its value (before UV-3) which is the p-type doping with a K_H around 1000 Ω/T. During the UV-4 treatment (Fig. 5.10 (c)), we have modified the sample from p-type to n-type doping as expected. Later, unlike all the

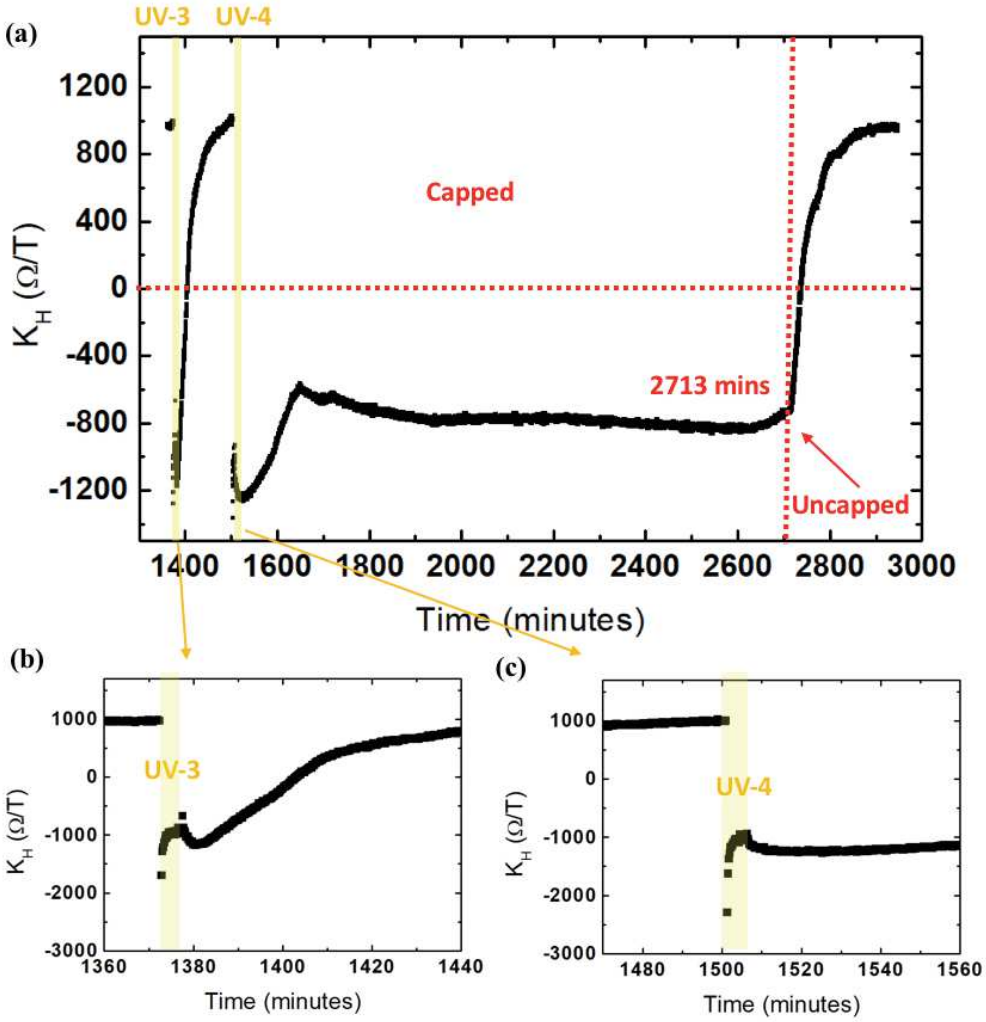

Fig. 5.10 (a) Evolution of K_H (Ω/T) and ρ (Ω) as a function of time, before, during, and after the (b) UV-3 and (c) UV-4 treatments on 1LG sample in Hall bar devices. The UV illumination windows are highlighted by yellow background. The moment when we remove the cap is indicated by vertical red dashed line. The zero level of doping is shown in red horizontal dashed line.

measurements that we have done before, after turning off the UV source, we immediately cap the sample. We stress that this cap design cannot perfectly isolate the sample from air ambient and we only aim to slow down the contact of ambient air with sample surface. As we see in Fig. 5.10 (a), the doping remained n-type for ~1200 mins despite the fluctuation of K_H. Seeing the K_H is almost stable at -800 Ω/T for a long duration (~830 mins), we have removed the cap and exposed the sample directly to the air (at time of 2713 mins). Obviously, the K_H rapidly changed to a positive value and returned back to the value of 1000 Ω/T. We underline that this observation could clearly evidence the atmospheric effect on doping characteristic of our samples by comparing the fast and slow exposure to air after UV-3 and UV-4 treatment, respectively.

We highlight that, in these UV illumination experiments, we are able to alter the doping characteristic of our samples at RT. We plot ρ versus K_H of all these four UV illuminations in Fig. A6.1 in appendix 6. Based on the evolution of ρ as a function of K_H, the potential disorder in our samples can be estimated by a model developed in L2C [180]. We note a considerable potential disorder s = 40 meV and a ratio of hole and electron mobilities $\mu_e/\mu_h \simeq 1$ in our sample, as demonstrated in Fig. A6.2 (appendix 6). More detail is shown in appendix 6.

In the literature, the UV response of a top-gated CVD graphene has been commonly observed [196,197]. Lin *et al*. [196] found that the carrier concentration has decreased to a lower value but remain p-type (Dirac point of device from 70 V to 5 V) while the sheet resistance increased during the illumination. Luo *et al.* [197] have reported that the carrier concentration changed from p-type to n-type upon UV-doping. After switching off the UV light, the sample was exposed to the air and the adsorbates have been gradually trapped again on graphene, bringing it back to p-type doped. This inverse of doping type and reversibility of UV treatment are consistent with our results. Indeed, both of these two works have attributed the shift of the Fermi level to the change of sample surface charge. As we discussed in early sections, the electron trapping adsorbate groups (such as oxygen, water, etc.…) on the graphene surface or graphene-substrate interface would lead to p-type doping as a natural consequence of exposure to air. During UV exposure, an electron-hole pair is generated that liberates the adsorbates via hole recombination. In other words, the UV light could result in a desorption of potential impurities and thus 'clean' the sample surface. Consequently, the doping characteristic is modified due to the change in charge surface.

In our case, the inverse in doping type can be understood by the photodesorption of the charged impurities as explained in two mentioned works. On the other hand, the UV response observed in our samples show some specific behaviors compared to the results of other works:

i) the most obvious difference is the fluctuation of carrier density and resistivity. For example, in the Van der Pauw device case, both the carrier density and resistivity have increased and then decreased their values during the illumination, indicating a complicated doping mechanism. Contrarily, the continued changes were observed in the mentioned work. Furthermore, the variation in resistivity is conflict with the results

of Lin *et al.* [196]. They found a continuous increase of resistivity under UV illumination;

ii) the change rate in our samples seems more rapid than other works. In our case, the doping type changed steeply from p-type to n-type in a few minutes. Lin *et al.* have turned on the UV light for 60 minutes and the Dirac point of device has decreased from 70 V to 5 V [196]. Luo *et al.* have inverted the doping type in 16 minutes [197].

To elucidate these discrepancies of our results with respect to the literature, we have first examined the heating effect in these experiments and we found a negligible shift in temperature. Then, one might relate these mentioned discrepancies to the nature of the sample, i.e. epitaxial graphene vs. transferred graphene on Si/SiO_2. To this purpose, the pure SiC substrate has been measured in the same manner as graphene sample and no obvious reaction to UV was found in SiC substrate (not shown). This rule out the substrate effect on these series of experiments. However, the BL effect cannot be overlooked which worth investigating. One another important difference is the experimental setup. The samples were measured under a vacuum condition in these two mentioned works while we exposed the sample in air ambient during the experiment. Thus, we cannot rule out the air influence on the results.

In conclusion, UV treatments performed on our 1LG samples have further supported the argument of atmospheric doping effects on our graphene films. Besides, this experiment shows its potential importance as an alternative manner to understand the doping mechanism in our samples by revealing several puzzling results. To this end, a systematic study of UV treatment needs to be continued in a near future in order to elucidate these puzzles. For instance, the samples with different characteristics in terms of the number of graphene layers or the various morphology are worth to be studied and compared in a controlled experimental condition. Most importantly, these experiments show a feasibility to modify the doping characteristic by a simple UV treatment due to the sensibility of our samples to the atmosphere. Indeed, an intentional control of doping is one of the objectives of epitaxial graphene which could be considered in applications such as sensors, etc.

5.4 Summary and perspectives

A low p-type residual Hall concentration has been commonly obtained in 1LG samples of this thesis. In this chapter, we have further completed the understanding of this doping characteristics. Supporting by the calculation model study and experimental observations (vacuum or UV treatment), we now strongly suggest that the charged impurities such as oxygen, water…in the atmosphere could be responsible for our low p-type doping. This is absolutely an important result of this thesis because we have now further understood the origin of this unusual doping characteristic observed in our samples. Most importantly, all the measurements aiming to interpret the low p-type doping lead to a consistent result. In addition, we found that our samples possess a high sensitivity to the surrounding external influences (vacuum or UV treatment). In other words, the electrical properties of our as-grown film are not stable in ambient atmosphere. On the other hand, the accessibility to control the doping characteristic is evidenced by UV treatment. For example, thanks to the proximity to Dirac point of our graphene samples, the inverse of the doping type is achievable by exposing the sample to UV light for few minutes. Based on this specific characteristic, we can envisage various application such as sensors, detectors, etc. Thus, to stabilize our graphene films and to tune the doping in a controllable manner is one of our objectives. To accomplish this work, the lithography process has been developed for the fabrication of Hall bar in L2C by C. Roblin, S. Nanot and A. Natchawaty, as shown in Fig. 5.11. An encapsulation post-treatment is proposed in which we use a resist layer to protect the graphene. In addition, a carrier density could be tuned by gate control or ion projection onto this resist layer. For example, negative ions were produced by repeated corona discharges and the deposited ions could alter the electrical properties of graphene [180]. This ongoing work might give us a clue about the doping mechanism of our sample as well. Moreover, the Hall bars with different size and orientation allows an explicit study of SiC step effect on electrical properties of graphene (under UV light or not) as mentioned in **Chapter 3**.

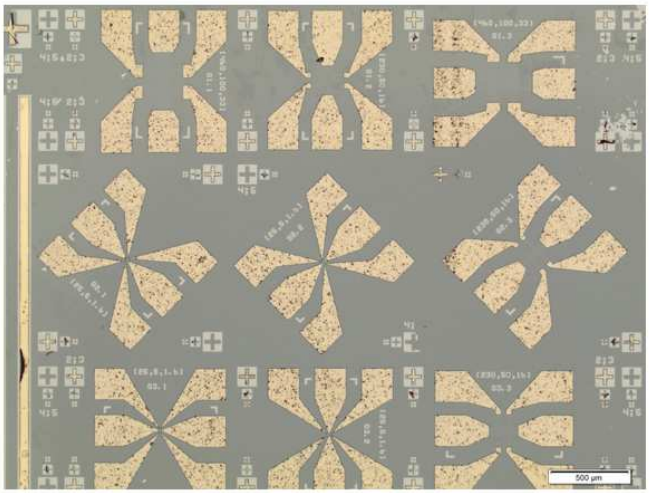

Fig. 5.11 Hall bars fabricated on 1LG sample by lithography technique developed in L2C.

General conclusion and perspectives

In this manuscript, we present a study of graphene growth on SiC (0001) by sublimation at low argon pressure, i.e. 10 mbar. The synthesis of graphene was realized in L2C by using the prototype Annealsys furnace. We highlight the low argon pressure used in this study which differs from the one usually used in the literature (1 atmospheric argon pressure or ultra-high vacuum). More than 230 samples have been produced in order to study the influences of growth parameters, such as growth time, annealing temperature and temperature ramp, on the obtained graphene films. Characterization techniques such as optical microscopy, Raman spectroscopy, atomic force microscope, scanning tunneling microscope and Hall effect transport experiments have been performed on these grown samples. By appropriately tuning the growth parameter, a reproducible and controlled monolayer graphene growth process has been optimized (1750°C, 300 s, 10 mbar). All the results obtained from characteristics measurements consistently suggest that the homogeneous and large-size (6 mm × 6 mm) monolayer graphene film can be achieved by using our optimized growth process. More precisely, $A_{G\text{-graphene}}/A_{G\text{-HOPG}}$ ratio in Raman experiment allowing the first estimation on the number of graphene layers and homogeneity of samples indicates the homogeneous monolayer graphene film present on our samples. Besides, the 6 × 6 superlattices have been revealed by STM images which are the typical characteristic of monolayer graphene on SiC (0001) with buffer layer underneath. Furthermore, the plateau in Hall resistance situated at about 12 kΩ is observed in transport measurement as a hallmark of monolayer graphene. Regarding the growth mechanism, the presence of step-flow growth mode is evidenced by the formation of step-terrace surface shown in AFM images of our sample surface. In addition, we found the large terraces could be obtained by using a low temperature ramp. For example, samples with terraces more than 10 μm has been achieved with a temperature ramp of 0.1°C/s. Most importantly, the reproducibility of this growth method has been confirmed by successfully repeat more than 50 monolayer graphene samples with comparable characteristics.

We have investigated, in detail, the well-known buffer layer at graphene / SiC (0001) interface. Graphene layer was mechanically removed by depositing glue or nickel thin layer on graphene surface then subsequently releasing them. Thus, only the interfacial buffer layer remains on the SiC. In this case, we have the access to three types of buffer layer:

i) the bare buffer layer obtained directly from growth;
ii) uncovered interfacial buffer layer obtained by graphene transfer experiment;
iii) interfacial buffer layer covered by graphene above.

By collecting more than 15,000 Raman spectra from these mentioned buffer layer, we have highlighted its inhomogeneity in Raman signature. In the case of the uncovered interfacial buffer layer, the integrated intensity of two peaks situated close to D- and G-mode of graphene, around 1390 cm^{-1} and 1610 cm^{-1} show a continuous variation and a positive linear relationship between these two terms. On the other hand, the bare buffer layer samples show relatively homogenous results on one single terrace while topology effect on Raman signature was also been found. Furthermore, the bare buffer layer has been produced at an annealing temperature ranged from 1600°C to 1720°C. No obvious growth temperature effect on Raman response of buffer layer has been noticed. Comparable peak positions and integrated areas were found independent on growth temperature. Moreover, Raman spectra collected from a same area of buffer layer with or without graphene coverage have allowed a precise study of buffer layer evolution in these two cases. We believe the three observed evolutions after graphene formation could be related to the coupling between the buffer layer and graphene:

i) the appearence of two fine peaks at 1250 cm^{-1} and 1375 cm^{-1};
ii) the down-shift at least 8 cm^{-1} in buffer layer peaks close to 1600 cm^{-1};
iii) a decrease in total Raman integrated intensity of buffer layer contribution between 1200 cm^{-1} and 1800 cm^{-1}.

Besides, we also highlight the presence of a peak at about 3000 cm^{-1} in bare buffer layer sample which could be a Raman response of buffer layer. Hence, we believe our statistic study of buffer layer will contribute valuable results to the understanding of graphene / SiC interface.

Lastly, the electrical properties of graphene films have been studied. Indeed, a low p-type residual Hall concentration (from few 10^{10} cm^{-2} to 10^{11} cm^{-2} at 1.7 K) has been usually observed in our monolayer graphene samples, contrary to the typical n-type doping reported in the literature for epitaxial graphene on SiC. Our experimental results clearly indicated that the atmosphere has a considerable effect on the doping characteristic of our samples. More precisely, the charged impurities unintentionally deposited on the sample surface could lead to an inhomogeneous doping with the formation of electron-hole puddles. An adapted model in which we fit the measured Hall concentrations versus temperature was used to estimate the potential fluctuation. We found a doping disorder of about 27 ± 10 meV around average Fermi level in our monolayer graphene films. Moreover, we have shown that both vacuum condition and UV light have effect on the doping characteristic of our samples. The transition from p-type to n-type doping was observed during vacuum or UV treatment. Then, the sample returns back to its initial doping level (p-type) after a re-contact to air ambient. The change in doping characteristic could be explained by desorption, during the pumping or UV illumination, of adsorbed charges. These results demonstrate the possibilities of tuning the electrical properties of our samples by an external factor such as vacuum condition or UV light.

All of these studies have led us to a deeper understanding of the growth mechanism and characteristics of epitaxial graphene on SiC (0001). However, further studies will be forthcoming following this work:

1) *Buffer layer at graphene / SiC (0001) interface*. Regarding the existence of various Raman response of buffer layer (BL), several possible experiments will continue. One idea is to intentionally dope our buffer layer and study the doping effect on the Raman spectrum of BL. The doping will be accomplished by corona source or SEM and the analysis such as Raman and ARPES will be combined. Another idea is to study the Raman signature of buffer layer grown on terraces with different terrace width to elucidate the topology effect on BL. Then, Raman map collection by using different excitation laser wavelength is also required which allows further evidencing the characteristic of BL in each laser energy, i.e. homogeneity of BL. Thus, the laser wavelength effect could be better revealed by eliminating the influence of intrinsic characteristic of BL. Furthermore, the intercalation treatment by nitrogen is another ongoing study in which we are expecting to understand the disorder in different BL by detecting the reaction between nitrogen atoms with our BL and graphene samples. Moreover, to further confirm the graphene coverage effect on BL, we propose to transfer a mechanical exfoliated 1LG film onto our uncovered BL_{1LG} samples.

2) *Tuning the electrical properties of graphene on SiC (0001)*. Since the inverse of the doping type is achievable in our low-doped monolayer graphene films by exposing the sample to UV light for a few minutes, one perspective is to tune the doping in a controllable manner. To this end, an encapsulation post-treatment is proposed in which we use a resist layer to protect the graphene. In addition, a carrier density could be tuned by gate control or ion projection onto this resist layer. Moreover, scattering mechanisms in samples with different device geometry could be investigated by transport measurement with or without UV light. Hall bars with different size and orientation allows an explicit study of SiC step effect on electrical properties of graphene. In addition, a Hall bar fabricated on one single wide terrace (more than 10 μm) could eliminate the step effect and reveal the electrical properties of the flat graphene film.

3) *Epitaxial graphene on SiC (*$000\bar{1}$*)*. Compared to the Si-face, graphene on C-face has been less studied. The major problem with the growth of epitaxial graphene on C-face of SiC is the lack of precise control in graphene thickness distribution. However, the outstanding advantage is the absence of a buffer layer. Indeed, the buffer layer is a considerable limitation in the development of future electronic devices from graphene on the Si-face of SiC due to its effect on the transport properties. We expect that the unclassical growth conditions in our prototype equipment could contribute to the understanding of graphene synthesis on SiC ($000\bar{1}$).

Appendix 1

Optical microscope and repositioning software

Several systems of optical microscopes were used in this thesis. The mainly used one is a Nikon eclipse LV100 (https://www.nikoninstruments.com/fr). This measurement allows us to have first impression of sample surface by visualizing the entire sample, as shown in the example in Fig. A1.1 (a). The red arrow points at a slight edge effect of sample. For the sample possess a step-terraces morphology, the steps could be observed in the high-resolution image with the use of differential interference contrast (DIC) and polarized light (Fig. A1.1 (b)). Besides, our Raman spectroscopy and AFM system are combined with microscope operators for the visualization of detected areas during measurement.

A home-made software developed by J.-R. Huntzinger (L2C) allows a retraceable image collection in between these microscope systems (Nikon, Raman spectroscopy or AFM). First, two coordinated positions (e.g. two corners of the sample) and that of interest area are recorded by one of the systems. Then in another system, we found the exact positions of two former positions, thus the third position (interest area) could be retraced by using software calculation in which we eliminate the sample tilt. Thanks to this powerful tool, we are able to reposition the exact area on sample surface. For example, in **chapter 4**, we have examined the same area before and after the mechanical removal of graphene by using this software. The evolution between these cases (before and after graphene transfer) can thus be compared with a very high precision.

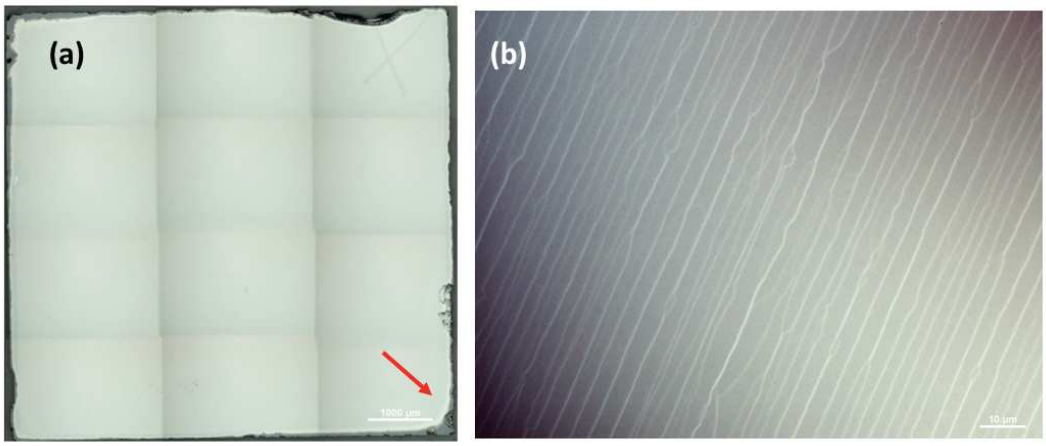

A1.1 Optics images of sample (a) entire sample surface. Edge effects sometimes show in our sample as indicated by red arrow. (b) High resolution image with visualization of white stripes which correspond to steps.

Appendix 2

Micro-Raman spectroscopy and analysis software

Fig. A2.1 is the schematic illustration of the home-made setup in L2C which is an Acton SP2500 spectrometer fitted with a Pylon CCD detector and a grating that enables the measurement of the full spectrum in the range 1000-3000 cm^{-1} within a single acquisition (i.e. for a 532 nm laser, 600 grooves/mm grating corresponding to ~ 2 cm^{-1} between each CCD pixel). Three excitation wavelengths are possible: 457 nm (2.7 eV), 532 nm (2.33 eV) and 633 nm (1.96 eV). The samples were excited with a Nd: Yag laser through 100 × objective (Numerical Aperture 0.9). The width of the focused laser spot was ~ 400 nm. The samples are mounted on a 3-axis piezoelectric stage (Physik Instrumente) to ensure the precise positioning and focusing of the laser spot. The Raman maps were recorded at a designed and retraceable position. The laser power was continuously collected during the mapping which enable to correct the laser power fluctuations. The acquisition time for each individual spectrum was adjusted according to the laser power and measurement interests. For example, the most commonly used measurement condition was 532 nm, 1mW and 600 grooves/mm, in which we adapt the acquisition time to 60 s. The whole experimental setup was controlled by a dedicated, home-made Labview application.

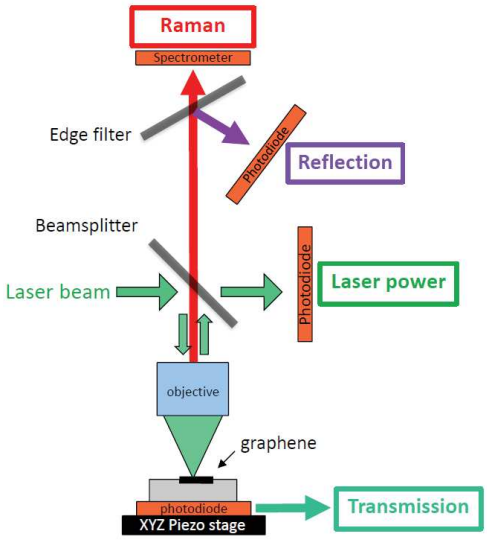

A2.1 Schematic illustration of Raman spectroscopy setup.

As we know, the second order signal of SiC substrate overlaps the graphene D- and G-peaks in the Raman shift range of 1000-2000 cm^{-1}. In this case, a subtraction of SiC signal is necessary to reveal the graphene signature. The SiC reference is always acquired in the same experimental condition with the studied spectra. Fig. A2.2 illustrates an example of subtraction process realized by home-made software (developed by A.-A. Zahab, L2C). Fig. A2.2 (a) and (b) are the spectra of SiC reference and our studied spectrum. Then, we choose a frequency region where there is only contribution of SiC reference but no graphene or buffer layer contribution, as shown in A2.2 (c). The software can analyze and give the results in A2.2 (d). In this example, we can obtain the Raman signature of D- and G-peaks of epitaxial graphene.

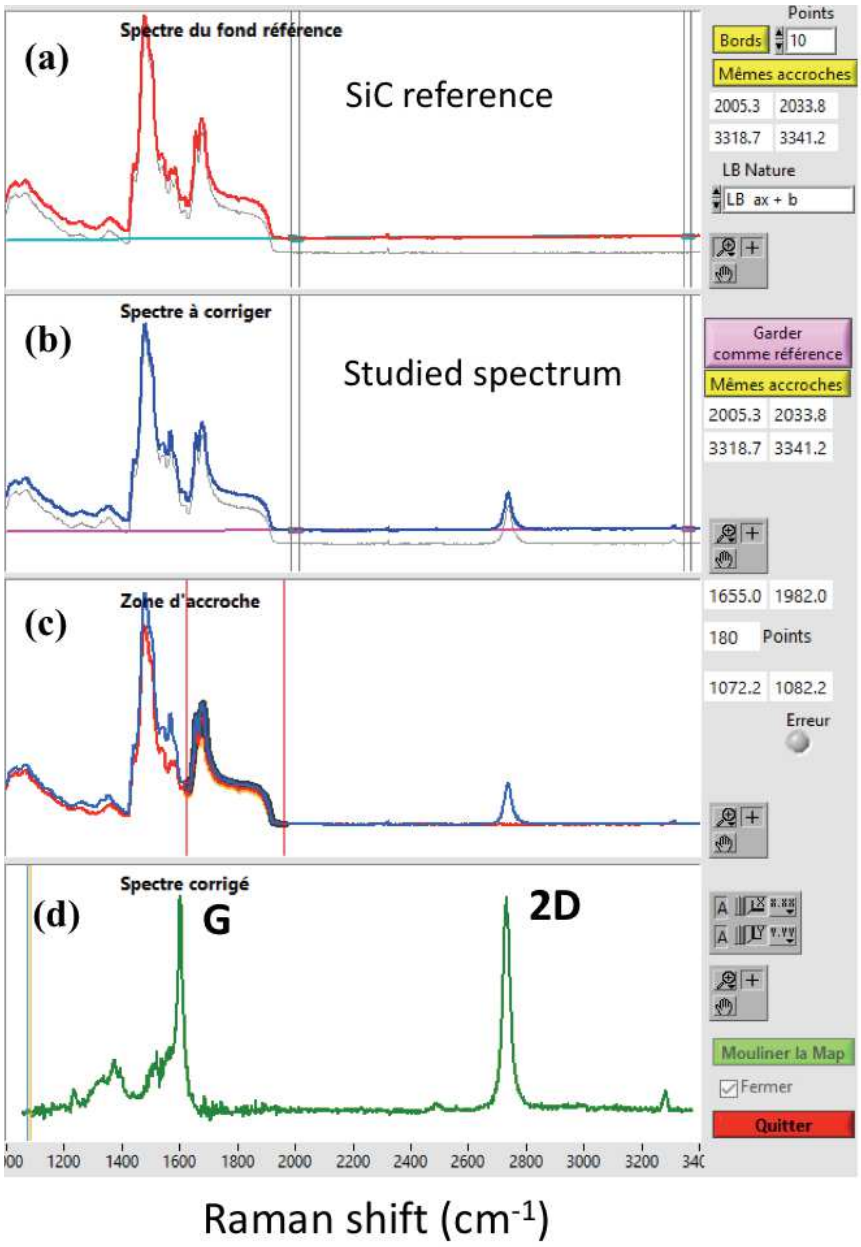

A2.2 Subtraction of SiC. (a) and (b) show SiC reference and studied spectrum, respectively. The vertical solid lines represent the zone reference for subtraction of background. (c) Vertical red lines choose the zone where there is only SiC contribution. (d) Spectrum after SiC subtraction.

In addition, in order to highlight the appropriate subtraction in this work, we intentionally carry out a bad subtraction. Fig. A2.3 compare the results of this appropriate subtraction (black spectrum) and a bad subtraction (red spectrum), respectively, effectuated on same buffer layer spectrum. As we see, the red spectrum is clearly over-subtraction evidenced by a negative value at 1750 cm^{-1}.

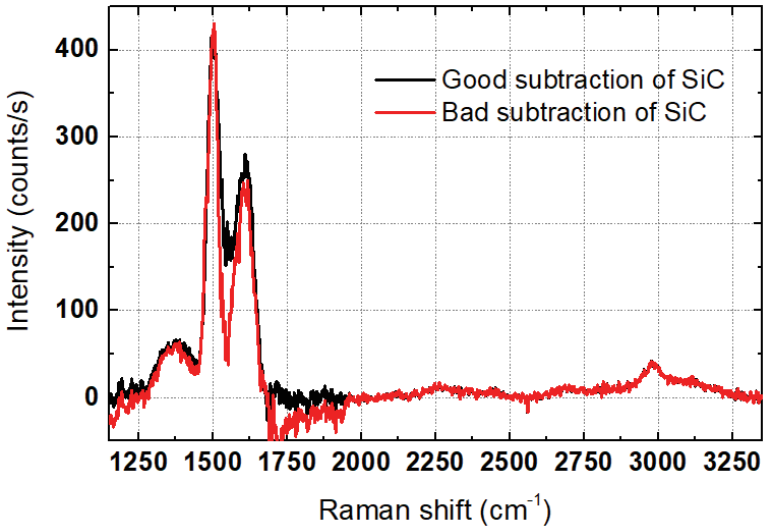

A2.3 Example of appropriate (black spectrum) and bad subtraction (red spectrum) of SiC.

Regarding the analysis of the BL spectra, we also use the home-made software. As mentioned in **chapter 2 and 4**, we can fit the spectra with Lorentzian or Gaussian functions with peak intensity, peak position and FWHM of the peak (Fig. A2.4 (a)). In our case, both 2-, 3- and 4-component fittings has been investigated. As we can see in Fig. A2.4 (b), we compared the 3- and 4-component fitting by fitting one spectrum of BL_0. The advantage of 4-component fitting is obvious because there is residue left around 1550 cm^{-1} in 3-component fit. It is also evidenced by R-square value which indicate the goodness of fitting.

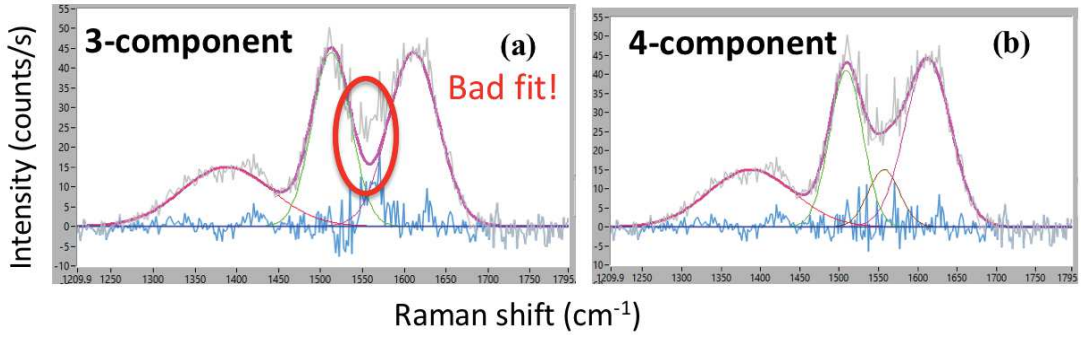

A2.4 3-component (left) and 4-component fit (right) of bare buffer layer Raman spectrum.

Appendix 3

Atomic force microscopy

In this thesis, the surface morphology of the grown samples was characterized by two atomic force microscopy (AFM) system in L2C. The NanoScope V, Bruker AFM system in tapping mode use a commercial silicon probe (resonant frequency ~300 kHz and spring constant ~20 N/m) in ambient conditions. This system is equipped by a microscopy which allow a precise image-tracking. We will show in the following chapters that the combined AFM and Raman techniques is a truly powerful tool which enable a material identification, the estimation of number of graphene layer and the investigation of the surface morphology, etc.

Another AFM system is a SMEMA NTMDT equipment which was often used to investigate the morphology of the samples. The measurements were carried out in tapping mode using a silicon cantilever with a radius lower than 10 nm (resonant frequency 150-300 kHz and spring constant 5.4 -16 N/m dependent on tips).

Both morphology and phase data were analyzed with WSxM software package (v4.0 Beta 8.1) [157]. Data have been locally plane fitted and line flattened to better show their morphology.

Appendix 4

Graphene removal by thin epoxy-based glue layer or Ni layer

Graphene transfer process has been realized by the deposition and mechanical removal of a thin epoxy-glue layer or Ni layer. In the former case, we use an epoxy-phenolic adhesive (M-Bond 610 Vishay) as glue layer. The adhesive viscosity is further reduced by dissolving the adhesive in a tetra-hydro-furan THF solution (5 droplets of mother solution in 15 droplets of THF, which give roughly a 1:3 dilution ratio). The mixed solution is then deposited on sample surface and then a glass substrate is covered on top of the sample. The solution diffuses and covers the entire sample surface. The resulting sandwich (sample/ adhesive film/ glass slide) is then cured at 100°C for 2h under compression. An even compression is achieved through the use of a mass weight put on the top of the sandwich set. After the cure process, the glass substrate is separated from sample. As we can see in Fig. A4.1 (a), the glue film is transferred to the glass substrate. The outline of the glue film is obviously recognized on glass substrate due to the same shape with that of sample (6 mm × 6 mm). Fig. A4.1 (b) show the optical microscopy image acquired from entire sample surface after graphene removal. The glue residues are clearly shown on sample surface.

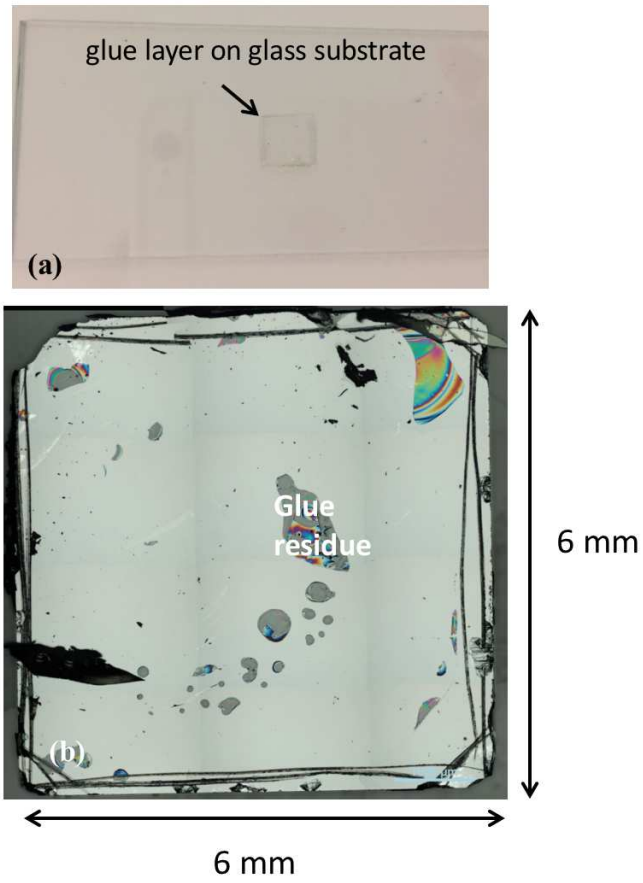

A4.1 (a) Photo of thin glue layer deposited on glass substrate. (b) Optical image of entire sample surface after the removal of thin glue layer.

On the other hand, a Ni layer could homogeneously cover sample surface by thermal evaporation technique as well. The thickness of the Ni layer is chosen based on the calculation in reference [37] and can be controlled by the time of deposition process. In our case, we measured a thickness ranged of 100-300 nm. Then a scotch is pasted on the Ni covered sample surface. The removal of the scotch lead to the release of Ni layer from sample surface. The photo of scotch and sample is shown in Fig. A4.2 (a) left and right respectively. Besides, the sample surface has been probed by optic microscope after the Ni layer deposition and removal as shown in Fig. A4.2 (b).

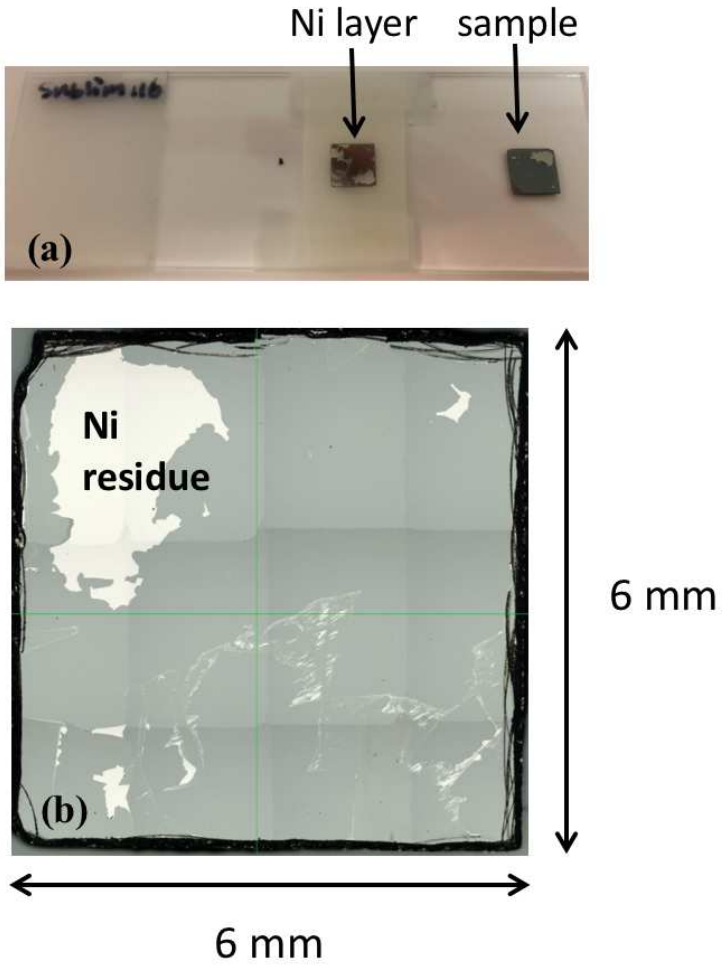

A4.2 (a) Photo of thin Ni layer released by scotch (left) and sample (right) after mechanical removal of graphene from SiC substrate. (b) Optical image of entire sample surface after the removal of thin Ni layer.

Fig. A4.3 illustrate the sample surface after the deposition and removal of thin epoxy-based glue and Ni layer, respectively. As we see, the sample surface after graphene transfer experiment remain relatively clean without large portion of residue of glue or Ni layer. The white contrast corresponds to the graphene according to the Raman analysis.

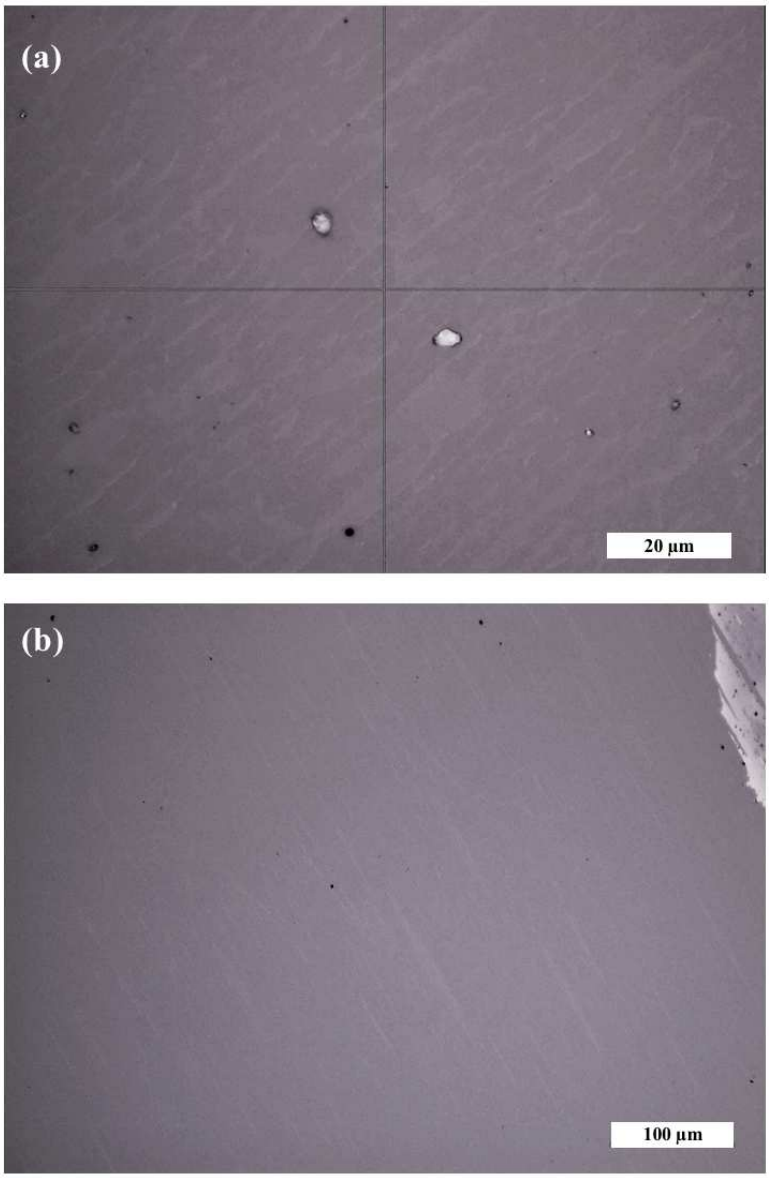

A4.3 Sample surface after graphene removal by glue (a) and Ni (b) deposition and release method. The white contrast is related to graphene.

Appendix 5

Buffer layer investigation by Raman spectroscopy

In section 4.3, we have investigated the homogeneity of obtained buffer layer (BL): i) bare buffer layer from direct growth (BL_0); ii) uncovered interfacial buffer layer (uncovered BL_{1LG}). We have used 3-region analysis method to study the Raman fingerprint of BL (detail in section 4.2). We have mentioned that the relationship between R2 and R1 (or R3) in these buffer layer spectra is still unclear. Fig. A5.1 (a) and (b) show the integrated intensity of R2 as a function of that of R1 and R3, respectively, of the spectra collected from several BL_0 and uncovered BL_{1LG} samples.

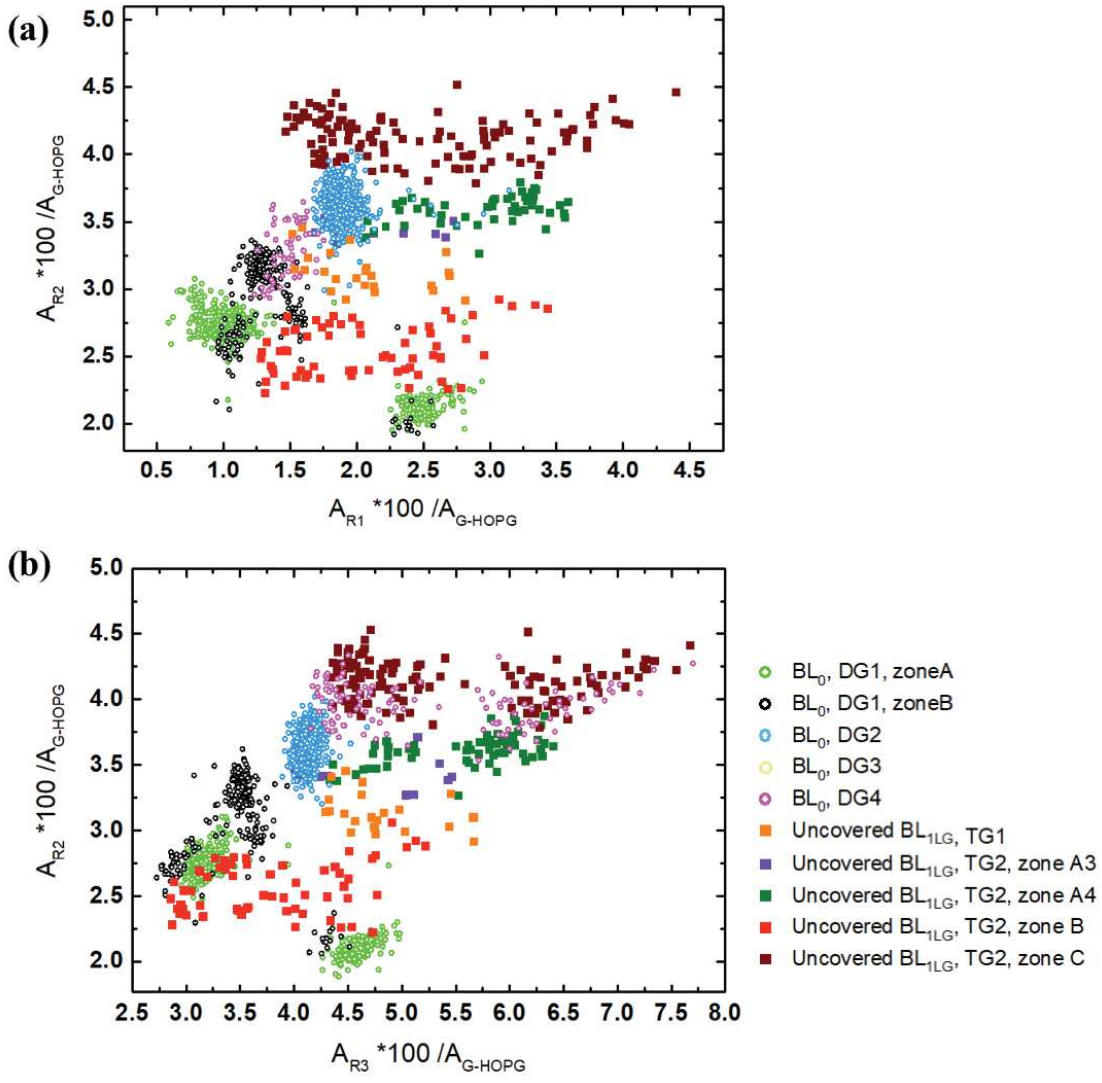

A5.1 A_{R2} as a funtion of (a) A_{R1} and (b) A_{R3} in spectra collected from bare buffer layer samples (BL_0 DG1, DG2, DG3 and DG4) and uncovered BL_{1LG} samples (TG1, TG2).

One another uncovered BL_{1LG} sample obtained by glue layer deposition method has been studied using different laser energy: 457 nm (2.7 eV), 532 nm (2.33 eV), 633 nm (1.96 eV). The individual spectra are shown in Fig. A5.2. The results shown in this sample is consistent with that of sample shown in Fig. 4.15. in terms of the peak shift in peak 2 and peak 4. The discrepancy can be regarded as the inhomogeneity of the buffer layer. Indeed, the discrepancy of results obtained from these two samples (appendix 5 and section 4.5) motivate us to acquire the Raman maps using different laser energy.

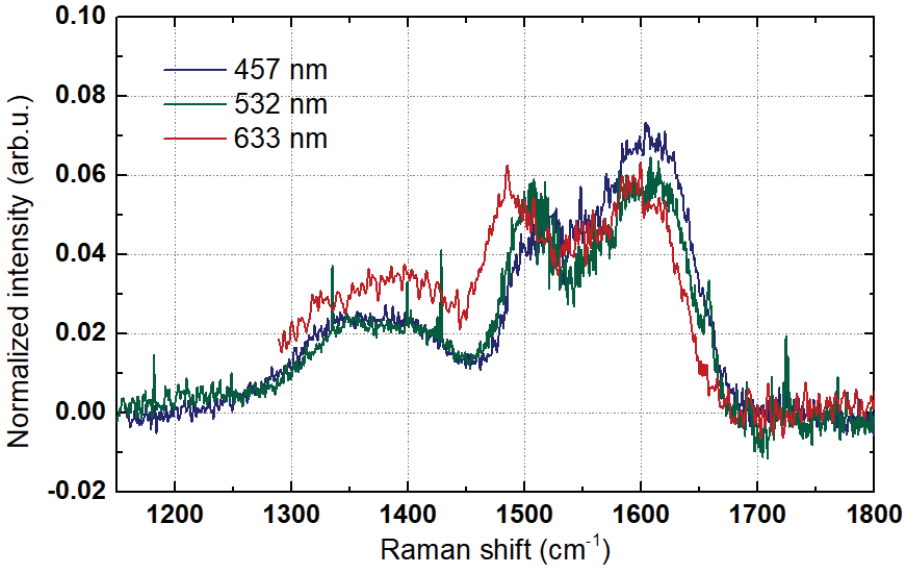

A5.2 Laser energy dependent Raman response of uncovered BL_{1LG} sample. The blue, green and red spectra represent the spectra acquried using 457 nm, 532 nm and 633 nm, respectively.

Table. A5.1 3-region method of analysis of spectrum shown in Fig. A5.2.

	R1 ($A\times100/A_{G-HOPG}$)	R2 ($A\times100/A_{G-HOPG}$)	R3 ($A\times100/A_{G-HOPG}$)	Total ($A\times100/A_{G-HOPG}$)
BL_{1LG} 457 nm	3.5	3.2	6.3	13
BL_{1LG} 532 nm	3.4	3.4	5.1	11.9
BL_{1LG} 632 nm	5.0	4.2	4.7	13.9

Appendix 6

Doping type transition by UV illumination

Fig. A6.1 plots ρ versus K_H during and after these four UV treatments in section 5.3.2. As we see, the red rectangles represent the data starting from UV-1 until the end of UV-2 illumination. No doping type transition was found until the post-UV-2 illumination (green rectangles). We assume that the resin effect is considerable during these first two experiments. Then the behavior of ρ and K_H during and after UV-3 (blue rectangles) can be overlapped by that of UV-4 (magenta rectangles), highlighting the reversibility of this UV experiment. We emphasize that, the sample surface stablize at same state in ambient in terms of doping level and resistivity (black dashed cirlce in Fig. A6.1) .

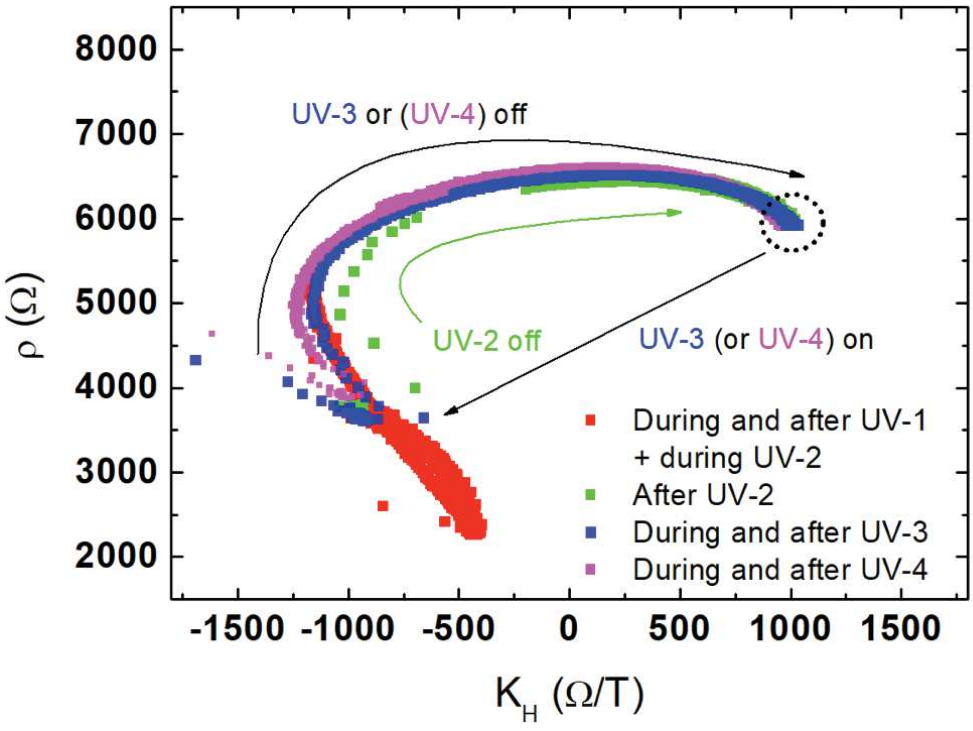

Fig. A6.1 Resistivity ρ versus K_H before, during and after the four UV illuminations: red rectangles represent during and after UV-2 as well as during long exposition UV-2, green rectangles show the results of after UV-2 illumination, blue and magenta rectangles show the results during and after UV-3 and UV-4, respectively. The dashed circle highlights the stabilized states of sample in ambient.

The data shown in blue and magenta curves in Fig. A6.1 (UV-3 and UV-4) allow an estimation of potential disorder by using a simple model developed in L2C. Fig. A6.2 (a) and (b) illustrated the results of fitting (solid red lines) and the experimental data of ρ (K_H) (blue dot) without and with a disorder s, respectively. The results clearly show that the fit data is closer to experimental results if we consider a disorder $s = 41$ meV, indicating the presence of potential disorder in our samples. However, the discrepancy in Fig. A6.2 (b) between fit and experimental data is attributed to the constant mobility assumed in this model, which is not real. We postpone a more detailed fitting in near future while here we only highlight the existence of disorder in our samples.

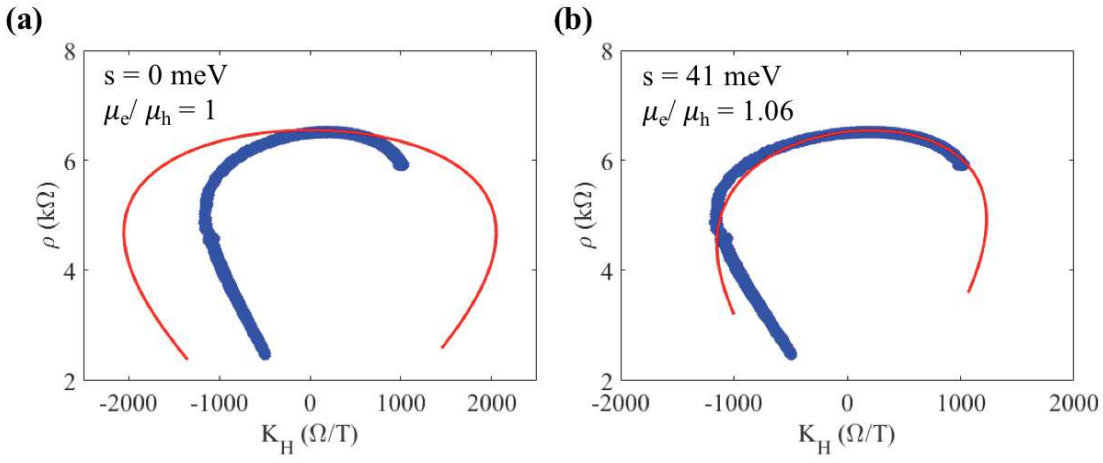

Fig. A6.2 Resistivity ρ versus K_H fitted by a model for the estimation of disorder. (a) $s = 0$. (b) $s = 41$ meV.

References

[1] Novoselov KS. Electric Field Effect in Atomically Thin Carbon Films. Science 2004;306:666–9. doi:10.1126/science.1102896.

[2] Novoselov KS, Geim AK, Morozov SV, Jiang D, Katsnelson MI, Grigorieva IV, et al. Two-dimensional gas of massless Dirac fermions in graphene. Nature 2005;438:197–200. doi:10.1038/nature04233.

[3] Nair RR, Blake P, Grigorenko AN, Novoselov KS, Booth TJ, Stauber T, et al. Fine Structure Constant Defines Visual Transparency of Graphene. Science 2008;320:1308–1308. doi:10.1126/science.1156965.

[4] Lee C, Wei X, Kysar JW, Hone J. Measurement of the Elastic Properties and Intrinsic Strength of Monolayer Graphene. Science 2008;321:385–8. doi:10.1126/science.1157996.

[5] Morozov SV, Novoselov KS, Katsnelson MI, Schedin F, Elias DC, Jaszczak JA, et al. Giant Intrinsic Carrier Mobilities in Graphene and Its Bilayer. Physical Review Letters 2008;100. doi:10.1103/PhysRevLett.100.016602.

[6] Berger C, Song Z, Li T, Li X, Ogbazghi AY, Feng R, et al. Ultrathin Epitaxial Graphite: 2D Electron Gas Properties and a Route toward Graphene-based Nanoelectronics. The Journal of Physical Chemistry B 2004;108:19912–6. doi:10.1021/jp040650f.

[7] Virojanadara C, Syväjarvi M, Yakimova R, Johansson LI, Zakharov AA, Balasubramanian T. Homogeneous large-area graphene layer growth on 6 H - SiC(0001). Physical Review B 2008;78. doi:10.1103/PhysRevB.78.245403.

[8] Emtsev KV, Bostwick A, Horn K, Jobst J, Kellogg GL, Ley L, et al. Towards wafer-size graphene layers by atmospheric pressure graphitization of silicon carbide. Nature Materials 2009;8:203–7. doi:10.1038/nmat2382.

[9] Castro Neto AH, Guinea F, Peres NMR, Novoselov KS, Geim AK. The electronic properties of graphene. Reviews of Modern Physics 2009;81:109–62. doi:10.1103/RevModPhys.81.109.

[10] Reich S, Maultzsch J, Thomsen C, Ordejón P. Tight-binding description of graphene. Physical Review B 2002;66. doi:10.1103/PhysRevB.66.035412.

[11] Hattab H, N'Diaye AT, Wall D, Klein C, Jnawali G, Coraux J, et al. Interplay of Wrinkles, Strain, and Lattice Parameter in Graphene on Iridium. Nano Letters 2012;12:678–82. doi:10.1021/nl203530t.

[12] Anthony J., Bideaux R., Bladh K., Nichols M. Handbook of Mineralogy, Mineralogical Society of Amercia. Mineral Data Pub. 1990.

[13] Wallace PR. The Band Theory of Graphite. Physical Review 1947;71:622–34. doi:10.1103/PhysRev.71.622.

[14] Sarma SD, Adam S, Hwang EH, Rossi E. Electronic transport in two dimensional graphene. Reviews of Modern Physics 2011;83:407–70. doi:10.1103/RevModPhys.83.407.

[15] Zhang F, Chen X, Yu C, Xu X, Hu X, Qin X, et al. High mobility and large domain decoupled epitaxial graphene on SiC (000 $\bar{1}$) surface obtained by nearly

balanced hydrogen etching. Materials Letters 2017;195:82–5. doi:10.1016/j.matlet.2017.02.105.

[16] Novoselov KS, Morozov SV, Mohinddin TMG, Ponomarenko LA, Elias DC, Yang R, et al. Electronic properties of graphene. Physica Status Solidi (B) 2007;244:4106–11. doi:10.1002/pssb.200776208.

[17] Novoselov KS. Electric Field Effect in Atomically Thin Carbon Films. Science 2004;306:666–9. doi:10.1126/science.1102896.

[18] Morozov SV, Novoselov KS, Katsnelson MI, Schedin F, Elias DC, Jaszczak JA, et al. Giant Intrinsic Carrier Mobilities in Graphene and Its Bilayer. Physical Review Letters 2008;100. doi:10.1103/PhysRevLett.100.016602.

[19] Han MY, Özyilmaz B, Zhang Y, Kim P. Energy Band-Gap Engineering of Graphene Nanoribbons. Physical Review Letters 2007;98. doi:10.1103/PhysRevLett.98.206805.

[20] Xia F, Farmer DB, Lin Y, Avouris P. Graphene Field-Effect Transistors with High On/Off Current Ratio and Large Transport Band Gap at Room Temperature. Nano Letters 2010;10:715–8. doi:10.1021/nl9039636.

[21] Giovannetti G, Khomyakov PA, Brocks G, Kelly PJ, van den Brink J. Substrate-induced band gap in graphene on hexagonal boron nitride: *Ab initio* density functional calculations. Physical Review B 2007;76. doi:10.1103/PhysRevB.76.073103.

[22] Zhang Y, Tan Y-W, Stormer HL, Kim P. Experimental observation of the quantum Hall effect and Berry's phase in graphene. Nature 2005;438:201–4. doi:10.1038/nature04235.

[23] Laughlin RB. Quantized motion of three two-dimensional electrons in a strong magnetic field. Physical Review B 1983;27:3383–9. doi:10.1103/PhysRevB.27.3383.

[24] Kittel C. Introduction to solid state physics. 8th ed. Hoboken, NJ: Wiley; 2005.

[25] Lafont F, Ribeiro-Palau R, Kazazis D, Michon A, Couturaud O, Consejo C, et al. Quantum Hall resistance standards from graphene grown by chemical vapour deposition on silicon carbide. Nature Communications 2015;6. doi:10.1038/ncomms7806.

[26] Malard LM, Pimenta MA, Dresselhaus G, Dresselhaus MS. Raman spectroscopy in graphene. Physics Reports 2009;473:51–87. doi:10.1016/j.physrep.2009.02.003.

[27] Balandin AA. Thermal properties of graphene and nanostructured carbon materials. Nature Materials 2011;10:569–81. doi:10.1038/nmat3064.

[28] Renteria J, Nika D, Balandin A. Graphene Thermal Properties: Applications in Thermal Management and Energy Storage. Applied Sciences 2014;4:525–47. doi:10.3390/app4040525.

[29] Bernardi M, Ataca C, Palummo M, Grossman JC. Optical and Electronic Properties of Two-Dimensional Layered Materials. Nanophotonics 2017;6. doi:10.1515/nanoph-2015-0030.

[30] Group for Physics of Ordered Nanostructures and New Materials in Photonics n.d.

[31] Blake P, Hill EW, Castro Neto AH, Novoselov KS, Jiang D, Yang R, et al. Making graphene visible. Applied Physics Letters 2007;91:063124. doi:10.1063/1.2768624.

[32] Novoselov KS, Fal′ko VI, Colombo L, Gellert PR, Schwab MG, Kim K. A roadmap for graphene. Nature 2012;490:192–200. doi:10.1038/nature11458.

[33] Li X, Cai W, An J, Kim S, Nah J, Yang D, et al. Large-Area Synthesis of High-Quality and Uniform Graphene Films on Copper Foils. Science 2009;324:1312–4. doi:10.1126/science.1171245.

[34] Reina A, Jia X, Ho J, Nezich D, Son H, Bulovic V, et al. Large Area, Few-Layer Graphene Films on Arbitrary Substrates by Chemical Vapor Deposition. Nano Letters 2009;9:30–5. doi:10.1021/nl801827v.

[35] Sutter PW, Flege J-I, Sutter EA. Epitaxial graphene on ruthenium. Nature Materials 2008;7:406–11. doi:10.1038/nmat2166.

[36] T N'Diaye A, Engler M, Busse C, Wall D, Buckanie N, Meyer zu Heringdorf F-J, et al. Growth of graphene on Ir(111). New Journal of Physics 2009;11:023006. doi:10.1088/1367-2630/11/2/023006.

[37] Kim J, Park H, Hannon JB, Bedell SW, Fogel K, Sadana DK, et al. Layer-Resolved Graphene Transfer via Engineered Strain Layers. Science 2013;342:833–6. doi:10.1126/science.1242988.

[38] Bae S, Kim H, Lee Y, Xu X, Park J-S, Zheng Y, et al. Roll-to-roll production of 30-inch graphene films for transparent electrodes. Nature Nanotechnology 2010;5:574–8. doi:10.1038/nnano.2010.132.

[39] Pirkle A, Chan J, Venugopal A, Hinojos D, Magnuson CW, McDonnell S, et al. The effect of chemical residues on the physical and electrical properties of chemical vapor deposited graphene transferred to SiO_2. Applied Physics Letters 2011;99:122108. doi:10.1063/1.3643444.

[40] Hwang J, Kim M, Campbell D, Alsalman HA, Kwak JY, Shivaraman S, et al. van der Waals Epitaxial Growth of Graphene on Sapphire by Chemical Vapor Deposition without a Metal Catalyst. ACS Nano 2013;7:385–95. doi:10.1021/nn305486x.

[41] Strupinski W, Grodecki K, Wysmolek A, Stepniewski R, Szkopek T, Gaskell PE, et al. Graphene Epitaxy by Chemical Vapor Deposition on SiC. Nano Letters 2011;11:1786–91. doi:10.1021/nl200390e.

[42] Michon A, Vézian S, Roudon E, Lefebvre D, Zielinski M, Chassagne T, et al. Effects of pressure, temperature, and hydrogen during graphene growth on SiC(0001) using propane-hydrogen chemical vapor deposition. Journal of Applied Physics 2013;113:203501. doi:10.1063/1.4806998.

[43] Michon A, Largeau L, Mauguin O, Ouerghi A, Vézian S, Lefebvre D, et al. Graphene growth using propane-hydrogen CVD on 6H-SiC(0001): temperature dependent interface and strain. Physica Status Solidi (C) 2012;9:175–8. doi:10.1002/pssc.201100225.

[44] Srivastava N, He G, Luxmi, Mende PC, Feenstra RM, Sun Y. Graphene formed on SiC under various environments: comparison of Si-face and C-face. Journal of Physics D: Applied Physics 2012;45:154001. doi:10.1088/0022-3727/45/15/154001.

[45] Portail M, Michon A, Vézian S, Lefebvre D, Chenot S, Roudon E, et al. Growth mode and electric properties of graphene and graphitic phase grown by argon–propane assisted CVD on 3C–SiC/Si and 6H–SiC. Journal of Crystal Growth 2012;349:27–35. doi:10.1016/j.jcrysgro.2012.04.004.

[46] Jabakhanji B, Michon A, Consejo C, Desrat W, Portail M, Tiberj A, et al. Tuning the transport properties of graphene films grown by CVD on SiC(0001): Effect of *in situ* hydrogenation and annealing. Physical Review B 2014;89. doi:10.1103/PhysRevB.89.085422.

[47] Ribeiro-Palau R, Lafont F, Brun-Picard J, Kazazis D, Michon A, Cheynis F, et al. Quantum Hall resistance standard in graphene devices under relaxed experimental conditions. Nature Nanotechnology 2015;10:965–71. doi:10.1038/nnano.2015.192.

[48] Van Bommel AJ, Crombeen JE, Van Tooren A. LEED and Auger electron observations of the SiC(0001) surface. Surface Science 1975;48:463–72. doi:10.1016/0039-6028(75)90419-7.

[49] Starke U, Riedl C. Epitaxial graphene on SiC(0001) and \mathrm {SiC}(000\bar {1}) : from surface reconstructions to carbon electronics. Journal of Physics: Condensed Matter 2009;21:134016. doi:10.1088/0953-8984/21/13/134016.

[50] Tromp RM, Hannon JB. Thermodynamics and Kinetics of Graphene Growth on SiC(0001). Physical Review Letters 2009;102. doi:10.1103/PhysRevLett.102.106104.

[51] Hannon JB, Tromp RM. Pit formation during graphene synthesis on SiC(0001): *In situ* electron microscopy. Physical Review B 2008;77. doi:10.1103/PhysRevB.77.241404.

[52] Hibino H, Tanabe S, Mizuno S, Kageshima H. Growth and electronic transport properties of epitaxial graphene on SiC. Journal of Physics D: Applied Physics 2012;45:154008. doi:10.1088/0022-3727/45/15/154008.

[53] Bolen ML, Harrison SE, Biedermann LB, Capano MA. Graphene formation mechanisms on 4 H -SiC (0001). Physical Review B 2009;80. doi:10.1103/PhysRevB.80.115433.

[54] Riedl C, Coletti C, Starke U. Structural and electronic properties of epitaxial graphene on SiC(0 0 0 1): a review of growth, characterization, transfer doping and hydrogen intercalation. Journal of Physics D: Applied Physics 2010;43:374009. doi:10.1088/0022-3727/43/37/374009.

[55] Borovikov V, Zangwill A. Step-edge instability during epitaxial growth of graphene from SiC(0001). Physical Review B 2009;80. doi:10.1103/PhysRevB.80.121406.

[56] Kageshima H, Hibino H, Yamaguchi H, Nagase M. Stability and reactivity of steps in the initial stage of graphene growth on the SiC(0001) surface. Physical Review B 2013;88. doi:10.1103/PhysRevB.88.235405.

[57] Sun GF, Liu Y, Rhim SH, Jia JF, Xue QK, Weinert M, et al. Si diffusion path for pit-free graphene growth on SiC(0001). Physical Review B 2011;84. doi:10.1103/PhysRevB.84.195455.

[58] Syväjärvi M. Interfacial Properties in Liquid Phase Growth of SiC. Journal of The Electrochemical Society 1999;146:1565. doi:10.1149/1.1391805.

[59] de Heer WA, Berger C, Ruan M, Sprinkle M, Li X, Hu Y, et al. Large area and structured epitaxial graphene produced by confinement controlled sublimation of silicon carbide. Proceedings of the National Academy of Sciences 2011;108:16900–5. doi:10.1073/pnas.1105113108.

[60] Wu YQ, Farmer DB, Valdes-Garcia A, Zhu WJ, Jenkins KA, Dimitrakopoulos C, et al. Record high RF performance for epitaxial graphene transistors, IEEE; 2011, p. 23.8.1-23.8.3. doi:10.1109/IEDM.2011.6131601.

[61] Panchal V, Cedergren K, Yakimova R, Tzalenchuk A, Kubatkin S, Kazakova O. Small epitaxial graphene devices for magnetosensing applications. Journal of Applied Physics 2012;111:07E509. doi:10.1063/1.3677769.

[62] Mueller T, Xia F, Avouris P. Graphene photodetectors for high-speed optical communications. Nature Photonics 2010;4:297–301. doi:10.1038/nphoton.2010.40.

[63] Pearce R, Iakimov T, Andersson M, Hultman L, Spetz AL, Yakimova R. Epitaxially grown graphene based gas sensors for ultra sensitive NO2 detection. Sensors and Actuators B: Chemical 2011;155:451–5. doi:10.1016/j.snb.2010.12.046.

[64] Schedin F, Geim AK, Morozov SV, Hill EW, Blake P, Katsnelson MI, et al. Detection of individual gas molecules adsorbed on graphene. Nature Materials 2007;6:652–5. doi:10.1038/nmat1967.

[65] Wu Y, Jenkins KA, Valdes-Garcia A, Farmer DB, Zhu Y, Bol AA, et al. State-of-the-Art Graphene High-Frequency Electronics. Nano Letters 2012;12:3062–7. doi:10.1021/nl300904k.

[66] Tzalenchuk A, Lara-Avila S, Cedergren K, Syväjärvi M, Yakimova R, Kazakova O, et al. Engineering and metrology of epitaxial graphene. Solid State Communications 2011;151:1094–9. doi:10.1016/j.ssc.2011.05.020.

[67] Giesbers AJM, Rietveld G, Houtzager E, Zeitler U, Yang R, Novoselov KS, et al. Quantum resistance metrology in graphene. Applied Physics Letters 2008;93:222109. doi:10.1063/1.3043426.

[68] Beshkova M, Hultman L, Yakimova R. Device applications of epitaxial graphene on silicon carbide. Vacuum 2016;128:186–97. doi:10.1016/j.vacuum.2016.03.027.

[69] Jia Y, Guo L, Lin J, Chen L, Chen X. Wafer-scale graphene on 2 inch SiC with uniform structural and electrical characteristics. Chinese Science Bulletin 2012;57:3022–5. doi:10.1007/s11434-012-5161-8.

[70] Dimitrakopoulos C, Lin Y-M, Grill A, Farmer DB, Freitag M, Sun Y, et al. Wafer-scale epitaxial graphene growth on the Si-face of hexagonal SiC (0001) for high frequency transistors. Journal of Vacuum Science & Technology B, Nanotechnology and Microelectronics: Materials, Processing, Measurement, and Phenomena 2010;28:985–92. doi:10.1116/1.3480961.

[71] Ni ZH, Ponomarenko LA, Nair RR, Yang R, Anissimova S, Grigorieva IV, et al. On Resonant Scatterers As a Factor Limiting Carrier Mobility in Graphene. Nano Letters 2010;10:3868–72. doi:10.1021/nl101399r.

[72] Li X, Magnuson CW, Venugopal A, An J, Suk JW, Han B, et al. Graphene Films with Large Domain Size by a Two-Step Chemical Vapor Deposition Process. Nano Letters 2010;10:4328–34. doi:10.1021/nl101629g.

[73] Liu Q, Yu C, He Z, Gu G, Wang J, Zhou C, et al. Chemical vapor deposition graphene of high mobility by gradient growth method on an 4H-SiC (0 0 0 1) substrate. Applied Surface Science 2018;454:68–73. doi:10.1016/j.apsusc.2018.05.131.

[74] Arslan E, Çakmakyapan S, Kazar Ö, Bütün S, Lişesivdin SB, Cinel NA, et al. SiC Substrate effects on electron transport in the epitaxial graphene layer. Electronic Materials Letters 2014;10:387–91. doi:10.1007/s13391-013-3159-2.

[75] Schall D, Neumaier D, Mohsin M, Chmielak B, Bolten J, Porschatis C, et al. 50 GBit/s Photodetectors Based on Wafer-Scale Graphene for Integrated Silicon Photonic Communication Systems. ACS Photonics 2014;1:781–4. doi:10.1021/ph5001605.

[76] Avouris P. Graphene: Electronic and Photonic Properties and Devices. Nano Letters 2010;10:4285–94. doi:10.1021/nl102824h.

[77] Sarkar S, Amin KR, Modak R, Singh A, Mukerjee S, Bid A. Role of different scattering mechanisms on the temperature dependence of transport in graphene. Scientific Reports 2015;5. doi:10.1038/srep16772.

[78] Tzalenchuk A, Lara-Avila S, Kalaboukhov A, Paolillo S, Syväjärvi M, Yakimova R, et al. Towards a quantum resistance standard based on epitaxial graphene. Nature Nanotechnology 2010;5:186–9. doi:10.1038/nnano.2009.474.

[79] Matsunami H, Kimoto T. Step-controlled epitaxial growth of SiC: High quality homoepitaxy. Materials Science and Engineering: R: Reports 1997;20:125–66. doi:10.1016/S0927-796X(97)00005-3.

[80] Råback P. Modeling of the sublimation growth of silicon carbide crystals. n.d.

[81] Forbeaux I, Themlin J-M, Debever J-M. Heteroepitaxial graphite on 6 H − SiC (0001) : Interface formation through conduction-band electronic structure. Physical Review B 1998;58:16396–406. doi:10.1103/PhysRevB.58.16396.

[82] Mallet P, Varchon F, Naud C, Magaud L, Berger C, Veuillen J-Y. Electron states of mono- and bilayer graphene on SiC probed by scanning-tunneling microscopy. Physical Review B 2007;76. doi:10.1103/PhysRevB.76.041403.

[83] Hass J, Millán-Otoya JE, First PN, Conrad EH. Interface structure of epitaxial graphene grown on 4H-SiC(0001). Physical Review B 2008;78. doi:10.1103/PhysRevB.78.205424.

[84] Prakash G, Capano MA, Bolen ML, Zemlyanov D, Reifenberger RG. AFM study of ridges in few-layer epitaxial graphene grown on the carbon-face of 4H–SiC. Carbon 2010;48:2383–93. doi:10.1016/j.carbon.2010.02.026.

[85] Landois P, Wang T, Nachawaty A, Bayle M, Decams J-M, Desrat W, et al. Growth of low doped monolayer graphene on SiC(0001) via sublimation at low argon pressure. Phys Chem Chem Phys 2017;19:15833–41. doi:10.1039/C7CP01012E.

[86] Ni ZH, Chen W, Fan XF, Kuo JL, Yu T, Wee ATS, et al. Raman spectroscopy of epitaxial graphene on a SiC substrate. Physical Review B 2008;77. doi:10.1103/PhysRevB.77.115416.

[87] Lee JE, Ahn G, Shim J, Lee YS, Ryu S. Optical separation of mechanical strain from charge doping in graphene. Nature Communications 2012;3. doi:10.1038/ncomms2022.

[88] Camara N, Huntzinger J-R, Rius G, Tiberj A, Mestres N, Pérez-Murano F, et al. Anisotropic growth of long isolated graphene ribbons on the C face of graphite-capped 6 H -SiC. Physical Review B 2009;80. doi:10.1103/PhysRevB.80.125410.

[89] de Heer WA, Berger C, Wu X, Sprinkle M, Hu Y, Ruan M, et al. Epitaxial graphene electronic structure and transport. Journal of Physics D: Applied Physics 2010;43:374007. doi:10.1088/0022-3727/43/37/374007.

[90] Jouault B, Camara N, Jabakhanji B, Caboni A, Consejo C, Godignon P, et al. Quantum Hall effect in bottom-gated epitaxial graphene grown on the C-face of SiC. Applied Physics Letters 2012;100:052102. doi:10.1063/1.3680564.

[91] Emtsev KV, Speck F, Seyller T, Ley L, Riley JD. Interaction, growth, and ordering of epitaxial graphene on SiC{0001} surfaces: A comparative photoelectron spectroscopy study. Physical Review B 2008;77. doi:10.1103/PhysRevB.77.155303.

[92] Goler S, Coletti C, Piazza V, Pingue P, Colangelo F, Pellegrini V, et al. Revealing the atomic structure of the buffer layer between SiC(0001) and epitaxial graphene. Carbon 2013;51:249–54. doi:10.1016/j.carbon.2012.08.050.

[93] Hannon JB, Copel M, Tromp RM. Direct Measurement of the Growth Mode of Graphene on SiC(0001) and SiC (000 $\bar{1}$). Physical Review Letters 2011;107. doi:10.1103/PhysRevLett.107.166101.

[94] Hass J, de Heer WA, Conrad EH. The growth and morphology of epitaxial multilayer graphene. Journal of Physics: Condensed Matter 2008;20:323202. doi:10.1088/0953-8984/20/32/323202.

[95] Delhaès P, editor. Graphite and precursors. Amsterdam [u.A]: Gordon and Breach; 2001.

[96] Charrier A, Coati A, Argunova T, Thibaudau F, Garreau Y, Pinchaux R, et al. Solid-state decomposition of silicon carbide for growing ultra-thin heteroepitaxial graphite films. Journal of Applied Physics 2002;92:2479–84. doi:10.1063/1.1498962.

[97] Norimatsu W, Kusunoki M. Selective formation of ABC-stacked graphene layers on SiC(0001). Physical Review B 2010;81. doi:10.1103/PhysRevB.81.161410.

[98] Bernhardt J, Nerding M, Starke U, Heinz K. Stable surface reconstructions on 6H–SiC(000). Materials Science and Engineering: B 1999;61–62:207–11. doi:10.1016/S0921-5107(98)00503-0.

[99] Forbeaux I, Themlin J-M, Charrier A, Thibaudau F, Debever J-M. Solid-state graphitization mechanisms of silicon carbide 6H–SiC polar faces. Applied Surface Science 2000;162–163:406–12. doi:10.1016/S0169-4332(00)00224-5.

[100] Forbeaux I, Themlin J-M, Debever J-M. High-temperature graphitization of the 6H-SiC face. Surface Science 1999;442:9–18. doi:10.1016/S0039-6028(99)00891-2.

[101] Tiberj A, Huntzinger J-R, Camassel J, Hiebel F, Mahmood A, Mallet P, et al. Multiscale investigation of graphene layers on 6H-SiC(000-1). Nanoscale Research Letters 2011;6:171. doi:10.1186/1556-276X-6-171.

[102] Hass J, Varchon F, Millán-Otoya JE, Sprinkle M, Sharma N, de Heer WA, et al. Why Multilayer Graphene on 4 H − SiC (000 $\bar{1}$) Behaves Like a Single Sheet

of Graphene. Physical Review Letters 2008;100. doi:10.1103/PhysRevLett.100.125504.

[103] Nemec L, Lazarevic F, Rinke P, Scheffler M, Blum V. Why graphene growth is very different on the C face than on the Si face of SiC: Insights from surface equilibria and the (3$\times$3)-3C-SiC($\bar{\text{1}}\bar{\text{1}}\bar{\text{1}}$) reconstruction. Physical Review B 2015;91. doi:10.1103/PhysRevB.91.161408.

[104] Daas BK, Omar SU, Shetu S, Daniels KM, Ma S, Sudarshan TS, et al. Comparison of Epitaxial Graphene Growth on Polar and Nonpolar 6H-SiC Faces: On the Growth of Multilayer Films. Crystal Growth & Design 2012;12:3379–87. doi:10.1021/cg300456v.

[105] Tedesco JL, Jernigan GG, Culbertson JC, Hite JK, Yang Y, Daniels KM, et al. Morphology characterization of argon-mediated epitaxial graphene on C-face SiC. Applied Physics Letters 2010;96:222103. doi:10.1063/1.3442903.

[106] Tedesco JL, VanMil BL, Myers-Ward RL, McCrate JM, Kitt SA, Campbell PM, et al. Hall effect mobility of epitaxial graphene grown on silicon carbide. Applied Physics Letters 2009;95:122102. doi:10.1063/1.3224887.

[107] Wu X, Hu Y, Ruan M, Madiomanana NK, Berger C, de Heer WA. Thermoelectric effect in high mobility single layer epitaxial graphene. Applied Physics Letters 2011;99:133102. doi:10.1063/1.3641424.

[108] Rutter GM, Guisinger NP, Crain JN, Jarvis EAA, Stiles MD, Li T, et al. Imaging the interface of epitaxial graphene with silicon carbide via scanning tunneling microscopy. Physical Review B 2007;76. doi:10.1103/PhysRevB.76.235416.

[109] Lauffer P, Emtsev KV, Graupner R, Seyller T, Ley L, Reshanov SA, et al. Atomic and electronic structure of few-layer graphene on SiC(0001) studied with scanning tunneling microscopy and spectroscopy. Physical Review B 2008;77. doi:10.1103/PhysRevB.77.155426.

[110] Conrad M, Wang F, Nevius M, Jinkins K, Celis A, Narayanan Nair M, et al. Wide Band Gap Semiconductor from a Hidden 2D Incommensurate Graphene Phase. Nano Letters 2017;17:341–7. doi:10.1021/acs.nanolett.6b04196.

[111] Riedl C, Coletti C, Iwasaki T, Zakharov AA, Starke U. Quasi-Free-Standing Epitaxial Graphene on SiC Obtained by Hydrogen Intercalation. Physical Review Letters 2009;103. doi:10.1103/PhysRevLett.103.246804.

[112] Seyller T, Emtsev KV, Gao K, Speck F, Ley L, Tadich A, et al. Structural and electronic properties of graphite layers grown on SiC(0001). Surface Science 2006;600:3906–11. doi:10.1016/j.susc.2006.01.102.

[113] Pallecchi E, Lafont F, Cavaliere V, Schopfer F, Mailly D, Poirier W, et al. High Electron Mobility in Epitaxial Graphene on 4H-SiC(0001) via post-growth annealing under hydrogen. Scientific Reports 2015;4. doi:10.1038/srep04558.

[114] Schumann T, Dubslaff M, Oliveira MH, Hanke M, Lopes JMJ, Riechert H. Effect of buffer layer coupling on the lattice parameter of epitaxial graphene on SiC(0001). Physical Review B 2014;90. doi:10.1103/PhysRevB.90.041403.

[115] P.G. Neudeck. SiC Technology. The Electrical Engineering Handbook Series. CRC Press and IEEE Press; 2000.

[116] Yazdi G, Iakimov T, Yakimova R. Epitaxial Graphene on SiC: A Review of Growth and Characterization. Crystals 2016;6:53. doi:10.3390/cryst6050053.

[117] Norimatsu W, Kusunoki M. Epitaxial graphene on SiC{0001}: advances and perspectives. Physical Chemistry Chemical Physics 2014;16:3501. doi:10.1039/c3cp54523g.

[118] Tanaka S, Morita K, Hibino H. Anisotropic layer-by-layer growth of graphene on vicinal SiC(0001) surfaces. Physical Review B 2010;81. doi:10.1103/PhysRevB.81.041406.

[119] Ming F, Zangwill A. Model for the epitaxial growth of graphene on 6 H - SiC(0001). Physical Review B 2011;84. doi:10.1103/PhysRevB.84.115459.

[120] Oliveira MH, Schumann T, Ramsteiner M, Lopes JMJ, Riechert H. Influence of the silicon carbide surface morphology on the epitaxial graphene formation. Applied Physics Letters 2011;99:111901. doi:10.1063/1.3638058.

[121] Bao J, Yasui O, Norimatsu W, Matsuda K, Kusunoki M. Sequential control of step-bunching during graphene growth on SiC (0001). Applied Physics Letters 2016;109:081602. doi:10.1063/1.4961630.

[122] Kruskopf M, Pierz K, Wundrack S, Stosch R, Dziomba T, Kalmbach C-C, et al. Epitaxial graphene on SiC: modification of structural and electron transport properties by substrate pretreatment. Journal of Physics: Condensed Matter 2015;27:185303. doi:10.1088/0953-8984/27/18/185303.

[123] Dimitrakopoulos C, Grill A, McArdle TJ, Liu Z, Wisnieff R, Antoniadis DA. Effect of SiC wafer miscut angle on the morphology and Hall mobility of epitaxially grown graphene. Applied Physics Letters 2011;98:222105. doi:10.1063/1.3595945.

[124] Eriksson J, Pearce R, Iakimov T, Virojanadara C, Gogova D, Andersson M, et al. The influence of substrate morphology on thickness uniformity and unintentional doping of epitaxial graphene on SiC. Applied Physics Letters 2012;100:241607. doi:10.1063/1.4729556.

[125] Ji S-H, Hannon JB, Tromp RM, Perebeinos V, Tersoff J, Ross FM. Atomic-scale transport in epitaxial graphene. Nature Materials 2011;11:114–9. doi:10.1038/nmat3170.

[126] Low T, Perebeinos V, Tersoff J, Avouris P. Deformation and Scattering in Graphene over Substrate Steps. Physical Review Letters 2012;108. doi:10.1103/PhysRevLett.108.096601.

[127] Guo Y, Guo LW, Huang J, Yang R, Jia YP, Lin JJ, et al. The correlation of epitaxial graphene properties and morphology of SiC (0001). Journal of Applied Physics 2014;115:043527. doi:10.1063/1.4863796.

[128] Weingart S, Bock C, Kunze U, Emtsev KV, Seyller T, Ley L. Influence of the growth conditions of epitaxial graphene on the film topography and the electron transport properties. Physica E: Low-Dimensional Systems and Nanostructures 2010;42:687–90. doi:10.1016/j.physe.2009.11.006.

[129] Aritsuki T, Nakashima T, Kobayashi K, Ohno Y, Nagase M. Epitaxial graphene on SiC formed by the surface structure control technique. Japanese Journal of Applied Physics 2016;55:06GF03. doi:10.7567/JJAP.55.06GF03.

[130] http://www.annealsys.com n.d.

[131] Wang YG, Zhang LC. A Review on the CMP of SiC and Sapphire Wafers. Advanced Materials Research 2010;126–128:429–34. doi:10.4028/www.scientific.net/AMR.126-128.429.

[132] Ferrari AC, Robertson J. Interpretation of Raman spectra of disordered and amorphous carbon. Physical Review B 2000;61:14095–107. doi:10.1103/PhysRevB.61.14095.

[133] Ferrari AC, Meyer JC, Scardaci V, Casiraghi C, Lazzeri M, Mauri F, et al. Raman Spectrum of Graphene and Graphene Layers. Physical Review Letters 2006;97. doi:10.1103/PhysRevLett.97.187401.

[134] Cançado LG, Jorio A, Ferreira EHM, Stavale F, Achete CA, Capaz RB, et al. Quantifying Defects in Graphene via Raman Spectroscopy at Different Excitation Energies. Nano Letters 2011;11:3190–6. doi:10.1021/nl201432g.

[135] Beams R, Gustavo Cançado L, Novotny L. Raman characterization of defects and dopants in graphene. Journal of Physics: Condensed Matter 2015;27:083002. doi:10.1088/0953-8984/27/8/083002.

[136] Casiraghi C. Doping dependence of the Raman peaks intensity of graphene close to the Dirac point. Physical Review B 2009;80. doi:10.1103/PhysRevB.80.233407.

[137] Raman CV. A new radiation [Reproduced from Indian J. Phys., 1928, 2, 387–398]. Current Science 1998;74:382–6.

[138] Ferrari AC, Meyer JC, Scardaci V, Casiraghi C, Lazzeri M, Mauri F, et al. Raman Spectrum of Graphene and Graphene Layers. Physical Review Letters 2006;97. doi:10.1103/PhysRevLett.97.187401.

[139] Ferrari AC, Basko DM. Raman spectroscopy as a versatile tool for studying the properties of graphene. Nature Nanotechnology 2013;8:235–46. doi:10.1038/nnano.2013.46.

[140] Martins Ferreira EH, Moutinho MVO, Stavale F, Lucchese MM, Capaz RB, Achete CA, et al. Evolution of the Raman spectra from single-, few-, and many-layer graphene with increasing disorder. Physical Review B 2010;82. doi:10.1103/PhysRevB.82.125429.

[141] Bayle M, Reckinger N, Huntzinger J-R, Felten A, Bakaraki A, Landois P, et al. Dependence of the Raman spectrum characteristics on the number of layers and stacking orientation in few-layer graphene: Raman spectrum dependence on layers and stacking orientation in FLG. Physica Status Solidi (B) 2015;252:2375–9. doi:10.1002/pssb.201552204.

[142] Camara N, Huntzinger J-R, Rius G, Tiberj A, Mestres N, Pérez-Murano F, et al. Anisotropic growth of long isolated graphene ribbons on the C face of graphite-capped 6 H -SiC. Physical Review B 2009;80. doi:10.1103/PhysRevB.80.125410.

[143] Bayle M, Reckinger N, Felten A, Landois P, Lancry O, Dutertre B, et al. Determining the number of layers in few-layer graphene by combining Raman spectroscopy and optical contrast: Number of graphene layers by combining Raman spectroscopy and optical contrast. Journal of Raman Spectroscopy 2018;49:36–45. doi:10.1002/jrs.5279.

[144] Fromm F, Oliveira Jr MH, Molina-Sánchez A, Hundhausen M, Lopes JMJ, Riechert H, et al. Contribution of the buffer layer to the Raman spectrum of epitaxial graphene on SiC(0001). New Journal of Physics 2013;15:043031. doi:10.1088/1367-2630/15/4/043031.

[145] Das A, Pisana S, Chakraborty B, Piscanec S, Saha SK, Waghmare UV, et al. Monitoring dopants by Raman scattering in an electrochemically top-gated graphene transistor. Nature Nanotechnology 2008;3:210–5. doi:10.1038/nnano.2008.67.

[146] Ferralis N, Maboudian R, Carraro C. Evidence of Structural Strain in Epitaxial Graphene Layers on 6H-SiC(0001). Physical Review Letters 2008;101. doi:10.1103/PhysRevLett.101.156801.

[147] Wang Y ying, Ni Z hua, Yu T, Shen ZX, Wang H min, Wu Y hong, et al. Raman Studies of Monolayer Graphene: The Substrate Effect. The Journal of Physical Chemistry C 2008;112:10637–40. doi:10.1021/jp8008404.

[148] Schmidt DA, Ohta T, Beechem TE. Strain and charge carrier coupling in epitaxial graphene. Physical Review B 2011;84. doi:10.1103/PhysRevB.84.235422.

[149] Cleveland JP, Anczykowski B, Schmid AE, Elings VB. Energy dissipation in tapping-mode atomic force microscopy. Applied Physics Letters 1998;72:2613–5. doi:10.1063/1.121434.

[150] Byers JC, Tamiasso-Martinhon P, Deslouis C, Pailleret A, Semenikhin OA. Atomic Force Microscopy Studies of Carbon Nitride (CNx) Films Deposited on a Conducting Polymer Substrate. The Journal of Physical Chemistry C 2010;114:18474–80. doi:10.1021/jp103795c.

[151] Ferrer FJ, Moreau E, Vignaud D, Deresmes D, Godey S, Wallart X. Initial stages of graphitization on SiC(000-1), as studied by phase atomic force microscopy. Journal of Applied Physics 2011;109:054307. doi:10.1063/1.3560896.

[152] Varchon F, Feng R, Hass J, Li X, Nguyen BN, Naud C, et al. Electronic Structure of Epitaxial Graphene Layers on SiC: Effect of the Substrate. Physical Review Letters 2007;99. doi:10.1103/PhysRevLett.99.126805.

[153] Vesapuisto E, Kim W, Novikov S, Lipsanen H, Kuivalainen P. Growth temperature dependence of the electrical and structural properties of epitaxial graphene on SiC(0001). Physica Status Solidi (B) 2011;248:1908–14. doi:10.1002/pssb.201046368.

[154] Hupalo M, Conrad EH, Tringides MC. Growth mechanism for epitaxial graphene on vicinal 6 H -SiC (0001) surfaces: A scanning tunneling microscopy study. Physical Review B 2009;80. doi:10.1103/PhysRevB.80.041401.

[155] Bolen ML, Harrison SE, Biedermann LB, Capano MA. Graphene formation mechanisms on 4 H -SiC (0001). Physical Review B 2009;80. doi:10.1103/PhysRevB.80.115433.

[156] Hibino H, Kageshima H, Nagase M. Epitaxial few-layer graphene: towards single crystal growth. Journal of Physics D: Applied Physics 2010;43:374005. doi:10.1088/0022-3727/43/37/374005.

[157] Horcas I, Fernández R, Gómez-Rodríguez JM, Colchero J, Gómez-Herrero J, Baro AM. A software for scanning probe microscopy and a tool for

nanotechnology. Review of Scientific Instruments 2007;78:013705. doi:10.1063/1.2432410.

[158] van der PAUW LJ. A METHOD OF MEASURING SPECIFIC RESISTIVITY AND HALL EFFECT OF DISCS OF ARBITRARY SHAPE. Semiconductor Devices: Pioneering Papers, WORLD SCIENTIFIC; 1991, p. 174–82. doi:10.1142/9789814503464_0017.

[159] Kruskopf M, Elmquist RE. Epitaxial graphene for quantum resistance metrology. Metrologia 2018;55:R27–36. doi:10.1088/1681-7575/aacd23.

[160] Alexander-Webber JA, Huang J, Maude DK, Janssen TJBM, Tzalenchuk A, Antonov V, et al. Giant quantum Hall plateaus generated by charge transfer in epitaxial graphene. Scientific Reports 2016;6. doi:10.1038/srep30296.

[161] Rutter GM, Crain JN, Guisinger NP, Li T, First PN, Stroscio JA. Scattering and Interference in Epitaxial Graphene. Science 2007;317:219–22. doi:10.1126/science.1142882.

[162]Chen L, Cheng P, Wu K. Quasiparticle interference in unconventional 2D systems. Journal of Physics: Condensed Matter 2017;29:103001. doi:10.1088/1361-648X/aa54da.

[163] Strupinski W, Grodecki K, Caban P, Ciepielewski P, Jozwik-Biala I, Baranowski JM. Formation mechanism of graphene buffer layer on SiC(0001). Carbon 2015;81:63–72. doi:10.1016/j.carbon.2014.08.099.

[164] Tiberj A, Huntzinger J-R, Camara N, Godignon P, Camassel J. Raman spectrum and optical extinction of graphene buffer layers on the Si-face of 6H-SiC. ArXiv 2012.

[165] Ferrari AC, Robertson J. Interpretation of Raman spectra of disordered and amorphous carbon. Physical Review B 2000;61:14095–107. doi:10.1103/PhysRevB.61.14095.

[166] Tiberj A, Rubio-Roy M, Paillet M, Huntzinger J-R, Landois P, Mikolasek M, et al. Reversible optical doping of graphene. Scientific Reports 2013;3. doi:10.1038/srep02355.

[167] Kruskopf M, Pakdehi DM, Pierz K, Wundrack S, Stosch R, Dziomba T, et al. Comeback of epitaxial graphene for electronics: large-area growth of bilayer-free graphene on SiC. 2D Materials 2016;3:041002. doi:10.1088/2053-1583/3/4/041002.

[168] Morita M, Norimatsu W, Qian H-J, Irle S, Kusunoki M. Atom-by-atom simulations of graphene growth by decomposition of SiC (0001): Impact of the substrate steps. Applied Physics Letters 2013;103:141602. doi:10.1063/1.4824425.

[169] Norimatsu W, Kusunoki M. Formation process of graphene on SiC (0001). Physica E: Low-Dimensional Systems and Nanostructures 2010;42:691–4. doi:10.1016/j.physe.2009.11.151.

[170] Kumar B, Baraket M, Paillet M, Huntzinger J-R, Tiberj A, Jansen AGM, et al. Growth protocols and characterization of epitaxial graphene on SiC elaborated in a graphite enclosure. Physica E: Low-Dimensional Systems and Nanostructures 2016;75:7–14. doi:10.1016/j.physe.2015.07.022.

[171] Robinson J, Weng X, Trumbull K, Cavalero R, Wetherington M, Frantz E, et al. Nucleation of Epitaxial Graphene on SiC(0001). ACS Nano 2010;4:153–8. doi:10.1021/nn901248j.

[172] Kazakova O, Panchal V, Burnett T. Epitaxial Graphene and Graphene–Based Devices Studied by Electrical Scanning Probe Microscopy. Crystals 2013;3:191–233. doi:10.3390/cryst3010191.

[173] Ohta T, Bartelt NC, Nie S, Thürmer K, Kellogg GL. Role of carbon surface diffusion on the growth of epitaxial graphene on SiC. Physical Review B 2010;81. doi:10.1103/PhysRevB.81.121411.

[174] Ohta T, El Gabaly F, Bostwick A, McChesney JL, Emtsev KV, Schmid AK, et al. Morphology of graphene thin film growth on SiC(0001). New Journal of Physics 2008;10:023034. doi:10.1088/1367-2630/10/2/023034.

[175] Sun GF, Jia JF, Xue QK, Li L. Atomic-scale imaging and manipulation of ridges on epitaxial graphene on 6H-SiC(0001). Nanotechnology 2009;20:355701. doi:10.1088/0957-4484/20/35/355701.

[176] Galeckas A, Linnros J, Pirouz P. Recombination-Induced Stacking Faults: Evidence for a General Mechanism in Hexagonal SiC. Physical Review Letters 2006;96. doi:10.1103/PhysRevLett.96.025502.

[177] Panchal V, Giusca CE, Lartsev A, Martin NA, Cassidy N, Myers-Ward RL, et al. Atmospheric doping effects in epitaxial graphene: correlation of local and global electrical studies. 2D Materials 2016;3:015006. doi:10.1088/2053-1583/3/1/015006.

[178] McCreary KM, Pi K, Swartz AG, Han W, Bao W, Lau CN, et al. Effect of cluster formation on graphene mobility. Physical Review B 2010;81. doi:10.1103/PhysRevB.81.115453.

[179] Huang J, Alexander-Webber JA, Baker AMR, Janssen TJBM, Tzalenchuk A, Antonov V, et al. Physics of a disordered Dirac point in epitaxial graphene from temperature-dependent magnetotransport measurements. Physical Review B 2015;92. doi:10.1103/PhysRevB.92.075407.

[180] Nachawaty A, Yang M, Desrat W, Nanot S, Jabakhanji B, Kazazis D, et al. Magnetic field driven ambipolar quantum Hall effect in epitaxial graphene close to the charge neutrality point. Physical Review B 2017;96. doi:10.1103/PhysRevB.96.075442.

[181] Schumann T, Friedland K-J, Oliveira MH, Tahraoui A, Lopes JMJ, Riechert H. Anisotropic quantum Hall effect in epitaxial graphene on stepped SiC surfaces. Physical Review B 2012;85. doi:10.1103/PhysRevB.85.235402.

[182] Giannazzo F, Deretzis I, La Magna A, Roccaforte F, Yakimova R. Electronic transport at monolayer-bilayer junctions in epitaxial graphene on SiC. Physical Review B 2012;86. doi:10.1103/PhysRevB.86.235422.

[183] Conrad M, Rault J, Utsumi Y, Garreau Y, Vlad A, Coati A, et al. Structure and evolution of semiconducting buffer graphene grown on SiC(0001). Physical Review B 2017;96. doi:10.1103/PhysRevB.96.195304.

[184] Huc V, Bendiab N, Rosman N, Ebbesen T, Delacour C, Bouchiat V. Large and flat graphene flakes produced by epoxy bonding and reverse exfoliation of highly

oriented pyrolytic graphite. Nanotechnology 2008;19:455601. doi:10.1088/0957-4484/19/45/455601.

[185] Filleter T, McChesney JL, Bostwick A, Rotenberg E, Emtsev KV, Seyller T, et al. Friction and Dissipation in Epitaxial Graphene Films. Physical Review Letters 2009;102. doi:10.1103/PhysRevLett.102.086102.

[186] Conrad MD. Structure and properties of incommensurate and commensurate phases of graphene on SiC(0001). n.d.

[187] Martins Ferreira EH, Moutinho MVO, Stavale F, Lucchese MM, Capaz RB, Achete CA, et al. Evolution of the Raman spectra from single-, few-, and many-layer graphene with increasing disorder. Physical Review B 2010;82. doi:10.1103/PhysRevB.82.125429.

[188] Ferrari AC, Robertson J. Interpretation of Raman spectra of disordered and amorphous carbon. Physical Review B 2000;61:14095–107. doi:10.1103/PhysRevB.61.14095.

[189] Martin SC, Samaddar S, Sacépé B, Kimouche A, Coraux J, Fuchs F, et al. Disorder and screening in decoupled graphene on a metallic substrate. Physical Review B 2015;91. doi:10.1103/PhysRevB.91.041406.

[190] Martin J, Akerman N, Ulbricht G, Lohmann T, Smet JH, von Klitzing K, et al. Observation of electron–hole puddles in graphene using a scanning single-electron transistor. Nature Physics 2008;4:144–8. doi:10.1038/nphys781.

[191] Li Q, Hwang EH, Das Sarma S. Disorder-induced temperature-dependent transport in graphene: Puddles, impurities, activation, and diffusion. Physical Review B 2011;84. doi:10.1103/PhysRevB.84.115442.

[192] Kurganova EV, Wiedmann S, Giesbers AJM, Gorbachev RV, Novoselov KS, Katsnelson MI, et al. Quantized coexisting electrons and holes in graphene measured using temperature-dependent magnetotransport. Physical Review B 2013;87. doi:10.1103/PhysRevB.87.085447.

[193] Pallecchi E, Ridene M, Kazazis D, Mathieu C, Schopfer F, Poirier W, et al. Observation of the quantum Hall effect in epitaxial graphene on SiC(0001) with oxygen adsorption. Applied Physics Letters 2012;100:253109. doi:10.1063/1.4729824.

[194] Mallet P, Brihuega I, Bose S, Ugeda MM, Gómez-Rodríguez JM, Kern K, et al. Role of pseudospin in quasiparticle interferences in epitaxial graphene probed by high-resolution scanning tunneling microscopy. Physical Review B 2012;86. doi:10.1103/PhysRevB.86.045444.

[195] Lee K, Asbeck P. Numerical study of inhomogeneity effects on Hall measurements of graphene films. Solid-State Electronics 2015;106:34–43. doi:10.1016/j.sse.2014.12.016.

[196] Lin J, Zhong J, Reiber Kyle J, Penchev M, Ozkan M, Ozkan CS. Molecular absorption and photodesorption in pristine and functionalized large-area graphene layers. Nanotechnology 2011;22:355701. doi:10.1088/0957-4484/22/35/355701.

[197] Luo Z, Pinto NJ, Davila Y, Charlie Johnson AT. Controlled doping of graphene using ultraviolet irradiation. Applied Physics Letters 2012;100:253108. doi:10.1063/1.4729828.

[198] Iqbal MZ, Iqbal MW, Khan MF, Eom J. Ultraviolet-light-driven doping modulation in chemical vapor deposition grown graphene. Physical Chemistry Chemical Physics 2015;17:20551–6. doi:10.1039/C5CP02159F.

[199] Suk JW, Lee WH, Lee J, Chou H, Piner RD, Hao Y, et al. Enhancement of the Electrical Properties of Graphene Grown by Chemical Vapor Deposition via Controlling the Effects of Polymer Residue. Nano Letters 2013;13:1462–7. doi:10.1021/nl304420b.

[200] Prudkovskiy VS, Katin KP, Maslov MM, Puech P, Yakimova R, Deligeorgis G. Efficient cleaning of graphene from residual lithographic polymers by ozone treatment. Carbon 2016;109:221–6. doi:10.1016/j.carbon.2016.08.013.